Does it Matter?

Novel Background Modelling and First Application of Asimov Datasets for Dark Matter Searches in the Coma Dwarf Galaxy with MAGIC

Stefan Fröse
2025

A document submitted in partial fulfillment of the requirements for the degree of
Doctor rerum naturalium
at
TU Dortmund University, Department of Physics

Supervised by
Dr. habil. Dominik Martin Elsässer and Dr. Chris Malena Delitzsch

Abstract

Despite its elusive nature, dark matter is suspected of shaping the universe as we know it today. Over the past decades, various theories for its properties have emerged, most of them allowing for a coupling of the dark sector to the standard model. Dark matter candidates, such as Weakly Interacting Massive Particles (WIMPs), can annihilate to standard model particles, leading to the subsequent production of photons, whose direct production is otherwise suppressed. A substantial rate of gamma rays is expected to emerge in regions with high dark matter density, such as dwarf galaxies.

This thesis studies gamma-ray signals that are expected from CBe dSph with the MAGIC telescopes in both energy and spatial dimensions. Since the telescopes detect extensive air showers produced by the interaction of the gamma rays with Earth's atmosphere, the high rate of cosmic rays dominates the background of these observations. The impurity of signal-background separation methods necessitates the construction of a three-dimensional background model for this analysis, leading to the proposal of a novel modeling approach, the *exclusion-rotation* method.

Preceding studies relied on the one-dimensional, energy-only analysis of CBe dSph. By incorporating two additional dimensions in this work, the computational construction of upper limits on the thermally averaged cross-section of the dark matter models demands a robust and efficient calculation of statistical tests. *Asimov* datasets are introduced and applied for the first time in the context of a dark matter search using the MAGIC telescopes. These datasets enable the approximation of the test statistics, allowing for the first-ever construction of upper limits on the strength modifier of the dark matter model with the CL_s method. The implementation of these novel methods in this work is provided through the open-source Python package `TITRATE`.

No evidence of a dark matter-induced signal for annihilation to $b\bar{b}$, W^+W^-, $\mu^+\mu^-$, and $\tau^+\tau^-$ and dark matter masses m_χ between 0.17 TeV and 100 TeV in CBe dSph is found. The performance of the upper limits on the thermally averaged cross-section calculated with the Asimov datasets in one and three dimensions is compared to the classical construction with Wilks' theorem. The three-dimensional Asimov CL_s sensitivity outperforms preceding studies of CBe dSph by the MAGIC collaboration when scaled to the appropriate dark matter density assumed by MAGIC except for annihilation to $\mu^+\mu^-$ and $\tau^+\tau^-$ above $m_\chi > 8\,\mathrm{TeV}$ and $m_\chi > 13\,\mathrm{TeV}$, respectively.

Kurzfassung

Trotz ihrer unbekannten Eigenschaften wird vermutet, dass Dunkle Materie das Universum, wie wir es heute kennen, geformt hat. In den letzten Jahrzehnten sind verschiedene Theorien entstanden, von denen die meisten eine Kopplung des dunklen Sektors an das Standardmodell zulassen. Kandidaten für Dunkle Materie, wie beispielsweise Weakly Interacting Massive Particles (WIMPs), können zu Standardmodell-Teilchen annihilieren. Konsequent führt dies zur Produktion von Photonen, deren direkte Erzeugung sonst unterdrückt wäre. In Regionen mit hoher Dichte an Dunkler Materie, unter anderem Zwerggalaxien, wird eine erhebliche Rate an Gammastrahlen erwartet.
Diese Dissertation untersucht Gammasignale aus der Region von CBe dSph mit den MAGIC-Teleskopen sowohl in energetischer als auch in räumlicher Auflösung. Da die Teleskope ausgedehnte Luftschauer erfassen, die durch die Wechselwirkung der Gammastrahlen mit der Erdatmosphäre entstehen, wird der Hintergrund dieser Beobachtungen von einer hohen Rate an kosmischen Strahlen dominiert. Die Imperfektion der Methoden zur Trennung von Signal und Hintergrund erfordert die Konstruktion eines dreidimensionalen Hintergrundmodells für diese Analyse, was zur Entwicklung eines neuartigen Methode, der *exclusion-rotation* Methode, führt.
Frühere Studien basieren auf einer eindimensionalen Analyse (energetisch) von CBe dSph. Durch die Einbeziehung von zwei zusätzlichen Dimensionen in dieser Arbeit erfordert die Berechnung von Obergrenzen für den thermisch gemittelten Wirkungsquerschnitt der Dunkle-Materie-Modelle eine robuste und effiziente Berechnung statistischer Tests. *Asimov*-Datensätze werden in diesem Kontext erstmals im Rahmen einer Suche nach Dunkler Materie mit den MAGIC-Teleskopen eingeführt und angewendet. Diese Datensätze ermöglichen die Approximation der Teststatistik und erlauben erstmals die Konstruktion von Obergrenzen für den Stärkeparameter des Dunkle-Materie-Modells mit der CL_s-Methode. Die Implementierung dieser neuartigen Methoden wird über das Open-Source-Python-Paket `TITRATE` zur Verfügung gestellt.
Es konnte kein Hinweis auf ein von Dunkler Materie induziertes Signal für Annihilationen zu $b\bar{b}$, W^+W^-, $\mu^+\mu^-$ und $\tau^+\tau^-$ sowie für Dunkle-Materie-Massen m_χ zwischen 0,17 TeV und 100 TeV in CBe dSph gefunden werden. Die Obergrenzen für den thermisch gemittelten Wirkungsquerschnitt, berechnet mit den Asimov-Datensätzen in einer und drei Dimensionen, werden mit der klassischen Konstruktion nach Wilks' Theorem verglichen. Die dreidimensionale Asimov-CL_s-Sensitivität übertrifft frühere Studien der MAGIC-Kollaboration zu CBe dSph, wenn die Ergebnisse auf die von MAGIC angenommene Dunkle-Materie-Dichte skaliert werden, mit Ausnahme der Annihilation zu $\mu^+\mu^-$ und $\tau^+\tau^-$ oberhalb von $m_\chi > 8\,\mathrm{TeV}$ und $m_\chi > 13\,\mathrm{TeV}$.

Contents

1 Introduction

Imagine standing on the highest mountain on a small island west of Africa, in the midst of the night. As your eyes adjust to the darkness, hundreds of thousands of stars become visible. If the conditions are ideal, you might notice a bright band of stars stretching across the sky – the Galactic Plane.

"How is it that the stars seem to have assembled in this region?"

"Did the stars shape the Galactic Plane, or did the Galactic Plane guide the stars into this structure?"

"How do galaxies themselves arrange in the universe?"

"What drives structural formation?"

Answers to these questions have been found throughout scientific history by studying the motions of stars and galaxies. Notably, the work by Fritz Zwicky [1, 2] and Vera Rubin [3] laid the foundation for the widely accepted concept of an unknown type of matter – Dark Matter (DM) – which acts as an optically invisible driving force shaping our universe.

Although invisible, DM is expected to interact with Standard Model (SM) particles [4, 5]. The annihilation or decay of DM particles could produce SM particles that traverse the cosmos, carrying information about their origin and fundamental properties. The measurement of ionizing radiation in the Earth's atmosphere conducted by Victor Hess, lead to the groundbreaking discovery that these cosmic particles could travel vast distances to reach Earth [6]. A new observational window has been opened, enabling the study of particles from space and marking the birth of astroparticle physics.

More than a century after Victor Hess's discovery, the scientific community is capable of studying Cosmic Rays (CRs), neutrinos, and gamma rays reaching our planet using complex instruments placed in some of the most remote locations on Earth. One such location is the Roque de los Muchachos on the Spanish island of La Palma – the very setting where the journey of questions in this chapter began. Here, the Major Atmospheric Gamma-Ray Imaging Cherenkov Telescopes (MAGIC) capture the footprint of cosmic gamma rays interacting with the Earth's atmosphere, enabling the investigation of particle energies up to several TeV. To date, MAGIC has been utilized to search for gamma-ray signatures arising from DM in the Galactic Center [7], dwarf galaxies [8], and galaxy clusters [9].
Despite significant advancement in the reconstruction of the gamma-ray properties, several challenges remain. One of the key difficulties in the search for DM is the accurate modelling of background signals that are introduced by the imperfect separation of the gamma rays from the CR events captured by the telescopes.
Another major challenge lies in the statistical testing required to claim a signal or set upper limits (ULs) on a DM model parameter. Such testing must be both robust and computationally efficient to be practical for complex analyses.

The goal of this work is to perform a first-ever three-dimensional DM search in Coma Berenices (CBe) Dwarf Spheroidal Galaxy (dSph), a region with high DM density, with the MAGIC telescopes. This complex analysis necessitates the development of a novel background model in both energy and spatial dimensions directly from source observations, as well as the introduction of novel statistical methods – known as *Asimov* approximations – for constructing robust ULs on the thermally averaged cross-section of annihilating DM efficiently.
The observations of CBe dSph by MAGIC are processed to a higher data format using the Automatic Analysis of MAGIC Data (autoMAGIC) pipeline [10] and further analyzed with the gamma ray analysis tool `Gammapy` [11]. The background modeling is cross-checked on Crab Nebula observations, as a standard candle in gamma ray astronomy, which are processed in a similar manner. Moreover, these novel statistical methods developed in this work are provided to the gamma-ray community through the open-source software package `TITRATE` [12].

In Chapter 2 DM is introduced in a brief historic context and various model candidates are discussed. Further, the expected gamma-ray flux arising from dSph is described.
Chapter 3 explores the propagation of the DM-induced gamma rays within the context of Multi-Messenger astronomy (MMA), from the origin of production, through their interaction with the Earth's atmosphere, their subsequent detection, and data acquisition with the MAGIC telescopes.
Chapter 4 details the data processing of MAGIC, from its raw data format to

the standardized Data Level 3 (DL3) format [13] with the autoMAGIC pipeline. Additionally, this chapter introduces various concepts for background modelling to produce full-enclosure Instrument Response Functions (IRFs) needed for the calculation of the expected DM signal.
Chapter 5 focuses on the statistical methods required to extract scientific results from the DL3 with `Gammapy`. It includes the introduction of test statistics (TSs) to calculate the significance of a source and set ULs on the strength parameter of a model. The integration of the novel Asimov datasets into `Gammapy` via the `TITRATE` package is explained.
Chapter 6 presents the novel *exclusion-rotation* method for background modelling and evaluates its performance using a blind dataset of Crab Nebula observations. This step goes beyond the standard cross-check conducted by MAGIC.
Chapter 7 highlights the results of the DM search for the CBe dSph using the newly developed methods. It includes a detailed comparison between *classical* and *Asimov* limits, as well as a comparison of the 3D analysis to the previous MAGIC publication of DM search in CBe dSph [14].
Finally, Chapter 8 summarizes the findings of this work and offers concluding remarks. Further, it discusses the future prospects and potential applications of the methods and results presented in this thesis.

2 Dark Matter

The origin and nature of dark matter remain one of the unresolved mysteries of modern astro- and particle physics. This chapter provides a comprehensive overview of the evolution of the universe, early discoveries of dark matter, and potential candidates for its composition. Dwarf galaxies are discussed as observational targets for indirect searches, and the expected gamma ray flux for annihilating dark matter from these regions is modelled.

2.1 History of the Universe

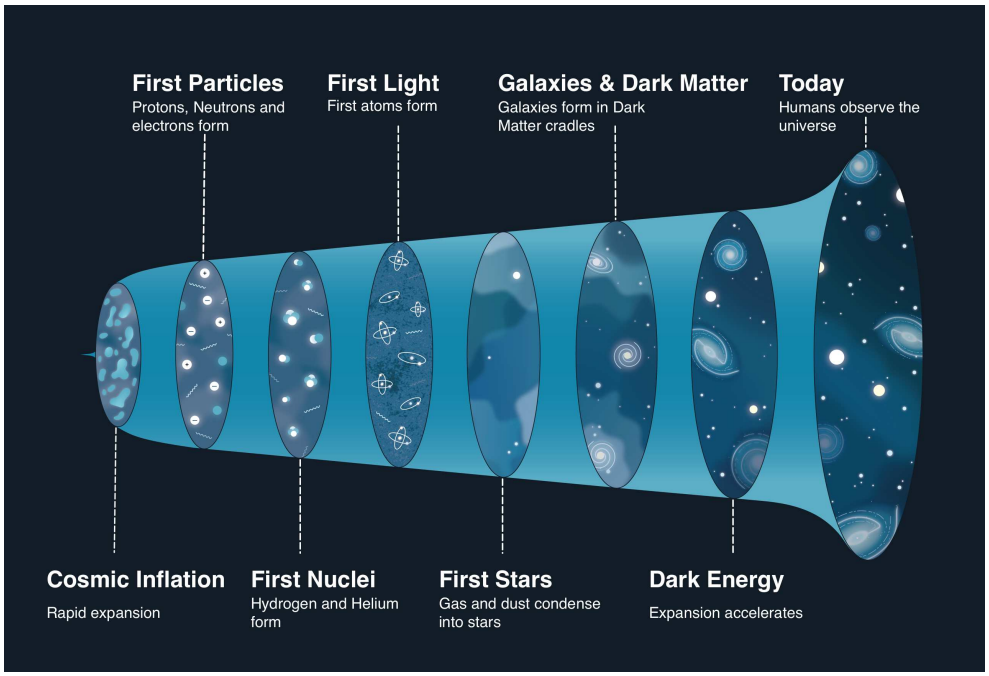

Figure 2.1: Sketch of the history of the universe as a series of phases. Figure adapted from [15].

From the moment of its inception, the universe expanded and cooled, creating a distinctive environment for the study of fundamental physics. Throughout its history, the universe has undergone a series of phases, presented in Figure 2.1, which are outlined in the following section according to the standard model of cosmology, the ΛCDM model [16].

Cosmic Inflation In the earliest moments of the universe's existence, it is estimated to have expanded rapidly, increasing in size by approximately 10^{26} [1] times [17]. This concept has been published for the first time by Alan Guth in [18]. Subsequent to inflation, the universe entered a hot, dense phase often referred to as the Big Bang, where temperatures were approximately $10^{32}\,\mathrm{K}$ [19]. At this juncture, the universe is constituted by a plasma of fundamental particles in thermal equilibrium.

First Particles The initial particles within the plasma interact via a unified force, which can be described by a Grand Unified Theory (GUT) [20, 21]. As the universe cools further, this force subsequently divides into the strong, weak, and electromagnetic forces. The formation of the first hadrons from the quark-gluon plasma is followed by their rapid annihilation and decay to leptons, leaving only light (semi-)stable baryons, such as protons and neutrons, in their wake.

First Nuclei The first nuclei are formed as the universe continued to cool [21]. This process involves the combination of protons and neutrons to form primordial elements, including hydrogen, helium, and traces of slightly heavier nuclei. The universe is composed of a plasma of nuclei, electrons, and photons.

First Light The epoch of First Light is also referred to as the epoch of recombination [21]. The universe cools to a temperature of less than $3000\,\mathrm{K}$ and the protons and electrons combine to form hydrogen atoms. With the formation of neutral hydrogen, the photons are no longer in thermal equilibrium with the electrons, resulting in the universe becoming transparent. This event is referred to as the surface of last scattering, which occurres at a redshift of $z \approx 1090$ [21].

Galaxies & Dark Matter The early universe is dominated by neutral hydrogen and the Cosmic Microwave Background (CMB) photons [21]. The only sources of light are the photons emitted from excited hydrogen. This epoch is referred to as the Dark Ages of the universe and ended with the forma-

[1] This number equates from the number of *e-folds* $N \approx 62$, which quantifies the amount of expansion.

tion of first stars, galaxies, and galaxy clusters. This formation is driven by irregularities in the density distribution of the universe, as baryonic matter fell into gravitational wells, which emerged from an already existing gravitational potential that was induced by a type of non-visible Dark Matter (DM).

Dark Energy The concept of dark energy is an additional, currently unidentified component that is thought to drive the large-scale evolution of the universe [22]. The ΛCDM model, is predicated on the description of the space-time geometry by the Friedmann–Lemaître–Robertson–Walker metric [23]. This metric accounts for both, the curvature of space-time and the time-dependent expansion of the universe. While our universe is observed to be flat, it appears to be undergoing an accelerated expansion, as inferred from distance measurements of astrophysical objects such as supernovae [24]. The introduction of the cosmological constant Λ into Einstein's field equations of general relativity provides a theoretical solution to this phenomenon. The contribution of Λ is designated as Dark Energy and is frequently referenced as a negative pressure that drives this expansion [21, 23, 25, 26].

The following section will provide a detailed examination of the observational evidence pertaining to Dark Matter (DM), ultimately offering insight into its implications for our comprehension of the universe.

2.2 Early Evidence of Dark Matter

In the 1930s Fritz Zwicky conducted a study of the dynamics of the Coma galaxy cluster by investigating the velocity dispersion of the galaxies within [1, 2]. Via the application of the virial theorem, he was able to identify discrepancies between the observable mass and the gravitational bound mass. Assuming the average kinetic energy of the galaxies is given as

$$\langle T \rangle = \frac{1}{2} N m \langle v^2 \rangle, \tag{2.1}$$

where N is the number of galaxies, m is the mass of each galaxy, and v is the velocity of the galaxies. Moreover, the mean potential energy of a uniform spherical density is given by

$$\langle U \rangle = -\frac{3}{5} \frac{G N^2 m^2}{R}, \tag{2.2}$$

where G is the gravitational constant and R is the radius of the density sphere. Equation 2.1 and Equation 2.2 can be combined via the virial theorem,

$$\langle T \rangle = -\frac{1}{2}\langle U \rangle, \tag{2.3}$$

to yield the gravitational bound mass of the cluster,

$$Nm = \frac{5\langle v^2 \rangle R}{3G}, \tag{2.4}$$

which turned out to be much higher than the observable mass. Based on these findings, Zwicky calculated the ratio of these values, also known as the mass-to-light ratio, as approximately 400-500, which led him to propose the existence of an as-yet-unobserved type of matter, Dark Matter (DM).

Building on this, Rubin, Ford, and Thonnard provided further evidence of non-visible matter in the 1970s through the study of galaxy rotation curves [3]. In accordance with Newtonian mechanics,

$$\begin{aligned} \underbrace{\frac{GMm}{r^2}}_{\text{Gravitational Force}} &\stackrel{!}{=} \underbrace{\frac{mv^2}{r}}_{\text{Centripetal Force}} \\ \Leftrightarrow v &= \sqrt{\frac{GM}{r}}, \end{aligned} \tag{2.5}$$

the rotational velocity v of an object with mass m in a system with mass M decreases with galactocentric distance r proportional to $\sqrt{r}^{-1}$. However, Rubin et al. observed a flat rotation curve, which could be explained by the existence of a larger mass distribution far outside the region of high luminosity. Figure 2.2 displays the original findings of Rubin et al.

Additional evidence of DM is observed in the CMB, which was first detected by Penzias and Wilson in 1965 [27]. However, it was not until 1992 that the Cosmic Background Explorer (COBE) satellite made measurements of anisotropies in the CMB [28]. These anisotropies manifest as µK temperature fluctuations, occurring in regions with slightly disparate densities, according to the Sachs-Wolfe effect [29]. Such dense regions could explain the gravitational wells, as previously described in Section 2.1, that are necessary for the structural formation of our universe and require the existence of DM prior to the epoch of recombination. Subsequent missions, such as the Wilkinson Microwave Anisotropy Probe (WMAP) [30] and the Planck satellite [31], provided more detailed results. Figure 2.3 displays the CMB map as observed by Planck.

In recent years, new experiments have been initiated with the objective to observe the effects of DM. Among these is the European Space Agency's Euclid

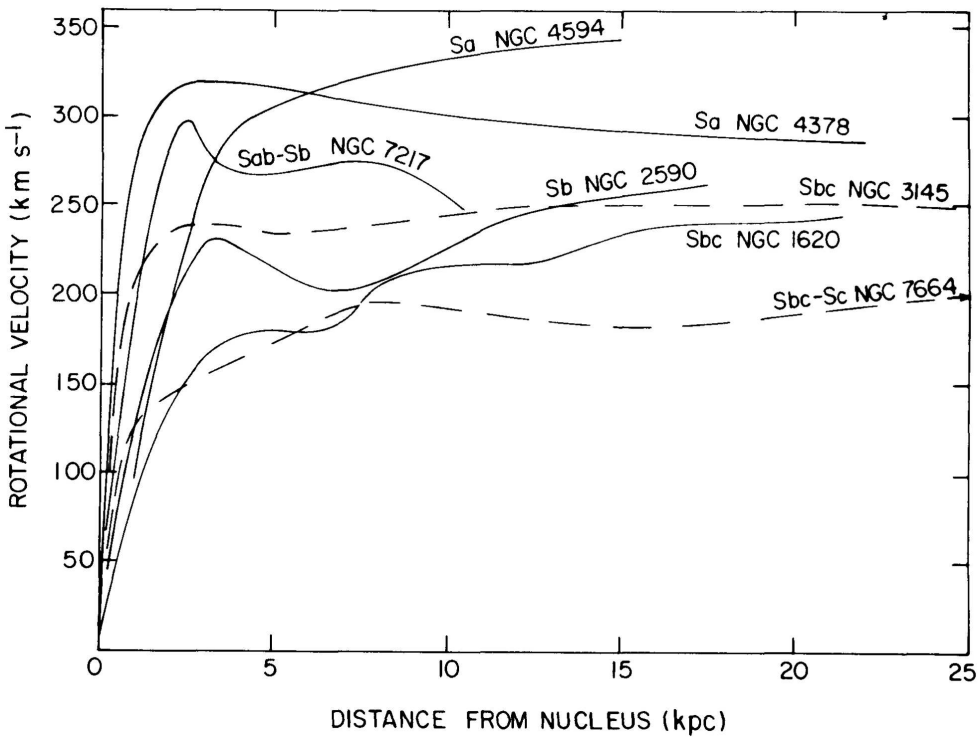

Figure 2.2: Rotational curves of galaxies inferred by Rubin et al. and taken from the original publication [3]. A general flatness of the curves can be observed with increasing distance from the galactic nucleus.

mission [32]. In a manner analogous to other astronomical missions, Euclid is situated in a stable orbit around Lagrange point L2, thereby enabling it to conduct continuous observation of the cosmos. In a historic time frame of 10 Gyr, the Euclid mission is capable of creating a three-dimensional map of the universe in both spatial and temporal dimensions. This 3D map is employed for a variety of purposes, including the investigation of gravitational weak lensing. This phenomenon occurs when the light from different galaxies is bent by regions of high DM density along its path to the observer [33]. The distortion can be quantified by the shear and convergence of the galaxy. As the original shape of an individual galaxy is unknown, the shear and convergence are evaluated over a set of galaxies. In return, it is possible to map the DM distribution in the universe. Figure 2.4 displays an exemplary shear map used for this inference by the Subaru Telescope [34].

As demonstrated in this section, the role of DM has become a fundamental pillar of modern cosmology and astrophysics. Its elusive nature and pivotal role in the formation of cosmic structures make it a compelling subject of study.

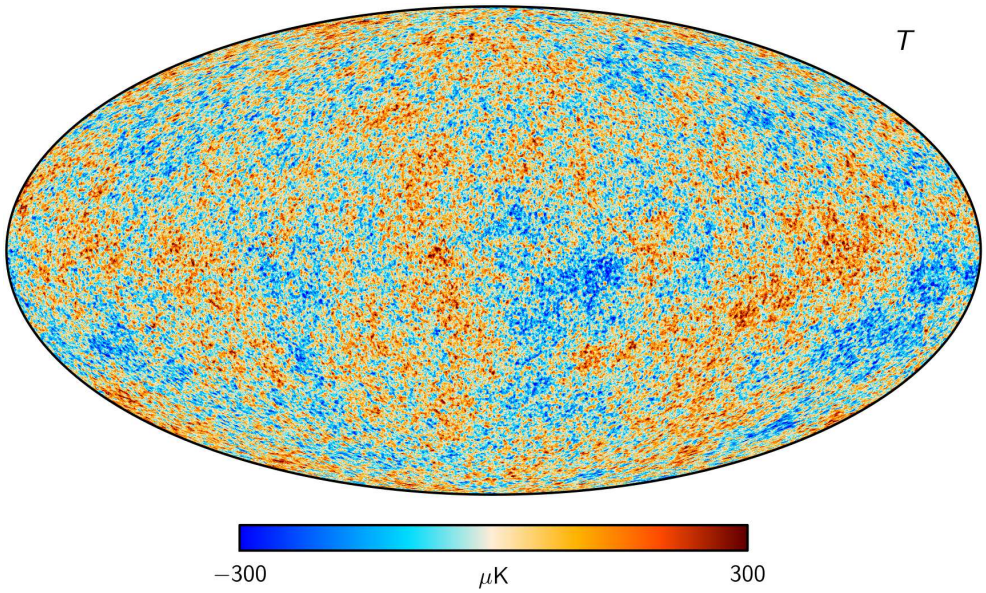

Figure 2.3: Temperature map of the CMB from Planck observations. Figure taken from [31].

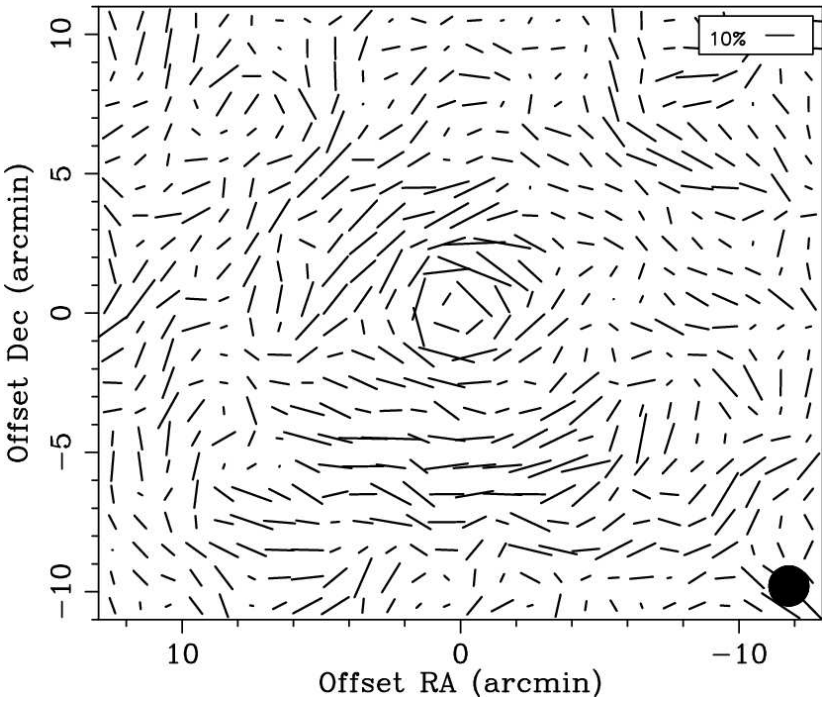

Figure 2.4: Shear map of Cl0024+1654 observed by the Subaru telescope, taken from [34]. During the processing, the field is smoothed with a Gaussian with a FWHM (black circle). A reference line for 10 % shear is given in the top right corner.

2.3 Dark Matter Candidates

In recent decades, numerous physical models and theories have been proposed in an effort to explain the observations and evidence pertaining to DM, as outlined in the preceding section. Among these, the following are the most extensively discussed:

MOND Modified Newtonian Dynamics (MOND) represents the most straightforward assumption that does not necessitate the introduction of a novel particle [35]. This theory proposes that Newtonian mechanics is not applicable on large scales. Rather, it is modified to

$$F_{\mathrm{MOND}} = ma\mu\left(\frac{a}{a_0}\right), \tag{2.6}$$

with $a_0 \approx 1.2 \times 10^{-10}\,\mathrm{m/s^2}$ and μ being a function that converges to one on large scales and to its argument on small scales. Upon applying Equation 2.6 to calculate the radial velocity distribution of galaxies, one finds that

$$\begin{aligned} a_{\mathrm{MOND}} &= \frac{\sqrt{GMa_0}}{r} \\ \Leftrightarrow v_{\mathrm{MOND}} &= \sqrt[4]{GMa_0}, \end{aligned} \tag{2.7}$$

with $a = v^2/r$. This results in the flat rotational curves that Rubin et al. observed, as detailed in Section 2.2. However, observations of the Bullet Cluster provide compelling evidence for the existence of dark matter [36], that is not compatible with MOND. These observations show a spatial separation between the hot gas, which contains most of the baryonic matter, and is observed in X-rays, and the regions of gravitational lensing, which trace the majority of the mass. Figure 2.5 displays this phenomenon.

ALPs The long-standing "strong CP problem" describes the discrepancy between the CP-violation observed in the Standard Model (SM) and its apparent absence in strong interactions driven by QCD[42]. One potential solution to this discrepancy is the Spontaneous Symmetry Breaking (SSB) mechanism proposed by Peccei and Quinn [43]. This introduces a new boson, the axion, which emerges as a consequence of SSB. Numerous theoretical frameworks, such as the hadronic axion [44, 45] and the Axion-Like Particles (ALPs), arising from string theory [46], are an active field of research [47–49]. These ALPs are optimal candidates for DM, as they could have been produced non-thermally through the misalignment mechanism during the early stages of the universe, thereby contributing as non-relativistic Cold Dark Matter

Figure 2.5: Optical image of the Bullet Cluster taken by the Magellan Telescopes [37] and by the Hubble Space Telescope [38], overlaid with X-ray data (pink) by Chandra [39]. The blue regions indicate a high mass density, inferred with gravitational lensing from the ESO Wide Field Imager [40] observations. Image taken from [41].

(CDM) to the structural formation [50]. In the context of Very-High Energy (VHE) gamma-ray astronomy, these particles can contribute to the observed gamma-ray flux at Earth via their coupling to photons in a strong magnetic field [51–53]. This environment permits the mixing between the ALP and photons. The probability of a photon oscillating to an ALP is given by $P_{\gamma\to a}$. One may extend this thought and investigate the oscillating photons with an intermediate ALP mixing. Therefore, the flux at Earth is given by

$$\frac{\mathrm{d}\Phi}{\mathrm{d}E} = \frac{\mathrm{d}\Phi_{\mathrm{int}}}{\mathrm{d}E} \cdot P_{\gamma\to a\to\gamma}, \tag{2.8}$$

where $\frac{\mathrm{d}\Phi_{\mathrm{int}}}{\mathrm{d}E}$ is the initial flux of the photons [54]. It should be noted that this does not take into account the absorption by the Extragalactic Background Light (EBL) [55] and free parameters of the model have been omitted for readability.

WIMPs As detailed in Section 2.1, the cosmological history demonstrates that DM does not interact via the strong or electromagnetic force. However, it is postulated that DM has left its imprint on the CMB through the aforementioned Sachs-Wolfe effect [29], thereby influencing the structural formation of the universe. Assuming the particles were produced in thermal equilibrium and "froze out" prior to the epoch of recombination, then the number density of the particles can be calculated using the Boltzmann equation

$$\frac{\mathrm{d}n_\chi}{\mathrm{d}t} + 3Hn_\chi = -\langle\sigma v\rangle(n_\chi^2 - n_{\chi,\mathrm{eq}}^2), \tag{2.9}$$

with the Hubble constant H, which describes the rate of expansion of the universe, the thermally averaged cross-section $\langle\sigma v\rangle$ of DM particle χ, and the number density at thermal-equilibrium $n_{\chi,\mathrm{eq}}$ [56]. This density freezes out once the interaction rate Γ of the equilibrium process is smaller than the rate of expansion, i.e. $\Gamma < H$. Figure 2.6 displays the mass density of particles with mass m_χ in dependence of the temperature in $x = m_\chi/T$. It is noted that the solid line displays the case of $n_\chi = n_{\chi,\mathrm{eq}}$ for $m_\chi = 100\,\mathrm{GeV}$. As the universe cools, x increases and the density deviates from the equilibrium state. DM with $T \ll m_\chi$ results in non-relativistic particles, referenced as CDM [57]. While Figure 2.6 illustrates this effect for different scales of cross-sections, the "weak" cross-section is able to explain the relic abundance [4] of DM as inferred by experiments such as Planck, $\Omega_c h^2 = 0.120 \pm 0.001$ [58]. This observation has led to the proposition of the concept of the Weakly Interacting Massive Particle (WIMP), which is referred to as the "WIMP miracle" [59].

The theory of Super Symmetry (SUSY) is capable of predicting the existence of such WIMPs by introducing superpartners to each of the bosons and fermions that comprise the SM [4, 5]. Furthermore, a theory such as the Minimal Supersymmetric Standard Model (MSSM) introduces the conservation of a novel quantum number, the R-parity, which suppresses processes where the lepton and baryon number can no longer be conserved [60]. While the SM has a parity of $R = 1$, this SUSY sector has $R = -1$. The introduction of R to SUSY also leads to the Lightest Supersymmetric Particle (LSP) being stable, thereby making it an optimal WIMP candidate.

This thesis is concerned with the detection of WIMPs via their annihilation to SM particles. A potential avenue for initial investigation within the field of astronomy is the detection of photon lines [61–64] produced via

$$\chi\chi \to \gamma\gamma. \tag{2.10}$$

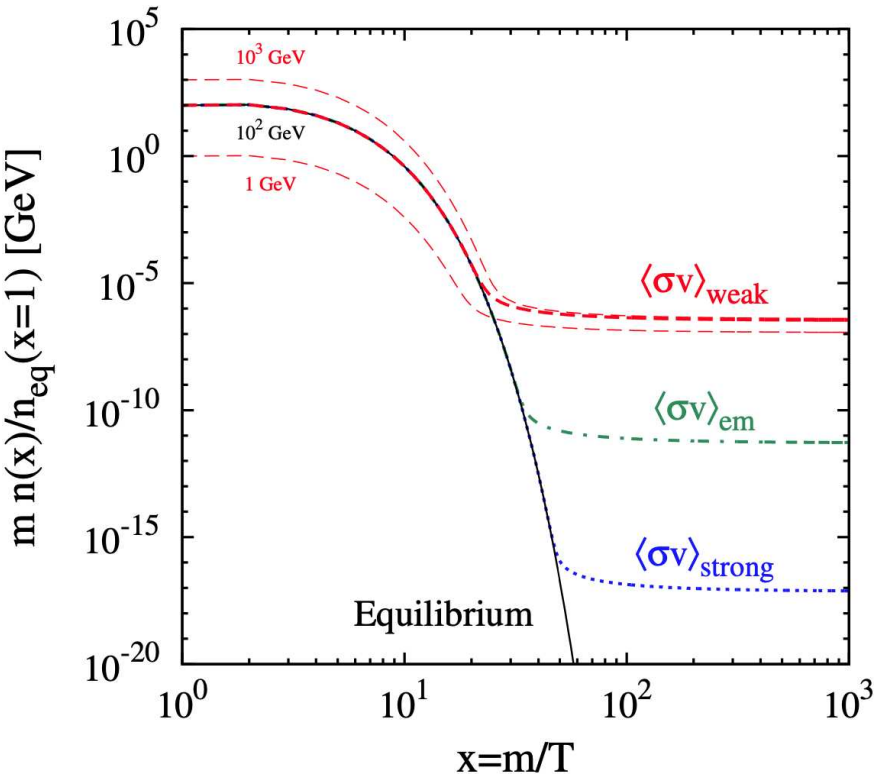

Figure 2.6: Mass density of WIMPs as a function of $x = m_\chi/T$. The solid line displays the equilibrium density for $m_\chi = 100\,\mathrm{GeV}$. The freeze out of the density is evident for cross-sections on the scale of weak (red), electromagnetic (green), and strong (blue) interactions of DM. Figure taken from [57].

However, since the DM does not interact electromagnetically, this process is strongly suppressed [2] and only possible via loop-level interactions [66]. More promising annihilation channels that produce SM particles lead to jet fragmentation and hadronization [67]. This process results in the production of pions, which subsequently decay into leptons and photons, that can be observed. This can be expressed as follows:

$$\chi\chi \rightarrow \text{SM particles} \rightarrow \pi^{\pm,0} \rightarrow \text{leptons} + \gamma. \tag{2.11}$$

This is also referred to as *indirect* detection of DM [68].
Direct detection of DM is possible via the scattering of DM with SM particles [69]. The energy depleted in the interaction medium can be determined by observing the thermal energy, charge, or light produced in a detector surrounding the interaction. This method necessitates a comprehensive understanding of the back-

[2] It is noted that extensions of the MSSM can enhance the photon-line signal [65].

ground processes that exhibit a comparable signature and robust shielding against background events. The aforementioned objective is accomplished by situating the experiments in subterranean laboratories. Notable examples of detectors include CRESST [70, 71], XENON1T [72]/XENONnT [73] and EDELWEISS [74, 75]. Recent advances reach a DM probing sensitivity up to the neutrino fog [76]. An alternative approach is the detection of DM with collider experiments, such as the Large Hadron Collider (LHC) [77–79]. In this method, the DM is *produced* via

$$\text{SM particles} \rightarrow \chi\chi + \text{SM particles}. \tag{2.12}$$

DM can be identified through the analysis of missing energy or transverse momentum in the detector.

2.4 Probing Dark Matter

Among the vast amount of possible astrophysical sources for DM, including the ones mentioned in the previous sections, this thesis focuses on Dwarf Spheroidal Galaxy (dSph). These galaxies are found to be satellites of the Milky Way, are spheroidal in shape, and exhibit a low luminosity [80]. Dwarf Spheroidal Galaxys (dSphs) represent one of the most promising astronomical targets for indirect DM searches due to their high mass-to-light ratio, which suggests the presence of a concentrated region of DM. This hypothesis was initially proposed by Zwicky and is discussed in greater detail in Section 2.2. Furthermore, these galaxies show a low astrophysical activity, exhibiting no active star formation [81], and are relatively close ($\sim \mathcal{O}(10) - \mathcal{O}(100)\,\text{kpc}$), which reduces the effects of EBL absorption [82]. The anticipated signal of DM within the galaxy observed at Earth can be expressed as a product of two distinct factors [83]. For annihilating DM these are given as

$$\frac{\mathrm{d}\Phi(\Delta\Omega)}{\mathrm{d}E} = \underbrace{\frac{1}{4\pi}\frac{\langle\sigma v\rangle}{2m_{\mathrm{DM}}^2}\frac{\mathrm{d}N_{\chi\chi\rightarrow\text{SM SM}}}{\mathrm{d}E}}_{\text{PP factor}} \times \underbrace{J(\Delta\Omega)}_{\text{AP factor}}. \tag{2.13}$$

The Particle Physics (PP) factor accounts for the contribution to the flux from a theoretical model of DM, which depends on the thermally averaged cross-section $\langle\sigma v\rangle$, the mass of the DM candidate m_{DM}, and the spectrum $\frac{\mathrm{d}N_{\chi\chi\rightarrow\text{SM SM}}}{\mathrm{d}E}$ for the annihilation to SM particles. The latter is a combination of the different annihilation channels

$$\frac{\mathrm{d}N_{\chi\chi\rightarrow\text{SM SM}}}{\mathrm{d}E} = \sum_i BR_{\chi\chi\rightarrow ii}\frac{\mathrm{d}N_{\chi\chi\rightarrow ii}}{\mathrm{d}E} \tag{2.14}$$

as given by the branching ratios $BR_{\chi\chi\to ii}$ of the model for $i \in \{\text{SM particles}\}$. Nevertheless, it is feasible to calculate the PP factor in a model-independent manner. This is based on the premise that one annihilation channel of the DM candidate contributes 100 % to the production of the SM particle i, $BR_{\chi\chi\to ii} = 1$. The designated flux is calculated through the simulation of final states i, which subsequently result in the production of gamma rays. Some of the most common model-independent spectra are the PPPC4DM [84], HDMSpectra [85], and CosmiXs [86] data. Figure 2.7 illustrates spectra provided by PPPC4DM for the production of gamma rays, with a mass of $m_\chi = 10\,\text{TeV}$ for the DM candidate. For the DM searches performed in this thesis, only stable candidates are taken into account and no fluxes for decaying DM are computed.

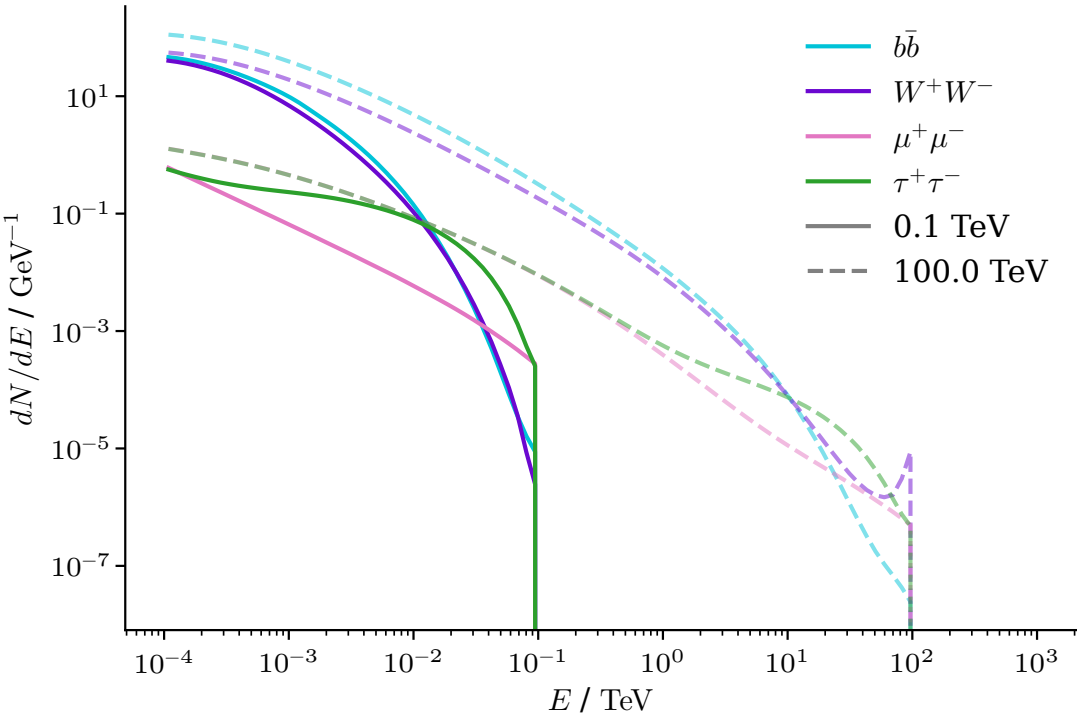

Figure 2.7: Primary spectra of secondary gamma rays for DM annihilation to $b\bar{b}$, W^+W^-, $\mu^+\mu^-$ and $\tau^+\tau^-$. Solid lines assume a mass of $m_\chi = 0.1\,\text{TeV}$, while the dashed lines show spectra with $m_\chi = 10\,\text{TeV}$. The maximum spectral energy is limited by the mass. The spectra are calculated on the basis of PPPC4DM [84].

The Astrophysical (AP) factor accounts for the dependence of the flux on the distribution of DM in the target region. In the case of annihilating DM, this is

referred to as the "J-Factor" and is defined as

$$J(\Delta\Omega) = \int_{\Delta\Omega}\int_{\text{l.o.s.}} \rho^2(l,\Omega)\mathrm{d}l\mathrm{d}\Omega, \tag{2.15}$$

where the squared density distribution of DM $\rho^2(l,\Omega)$ is integrated over the solid angle Ω and the line of sight (l.o.s.) l. The quadrature arises from the necessity of two DM particles being present for annihilation. The density $\rho(l,\Omega)$ is inferred from stellar-kinematic data obtained through observations of the target galaxy [87]. This inference is performed by solving the (spherical) Jeans equations, which are derived by integrating the collisionless Boltzmann equation,

$$\frac{1}{\nu}\frac{d}{dr}\left(\nu\bar{v_r^2}\right) + 2\frac{\beta_{\text{ani}}(r)\bar{v_r^2}}{r} = -\frac{GM(r)}{r^2}, \tag{2.16}$$

$$M(r) = 4\pi\int_0^r \rho_{\text{tot}}(s)s^2\mathrm{d}s \tag{2.17}$$

where v_r is the number density, $\bar{v_2^2}$ the radial velocity, and β_{ani} the velocity anisotropy of the stellar tracers. The latter describes the variance of the velocities in dependence of the tangential and radial dispersion. It is notable, that Equation 2.17 incorporates the gravitational dependence on the DM distribution. One may posit an isothermal profile for DM [88], which would result in a more constant density in the core of the galaxy. The same is the case for the Burkert profile [89], thus they are dubbed "cored" profiles. However, empirical profiles, such as the Navarro-Frenk-White (NFW) [90], Einasto [91, 92], Moore [93], and Zhao [94] profiles demonstrate a rapid increase of the density towards the core region. These profiles are referred to as "cuspy" profiles. The fact that observations, in contrast, show a cored density, is called "core-cusp" problem [95]. The mentioned profiles are defined in the following and illustrated in Figure 2.8:

NFW:
$$\rho_{\text{NFW}}(r) = \rho_s\frac{r_s}{r}\left(1+\frac{r}{r_s}\right)^{-2} \tag{2.18}$$

Einasto:
$$\rho_{\text{Ein}}(r) = \rho_s\exp\left\{-\frac{2}{\alpha}\left[\left(\frac{r}{r_s}\right)^{\alpha}-1\right]\right\} \tag{2.19}$$

Moore:
$$\rho_{\text{Moo}}(r) = \rho_s\left(\frac{r_s}{r}\right)^{1.16}\left(1+\frac{r}{r_s}\right)^{-1.84} \tag{2.20}$$

Isothermal:
$$\rho_{\text{Iso}}(r) = \frac{\rho_s}{1+(r/r_s)^2} \tag{2.21}$$

Burkert:
$$\rho_{\text{Bur}}(r) = \frac{\rho_s}{(1+r/r_s)(1+(r/r_s)^2)} \tag{2.22}$$

Zhao:
$$\rho_{\text{Zhao}}(r) = \rho_s\left(\frac{r_s}{r}\right)^{\gamma}\left(1+\left(\frac{r}{r_s}\right)^{\frac{1}{\alpha}}\right)^{(\gamma-\beta)\alpha} \tag{2.23}$$

Here, r_s and ρ_s are the scale radius and scale density, defining the transition region between the inner and outer part of the profiles, while α, β, and γ are shape parameters of the corresponding profiles, which change the curvature of the density distribution for the inner, outer and transition region, respectively. Based on Equation 2.18 to Equation 2.23, the J-factor can be calculated with Equation 2.15. Furthermore, in a hierarchical universe, the distribution of DM within a galaxy is expected to form substructures, so-called "subhalos" of DM [96], which contribute to the overall J-Factor. As part of this thesis, only the smooth component is calculated to maintain comparability to the published results that are introduced within the analysis.

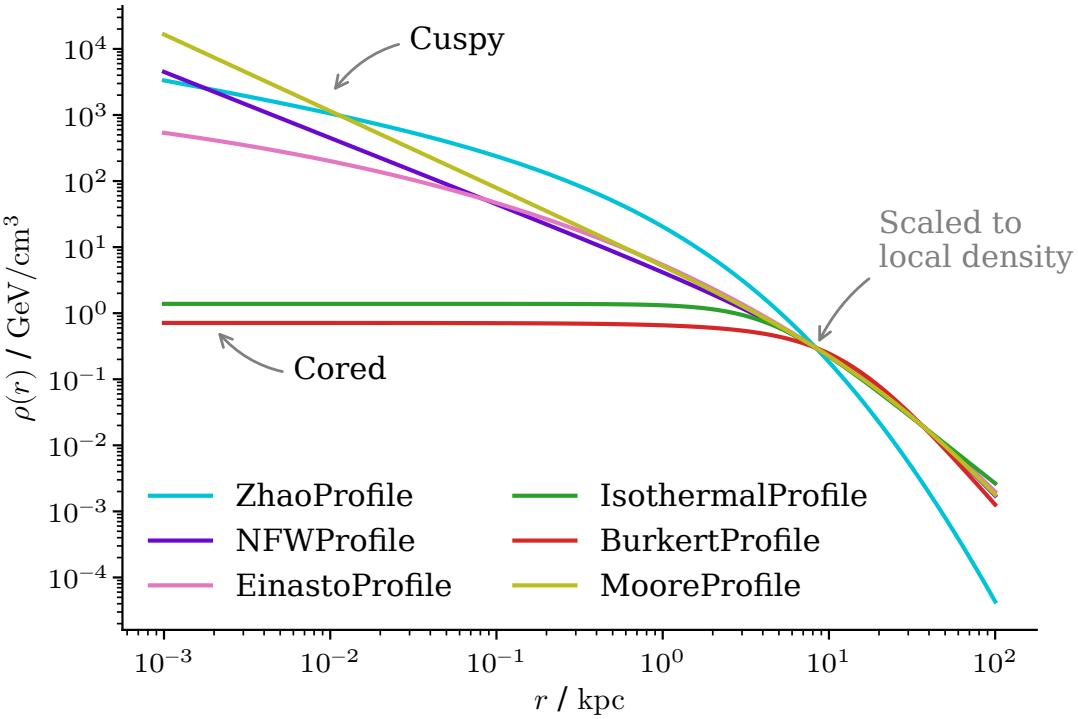

Figure 2.8: DM density profiles of Equation 2.18 to Equation 2.23 illustrated in dependence of the radial distance r to the core of the distribution. All profiles are scaled to the local density.

3 Gamma-Ray Detection – From Particle to Data

The substantial variety of potential particle types emitted by astrophysical sources, including DM-dominated dSphs, enables the combination of the signatures detected by multiple detectors. A particular avenue of Multi-Messenger astronomy (MMA) involves the observatios of gamma rays by Imaging Air Cherenkov Telescopes (IACTs). This chapter provides an overview of MMA, the physics of induced Extensive Air Showers (EASs), and the observations of these by the MAGIC telescopes through the Cherenkov effect.

3.1 Multi-Messenger Astronomy

Multi-messenger astronomy focuses on the detection of the various particles and observables, that are produced by an astrophysical source [99]. These particles originate from extreme physical environments, with particle energies up to EeV [100], beyond the capability of collider experiments. Figure 3.1 illustrates the following messengers:

Photons Depending on the wavelength, different regions of a source are probed, e.g. radio waves can reveal details of the accretion disk or jets of an AGN [101]. The most prominent example is the image of a black hole's shadow produced by the Event Horizon Telescope (EHT), a ground-based radio interferometer, published in [102].
High-energy photons, such as gamma rays, can give insight on acceleration mechanisms, galactic and extragalactic sources, and fundamental physics [103]. These particles can be detected with space-based telescopes such as Fermi-LAT (Fermi-LAT) [104]. Although such an experiment can continuously observe the sky, its sensitivity towards higher energies decreases due to its small detection area. Ground-based IACTs, such as H.E.S.S. [105] and MAGIC [106], can overcome this limitation, as they observe the interaction of the photons with Earth's atmosphere. This enor-

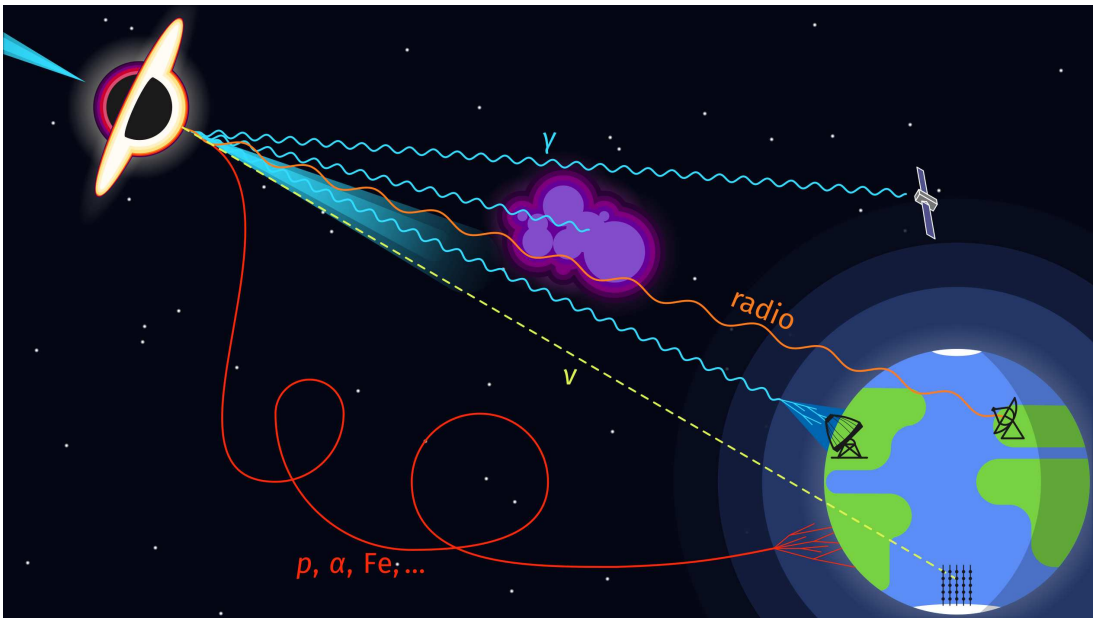

Figure 3.1: Illustration of MMA [97]. Different kinds of particles, called messengers, can be produced and emitted by a various type of astrophysical source, e.g. an Active Galactic Nucleus (AGN). The propagation of Cosmic Rays (CRs), gamma rays, radio waves, and neutrinos through the Universe is displayed. These messengers can be deflected, absorbed, or pass the interstellar medium with less to none interactions, depending on particle type. Various experiments have been built to detect the different particles. Satellite and ground-based telescopes detect gamma rays and CRs, either directly in space or indirectly via their interaction with Earth's atmosphere. Radio antennas or interferometers are used to observe the radio sky. Neutrinos can be detected by underground experiments, such as the IceCube Neutrino Observatory [98] in Antarctica.

mous mass of air behaves like a calorimeter, therefore the detection area is multiple orders of magnitude larger. This makes IACTs an ideal detector for observing low-flux regions like those associated with DM.
Other mentionable examples of experiments at other wavelengths include: XMM-Newton [107] (X-ray), James Webb Space Telescope [108] (optical, infrared), Planck [109] (microwave).

Cosmic Rays CRs consist of ionized nuclei, such as protons, helium, and heavier nuclei [110]. Due to their neutral charge, they get deflected, and their path cannot be traced back to their origin without additional knowledge of the medium. Nevertheless, the energy spectrum gives insight into their production mechanism. The CRs can be measured indirectly with ground-

based experiments such as the Pierre Auger Observatory (PAO) [111] and Telescope Array (TA) [112].

Neutrinos Due to their low interaction rate and non-existent charge, the majority of neutrinos can propagate through the universe without being absorbed or deflected. In principle, their path can be traced back to their source. An example for neutrinos in the context of MMA are the events from TXS 0506+056 and from NGC 1068 observed by the IceCube Observatory [113, 114].

Gravitational Waves These waves have their origin in the acceleration of masses, which induce oscillations in the metric of spacetime [115, 116]. The initial detection of gravitational waves resulting from the merger of two black holes was published by the Laser Interferometer Gravitational-Wave Observatory (LIGO) in [117].
Planned experiments include the space-based Laser Interferometer Space Antenna (LISA) [118] and the ground-based Einstein Telescope (ET) [119].

3.2 Extensive Air Showers

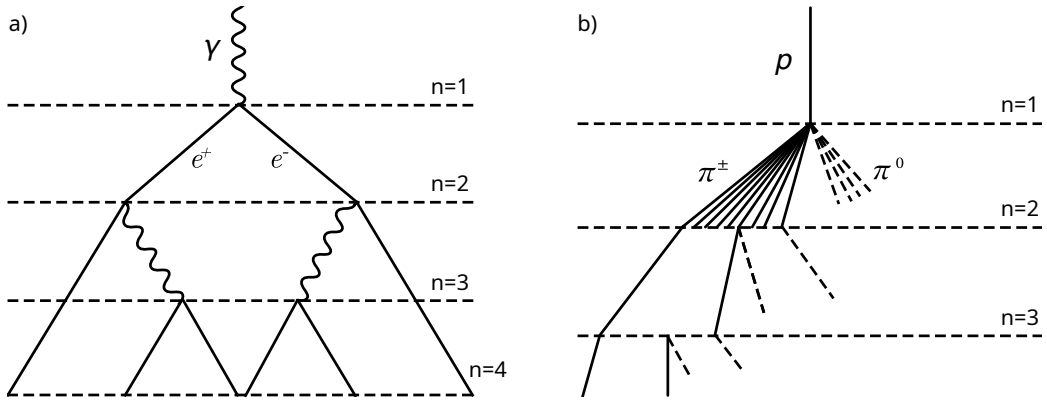

Figure 3.2: **a)** The Heitler model for a gamma-induced shower. At each step, the gamma ray produces an electron-positron pair in the presence of a nucleus. Due to Bremsstrahlung, new photons are radiated. The cascade ends once the energy of the initial gamma ray is completely depleted. **b)** The Heitler-Matthews model is an extension of the Heitler model and describes the production, decay, and propagation of π^0 and $\pi^\pm$ induced by a proton. The interaction carries on in steps until the interaction length is larger than the decay length. The schematic is adapted from [120].

As gamma rays and CRs hit the Earth's atmosphere, they interact with its molecular constituents. Similar to a particle hitting a calorimeter of a collider experi-

ment, the cosmic particle initiates a cascade of particles. The morphology of this Extensive Air Shower (EAS) [121] depends on the energy and particle type of the incoming candidate, whilst the shower axis, which is the axis following the longitudinal evolution of the shower, traces the trajectory of the primary particle. The development of electromagnetic cascades, initiatable by gamma rays, is explained by the Heitler model [122], illustrated in Figure 3.2. In this model, the atmosphere is divided into discrete layers, in which the cascade evolves stepwise. At the initial step, $n = 1$, the incoming gamma ray interacts with an atmospheric nucleus and produces an electron-positron pair: $\gamma \rightarrow e^+e^-$. The pair loses energy via Bremsstrahlung, $n = 2$, leading to the generation of new photons. New electrons and positrons are produced in the same manner. The process continues until a critical energy is reached at which the losses from collision exceed the radiation losses. Therefore, the number of particles increases exponentially with each step and is given as 2^n. This is known as an "electromagnetic shower".
In contrast, showers induced by CRs yield to the production of hadrons (e.g. $\pi^{\pm}, \pi^0$, $K^{\pm}$) and leptons (e.g. μ, ν_μ), as illustrated in Figure 3.3. Furthermore, the semi-empirical Heitler-Matthews model [120] divides the atmosphere into layers, similar to the Heitler model. An incoming proton produces charged and neutral pions after traversing the first atmospheric layer. The neutral pions, π^0, decay to photons, $\pi^0 \rightarrow \gamma\gamma$, which induce an electromagnetic shower. The charged pions, $\pi^{\pm}$, propagate through the layers until the interaction length is larger than their decay length. This propagation leads to the production of new leptons, according to $\pi^{\pm} \rightarrow \mu + \nu_\mu$. This is called the muonic component. Showers initiated by heavier nuclei, as part of the CR spectrum, are modelled with a superposition model. The EAS of a nucleus of energy E_A is approximated by evaluating the sum of A proton-induced showers, where A is the atomic number.

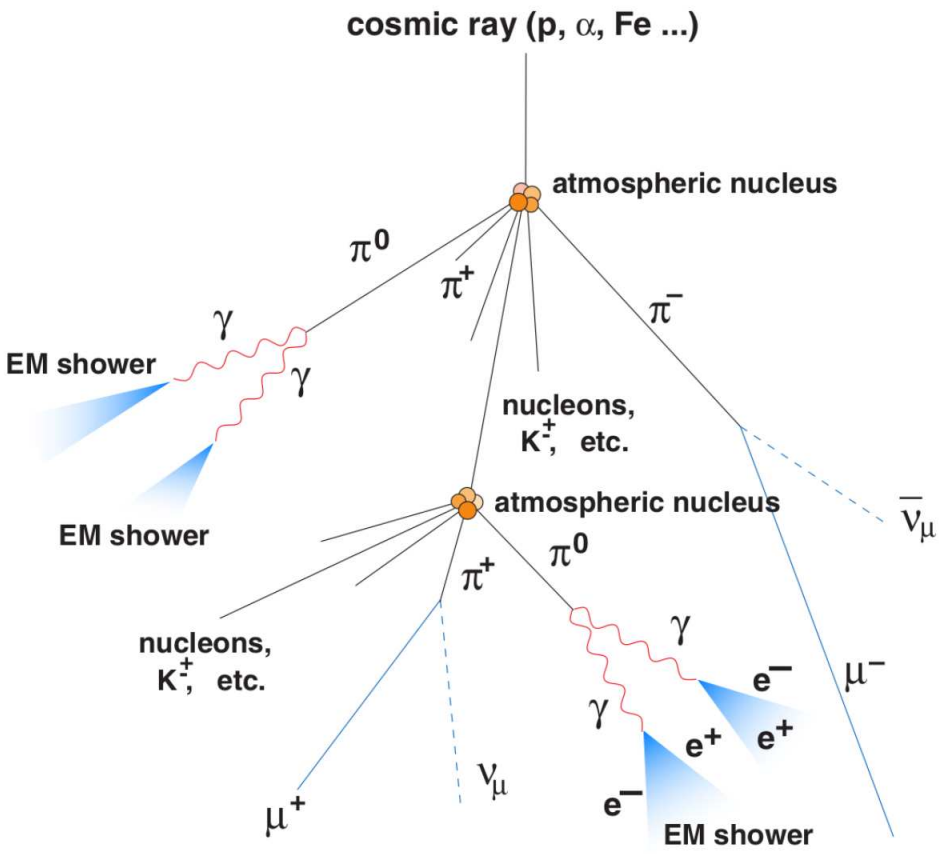

Figure 3.3: Illustration of an EAS induced by a CR. The CR interacts with an atmospheric nucleus in the upper atmosphere, which results in the production of mesons, such as $\pi^{0,\pm}$ and $K^{\pm}$. Neutral pions decay to photons which results in an electromagnetic shower. Charged pions and kaons either decay or drive the further evolution of the shower forward in a similar manner to the first interaction. Figure taken from [123].

3.3 Cherenkov Effect

As the charged particles, produced in the EAS, move through Earth's atmosphere, they polarize the surrounding atmospheric molecules. These molecules emit photons as they relax from their excited state back to their ground state. This effect is illustrated in Figure 3.4. Since the particles move faster than the speed of light in the medium, the radiation interferes constructively and a wavefront is formed under the angle

$$\theta = \cos^{-1}\left(\frac{1}{n\beta}\right), \tag{3.1}$$

where n is the refractive index of the atmosphere[1] and β is the particle velocity in units of the speed of light. The geometric construction of the angle from the coherent waveforms is shown in Figure 3.4. This emission process is known as the *Cherenkov effect* [124]. The spectrum of the Cherenkov radiation is dependent on the wavelength, λ^{-2}, and peaks in the visible spectrum, making it observable by optical instruments [125].

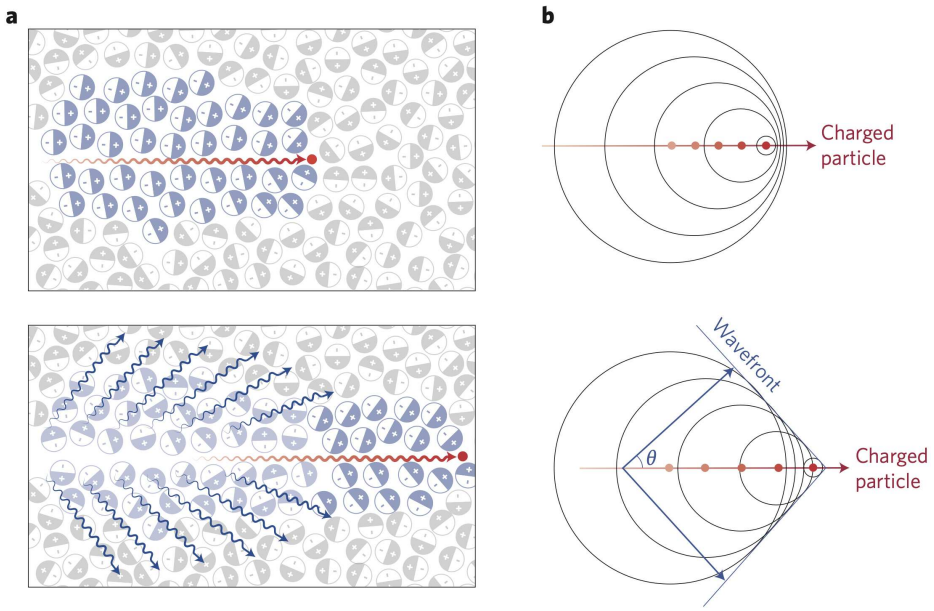

Figure 3.4: Illustration of the Cherenkov effect taken from [126].**a)** Before and after relaxation of the the polarized molecules due to a traversing charged particle. Photons are radiated along the track of the particle. **b)** Inference of the radiated photons for a charged particle with $v \leq c$ and $v > c$. The latter results in the constructive formation of a wavefront under the Cherenkov angle, detailed in Equation 3.1.

[1] The refractive index depends on the altitude.

3.4 The MAGIC Telescopes

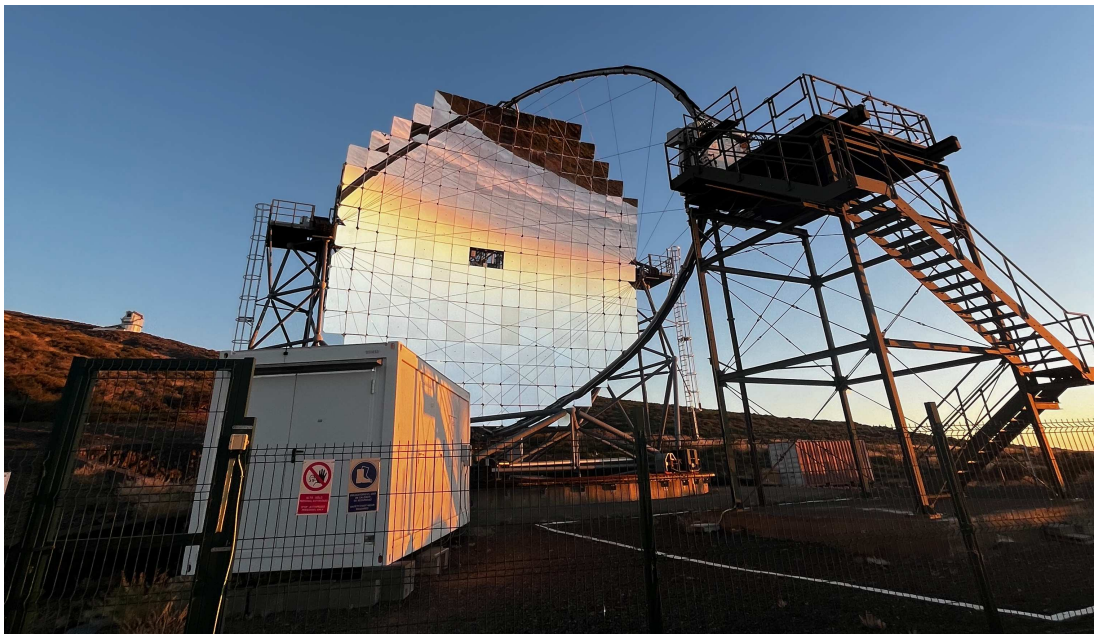

Figure 3.5: Picture of MAGIC-II taken in August 2024 on the Roque de los Muchachos.

The Cherenkov light emitted by the EASs can be detected by ground-based IACTs, such as the Major Atmospheric Gamma-Ray Imaging Cherenkov Telescopes (MAGIC) [106]. MAGIC consists of a stereoscopic system (M-I and M-II), which is located at the Roque de los Muchachos Observatory on La Palma, Canary Islands, Spain. The observational procedure of the telescopes is conceptually illustrated in Figure 3.6. Typically, one is interested in gamma-ray-induced showers, while the hadron-induced showers are considered background. These occur 10^5 times more frequently and thus represent the primary contributor to background within an analysis. A method for signal-background separation is explained in Chapter 4.

The M-I telescope was initiated in 2004 as a standalone instrument [127, 128], followed by the construction of the second telescope, M-II, in 2009 [129]. Figure 3.5 displays an image of M-II. In 2012, both systems underwent a comprehensive upgrade and unification, to allow for enhanced stereoscopic observations [106, 130]. The IACTs are mounted on an azimuth rail and were built with an elevation drive system to rotate the dish along its horizontal axis, allowing the telescopes to be pointing in Altitude and Azimuth (Alt-Az) directions. Interface plates (IF plates) mount the individual mirror segments on the 17 m dish, with each IF plate

holding multiple actuators at the back of the mirrors. The Active Mirror Control (AMC) orchestrates these actuators to focus the mirrors during the tracking of a source as the Alt-Az drive moves, a process made necessary by the bending of the structure for different pointings.
The Cherenkov light of an EAS is reflected onto the 1039 hexagonal Photo Multiplier Tube (PMT) pixels of the camera [131], as illustrated in Figure 3.7.

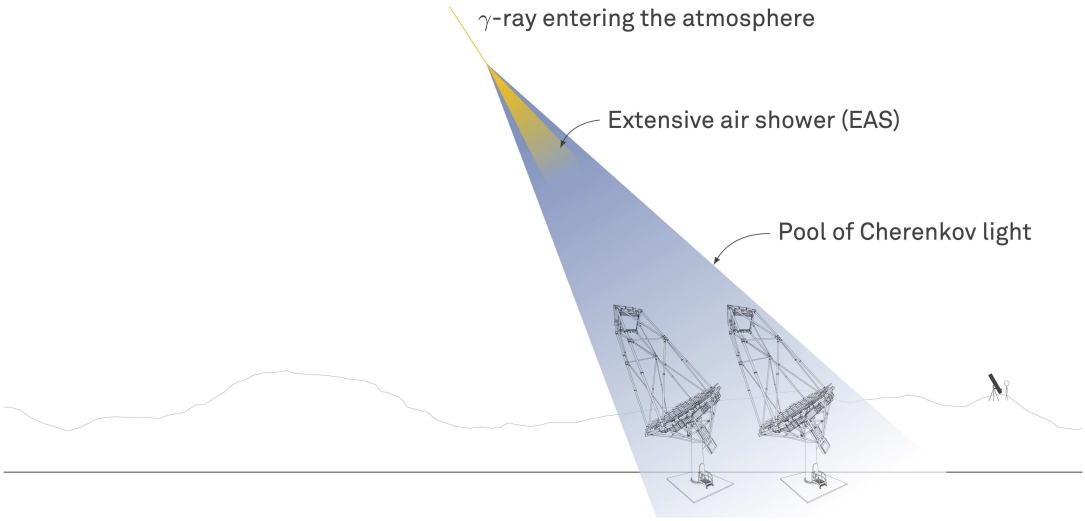

Figure 3.6: Schematic of two IACTs situated within a Cherenkov light pool. This light is produced as a consequence of a gamma-ray induced EAS, which occurs when a gamma-ray interacts with the Earth's atmosphere. Figure taken from [97].

To distinguish the Cherenkov light from the Night Sky Background (NSB), moonlight, and bright stars in the 3.5° Field of View (FoV), a multi-stage trigger system is employed [130].

L0 Trigger Should the signal from a PMT exceed a predetermined threshold, the L0 trigger is passed.

L1 Trigger The pixels are grouped into 19 macrocells, as illustrated in Figure 3.7. The L1 trigger is based on a Next-Neighbour (NN) coincidence logic, where a pattern of three adjacent L0-triggered pixels is required to pass the L1 stage. Different pattern sizes are chosen for non-generic observations.

L3 Stereo Trigger In the case of both telescopes detecting an event with a coincident L1 trigger within a specified time window, the L3 stereo trigger is passed, and the event is recorded by the Data Acquisition System (DAQ).

The PMTs are read out using the Domino Ring Sampler 4 (DRS4) chip, which operates at 650 MHz and captures an approximately 30 ns time frame for each pixel.

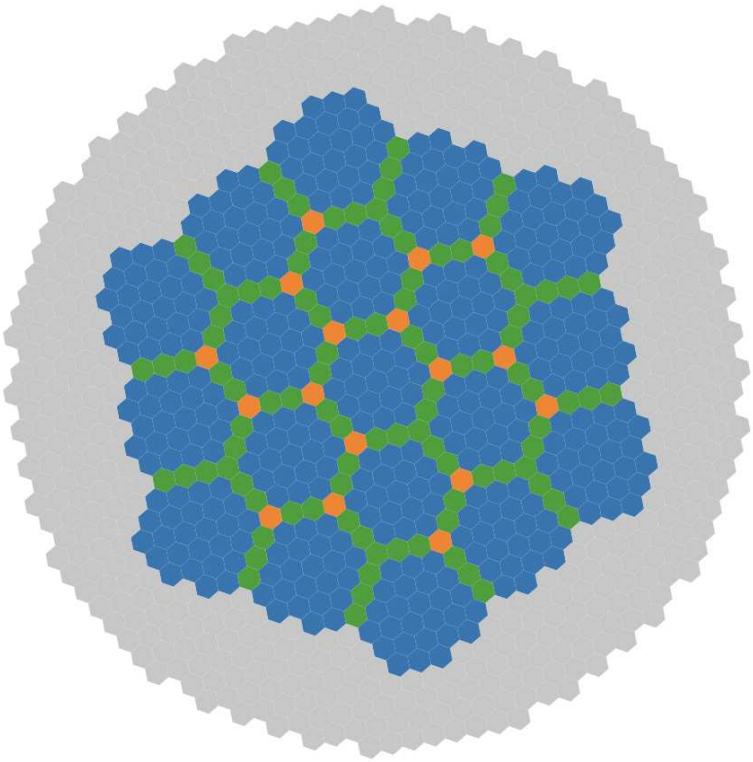

Figure 3.7: Illustration of the 1039 hexagonal pixel PMTs of the MAGIC camera. The colored pixels indicate the 19 macrocells of the L1 trigger. Orange, green, and blue pixels show the overlap of three, two, or none neighbouring macrocells, respectively. The gray pixels are not part of the trigger system. Figure taken from [132], as an adaption of the original figure in [130].

3.5 Data Taking

The MAGIC telescopes primarily operate during good environmental conditions, since the experiment has to be operated within its safety limits. Therefore, the time spent on the different targets each night has to be optimized. Intuitively, one might want to point the telescope directly at the source, but this requires a separate observation of a dark patch in the sky under the same conditions to estimate the background events.
This problem is solved with the so-called *Wobble mode* in which MAGIC obser-

vations are performed [130, 133]. A schematic of the Wobble mode is displayed in Figure 3.8. Instead of pointing directly at the source, the telescopes are moved to an adjacent position. Four different *Wobble positions* are used with 0.4 deg distance and polar angles of 0°, 90°, 180°, and 270° with respect to the source in Right Ascension (RA) and Declination (DEC). Alternative positions are used if bright astrophysical sources are near the target.
Three different types of data are taken during the observation:

Data Run The telescopes operate in the Wobble mode and change their pointing every 20 min among the Wobble positions. Each run is divided into multiple sub-runs to reduce the data in single files stored by the DAQ.

Calibration Run A calibration laser is used to illuminate the camera uniformly. Since the properties of the laser are known, the data is used to convert the counts of the PMTs to photo electrons (p.e.).

Pedestal Run To account for the baseline electronic noise of the PMTs and readout electronics, random triggers with no associated signal are taken for each pixel. Based on these pedestal runs, the baseline noise level in the system is inferred and subtracted from the 30 ns time frames stored by the DAQ. Commonly these runs are taken at the beginning of an observation. Longer observations require multiple pedestal runs to be taken to account for different NSB.

Moreover, atmospheric data is necessary to account for the different environmental conditions during the observation. A Light Detection and Ranging (LIDAR) laser is used to measure the reflection of aerosols in the air, allowing for the calculation of the transmission properties [134]. This quantity is directly related to the absorption of Cherenkov light by atmospheric dust, which is monitored by the Telescopio Nazionale Galileo (TNG) [135]. Alternatively, the cloudiness is used as a proxy for the transmission. It describes the cloud coverage during the observation and can be inferred from the thermal radiation of the sky measured by a Pyrometer along the l.o.s. of the astrophysical source [136].

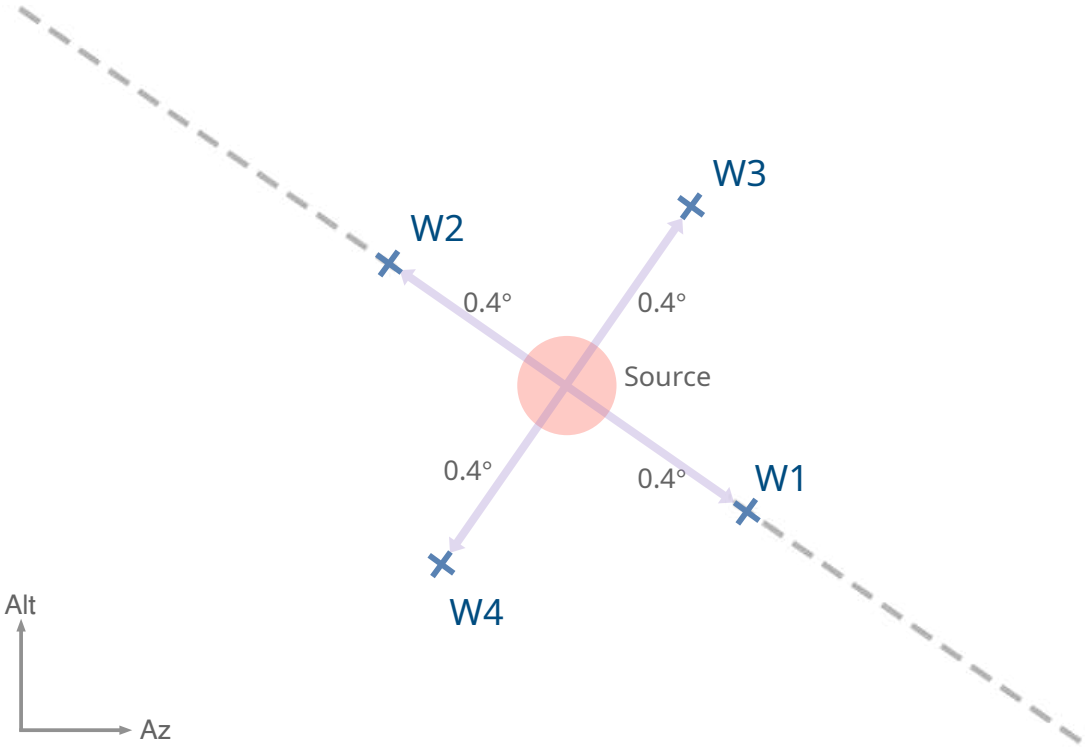

Figure 3.8: Schematic of the Wobble mode in Alt-Az coordinates as implemented by MAGIC. The track along the declination of the source is indicated as a dashed line. The Wobble positions W1, W2, W3, and W4 at 0°, 90°, 180°, and 270° with a distance of 0.4 deg relative to the source (shaded region) are displayed, respectively.

4 Data Processing – From La Palma to Dortmund

The raw data obtained from the MAGIC observations must undergo processing in order to facilitate the reconstruction of the properties of the primary particle that induced an EAS. This process entails the calibration of the PMTs, the cleaning of the camera image, and the implementation of Random Forest (RF) on image features for the reconstruction. The reconstruction metrics, designated as Instrument Response Functions (IRFs), are subsequently computed, and the final data is stored in Data Level 3 (DL3) files. The entire processing, encompassing calibration and culminating in the generation of DL3 files, is automated with the Automatic Analysis of MAGIC Data (autoMAGIC) framework.

4.1 From PMTs to Camera Images

As detailed in Section 3.5, the data run comprises counts from the DRS4 within a 30 ns frame for each pixel. Given the presence of noise in the PMT, the pedestal run is employed to establish a baseline for the noise level. The baseline is defined as the time-averaged noise for the recorded time frames. The subtraction of this baseline yields an almost noise-free signal with a consistent value range across all pixels. Figure 4.1 displays an arbitrary time frame.

The signal is extracted by applying the *sliding window extractor* [137]. This method calculates the signal by maximizing the sum of six consecutive time bins. These six bins are movable over the input signal, hence *sliding*. To convert the ADC counts into p.e., the *F-Factor method* [138] is applied. The relationship between the ADC counts and the number of p.e. $N_{\text{p.e.}}$ is determined by the gain g, i.e.

$$N_{\text{ADC}} = gN_{\text{p.e}}, \tag{4.1}$$

or on average, given statistical variations,

$$\overline{N_{\text{ADC}}} = g\overline{N_{\text{p.e}}}. \tag{4.2}$$

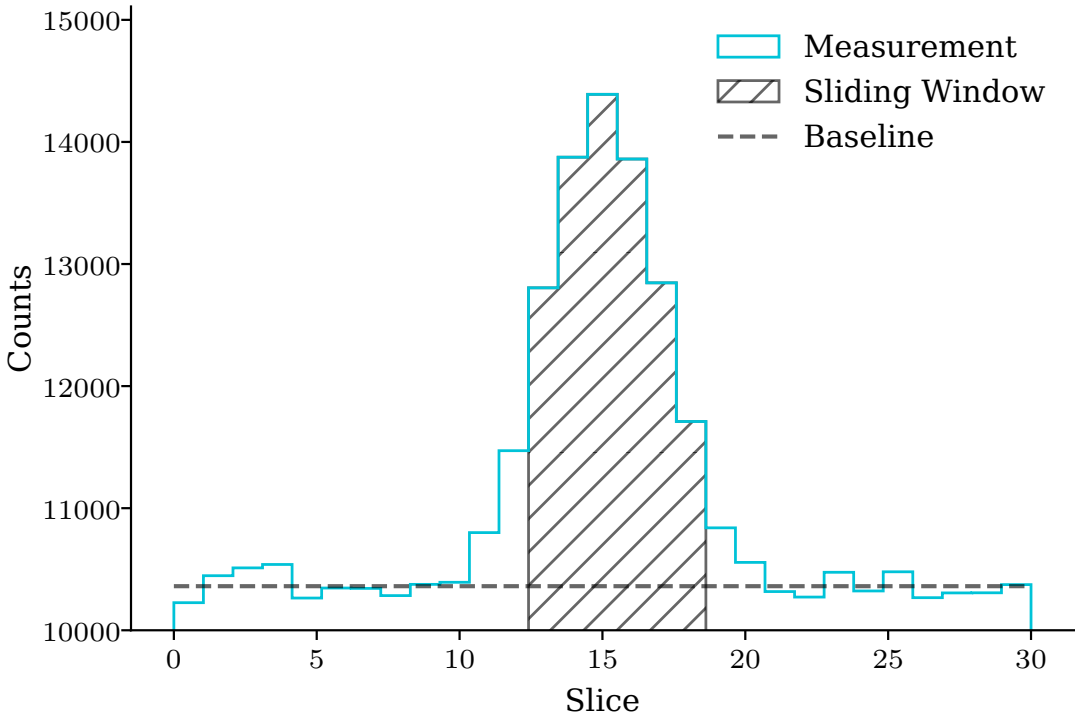

Figure 4.1: Schematic of a time frame for a single PMT as recorded by the DRS4. The hatched region indicates the six-bin-window of the *sliding window extractor*. The baseline of the pedestal event is displayed as a dashed horizontal line.

Assuming a Poissonian distribution of the p.e. counts of a calibration event, $N_{\text{p.e.}}$, the variance is $var(N_{\text{p.e.}}) = \sqrt{N_{\text{p.e}}}$. The variance σ_{ADC} of the ADC counts is given as

$$\sigma_{\text{ADC}} = g\sqrt{N_{\text{p.e.}}}. \tag{4.3}$$

Combining Equation 4.2 and Equation 4.3 results in the gain factor

$$g = \frac{\sigma^2_{\text{ADC}}}{\overline{N_{\text{ADC}}}}. \tag{4.4}$$

The number of p.e. is given as

$$\overline{N_{\text{p.e}}} = \frac{1}{g}\overline{N_{\text{ADC}}}, \tag{4.5}$$

where $1/g$ is known as the conversion factor. In practice, the value of g must be corrected for a non-Poissonian response of the PMT readout, taking into account the F-factor and the variance, σ^2_{ped}, of the pedestal run. This results in

$$g = \frac{\sigma^2_{\text{ADC}} - \sigma^2_{\text{ped}}}{F^2(\overline{N_{\text{ADC}}} - \overline{N_{\text{ped}}})}, \tag{4.6}$$

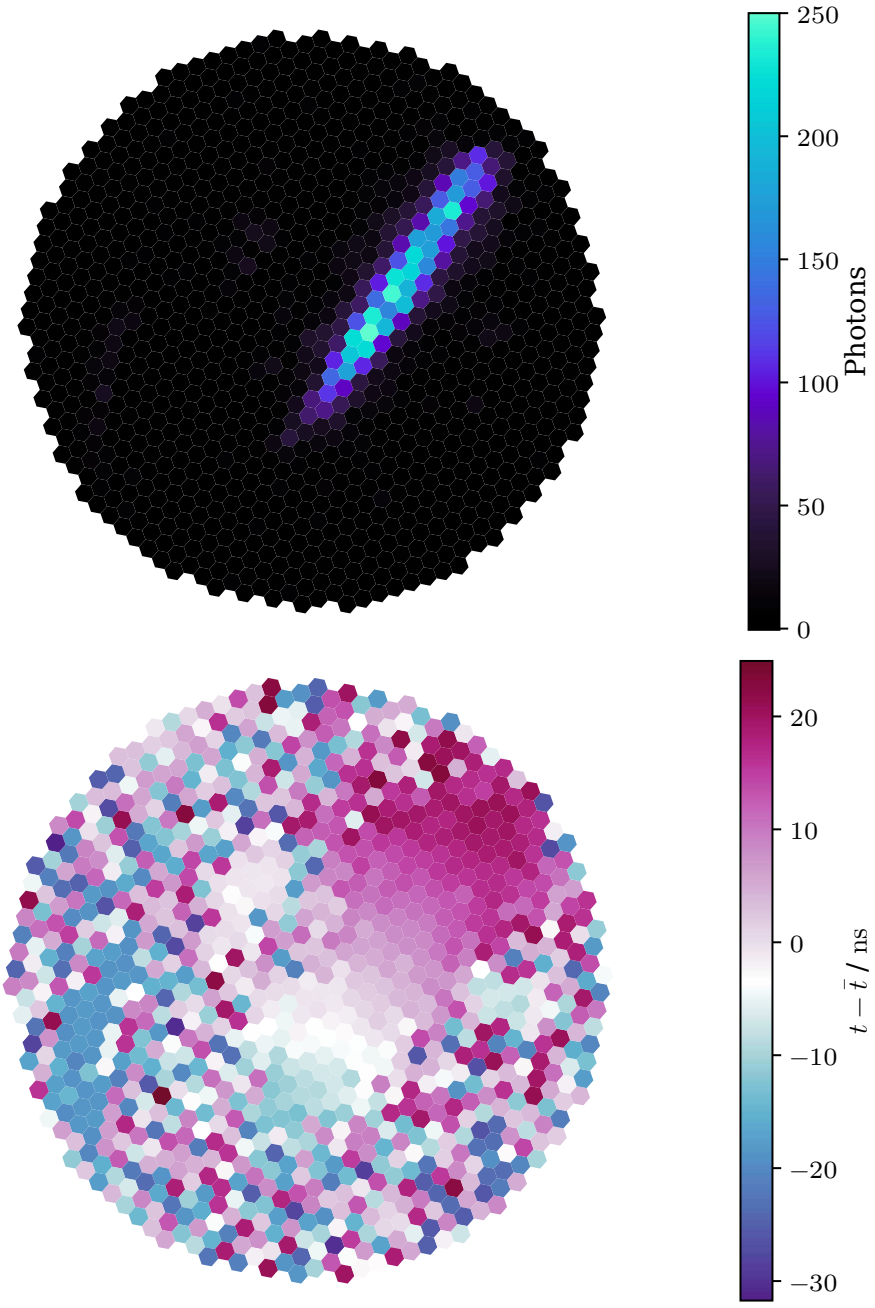

Figure 4.2: **Top view:** View of an event in the MAGIC camera after calibration. Each pixel contains the integrated counts extracted with the *sliding window extractor* and *F-Factor method*. **Bottom view:** The arrival time relative to the mean for each PMT after the same calibration as in the above view. **Both:** The large population of photons corresponds to the main shower, which is concluded from the linear development, which is visible in the arrival times of the image. The two minor populations show a constant illumination with respect to the arrival times and an overall earlier appearance in the camera. It is likely that these are originating from muons produced early in the shower development, indicating that this event is most likely induced by a CR.

where F is determined from a laboratory setup and corresponds to the single photon charge distribution width $F^2 = 1 + \sigma^2_{\text{spe}}$, given the single-photon variance σ^2_{spe} [139, 140].
Furthermore, the arrival time of the signal is calculated as the weighted average of the extracted signal window, i.e.

$$t = \frac{\sum_i t_i w_i}{\sum_i w_i}, \tag{4.7}$$

with t_i being the central time of bin i and w_i being the weight or height of the signal s_i for each bin [137].

Once the signal and arrival times have been extracted, the camera image can be viewed as the designated value for each pixel. The signal and arrival times for an arbitrary event are displayed in Figure 4.2. It should be noted that the morphology and intensity of the event in question depend on the direction, energy, and particle type.

4.2 Image Cleaning

The background noise visible in the calibrated camera image in Figure 4.2 arises from the NSB and is eliminated by *image cleaning*. The MAGIC standard analysis is based on the *dynamic sum cleaning method* [141]. This method initially removes the noisy pixels while categorizing the remaining pixels into a core and boundary population. The core region pixels of the EAS are recovered from the image by calculating the *sum* of the two-, three-, and four-NN pixels. In the event that the aforementioned sums are larger than a specific threshold q_c and within a specified time interval, the pixels are considered part of the core region. Moreover, a *dynamic* scaling of q_c is applied subsequently for each individual pixel. The scaling factor is equal to one below a threshold of 750 p.e. and is increased for brighter showers. Additionally, the pixels are required to exhibit a time deviation of Δt_c around the mean arrival time of the core. Boundary pixels are defined as those pixels that have a charge exceeding q_b, arrive within Δt_b, and have at least one direct neighbour belonging to one of the two populations. The specific cleaning parameters for *dynamic sum cleaning* are listed in Table 4.1. An illustrative example of the cleaning process on a camera image is provided in Figure 4.3.

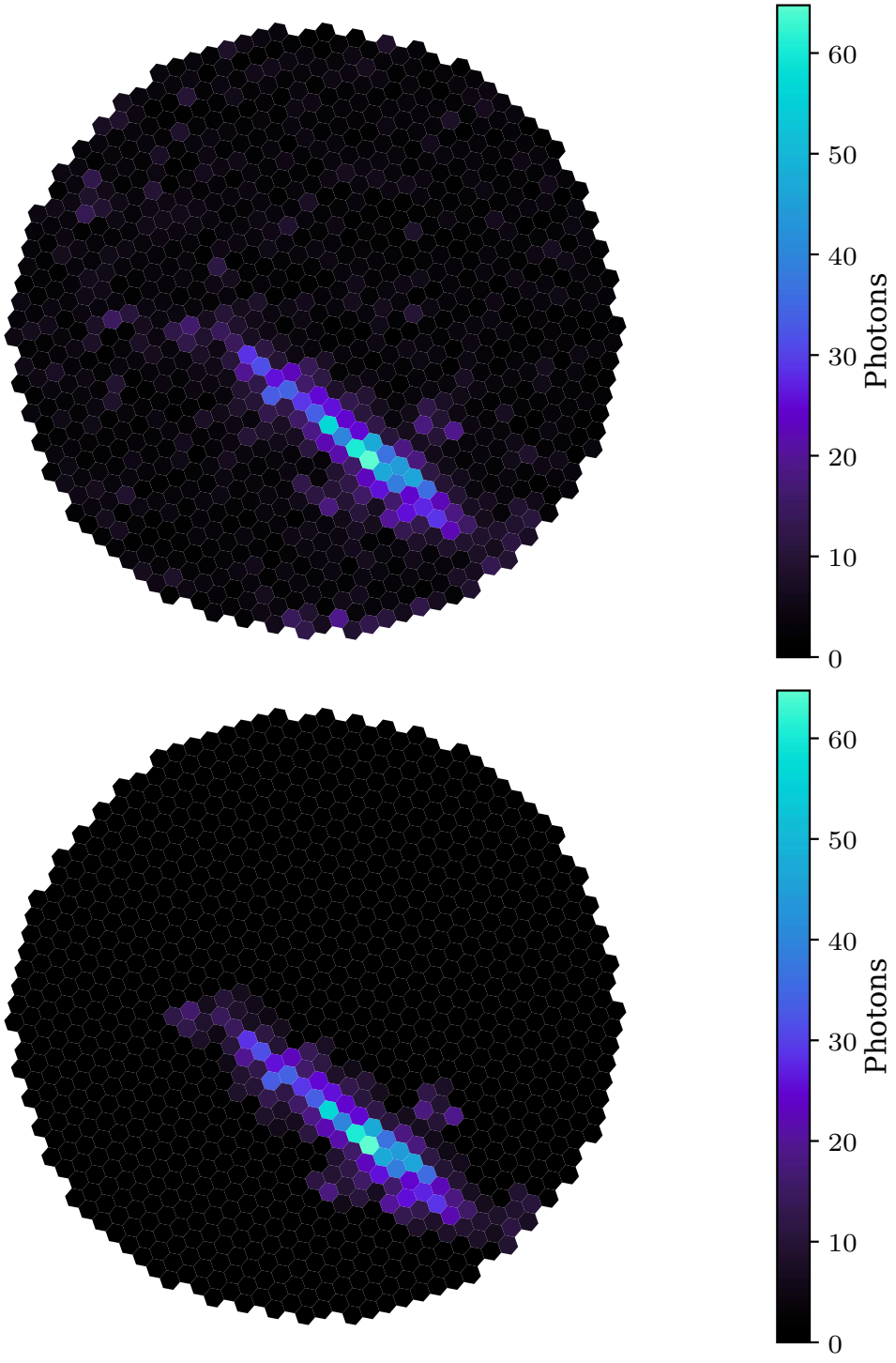

Figure 4.3: **Top view:** Camera image of an gamma-like EAS recorded by MAGIC after calibration. **Bottom view:** Event from the top view after the cleaning procedure. The noisy data has succesfully been removed.

	Charge Threshold	Arrival Time Constrain
2NN	$q_{\mathrm{NN}} = 21.6\,\mathrm{p.e.}$	$\Delta t_{\mathrm{NN}} = 0.5\,\mathrm{ns}$
3NN	$q_{\mathrm{NN}} = 24.6\,\mathrm{p.e.}$	$\Delta t_{\mathrm{NN}} = 0.7\,\mathrm{ns}$
4NN	$q_{\mathrm{NN}} = 25.2\,\mathrm{p.e.}$	$\Delta t_{\mathrm{NN}} = 1.1\,\mathrm{ns}$
Core	$q_c = 6\,\mathrm{p.e.}$	$\Delta t_c = 4.5\,\mathrm{ns}$
Boundary	$q_b = 3.5\,\mathrm{p.e.}$	$\Delta t_b = 1.5\,\mathrm{ns}$

Table 4.1: Charge threshold and arrival time constrains used by for the different pixel regions defined in the *dynamic sum cleaning method*. Values taken from [141].

4.3 Image Parameters

In this phase, the shower images are reduced to a parameterized version, designated as *Hillas parameters* [142]. The Hillas parameters of the MAGIC analysis are defined as follows:

Size The total charge present in all pixels, in p.e.. This parameter serves as an efficient proxy for the energy of the primary particle.

Length The length of the shower along its major axis. This is calculated as the first component of a Principal Component Analysis (PCA) applied to the shower image.

Width The width of the shower along its minor axis. This is calculated as the second component of a PCA applied to the shower image.

Frac2 The ratio of the p.e. in the two brightest pixels and the **Size**.

CoG The Center of Gravity (CoG) is defined as the cross-section of the minor and major axis.

Dist The distance of the CoG to the source position.

Alpha The angle between the CoG-source-position vector and the major axis of the shower.

These parameters are visualized in Figure 4.4.

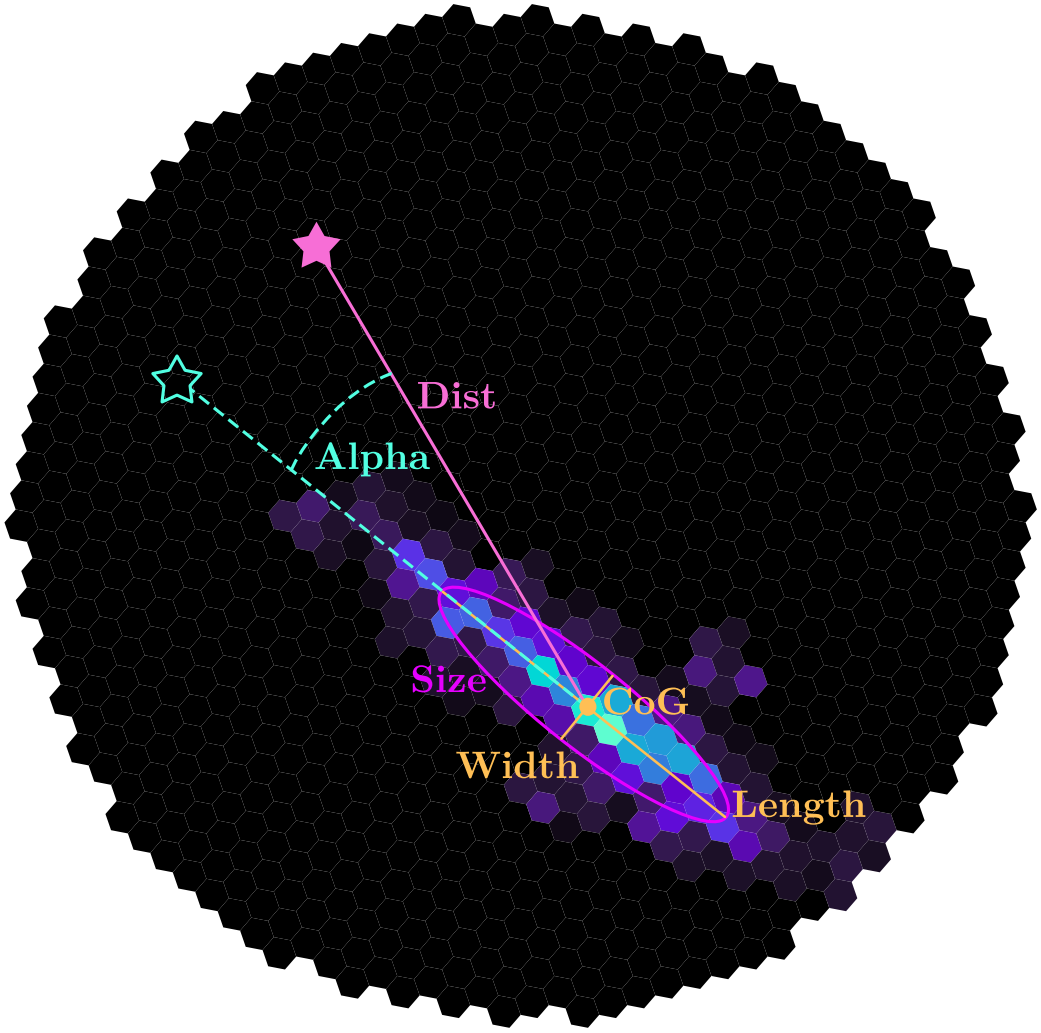

Figure 4.4: Hillas parameters overlayed on an arbitrary gamma-like event. The shaded star displays the origin of the gamma ray, while the star outline represents a possible reconstructed origin.

4.4 Stereo Reconstruction – Datasets

By employing the image parameters of both MAGIC telescopes, it is possible to reconstruct the properties of the primary particle that induced the EAS. To achieve this reconstruction, machine learning methods are utilized, with a particular focus on the training, testing, and application of RFs for MAGIC [106, 143, 144].
For the comprehensive analysis of an astrophysical source, three distinct datasets are required:

On Data The dataset contains events originating from the gamma-ray source of interest and represents the main data that is analyzed. As the observation contains hadron-induced shower events, the On data must be processed to a higher reconstruction level to remove the background events. The methodology for this signal-background separation is described in Section 4.5.

Off Data The dataset considered here comprises runs from observations where the occurrence of gamma-ray events is expected to be minimal. Either observations of faint sources that have not yet been detected or additional observations from dark patches in the sky are conducted. As the Off data primarily consists of hadronic events, it is treated as a background-only dataset for the training of the separation algorithms, as discussed in Section 4.5. To mitigate systematic errors, the observational conditions of the Off data is matched as closely as possible to those of the On data, including parameters such as zenith angle, moon phase, and atmospheric conditions.

MC Data Monte Carlo (MC) simulations are employed to generate gamma-ray events with predefined energy and incident direction. The simulations model the interaction of the gamma rays with the Earth's atmosphere, the production of the EASs, and the subsequent detection of the produced Cherenkov light with the telescopes, as detailed in Chapter 3. The MC datasets are employed as signal-only datasets. In conjunction with the Off data, it provides input for the training of the separation algorithms, which is discussed in Section 4.5. Moreover, the algorithms for energy and directional reconstruction are trained with this dataset, as detailed in Section 4.5.

The generation of gamma rays and simulation of the EASs are conducted using two modified versions of the Cosmic Ray Simulations for Kascade (CORSIKA) [145] software package, specifically versions 6.5.0.0 and 6.9.9. The aforementioned MCs simulate a spatially uniform distribution of gamma rays in the sky, with angular spreads of 1.5°, 2.5°, and 4.5°, or on a 0.4°

ring, depending on the specific analysis. MAGIC utilizes internal software, namely *reflector*, and *camera* [146], which simulate the mirror area and the camera response, respectively. Given the inherent variability of the environment, periodic adjustments to the MC production parameters are necessary to ensure the accuracy and reliability of the simulations. The two parameters of interest are the *mirror fraction* and the *axis deviation*. The former affects the reflectivity of the mirrors, thereby influencing the brightness of events recorded by the camera. *Axis deviation* modifies the scattering of the photons, thereby influencing the telescopes' directional resolution. These parameters are inferred from dedicated muon runs, i.e. observational runs that contain only events of muon showers. As discussed in Section 3.3, the Cherenkov light is emitted at an angle θ, resulting in a ring of photons being visible in the camera. This phenomenon occurs for single muons as part of a shower with a CR as the primary particle. The brightness and size of the Cherenkov ring provide insight into the reflection and scattering of the photons [147].

4.5 Stereo Reconstruction – Parameters

As outlined in the preceding section, the reconstruction of the primary particle properties is performed with RFs, which are trained on the *On*, *Off*, and *MC* datasets. The MC dataset is divided into two distinct sets: a training set and a test set. The latter is employed for the purpose of validating the performance of the reconstruction process. The performance metrics are referred to as IRFs and are introduced throughout this section.
The following properties are reconstructed:

Particle Type The observations by MAGIC are significantly influenced by the hadronic background, namely, EASs induced by CRs particles, as outlined in Section 3.4. To train the RF classifier, it is necessary to have access to both hadron and gamma-ray events. These two classes of events in question are provided by the Off data and MC data, as detailed in the preceding section. The application of the γ/h-separation RF to the On data results in the prediction of a *hadroness* for each event. This label characterizes the probability of an event being hadron-like or gamma-like. A hadronness of 1 indicates a hadronic primary, whereas a value of 0 corresponds to a gamma-ray primary. Figure 4.5 illustrates a sketched distribution of classified events. The On data is filtered by applying a hadroness cut, which can optionally depend on the energy. This cut is either defined as the hadroness with an efficiency of p_h for the distribution of events in each

energy bin or a fixed cut is selected.

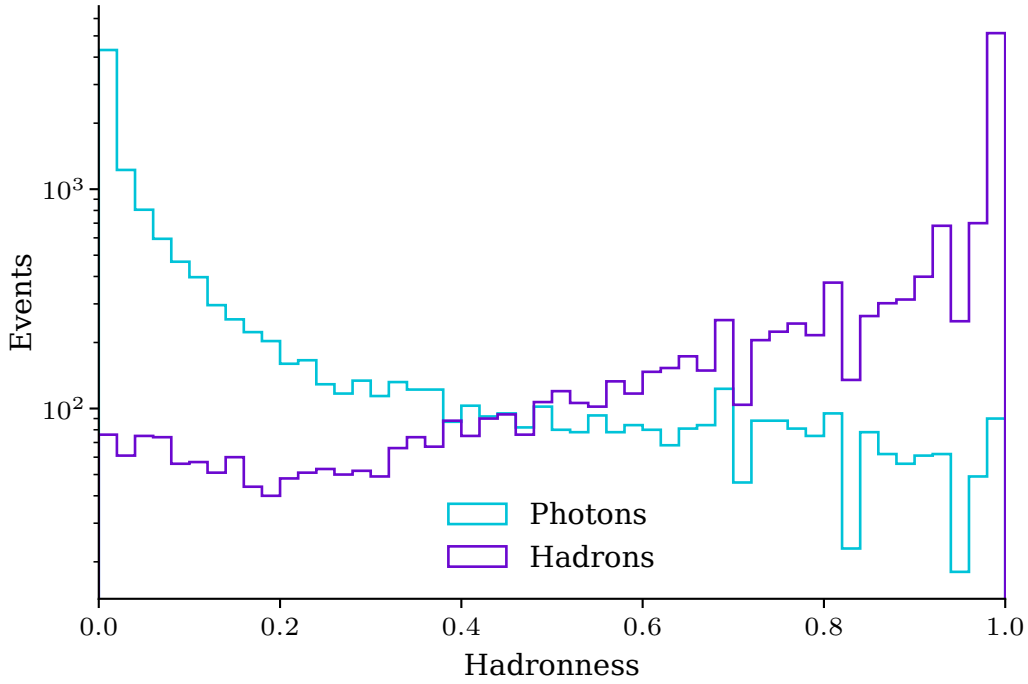

Figure 4.5: Sketch of the hadroness score assigned to test data by the trained RF for γ/h-separation. The γ data show a peak around score of 0, whereas the hadron data shows a peak around a score of 1.

The corresponding IRF to the hadroness parameter is the *effective area* of the telescopes, A_{eff}. This function is a measure for the number of events surviving all processing steps leading up to the γ/h-separation, including the trigger and image cleaning, and is defined as

$$A_{\text{eff}} = \epsilon A = \frac{N_{\text{detected}}}{N_{\text{total}}} A, \tag{4.8}$$

where A is the simulated area of the particles, N_{detected} is the number of successfully reconstructed events, and N_{total} the total number of events in the MC test split. The effective area for an arbitrary observation is displayed in Figure 4.6.

Energy Reconstruction Training the RF for energy reconstruction necessitates only MC data, as only the energies of the gamma-ray events are of interest. The Hillas parameter with the greatest impact on the reconstructed energy is the *Size* of the EAS in the cleaned camera image, as outlined in Section 4.3.

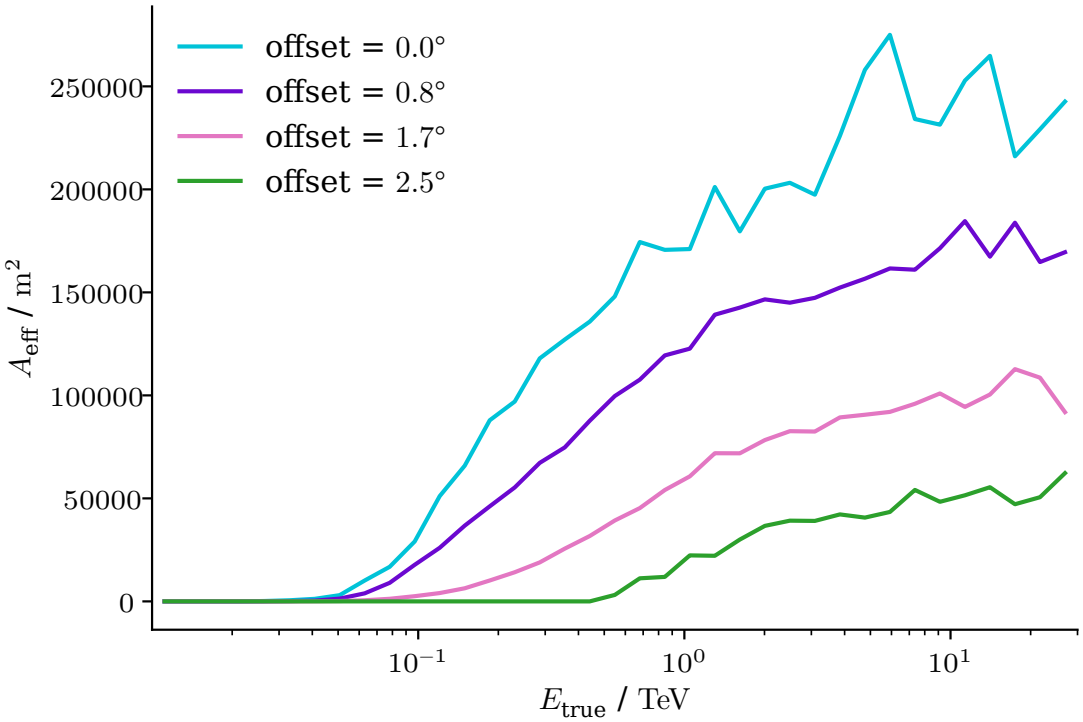

Figure 4.6: Effective area of an arbitrary observation for different offsets to the center of the FoV. As the EAS get larger with higher energies, more Cherenkov photons are produced. Therefore, the shower images are brighter and more events survive the trigger system, which is detailed in Section 3.4. As a result the effective area increases. The acceptance of the telescopes decreases with a higher distance to the center, marked as *offset*.

Since the reconstruction is not perfect, the energy is smeared around the true energy E of each event. The IRF representing this information is the *energy dispersion* or *migration matrix*, E_{disp}. It is constructed by populating a histogram of the reconstructed energy $\hat{E}$ and E for all events in the MC dataset. Figure 4.7 shows the migration matrix for an arbitrary observation. At low energies, the reconstruction shows a strong bias. This results from the low luminosity of the showers, which therefore do not survive the trigger and image cleaning.

Direction Reconstruction The direction of the incident particle is either reconstructed from the stereoscopic geometry of the shower images or with the RF-based `DISP` method [148]. The former is constructed by calculating the intersection of the two planes spanned by the pointing position of M-I and M-II and the major axis of the shower images in each telescope. In

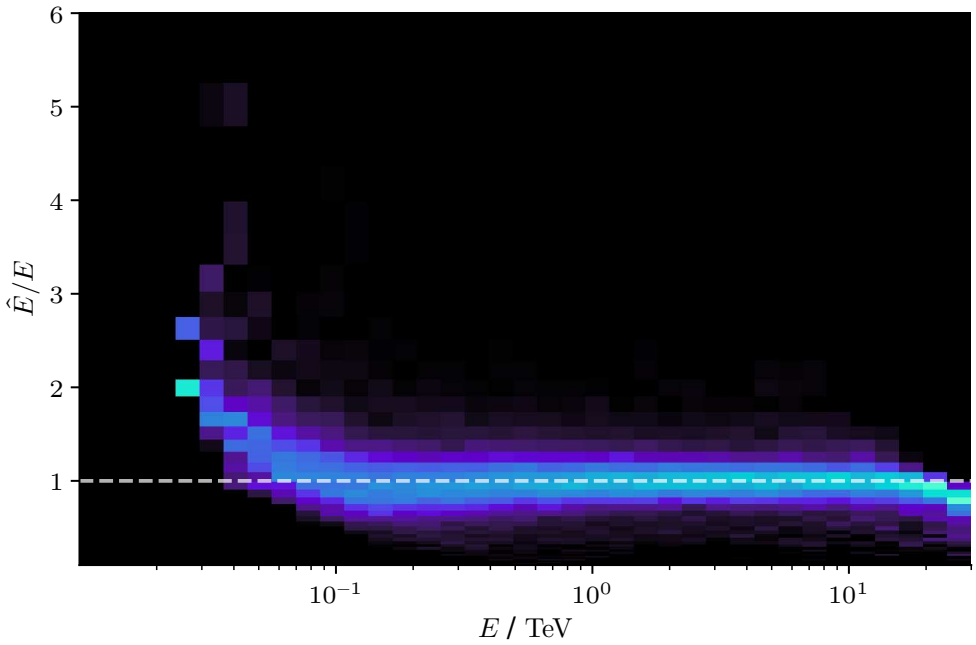

Figure 4.7: Energy migration matrix of an arbitrary observation. The ratio of reconstructed energy $\hat{E}$ and true energy E of the simulated events with respect to the true energy are binned in a 2D-histogram. A perfect reconstruction results in a horizontal line centered around a ratio of 1.

practice, the camera images are transformed to FoV coordinates, and the 2D-intersection of the lines extending the major axes is taken as the reconstructed direction.

The `DISP` method is based on an RF that predicts the distance between the CoG and the source position. Since the sign of this distance is unknown, two directions are possible. The reconstructed direction with the false sign is denoted as `DISP` *Ghost*. The population that contains the majority of all reconstructed directions, which in the case of MAGIC is a maximum of two, and has the smallest positional variation among the points, is taken as the reconstructed direction of the gamma ray [106].

Figure 4.8 illustrates both reconstruction methods. Similar to the reconstructed energy $\hat{E}$, the direction is smeared with respect to the true origin. The IRF that describes this smear is known as the Point Spread Function (PSF). Namely, it parameterizes the size of the region centered on the true event position. The containment radii for 68% and 95% at two different FoV offsets are displayed in Figure 4.9. For higher energies the reconstruction performance increases, since the showers are brighter and reconstruction is therefore easier.

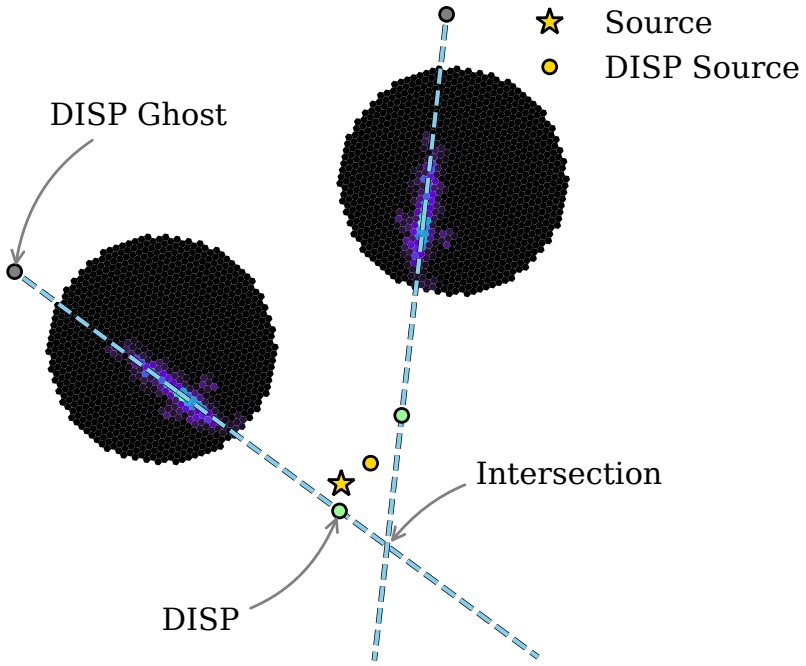

Figure 4.8: Sketch of the directional reconstruction of a gamma-like event seen by both MAGIC telescopes. The source position is displayed as a star. **Intersection:** The Hillas parameters are used to extend the projected shower axis to the point of intersection between both camera images. The intersection is taken as the reconstructed source direction. **`DISP`:** Alternatively the `DISP` method is used for reconstruction of the origin of the shower. The `DISP` origins with the wrong sign are denoted as gray dots, while the correct ones are shown in green. The reconstructed origin is the mean of the two mono `DISP` reconstructions.

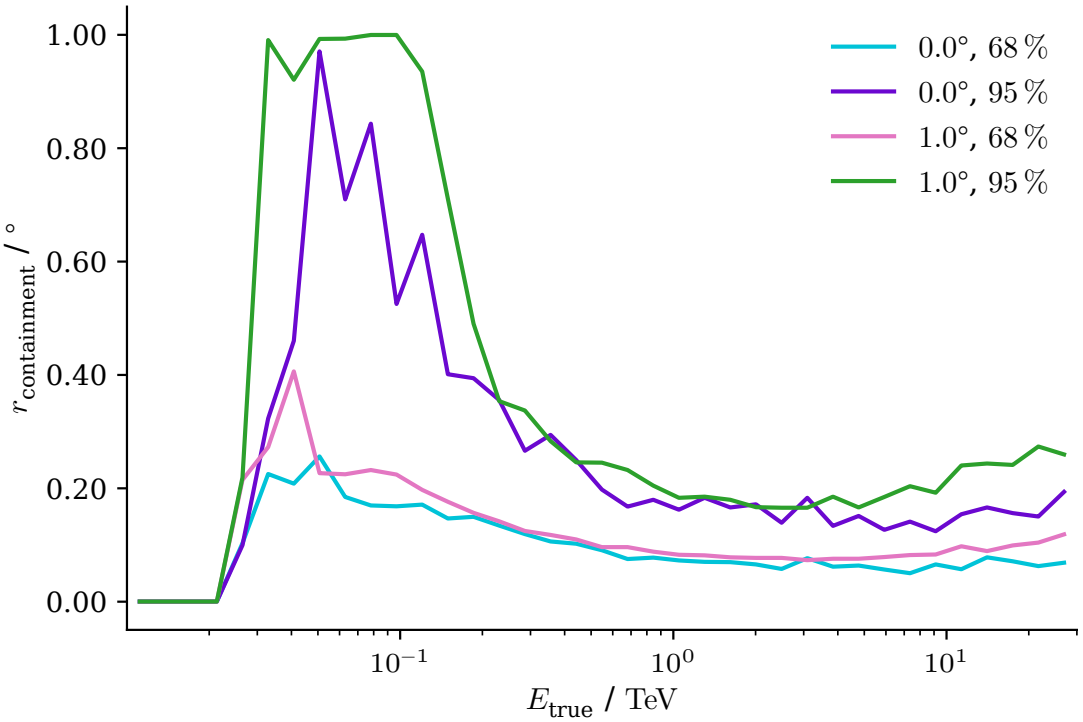

Figure 4.9: 68% and 95% containment radii of the PSF of an arbitrary observation. Two different offsets with respect to the center of the FoV are displayed. The radii are computed from the reconstructed direction of simulated events given their true origin.

4.6 MARS

The MAGIC Analysis and Reconstruction Software (MARS) is the software stack of MAGIC, offering a comprehensive toolset for the standard analysis and processing of the recorded gamma-ray data [149, 150]. The data is made available to the collaboration members via the Port d'Informació Científica (PIC). The following section describes the MARS programs and their respective functions. Figure 4.10 illustrates the workflow of an analysis.

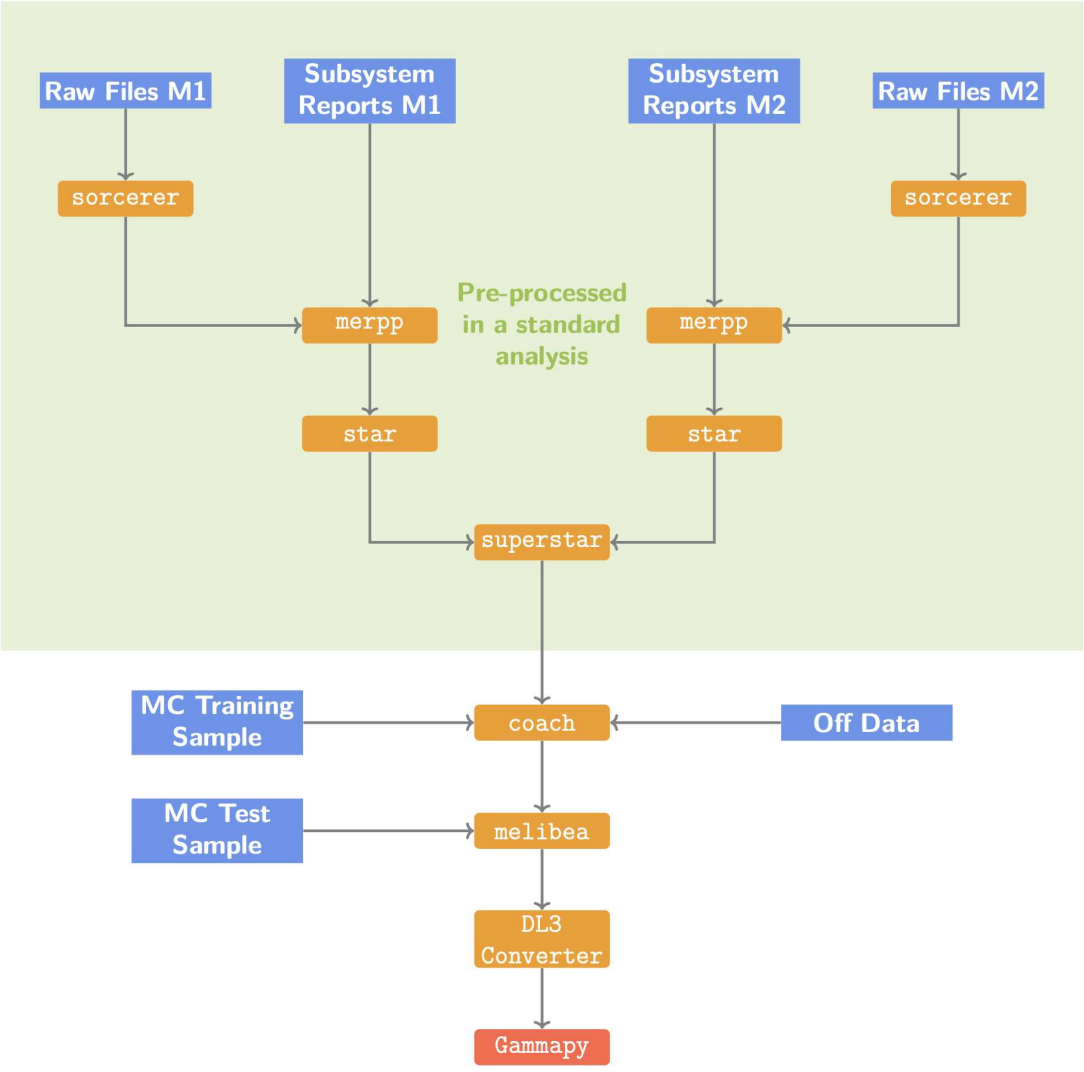

Figure 4.10: Schematic of the subprograms of MARS illustrated in orange. The blue squares indicate the input data needed for the analysis. Furthermore, the DL3 converter produces data readable by `Gammapy`. Figure taken from [151].

sorcerer This is the initial program in the MARS stack that must be executed. It takes the raw input data and performs the requisite calibration in accordance with the specifications set forth in Section 4.1. Therefore, the software has been designated Simple, Outright Raw Calibration; Easy, Reliable Extraction Routines (sorcerer). The charge in p.e. as well as the arrival times are extracted for each pixel.

merpp During the observation, each MAGIC subsystem reports its status and data to `SuperArehucas`, the central control. This encompasses, among other, data from the LIDAR, weather station, and camera. The subsystem metadata is merged with the calibrated files from sorcerer via `merpp`.

star Following the attachment of the meta information, the image cleaning process, as outlined in Section 4.2, and the computation of the Hillas parameters are conducted for each telescope image, as detailed in Section 4.3,

superstar This software is capable of combining the information from M-I and M-II to create stereoscopic data from the `star` output files. For this reason, it is referred to as `superstar`. It is capable to perform the directional reconstruction based on the geometry of the showers, as described in Section 4.5.

selectmc RFs are employed to reconstruct the primary particle information, as detailed in Section 4.5. The training necessitates the provision of an additional Off and MC dataset, as introduced in Section 4.4. The latter is split into a training and a test set by `selectmc`.

coach The definition of the RF hyperparameters and training of the RFs are conducted by Compressed Osteria Alias Computation of the Hadronness parameter (coach). In total, three RFs are trained for the purpose of particle type classification, energy reconstruction, and direction reconstruction, as further elaborated in Section 4.5. It is possible for the user to select a Look Up Table (LUT) as an alternative for the energy RF.

melibea The trained RFs computed by coach are applied to the On dataset. For each event, the hadroness, energy, and direction are estimated. This step is performed by `melibea`.
Furthermore, `melibea` applies the aforementioned RFs to the test split of the MC dataset, which produces the IRFs detailed in the preceding section.

DL3 Converter The Gamma Astro Data Formats (GADF) [13] establish a uniform data format for gamma-ray experiments through the definition of different *data levels*. A conversion of the `melibea` files to DL3 is necessary for

subsequent analysis with `Gammapy` [11]. A detailed explanation of DL3 is provided in Section 4.8. The conversion is performed by `magic_dl3` [152].

The MARS stack contains additional high-level software, such as `odie`, as an alternative to some `Gammapy` modules. However, these programs are not discussed further as they are not applied in this thesis.

4.7 AutoMAGIC

The advent of new experiments, such as the Cherenkov Telescope Array Observatory (CTAO) [153, 154], and modern analysis software, such as `Gammapy`, has made it possible to combine data from multiple observatories in a way that leverages the advantages of each experiment. In light of this, it has become increasingly important for MAGIC to provide their data in a format that is accepted by the wider scientific community. The objective of the MAGIC legacy program [155] is to reprocess observations with the DL3 standard. The reprocessing requires a considerable investment of human resources to run the MARS stack and achieve the desired output. To address this challenge, the autoMAGIC [10] project was initiated. autoMAGIC aims to automatize the MARS standard analysis, with minimal input from the user, who is required to provide only basic information, such as the source, observation period, and a few hyperparameters. The core architecture, illustrated in Figure 4.11, enables this functionality and is described in the following:

MARS Python Wrapper autoMAGIC is written in Python and is capable of calling the MARS subprograms, as introduced in Section 4.6, with wrapper functions. These wrappers make it possible to pipe the settings of the user to the individual processing steps, while the handling of the input and output data is performed by autoMAGIC.

Database Keeping track of the workflow while processing the data is a fundamental step towards a reproducible and automatic analysis. autoMAGIC is built around a PostgreSQL database, which stores the metadata pertaining to the observations, including file locations, information regarding the MAGIC subsystems, and the relational data between the MC periods and the time of the observations. A job is generated for each processing step, containing the settings, input data, and output directory for each execution of a MARS wrapper.

Submitter The jobs that are stored in the database are assigned an `ID` that describes their current state. Each job is executed on a node of the PIC

cluster via the `Submitter`. This tool oversees the number of jobs that are run simultaneously, monitors the status of each job during its execution, and stores the resulting output files on the PIC file system.

autoMAGIC generates the processing jobs in a "bottom-to-top" manner, meaning for every analysis the low-level jobs are created first, and the subsequent jobs are created based on this information. Moreover, autoMAGIC verifies whether a job for the identical processing step already exists. In the case of a job with existing output, autoMAGIC has the potential to reduce computational power consumption and associated CO_2 emission by skipping the execution. This represents a significant advancement in the field of resource-aware computing with regard to MAGIC analyses. Further information on resource-aware research on Universe and Matter can be found in [156].
The observational data utilized in the context of this thesis is processed with autoMAGIC up to DL3.

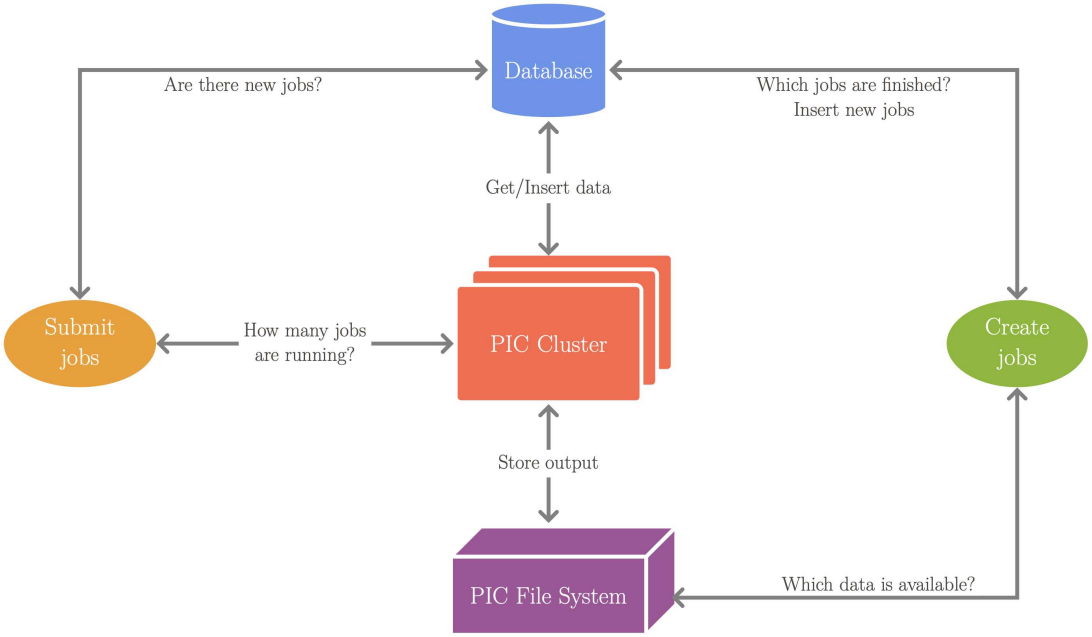

Figure 4.11: Schematic of autoMAGIC's workflow. Upon user input, a list of tasks is produced. For each task, a job is created if it does not already exist in the database, that holds information about old and new analyses. Newly created jobs are submitted to PIC cluster and their output is stored in the PIC file system. Figure taken from [151]

4.8 GADF – Data Level 3

DL3 provides a tabular representation of gamma-ray events, comprising the reconstructed energy, direction, and hadroness of the particle, as detailed in Section 4.5. Such a table or *event list* is displayed in Figure 4.12. Moreover, the IRFs introduced in the aforementioned section are appended to the DL3 file. They assess the performance of the detector and the reconstruction methods. It should be noted that a distinction is made between these *full-enclosure* IRFs and *point-like* IRFs, the latter being derived by applying a directional cut to the data. Furthermore, the full-enclosure IRFs necessitate a background model, which describes the rate of background events that are falsely classified as gamma rays. Different methods for background modelling are described in the following section.

EVENT_ID	TIME	RA	DEC	ENERGY	GAMMANESS
	s	deg	deg	TeV	
int64	float64	float32	float32	float32	float32
49573	494557484.4056609	83.55752	21.174353	0.37530714	0.63853174
49575	494557484.412652	84.996796	22.117865	0.16939677	0.743623
49599	494557484.48141736	83.35432	22.84225	0.91273344	0.7423276
49647	494557484.5969525	82.10264	22.390959	0.14952253	0.517
49778	494557484.95327914	84.06245	22.297728	1.2585704	0.97645164
49782	494557484.96293133	83.29229	22.621408	0.15302667	0.87982935
49879	494557485.3100421	81.84162	21.35705	0.18031162	0.5535436
49890	494557485.37707675	83.51765	22.150053	0.06262616	0.68647224
49892	494557485.39280474	82.66088	21.908197	0.11601091	0.5241468
49900	494557485.41568106	84.74319	20.97977	0.12480276	0.84132683

Figure 4.12: Figure displaying the tabulated events on DL3. The reconstructed parameters displayed are detailed in Section 4.5.

4.9 Background Modelling

Estimating the number of background events in the data is crucial for a correct analysis. They arise from a non-perfect signal-background separation, as described in Section 4.5. Taking advantage of the Wobble mode, as introduced

in Section 3.5, allows the use of different techniques for background modelling. The common modelling techniques in gamma-ray astronomy are described in the following [157]:

Reflected Regions $N_{\text{OFF-regions}}$ are placed on a circle in the FoV with respect to a Wobble position. Since they *reflect* the ON region and have the same properties regarding the acceptance of the telescopes if a radial symmetry is assumed, the number of background events is given as

$$b = \frac{N_{\text{OFF}}}{N_{\text{OFF-regions}}}, \tag{4.9}$$

with the summed number of events in the OFF regions N_{OFF}. This method is illustrated in Figure 4.13.

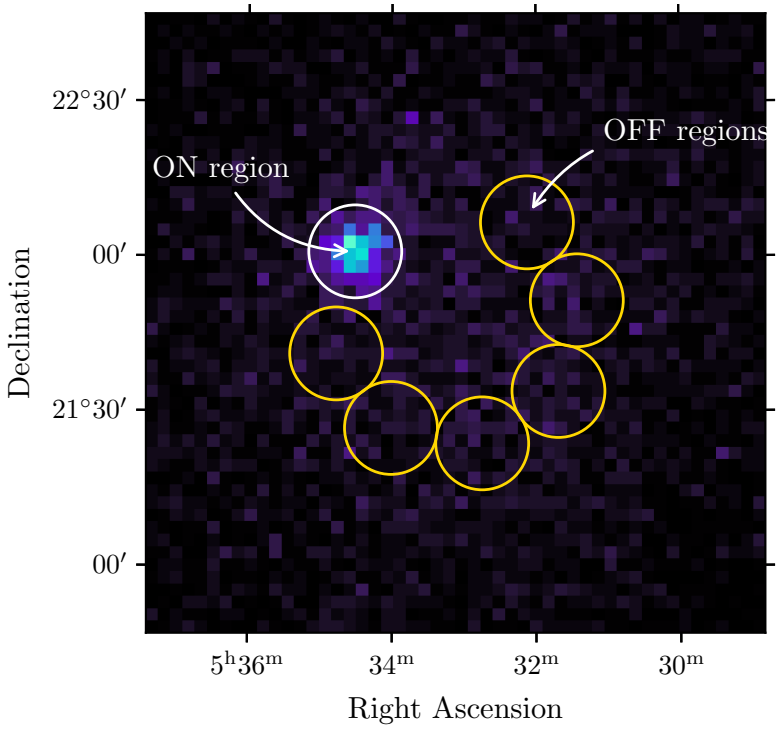

Figure 4.13: Illustration of the DL3 events in the FoV. The map is centered on the Wobble position. The ON region is defined as the 0.15° circular region around the position of the Crab Nebula. In contrast, the OFF regions are found by placing as many regions as possible, which have the same size as the ON region, at the circle defined by the Wobble distance. The OFF regions do not overlap.

Ring Background Method A ring is placed in the FoV centered around a trial position for which the background is to be estimated. This allows calculat-

ing the background for any position in the FoV. In first-order approximation, the background rate is given as the fraction of the solid angles for the trial position and for the ring,

$$b \approx \frac{\Omega_{\mathrm{ON}}}{\Omega_{\mathrm{OFF}}} \cdot N_{\mathrm{OFF}}, \tag{4.10}$$

where N_{OFF} are the counts contained in the ring. Since the acceptance for the ring is not radially symmetric, the calculation of the acceptance correction is not as trivial as for the *reflected regions* method. An acceptance map for the observation is required. The method is illustrated in Figure 4.14.

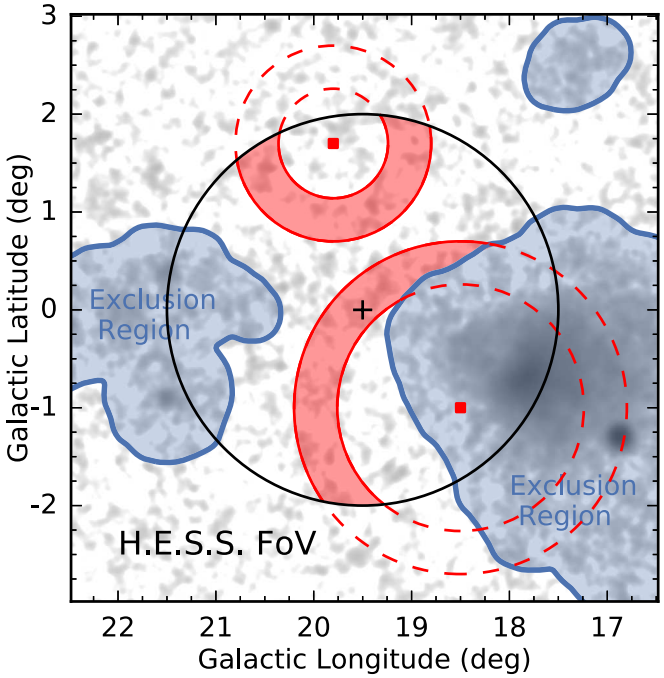

Figure 4.14: Illustration of the ring background method. The black circle shows the FoV used for the original analysis, while the blue regions are areas that are excluded from the calculation of the background, due to higher excess. The two red rings are the areas that are taken for the background estimation of the center of the ring (red squares). Figure taken from [105].

Template Modelling A template model is created from MCs or data from multiple observations. It is normalized to the data of each run during an observation. The method used in this thesis is based on the *exclusion method* [158] and is described in detail in Chapter 6. It takes advantage of the Wobble mode and excludes a region around the source position, which is filled with

data from one of the other Wobble positions. This method is illustrated in Figure 4.15 for two Wobble positions.

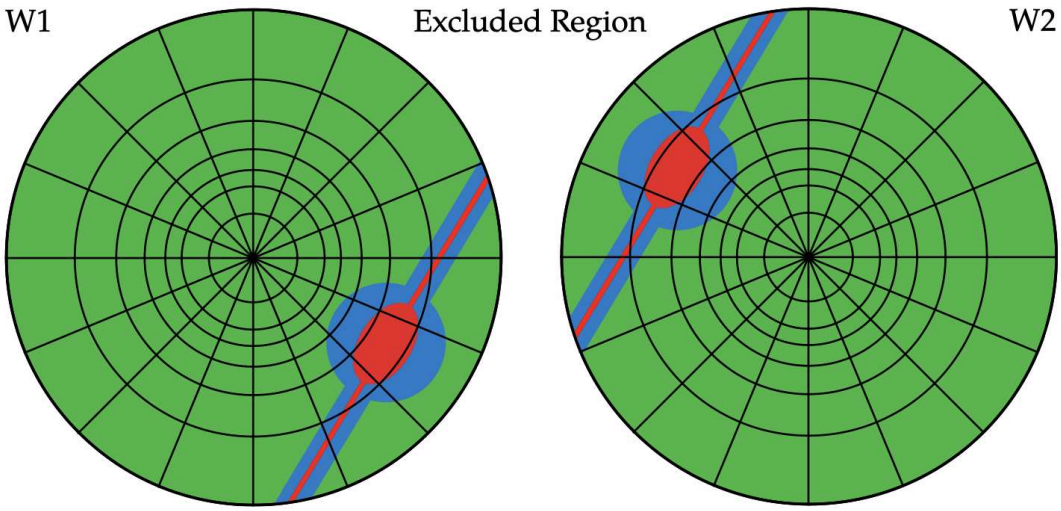

Figure 4.15: Schematic of the exclusion method. This method *excludes* an extended source region, shown in red and blue, from the FoV. The telescopes operate in Wobble mode, which leads to a change of the FoV center with respect to the source position. Therefore, regions on opposite sites at Wobble positions W1 and W2 are excluded. Stacking the data of both positions fills the excluded regions with background events. A source-free background model can be created. Figure taken from [158].

5 Statistical Methods – A Novel Application for Gamma-ray Astronomy

In order to facilitate the examination of a source, it is necessary to process the DL3 produced by autoMAGIC to a higher level such as spectra. `Gammapy` provides this through *data reduction*, *modelling*, and *fitting*.
This chapter introduces the statistical tests required for the search for DM and for setting upper limits (ULs) on the model parameters.
Furthermore, it introduces *Asimov* datasets for a more solidified construction of limits. The implementation of these novel statistical methodologies has been undertaken within the open-source Python package `TITRATE` [12], which has been developed for this thesis.

5.1 DL3 Analysis with Gammapy

`Gammapy` [11] is an open-source Python package for gamma-ray data analysis and one of the core science tools of CTAO [103]. In the past years, it has also been adopted by many other gamma-ray experiments like MAGIC [159], H.E.S.S. [160], VERITAS [161, 162], and HAWC [163, 164] and will be used for the analysis of the DL3 files produced with autoMAGIC, as outlined in Section 4.7.

Figure 5.1 illustrates the processing steps and functionalities of `Gammapy`, which are outlined in the following:

Data Reduction The analysis starts with reading the DL3 files, introduced in Section 4.8, of the observations and storing the information in the `Gammapy` container classes. Each of the tabulated events is described by three parameters, the origin (two-dimensional vector), the energy, and the arrival time. The latter is required for the analysis of variable sources. This data is subsequently reduced to Data Level 4 (DL4) with the *Maker* classes. DL4 encompasses n-dimensional histograms of the data known as *Datasets*. In the scope of this thesis one distinguishes between *1D* and *3D* datasets,

which have an energy or an energy plus two spatial axes, respectively. Figure 5.2 displays the conversion from DL3 to the DL4 *cube* schematically.

Modelling & Fitting Spectral and spatial sky models are fitted to the data, which results in Data Level 5 (DL5), e.g. sky maps, spectra, and light curves of the gamma-ray source. Data Level 6 (DL6) often consists of bundled results from larger analyses, such as source catalogs.
Throughout this chapter, the modelling and fitting is outlined in greater detail, and new statistical methods are introduced, that build on the implementations already provided by `Gammapy`.

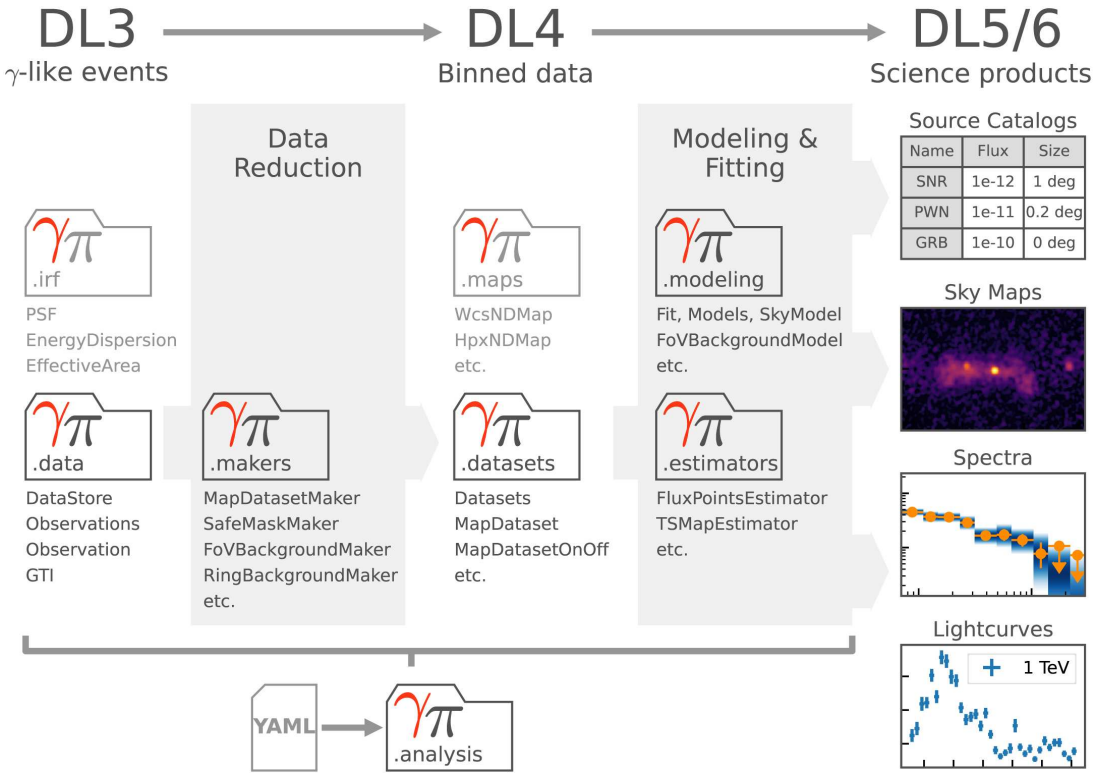

Figure 5.1: Schematic of the GADF data levels and classes throughout the `Gammapy` analysis. The processing starts with the conversion of DL3 to DL4. This step is called data reduction. The DL4 is transformed into DL5 and DL6 via modelling and fitting. Common data at these levels are source catalogs, sky maps, spectra, and light curves. Figure taken from [11].

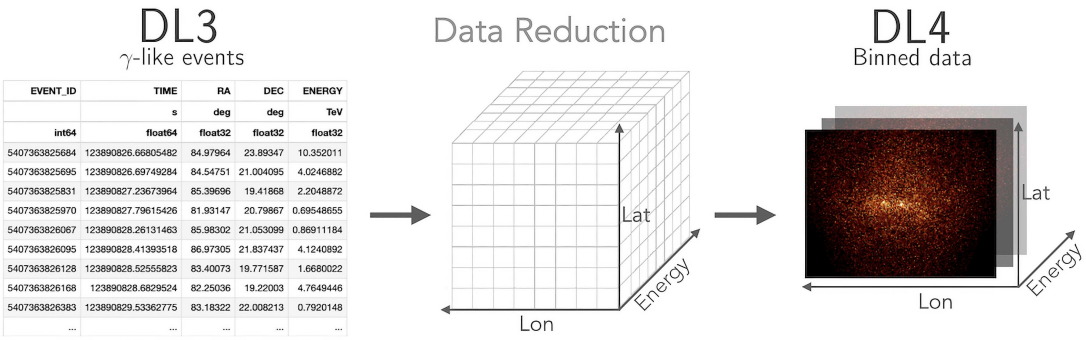

EVENT_ID	TIME	RA	DEC	ENERGY
	s	deg	deg	TeV
int64	float64	float32	float32	float32
5407363825684	123890826.66805482	84.97964	23.89347	10.352011
5407363825695	123890826.69749284	84.54751	21.004095	4.0246882
5407363825831	123890827.23673964	85.39696	19.41868	2.2048872
5407363825970	123890827.79615426	81.93147	20.79867	0.69548655
5407363826067	123890828.26131463	85.98302	21.053099	0.86911184
5407363826095	123890828.41393518	86.97305	21.837437	4.1240892
5407363826128	123890828.52555823	83.40073	19.771587	1.6680022
5407363826168	123890828.6829524	82.25036	19.22003	4.7649446
5407363826383	123890829.53362775	83.18322	22.008213	0.7920148
...	...	...	...	...

Figure 5.2: Schematic of the data reduction step. The DL3 is provided as a list of events with energy, direction, and time. Depending on the analysis different bin sizes are chosen by the user. The populated bins for energy and direction are referred to as the DL4 cube. Figure taken from [165].

5.2 Fitting a Model

Based on the DL4 cube, introduced in the preceding section, one is interested in computing physical properties, or DL5, e.g. the spectrum, of the gamma-ray source which is observed. `Gammapy` provides a variety of models that can describe these properties. In general, a model depends on a set of parameters $\vec{\theta}$, e.g. the spectral shape of the model, and the model flux is written in the factorized form

$$\phi(\vec{\theta}) = \underbrace{\phi(E|\vec{\theta}_E)}_{\text{Spectral Model}} \times \underbrace{\phi(\alpha, \delta|\vec{\theta}_{\alpha,\delta})}_{\text{Spatial Model}}, \tag{5.1}$$

where E denotes the energy and (α, δ) the origin of the emission in Right Ascension and Declination (Ra-Dec).
Under the assumption that the counts in the DL4 cube, $\vec{m}$, follow a Poissonian distribution,

$$P(m_i|n_i(\vec{\theta})) = \frac{n_i(\vec{\theta})^{m_i}}{m_i!} e^{-n_i(\vec{\theta})}, \tag{5.2}$$

where n_i is the number of events in each bin of the DL4 that are predicted by the model. The model parameters can be inferred with a maximum likelihood estimation (MLE). In detail, the negative log-likelihood (NLL) or Cash statistic [166],

$$-2 \log \mathcal{L} = 2(\vec{n}(\vec{\theta}) - \vec{m} \log(\vec{n}(\vec{\theta}))), \tag{5.3}$$

is minimized to find the best-fitting set of parameters $\hat{\vec{\theta}}$. Figure 5.3 displays a possible NLL and its minimum at $\hat{\vec{\theta}}$. The subsequent two sections describe the

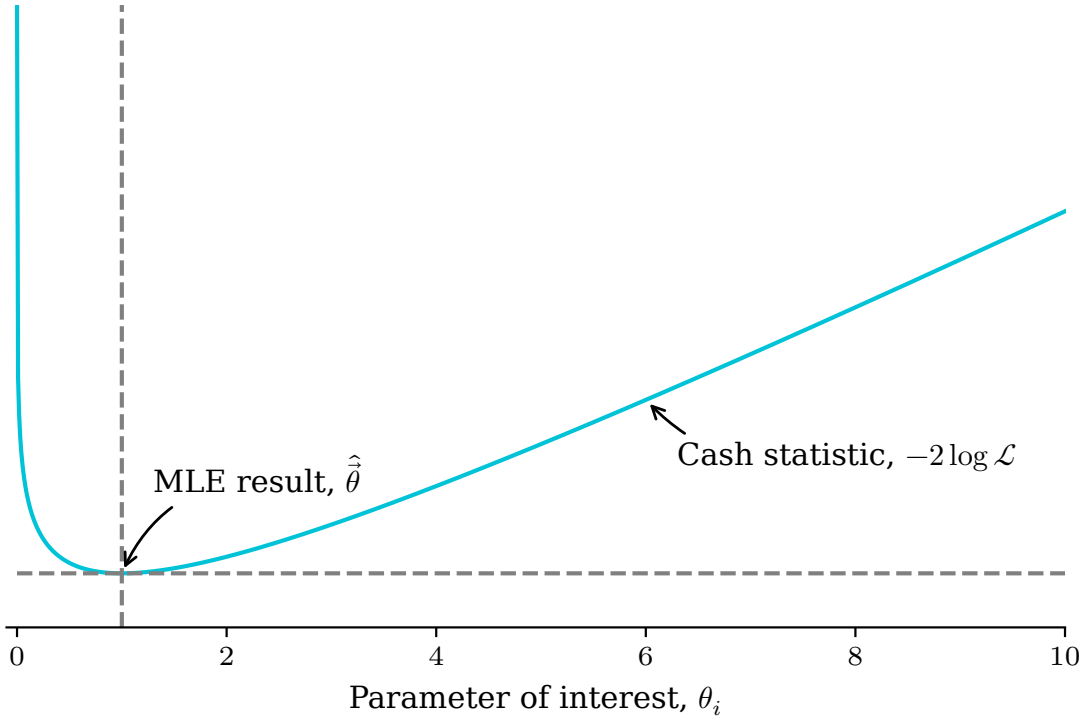

Figure 5.3: Schematic of the NLL profile during the MLE. The best fitting parameters $\hat{\vec{\theta}}$ are found at the minimum of the Cash statistic.

calculation for the expected number of events $\vec{n}(\vec{\theta})$.

5.3 How to Respond to a Gamma Ray

The IRFs introduced in Section 4.5 describe the response of the telescopes, i.e. how many gamma rays survive the trigger and reconstruction, and how the energies and incident directions are smeared, given a gamma-ray flux ϕ as defined in Equation 5.1. Moreover, the expected number of events is given as

$$n_i(\hat{E},\hat{\alpha},\hat{\delta}|\vec{\theta}) = \int_t\int_E\int_\Omega R(\hat{E},\hat{\alpha},\hat{\delta}|E,\alpha,\delta,t)\frac{\mathrm{d}^2\phi(E,\alpha,\delta,t|\vec{\theta})}{\mathrm{d}E\mathrm{d}\Omega}\mathrm{d}E\mathrm{d}\Omega\mathrm{d}t + \int_t b(\hat{E},\hat{\alpha},\hat{\delta},t)\mathrm{d}t, \tag{5.4}$$

where $\hat{E}$ is the reconstructed energy, $(\hat{\alpha}, \hat{\delta})$ the reconstructed direction of the gamma ray in Ra-Dec, and t the time of the observation [167] [1]. The differential of the solid angle is given as $\mathrm{d}\Omega = \sin\delta \mathrm{d}\alpha \mathrm{d}\delta$. In general, the detector response $R(\hat{E}, \hat{\alpha}, \hat{\delta}|E, \alpha, \delta, t)$ depends on observational conditions such as atmospheric transmission of the Cherenkov light and optical efficiency of the telescopes, therefore Equation 5.4 is assumed to be valid for a period of constant environmental conditions. In detail $R(\hat{E}, \hat{\alpha}, \hat{\delta}|E, \alpha, \delta, t)$ is the product of the IRFs,

$$\begin{aligned} R(\hat{E}, \hat{\alpha}, \hat{\delta}|E, \alpha, \delta, t) = A_{\mathrm{eff}}(E, \alpha, \delta, t) \cdot E_{\mathrm{DISP}}(\hat{E}|E, \alpha, \delta, t) \\ \cdot \mathrm{PSF}(\hat{\alpha}, \hat{\delta}|E, \alpha, \delta, t). \end{aligned} \tag{5.5}$$

$b(\hat{E}, \hat{\alpha}, \hat{\delta}, t)$ is the background model, as detailed in Section 4.9.
This method is referred to as *forward folding*.

5.4 1D Reduction

The DL4 cube can further be reduced to one dimension by integrating the events in a specified source region. For the calculation of the predicted events from a model, Equation 5.4 is integrated over the reconstructed spatial dimension inside the region of interest,

$$\begin{aligned} n_i(\hat{E}|\vec{\theta}) &= \int_t \int_E R(\hat{E}|E, t) \frac{\mathrm{d}^2\phi(E, t|\vec{\theta})}{\mathrm{d}E} \mathrm{d}E\mathrm{d}t + \int_t b(\hat{E}, t)\mathrm{d}t \\ &= \int_t \int_E A_{\mathrm{eff}}(E) \cdot E_{\mathrm{DISP}}(\hat{E}|E) \frac{\mathrm{d}^2\phi(E, t)}{\mathrm{d}E} \mathrm{d}E\mathrm{d}t + \int_t b(\hat{E}, t)\mathrm{d}t. \end{aligned} \tag{5.6}$$

This is referred to as a 1D analysis, with the energy axis being the remaining dimension.

5.5 Significance – Detecting a Source

Claiming a discovery of a signal requires the calculation of a statistical significance. Furthermore, a test statistic (TS) is defined under the null hypothesis that the data can be described by the background, dubbed background-only hypothesis. This requires the introduction of a strength parameter μ, that scales the model in the first integral in Equation 5.4 and Equation 5.6. Consequently, $\vec{\theta}$ becomes $\vec{\theta} \to (\mu, \vec{\theta})^{\mathrm{T}}$, where the previously defined parameters are referred to as nuisance

[1] Equation 5.4 is modified from [167] by time integration of the background model.

parameters (NPs). The generalized TS is given as the profile log-likelihood ratio (pLLR) [168]

$$q_\mu = \begin{cases} -2\log\frac{\mathcal{L}(\mu,\hat{\hat{\theta}}_\mu)}{\mathcal{L}(\hat{\mu},\hat{\hat{\theta}}_{\hat{\mu}})}, & \hat{\mu} \leq \mu \\ 0, & \hat{\mu} > \mu \end{cases}. \tag{5.7}$$

The set of NPs $\hat{\hat{\theta}}_\mu$ minimizes the numerator under a conditional value assumed for μ. This method retains the minimum of the NLL. For the null hypothesis, $\mu = 0$, the close to Equation 5.7 related TS is defined

$$q_0 = -2\log\frac{\mathcal{L}(0,\hat{\hat{\theta}}_0)}{\mathcal{L}(\hat{\mu},\hat{\hat{\theta}}_{\hat{\mu}})}. \tag{5.8}$$

A confidence level α [2] is set under which the null hypothesis gets rejected. A common value for α is the p-value of the 3σ- or 5σ-interval of a standard normal distribution $\mathcal{N}(0,1)$. In simplified terms, a signal is claimed when it is at least 5σ *away* from a background-only description of the data (the mean of $\mathcal{N}(0,1)$). Whereas a value of 3σ is considered the first evidence of a signal.
The p-value of the distribution of TS, given the TS value of the observed data $q_{0,\text{obs}}$, is given as

$$p = \int_{q_{0,\text{obs}}}^{\infty} f(q_0|0,\hat{\hat{\theta}}_0)\, dq_0. \tag{5.9}$$

and is displayed in Figure 5.4. $f(q_0|0,\hat{\hat{\theta}}_0)$ can be approximated with Wilks' theorem, which states that it is given by a χ^2 distribution with one degree of freedom [169]. Therefore, the p-value can be computed from the cumulative density function (CDF) Φ_{χ^2} and can be converted to a significance S with the CDF of the standard normal distribution,

$$\int_S^{\infty} \mathcal{N}(x|0,1)\, dx \stackrel{!}{=} p \tag{5.10}$$

Together with Equation 5.9 the significance is simply

$$S = \sqrt{q_0}. \tag{5.11}$$

[2] Not to be confused with the right ascension of a gamma-ray event α.

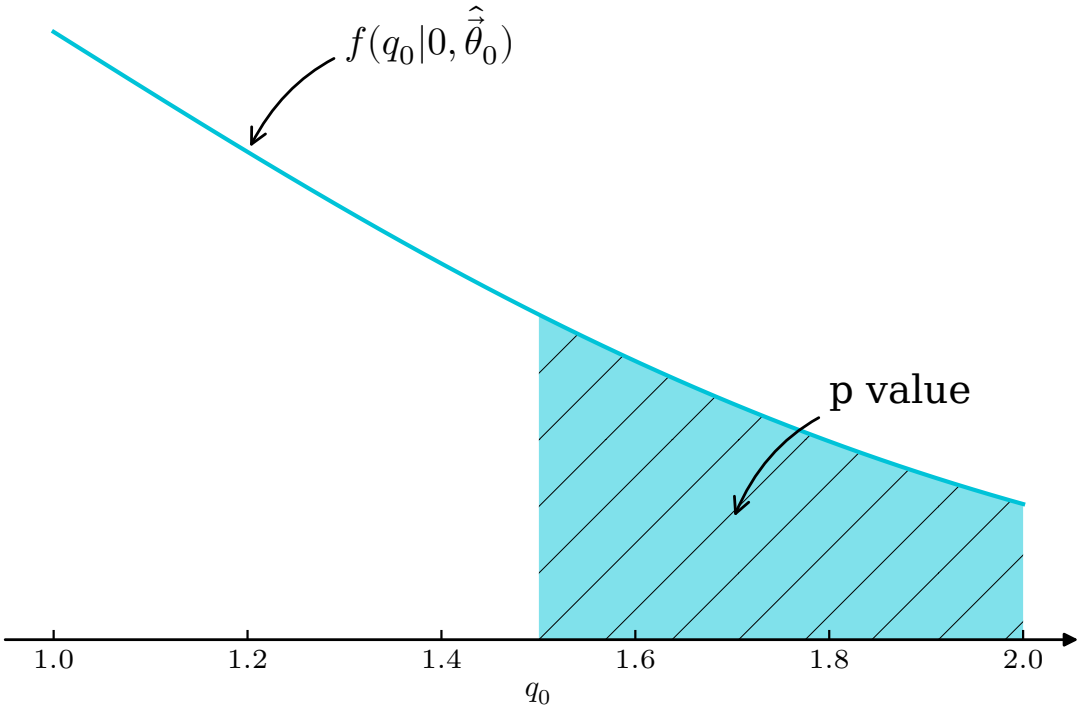

Figure 5.4: Illustration of the p-value, as the area under the curve of the TS distribution integrated from $q_{0,\text{obs}}$ to ∞.

5.6 Upper Limits

In case the calculated significance does not reach the 5σ threshold discussed in the preceding section, the UL on the flux of the model is calculated. Moreover, the ULs on any parameter that scales linearly with μ can be calculated in the same manner. Accordingly, μ is scanned until the p-value for a specific confidence level (CL) is reached, i.e.

$$p = \int_{q_{\mu,\text{obs}}}^{\infty} f(q_\mu|\mu,\hat{\vec{\theta}}_\mu)\, dq_\mu \tag{5.12}$$

$$\stackrel{!}{=} 1 - CL. \tag{5.13}$$

Similar to $f(q_0|0,\hat{\vec{\theta}}_0)$, the distribution can be approximated with Wilks' theorem, following a χ^2.
To calculate the expected exclusion limits, i.e. sensitivity, for the analysis, a set of background-only DL4 cubes is simulated with $\mu' = 0$, where μ' denotes the strength parameter for simulations. This MC set is used to calculate the median, 1σ, and 2σ regions of ULs, which is illustrated in Figure 5.5. This requires an

immense computational effort.

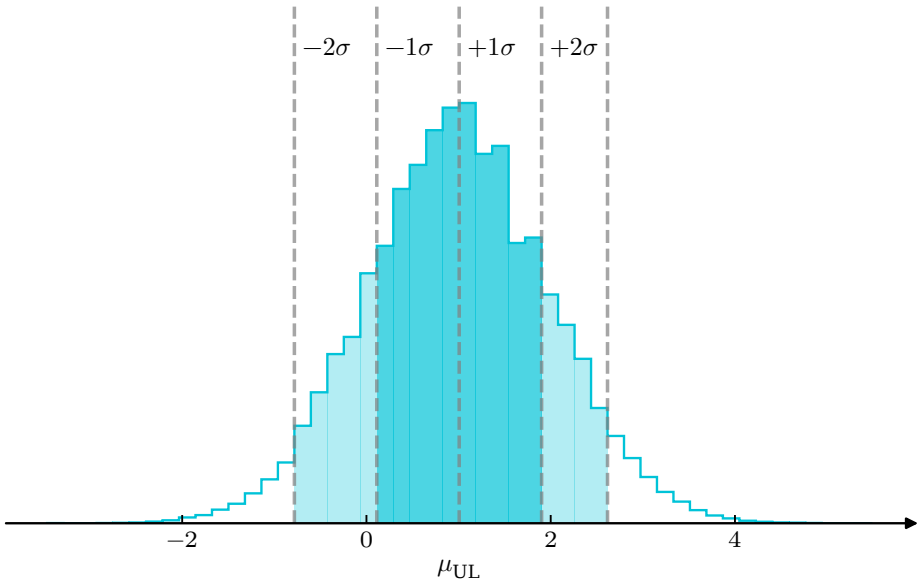

Figure 5.5: Illustration of the distribution of ULs for the parameter μ. The histogram can be created by calculating the UL on a set of MC DL4 cubes with $\mu' = 0$. The dashed vertical lines and shaded regions mark the $\pm 1\sigma$ and $\pm 2\sigma$ regions around the median UL.

5.7 The Novel Approach – Introducing Asimov Datasets

From the definitions in the preceding sections, two main problems arise:

$\hat{\mu} < 0$ In general, the MLE can result in a value for $\hat{\mu}$ that produces a negative flux for the model. Accordingly, Equation 5.7 and Equation 5.8 become negative, and neither the significance nor the UL can be calculated sufficiently.

Large MC set As detailed in the preceding section, one is interested in calculating the expected exclusion limits. The validity of these limits depends on the size of the MC set on which Equation 5.13 has to be solved to find μ_{UL}. In case of probing for example different DM models, this results in a vast amount of simulations and computations.

A solution to both problems is provided by Cowan et al. [170], which first introduces a new definition of the TS that covers the range of $\hat{\mu} < 0$,

$$\tilde{q}_\mu = -2\log \begin{cases} -2\log \frac{\mathcal{L}(\mu,\hat{\hat{\theta}}_\mu)}{\mathcal{L}(\hat{\mu},\hat{\hat{\theta}}_{\hat{\mu}})} & ,\hat{\mu} \geq 0 \\ -2\log \frac{\mathcal{L}(\mu,\hat{\hat{\theta}}_\mu)}{\mathcal{L}(0,\hat{\hat{\theta}}_0)} & ,\hat{\mu} < 0 \\ 0 & ,\hat{\mu} > \mu \end{cases} . \tag{5.14}$$

However, the distribution $f(\tilde{q}_\mu|\mu,\hat{\hat{\theta}}_\mu)$ can no longer be approximated with the χ^2. Instead, in the asymptotic limit, the pLLR is approximated as

$$-2\log\lambda(\mu) \approx \frac{(\mu-\hat{\mu})^2}{\sigma^2} + \mathcal{O}(1/\sqrt{N}), \tag{5.15}$$

where N is the sample size, i.e. the pLLR is a Gaussian distribution. Therefore,

$$\tilde{q}_\mu = \begin{cases} \frac{\mu^2}{\sigma^2} - \frac{2\mu\hat{\mu}}{\sigma^2} & ,\hat{\mu} \geq 0 \\ \frac{(\mu-\hat{\mu})^2}{\sigma^2} & ,\hat{\mu} < 0 \\ 0 & ,\hat{\mu} > \mu \end{cases} . \tag{5.16}$$

This leads to a (half) non-central χ^2 distribution,

$$\begin{aligned} f(\tilde{q}_\mu|\mu',\hat{\hat{\theta}}_{\mu'}) = {} & \Phi\left(\frac{\mu'-\mu}{\sigma}\right)\delta(\tilde{q}_\mu) \\ & + \begin{cases} \frac{1}{2}\frac{1}{\sqrt{2\pi}}\frac{1}{\sqrt{\tilde{q}_\mu}}\exp\left[-\frac{1}{2}\left(\sqrt{\tilde{q}_\mu} - \frac{\mu-\mu'}{\sigma}\right)^2\right], & 0 < \tilde{q}_\mu \leq \frac{\mu^2}{\sigma^2} \\ \frac{1}{\sqrt{2\pi}(2\mu/\sigma)}\exp\left[-\frac{1}{2}\frac{(\tilde{q}_\mu-(\mu^2-2\mu\mu')/\sigma^2)^2}{(2\mu/\sigma)^2}\right], & \tilde{q}_\mu > \frac{\mu^2}{\sigma^2} \end{cases} , \end{aligned} \tag{5.17}$$

which is used to calculate the p-value, given the CDF for $\mu = \mu'$ in case of UL computation

$$F(\tilde{q}_\mu|\mu) = \begin{cases} \Phi\left(\sqrt{\tilde{q}_\mu}\right), & 0 < \tilde{q}_\mu \leq \frac{\mu^2}{\sigma^2} \\ \Phi\left(\frac{\tilde{q}_\mu+\mu^2/\sigma^2}{2\mu/\sigma}\right), & \tilde{q}_\mu > \frac{\mu^2}{\sigma^2} \end{cases} , \tag{5.18}$$

with $\Phi(.)$ being the CDF of $\mathcal{N}(0,1)$.
The remaining task is to find the variance σ^2 of $\hat{\mu}$.

Cowan et al. introduce the so-called *Asimov dataset*, which has the property of returning the true parameters $(\mu',\vec{\theta}')$ on evaluation of the estimators. Furthermore, the TS of the Asimov DL4 cube is

$$\tilde{q}_{\mu,A} = -2\log\frac{\mathcal{L}_A(\mu,\hat{\hat{\theta}}_\mu)}{\mathcal{L}_A(\mu',\vec{\theta}')}. \tag{5.19}$$

The variance of $\hat{\mu}$, can be found with the Fisher information matrix

$$V_{jk}^{-1} = -E\left[\frac{\partial^2 ln\mathcal{L}}{\partial\theta_j \partial\theta_i}\right], \tag{5.20}$$

with $V_{00}^{-1} = \sigma^2$. The Asimov dataset can be used to directly evaluate this expectation value and the variance calculation in a simple way,

$$V_{jk}^{-1} = -\frac{\partial^2 ln\mathcal{L}_A}{\partial\theta_j \partial\theta_i}, \tag{5.21}$$

with $\mathcal{L}_A$ being the likelihood evaluated on the Asimov dataset from Equation 5.19. Alternatively, σ can be calculated from the non-centrality parameter,

$$\Lambda = \frac{(\mu - \mu')^2}{\sigma^2} \tag{5.22}$$

$$= \tilde{q}_{\mu,A}, \tag{5.23}$$

in Equation 5.17. Finally, the UL is found to be

$$\mu_{\text{UL}} = \hat{\mu} + \sigma\Phi^{-1}(1-\alpha) \tag{5.24}$$

by setting $p_\mu = 1 - F(\tilde{q}_\mu|\mu) \stackrel{!}{=} \alpha$ and using the approximation in Equation 5.16.

For the calculation of the expected exclusion limits no MC set is required. The median and error bands are derived equivalent to Equation 5.24 as

$$\text{med}[\mu_{\text{UL}}|\mu'] = \mu' + \sigma\Phi^{-1}(1-\alpha), \tag{5.25}$$

and

$$\text{band}_{N\sigma} = \mu' + \sigma(\Phi^{-1}(1-\alpha) \pm N), \tag{5.26}$$

where μ' is set to 0 for exclusion limits and N is the size of the error band in units of σ.

5.8 CL_s Limits

As introduced in Section 5.6, the basic concept for model testing lies in searching for $p \stackrel{!}{=} \alpha$ for different distributions. This values is also known as the Type I error α and is the probability of rejecting the null hypothesis, when the null hypothesis is true [171]. In contrast, the Type II error β is the probability of accepting the null hypothesis, when the alternative hypothesis is true. Furthermore, the *power* of a test is defined as $1-\beta$ and is the probability of rejecting the null hypothesis, when the alternative hypothesis is true.

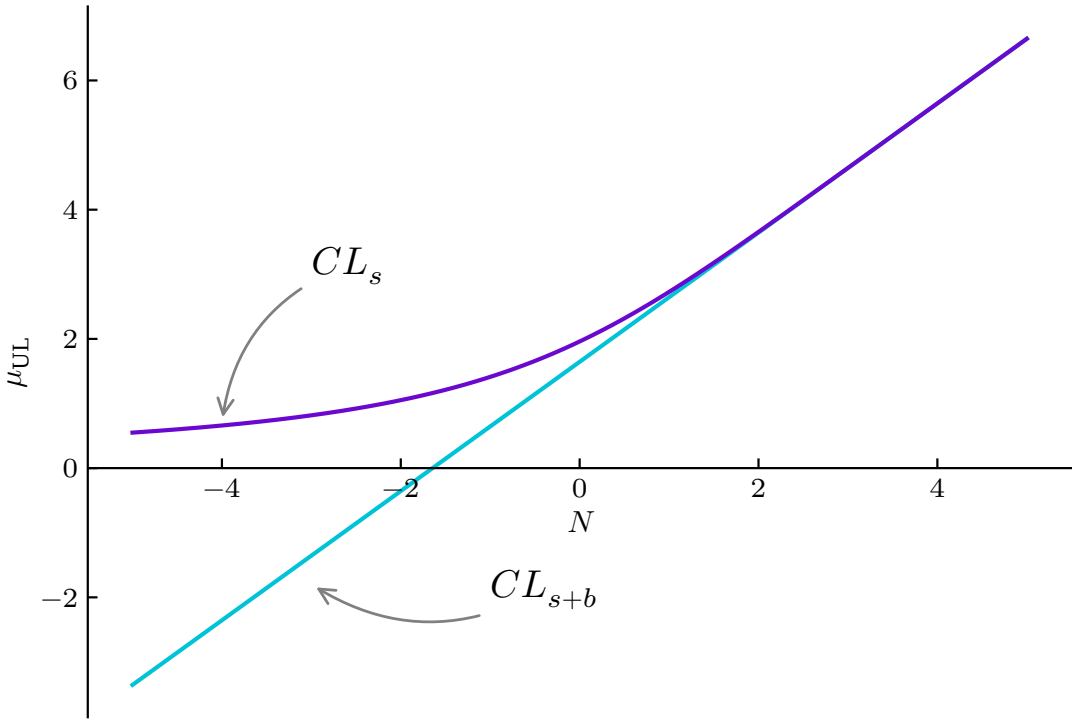

Figure 5.6: Illustration of the UL band obtained with the $CL_{\mathrm{s+b}}$ and CL_s method.

Translating this to the previous sections means, calculating the p-value of the signal and background hypothesis $s+b$ to find $p_{s+b} \leq \alpha$. The power translates to $Power = 1 - p_b$, with the p-value for the background-only hypothesis b. This leads to a problem when the signals $s \ll s+b$ and the distributions for $s+b$ and b overlap, and cannot be distinguished by the TS, which leads to small sensitivity in this region.
A solution to this problem is the redefinition of p_{s+b},

$$p'_{s+b} = \frac{p_{s+b}}{1-p_b}, \tag{5.27}$$

known as CL_s [172].

Given the definitions of Cowan et al., one finds

$$CL_S \stackrel{!}{=} \frac{1-\Phi(\sqrt{\tilde{q}_\mu})}{\Phi(\sqrt{\tilde{q}_{\mu,A}}-\sqrt{\tilde{q}_\mu})} \tag{5.28}$$

for the calculation of the UL and

$$\text{med}[\mu_{\text{UL}}] = \sigma\Phi^{-1}(1 - 0.5\alpha), \tag{5.29}$$

$$\text{band}_{N\sigma} = \sigma(\Phi^{-1}(1 - \alpha\Phi(N)) \pm N), \tag{5.30}$$

for the calculation of the median and error band of the expected exclusion limits, according to [171]. Figure 5.6 illustrates a direct comparison between the error band obtained with Equation 5.26 and Equation 5.30 and displays that μ_{UL} is constrained to $\mu_{\text{glsUL}} > 0$.

5.9 `TITRATE` - Finding the Right Concentration

As of version `1.2` [173], `Gammapy` does not provide built-in functionality for UL calculation for DM, nor an implementation of the Cowan et al. approximations detailed in the preceding sections. To address this, the new open-source Python package `TITRATE` (`asympTotic lIkelihood Tests for daRk mAtTer sEarch`) [12], was developed based on `Gammapy` to incorporate the *Asimov limits*. This package resembles one of the main contributions to this thesis and the gamma-ray community, implementing the equations and concepts of Section 5.5 to Section 5.8. Currently, a `SpectrumAsimovDataset` and a `MapAsimovDataset` are available for UL calculation, in case of a 1D or 3D analysis. The output is saved in `astropy QTables` [174] to guarantee a widely accepted data format. In addition to this, `TITRATE` provides two tools: one for the verification of the Cowan et al. approximations on the data, called `AsymptoticValidator`, and an `UpperLimitFactory`, which calculates the ULs on the thermal cross-section of a DM model as defined in `Gammapy`. `TITRATE` is available on `PyPi` and `conda-forge`. Competitive software such as `gLike` [175] and `LklCom` [176] have been utilised in previous MAGIC analyses, but do not provide the Cowan et al. approximations.
`TITRATE` employs a novel approach for DM search in combination with the community-wide accepted software `Gammapy`. Moreover, the application of `TITRATE` to the MAGIC observations represents a significant advancement in gamma-ray astronomy.

GitHub: https://github.com/StFroese/TITRATE
PyPi: https://pypi.org/project/titrate
Conda: https://anaconda.org/conda-forge/titrate

6 CBe dSph – A Novel Background Model and Cross-Check

The observational target selected for this thesis is the Coma Berenices (CBe) dwarf spheroidal galaxy (dSph). The data is processed to full-enclosure DL3 with autoMAGIC, as outlined in Section 4.7, and quality cuts are implemented based on the environmental information of the observations. Given that the `magic_dl3` converter does not provide a background model, a new one must be generated. A novel method for background modelling, dubbed the *exclusion-rotation* method, is proposed and a novel cross-check on Crab Nebula data, which is blind to the modelling, is performed. The Spectral Energy Density (SED) of the Crab Nebula is successfully recovered.

6.1 DL3 – autoMAGIC & Quality Cuts

The CBe constellation is situated in the northern celestial hemisphere and contains, among other objects, the North Galactic Pole, the Coma cluster, and the CBe dSph. While the Coma cluster has been the subject of the investigations led by Fritz Zwicky, as detailed in Section 2.2, the dSph acts as another unique target for DM search, as described in Section 2.4. Its location is illustrated in Figure 6.1. In the context of this thesis, MAGIC observations of the CBe dSph are utilized to search for DM. In total, MAGIC observed CBe dSph for approximately 50 h between 30/01/2019 and 04/06/2019, representing the most recent data available from this experiment on dSphs. The data is processed by autoMAGIC up to DL3, as detailed in Section 4.7. The input card for the processing can be found in Appendix A.

As discussed in Section 3.5, the LIDAR and pyrometer data serve as a proxy for the environmental conditions under which the observations were conducted. The data is appended to the DL3 files, along with the trigger rate of L3 and the mean Dark Current (DC). Moreover, the dust content in the atmosphere at the Roque de los Muchachos is recorded by the TNG and has been extracted for

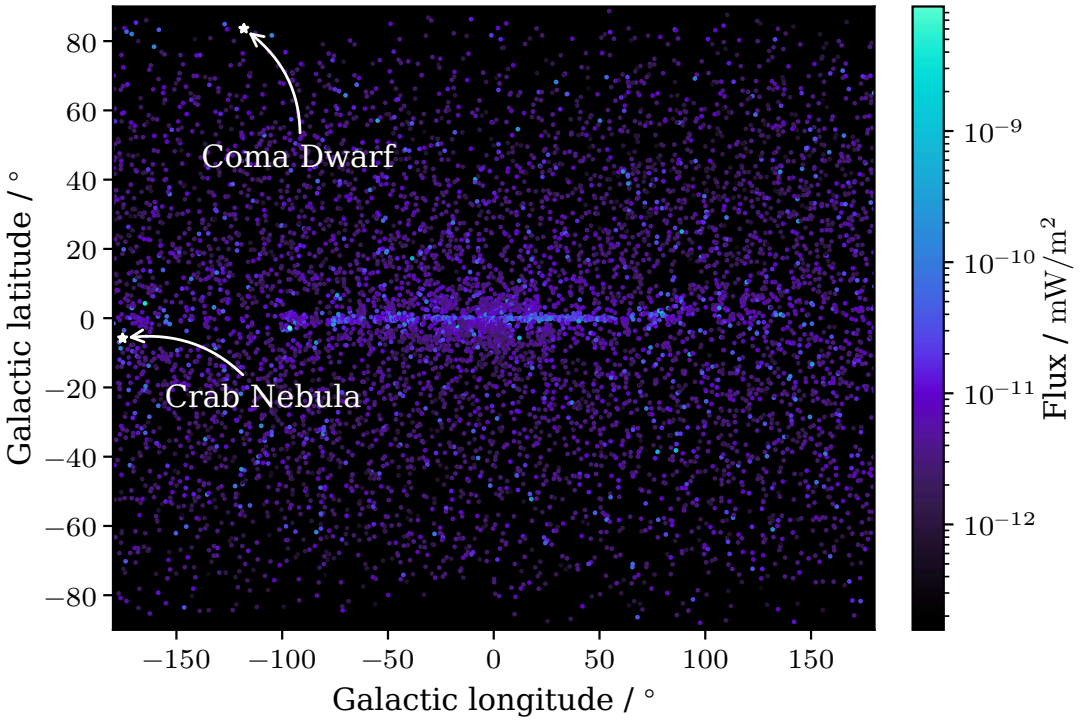

Figure 6.1: Illustration of all detected Fermi-LAT sources with a gamma-ray emission above 100 GeV, as published in the 4FGL catalogue [177, 178]. The source position of the dwarf galaxy CBe dSph and the Crab Nebula are marked with a white star. Figure adapted from [179].

the selected observations. The dust values are listed in Appendix B.1. The DL3 files are filtered by a set of cuts on this metadata, to improve the quality of the observations used for further analysis. These cuts are listed in Table 6.1 and the discarded observations are displayed in Figure 6.2.
Furthermore, the observations with the IDs 5079530, 5079531, 5079532, 5079533, 5079534, and 5079535 have been excluded from the data set, as they were obtained with an incorrect Wobble position. This results in a total observation time of 25.79 h available on DL3, with approximately 50 % of the measured data excluded from further analysis.

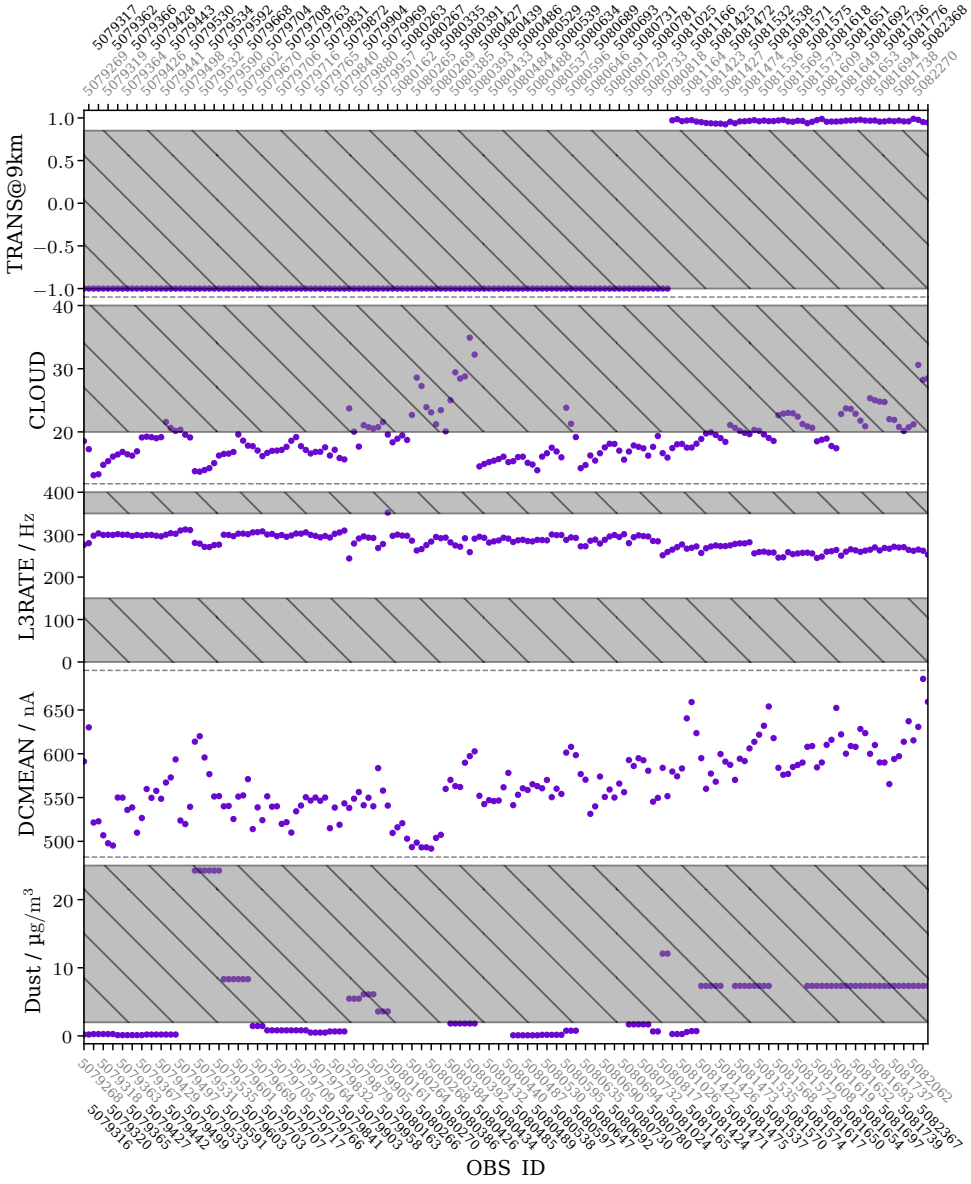

Figure 6.2: Illustration of the applied quality cuts from Table 6.1 to the CBe dSph observations. The shaded regions indicate the exclusion of observations. For readability, the observation IDs are divided over the top and bottom x-axis.

Table 6.1: Minimum and maximum cut for the quality parameters applied to the CBe dSph data.

Quality Parameter	Min Cut	Max Cut
Transmission @ 9 km	0.85	-
Cloudiness	-	20
L3 rate / Hz	150	350
DC mean / nA	-	1400
Dust / µg/m^3	-	2

6.2 The Exclusion-Rotation Method

The background models for the full-enclosure DL3 files are created using the *exclusion* method, as introduced in Section 4.9. The software package, entitled `BAccMod`[1], was developed by de Bony de Lavergne et al. [180]. and provides a series of methods for creating both two-dimensional and three-dimensional background models. The former model assumes a radial symmetry of the telescope acceptance and calculates the background rate at a reconstructed radial distance to the center of the FoV and reconstructed energy, i.e. $(\hat{r}, \hat{E})$. To construct the three-dimensional model, the background rate in two spatial dimensions is calculated. This is done either using reconstructed Ra-Dec or Alt-Az, in addition to the reconstructed energy, i.e. $(\hat{RA}, \hat{DEC}, \hat{E})$ or $(\hat{ALT}, \hat{AZ}, \hat{E})$. This thesis employs a parameterization in the Alt-Az system for the construction of the models. The specifications of the model dimensions are listed in Table 6.2. The modelisation is outlined as follows for a set of observations:

Cubes Three empty data cubes, as described in Section 5.1, are generated. The content of these cubes is denoted as N_{eff}, T_{eff}, and T_{tot}, and their definition is provided below.

Observations The cubes are populated with the events and exposure of each observation, while the data within a circular region centered on the source position is excluded. This region is referred to as the *exclusion region* and its size is determined by the Wobble distance, $r = 0.4°$, as introduced in Section 3.5 and illustrated in Figure 4.15. In the case of two opposing Wobble positions, the exclusion region is situated on opposite sites of the FoV center. The area excluded by one Wobble position is populated with events from the second position. Figure 6.3 illustrates this construction

[1]Formally known as `acceptance_modelisation`.

for two observations at different Wobble positions. Consequently, the fully populated N_{eff} cube contains all background events of the observation set. Similarly to N_{eff}, T_{eff} comprises the exposure of all observations, except the source region. T_{tot}, on the other hand, encompasses the overall exposure, including the excluded region. Furthermore, the observation runs can last for up to 20 min, which results in a rotation of the source position around the nominal pointing position in Alt-Az coordinates. Accordingly, the exclusion region needs to undergo a corresponding change in position over time. Figure 6.4 illustrates this rotation.

FoV Rotation To address the issue of the source rotation within the FoV, the computation of the count and exposure cubes is further refined through the division of each observation into sub-observations with reduced live time. This procedure divides the observation time into n_t bins. For each bin, the speed of rotation of the FoV is calculated and the total rotation within the bin is found by integration. Only the time bin edges, where the traveled distance of the outermost pixel in the FoV changes between time bins, are retained. The distance is measured in units of fraction of a pixel Δ_{pix}, which can be chosen by the user. Smaller values of Δ_{pix} result in a more sensitive division.

Background Rate The total background rate of the model is given as

$$\frac{\mathrm{d}N}{\mathrm{d}t\mathrm{d}E\mathrm{d}\Omega} = \frac{N_{\text{eff}}}{T_{\text{eff}}/T_{\text{tot}}\Delta\Omega\Delta E T_{\text{live time}}}, \tag{6.1}$$

where $\Delta\Omega$ and ΔE represent the solid angle and energy width of each bin, while $T_{\text{live time}}$ denotes the total time of all observations.

Table 6.2: Axial dimensions of the data cube used for background model creation.

Axis	Range	Bins	per Decade
Altitude (Alt)	−3° to 3°	30	no
Azimuth (Az)	−3° to 3°	30	no
Energy	0.05 TeV to 5 TeV	8	yes

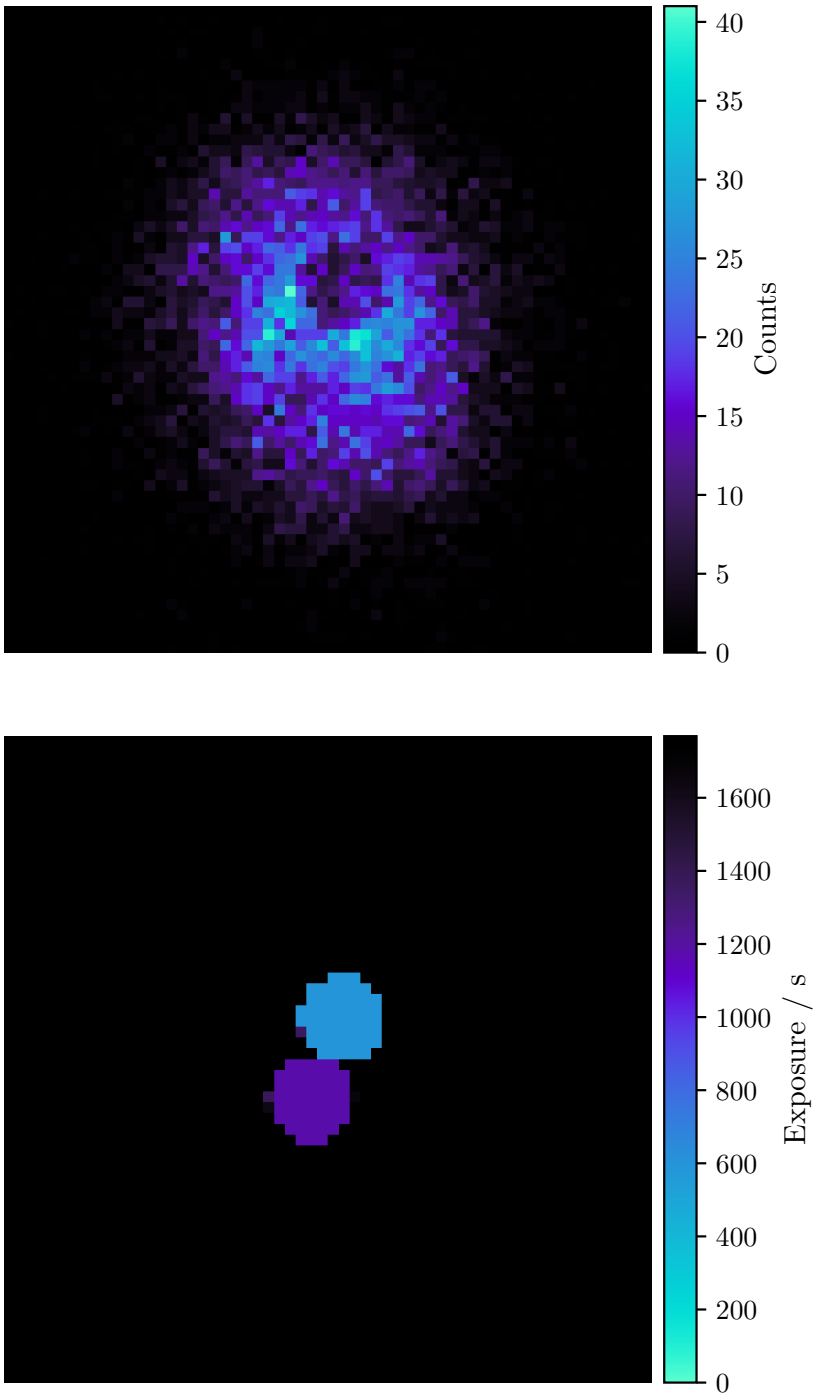

Figure 6.3: Illustration of the *exclusion method* for two observations with opposite Wobble positions. **Top view:** Slice of N_{eff} along the energy axis. The exclusion produces a circular hole during the population of the cube. **Bottom view:** Slice of T_{eff} along the energy axis. It is noted that the exposure map is the same for every energy bin. The circular cutouts of the exclusion region for both Wobble positions are evident.

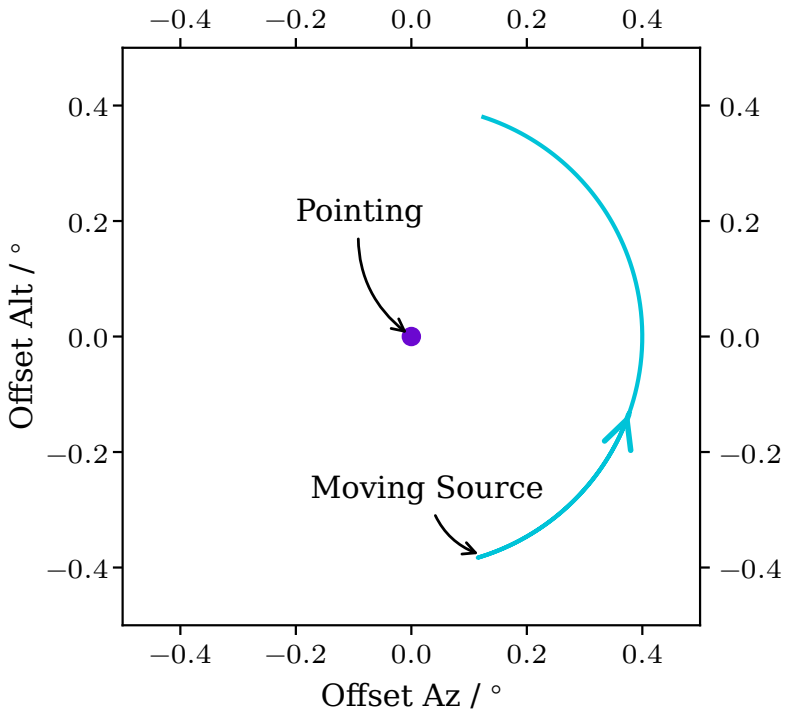

Figure 6.4: Schematic of the source rotation relative to the pointing position within the Alt-Az FoV during the observation.

As published recently [132, 159], the acceptance of MAGIC exhibits a highly asymmetric *stereo blob*. A direct correlation has been established between the orientation of the blob and the alignment of the MAGIC view cones.

$$\gamma_{\text{theory}} = Az - 34.23°. \tag{6.2}$$

The offset of $\Delta\gamma = 34.23°$ describes the rotation angle between the connection line of both telescopes and the North-South axis. The identical effect is found for the observations of CBe dSph by inferring the rotation angle from a PCA of the background map, as displayed in Figure 6.5. Moreover, Figure 6.6 demonstrates the relation to Equation 6.2.

To compensate for the rotation of the acceptance among the observations used for background construction, it is possible to perform the background modelling in multiple Az bins. However, this would result in sparsely populated bins at lower Zenith distance (Zd) and overall lower statistics, as can be concluded from the distribution of telescope pointings in Figure 6.7.

I propose a novel background method based on the *rotation* method by Simone Mender [132], which I will refer to as the *exclusion-rotation* method. The back-

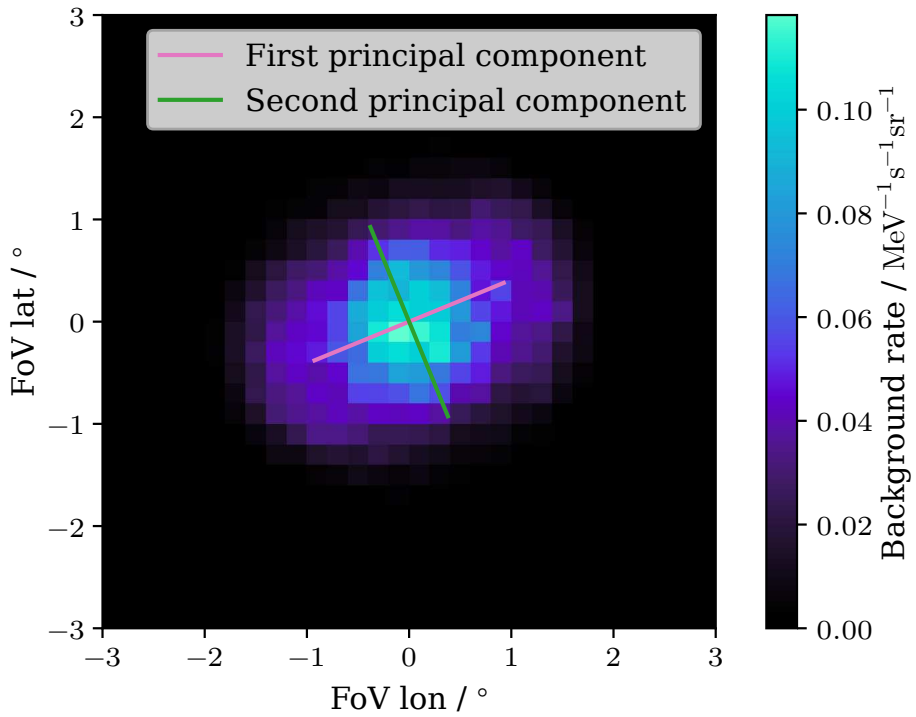

Figure 6.5: PCA applied to the first energy bin of an arbitrary observation during the background modelling. A clear rotation is evident.

ground model for each observation is constructed by derotating all sub-observations based on their PCA angle γ_{PCA}. The derotated events are then re-rotated using γ_{theory} from Equation 6.2 for each Az pointing of the sub-observations. This method diverges from the original *rotation* method by eliminating the utilization of Az bins for the re-rotation and accounting for the accurate rotation of the exclusion regions, which was not necessary for the non-simultaneous off data employed in [132]. To circumvent the secondary effects of the Zd on the background [132], the method is implemented in three Zd bins between 5° to 35°. The bin edges are indicated in Figure 6.7.

Figure 6.8 displays the background model for an arbitrary observation in four of the sixteen energy bins. At low energies, the rate is concentrated within the center of the FoV and the stereo blob is discernible. As the energy increases, the spatial distribution widens while the total background rate decreases. The highest energy bin exhibits a distinctive "donut"-like shape. Events within this energy range possess a larger Cherenkov footprint in the telescopes' cameras, resulting in a truncation at the edge of the camera. These truncated showers are challenging to reconstruct, and only events with a fully enclosed shower footprint

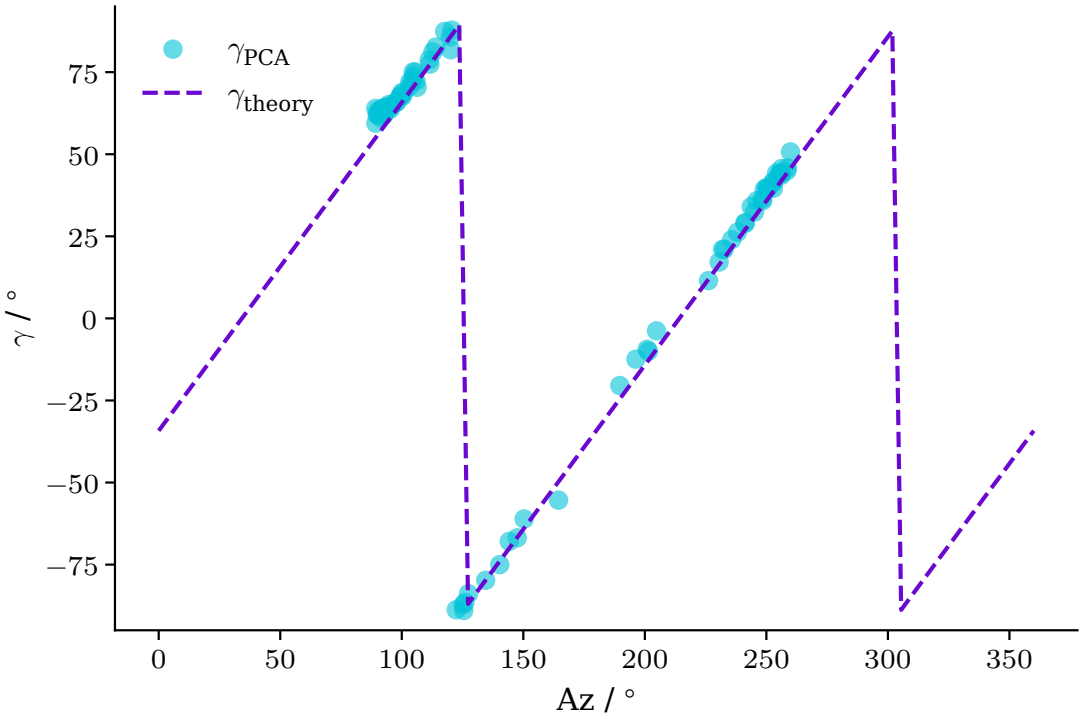

Figure 6.6: Illustration of the background rotation dependence on the Az of the MAGIC telescopes. γ_{PCA} is calculated by applying a PCA to the background events of the observations, whereas γ_{theory} is given by Equation 6.2.

remain. Consequently, their origin is located far beyond the central region of the camera and the acceptance region of the telescopes resembles a ring or "donut" shape.

Each background model is appended to the Header Data Unit (HDU) index file of the DL3 data set, which relates every model file to its corresponding observation ID.
The full-enclosure DL3 files are reduced to DL4 using `Gammapy`, as detailed in Section 5.1. Table 6.3 provides a list of the DL4 cube dimensions and the number of bins in each dimension. During the data reduction process, the background model is fitted outside the exclusion region using a `PiecewiseNormSpectralModel`. This model provides a normalisation parameter for each energy bin, which is optimized during the fitting procedure. A histogram of the fitted parameters for all background models is illustrated in Figure 6.9. In an ideal scenario, the normalisation parameters would be equal to one, indicating that the constructed background model aligns perfectly with the data. It is anticipated that a discrep-

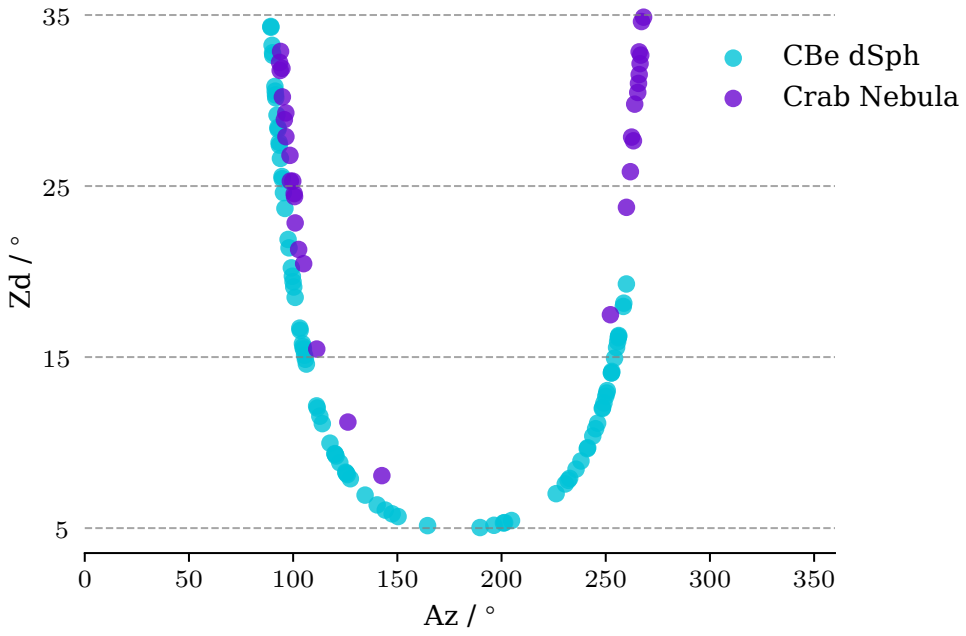

Figure 6.7: Alt-Az pointing for every observation of the CBe dSph and Crab Nebula dataset. The dashed horizontal lines indicate the Zd bins used for the background model construction. The CBe dSph data does not cover the high Az observations of the Crab Nebula between 25° and 35° Zd.

ancy will arise between the background models and the observation, given that the *exclusion-rotation* method corrects the Az dependence and does not take into account higher-order effects, such as the Earth's magnetic field.

To quantify the extent of the mismatch, a normal distribution is fitted to the histogram of the normalisation parameters. While the mean μ reveals an overall bias, indicated by values of $\mu \neq 1$, the standard deviation σ is an overall proxy for the uncertainty of the method.
For the CBe dSph, the values of $\mu = 0.92$ and $\sigma = 0.25$ were obtained. While the fit shows a minimal bias and small uncertainty, it is evident from the fitted curve in Figure 6.9 that the skewness of the distribution is not captured. This discrepancy is attributable to a strong concentration of the normalisation values around $\mu \approx 1$ and $\mu \approx 0.7$. In general, the majority of normalisation parameters remain within the area under the fitted curve. For completeness, the normalisation parameters are illustrated in dependence on the quality cut parameters in Appendix B.4. The figures demonstrate no empirical correlation.

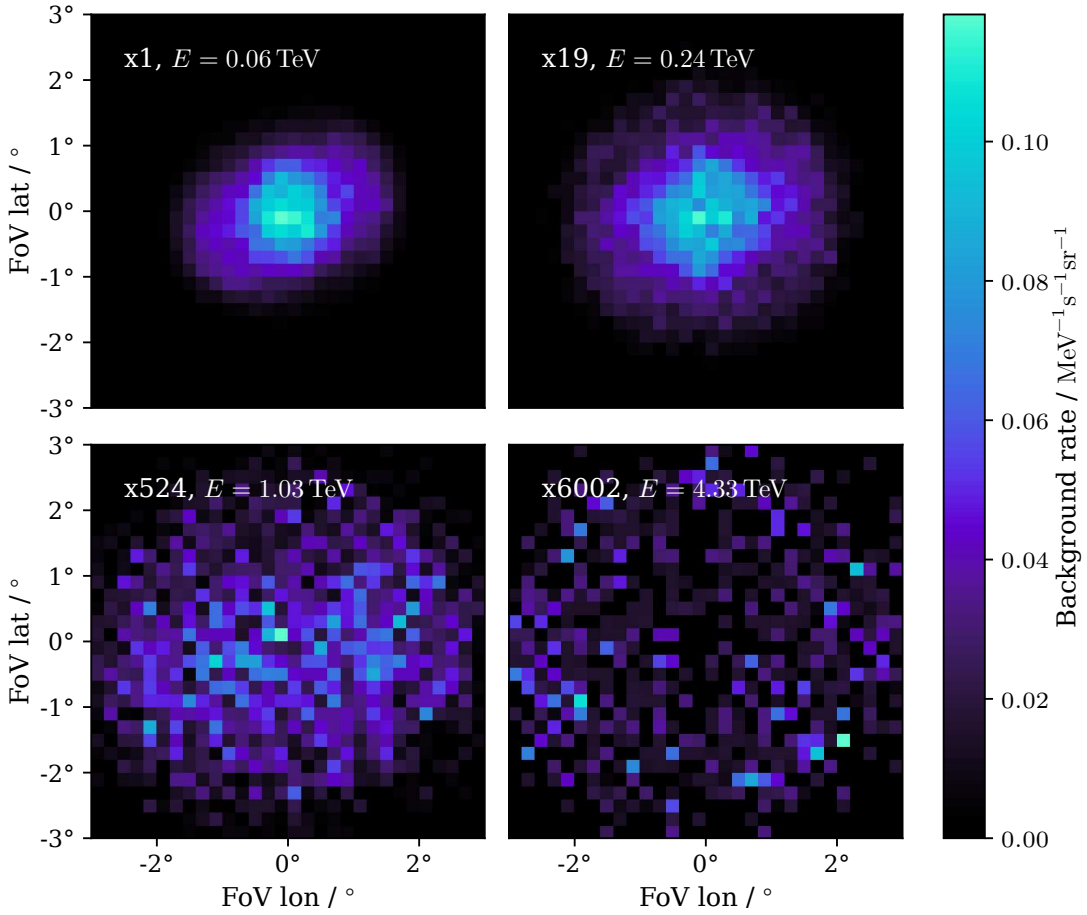

Figure 6.8: Background model of an arbitrary observation created with the novel *exclusion-rotation* method. The background rate for four of sixteen energy bins is displayed. To ensure the spatial comparison between the bins is possible, each background map is multiplied by the factor denoted in the sub-figures to match the rate of the first energy bin.

Table 6.3: Axial dimensions of the data cube used for the reduction from CBe dSph DL3 to DL4.

Axis	Range	Bins	per Decade
RA	−2° to 2°	150	no
DEC	−2° to 2°	150	no
Energy	0.05 TeV to 5 TeV	8	yes

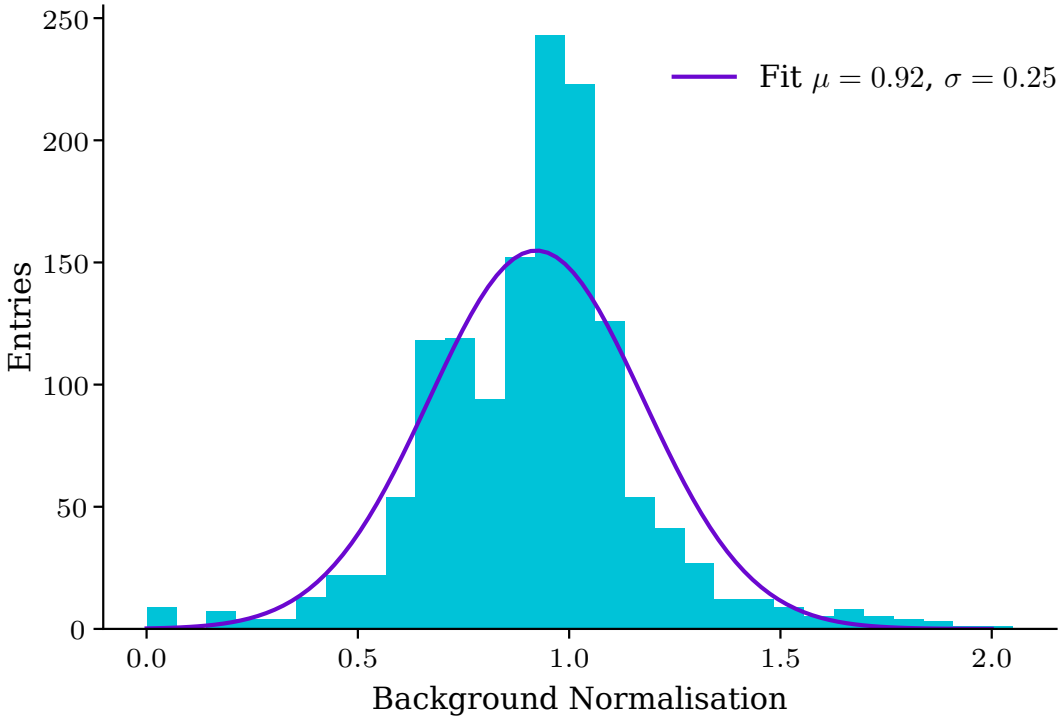

Figure 6.9: Histogram of the normalisation parameters of the `PiecewiseNormSpectralModel` for each observation of CBe dSph. The fit of the normal distribution is displayed as a purple curve.

6.3 Model Validation – Beyond MAGIC Requirements

Figure 6.10: Image of the Crab Nebula observed by the James Webb Space Telescope (JWST) and taken from [181].

Prior to undertaking a more detailed examination of the DL4 data, it is essential to ascertain the reliability of the background method. This is achieved by conducting a cross-check on a well-established target, namely the Crab Nebula. This supernova remnant resembles a standard candle in gamma-ray astronomy, exhibiting a continuous emission between a few GeV and multiple orders of TeV [182]. Consequently, it encompasses the complete sensitivity range of MAGIC. Although this target is a point source for MAGIC, the structural properties, as observed by the JWST in Figure 6.10, indicate the presence of the once-existing supernova at whose core lies the Crab pulsar [183, 184].

Given the consistent properties of the nebula, it has become a mandatory source for testing the quality of the event reconstruction in every MARS analysis. The standard cross-check is performed by first processing Crab Nebula observations from the same MC period as the primary source with the already trained RFs to DL3. The second step is to process the data from DL3 to DL5 and compare the resulting SED with the well-known published spectrum of the Crab Nebula [185].

The content of this section goes beyond the aforementioned requirement by providing a new, unbiased cross-check of the background method. Moreover, the *exclusion-rotation* method is validated by rotating the events of the CBe dSph observations to align with the pointings of the Crab Nebula observations during the model construction process. This is feasible due to the close alignment of the pointings between the CBe dSph and Crab Nebula data, as demonstrated in Figure 6.7. For the Zd bins between 5° to 25° the model construction is an interpolation task, whereas for the highest Zd bin, the construction is partially an extrapolation task, given the absence of CBe dSph observations for high Az. The Crab Nebula data is processed to full-enclosure DL3 using autoMAGIC and the input card for autoMAGIC is provided in Appendix A. The quality cuts listed in Table 6.4 are applied to the observations. Appendix B.3 provides the quality parameters and cuts for each observation. Similar to the CBe dSph data, the normalisation parameters are illustrated in dependence on the quality cut parameters, provided in Appendix B.5. The figures demonstrate no empirical correlation. The background models are appended to the HDU index file of the DL3 data.

Table 6.4: Minimum and maximum cut for the quality parameters of the DL3 files, together with the cuts on the recorded dust by TNG. The latter can be found in Appendix B.2. The cuts are applied to the Crab Nebula data.

Quality Parameter	Min Cut	Max Cut
Transmission 9 km	0.85	-
Cloudiness	-	30
L3 rate / Hz	200	350
DC mean / nA	-	1500
Dust / µg/m^3	-	10

The next step is the reduction of the data with `Gammapy`, as detailed in Section 5.1. Similarly to the CBe dSph data reduction, a `PiecewiseNormSpectralModel` is fitted to the background model outside the exclusion region. The result of this fit is illustrated in Figure 6.11, and the inferred parameters are $\mu = 0.87$ and $\sigma = 0.27$. This indicates that the background model performance for the Crab Nebula observations is similar to that observed in the CBe dSph data set, employing the *exclusion-rotation* method.

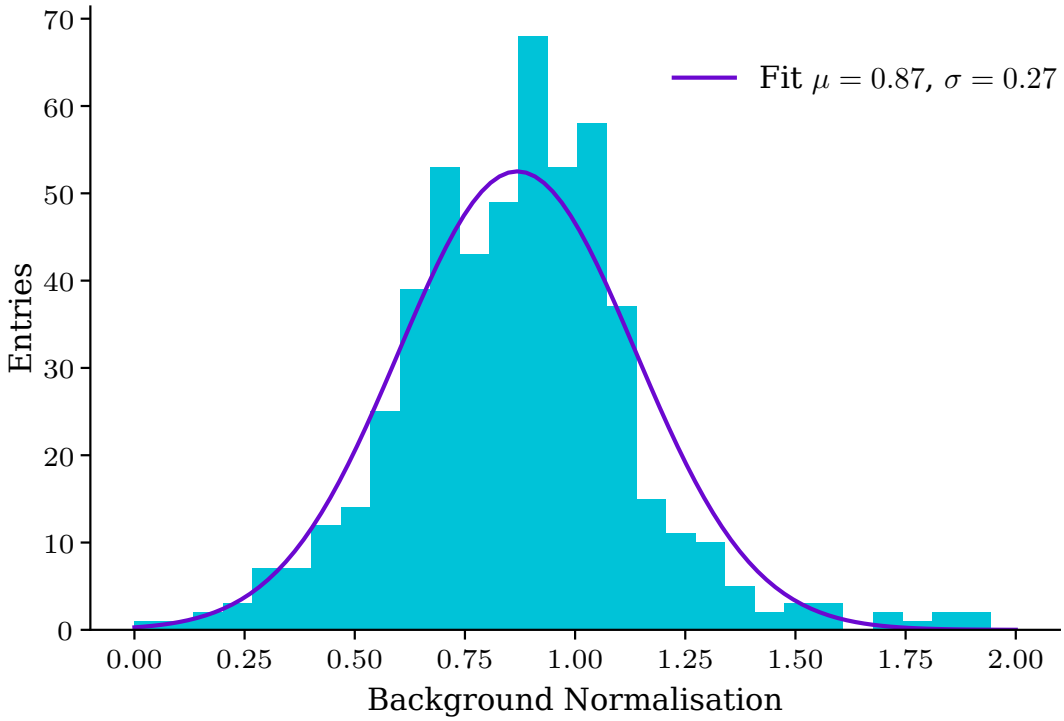

Figure 6.11: Histogram of the normalisation parameters of the `PiecewiseNormSpectralModel` for each observation of the Crab Nebula. The fit of the normal distribution is displayed as a purple curve.

Moreover, the integrated DL4 cube of an arbitrary observation over the energy axis is displayed in Figure 6.12. A clear correlation between the events and the coordinates of the Crab Nebula is evident. The maps of all DL4 cubes can be found in Appendix D.1.

The so-called significance map is computed by calculating the TS value for each spatial bin while integrating over energy. `Gammapy` offers this functionality through the `ExcessMapEstimator`, based on Wilks' theorem, as detailed in Section 5.5 and defined in Equation 5.11. This calculation relies on q_μ and not $\tilde{q}_\mu$, and therefore the evaluation of the TS results in unphysical values for $\hat{\mu} < 0$. A detailed description and solution to this problem are provided in Section 5.7. However, the significance in `Gammapy` is redefined to interpret the negative range, i.e.

$$S = \begin{cases} \sqrt{q_0} & , q_0 \geq 0 \\ -\sqrt{q_0} & , q_0 < 0 \end{cases} . \tag{6.3}$$

The significance map of the observation presented in Figure 6.12 is displayed in Figure 6.13. Subsequent to this, the distribution of TS values will be investigated in the following. Furthermore, the TS maps of all observations can be found in Appendix D.2.

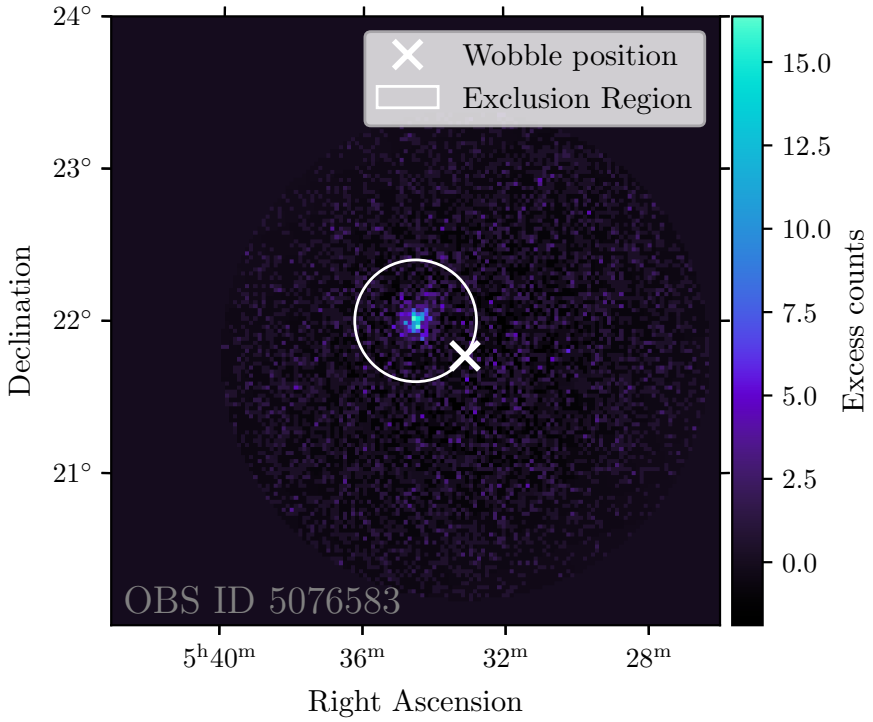

Figure 6.12: Excess counts of an arbitrary Crab Nebula observation integrated over the energy axis. The map is centered on the coordinates of the nebula. The white circle illustrates the exclusion region used for the background modelling, whereas the white cross denotes the Wobble position of the observation.

All bins located outside the delineated exclusion region on the map are defined as *Off* bins. In an ideal scenario, the distribution of the significance among these bins should adhere to a standard normal distribution. This is to say that the standard deviation is $\sigma = 1$. In practice, σ is given by

$$\sigma^2 = \sigma_{\text{stat}}^2 + \sigma_{\text{sys}}^2, \tag{6.4}$$

where σ_{stat} denotes the statistical error and σ_{sys} the systematic error of the model. To determine this parameter, a normal distribution is fitted to the histogram of significance values within the *Off* bins. The distribution, as well as the fit for the observation, is illustrated in Figure 6.14, which indicates $\sigma_{\text{sys}} = 0.25$ under the assumption that $\sigma_{\text{stat}} = 1$. The histogram of all TS values and the TS map in Figure 6.13 indicate a significant signal inside the exclusion region. Moreover, the histograms for all TS maps can be found in Appendix D.3.

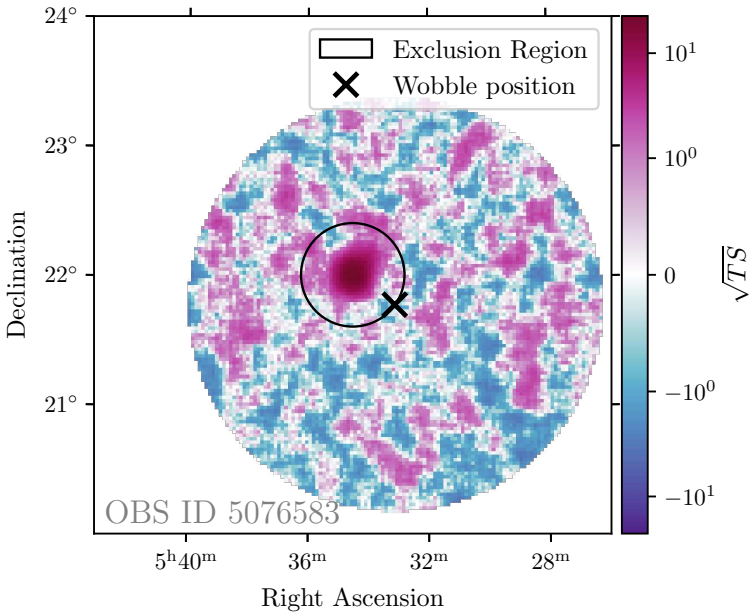

Figure 6.13: Significance map of an arbitrary Crab Nebula observation, same as in Figure 6.12, integrated over the energy axis. The map is centered on the coordinates of the nebula. The black circle illustrates the exclusion region used for the background modelling, whereas the black cross denotes the Wobble position of the observation.

To perform a comprehensive cross-check of the *exclusion-rotation* method, the DL4 datasets are stacked. Once more, the significance map and distribution of the significance values for the complete map and those outside the exclusion region are calculated. Figure 6.15 and Figure 6.16 display these, respectively.

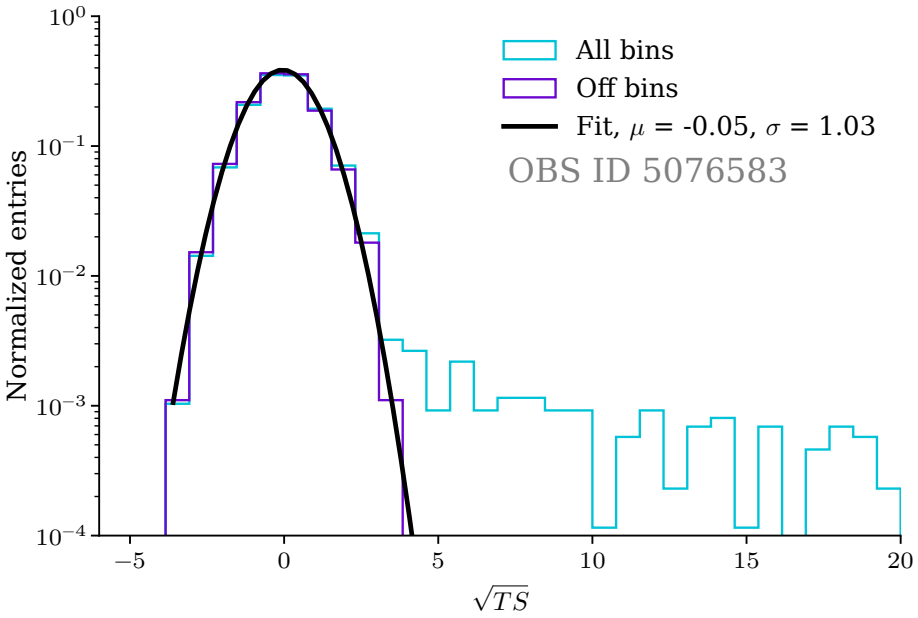

Figure 6.14: Histograms for the significance values of Figure 6.13 outside the exclusion regions, *Off* bins, and within the complete map, *All* bins. A normal distribution is fitted to the *Off* bins.

The value of σ_{sys} is calculated to be $\sigma_{\text{sys}} = 0.98$, which indicates that the systematic effects have been amplified during the stacking procedure. Furthermore, the histogram encompassing the exclusion region exhibits a pronounced signal, as anticipated. The SED of the Crab Nebula is inferred by fitting a `Gammapy` `LogParabolaSpectralModel` of the form

$$\phi(E) = \phi_0 \left(\frac{E}{1\,\text{TeV}} \right)^{-\alpha - \beta \log\left(\frac{E}{1\,\text{TeV}}\right)}, \tag{6.5}$$

where ϕ_0 is the amplitude, and α and β are shape parameters, to the stacked data. Figure 6.17 illustrates the fit, the calculated flux points, and the MAGIC reference spectrum [185]. The parameters of the fitted model, as well as the parameters of the MAGIC reference, are listed in Table 6.5. A slight discrepancy is evident between the computed SED and the flux point in the eighth bin. Moreover, the flux is overestimated at lower energies since the background models built from the CBe dSph are less contaminated than the background flux of a galactic source, such as the Crab Nebula, in this energy range. Overall, the SED achieved by applying the *exclusion-rotation* method to a second set of data, that is blind to the background model creation, demonstrates a satisfactory agreement with the reference spectrum.

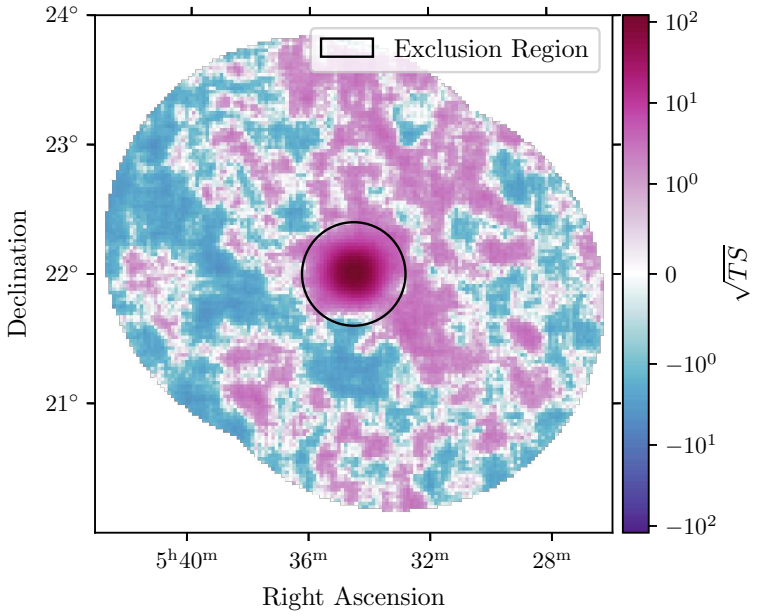

Figure 6.15: Significance map of the stacked DL4 Crab Nebula observations, integrated over the energy axis. The map is centered on the coordinates of the nebula. The black circle illustrates the exclusion regions used for the background modelling.

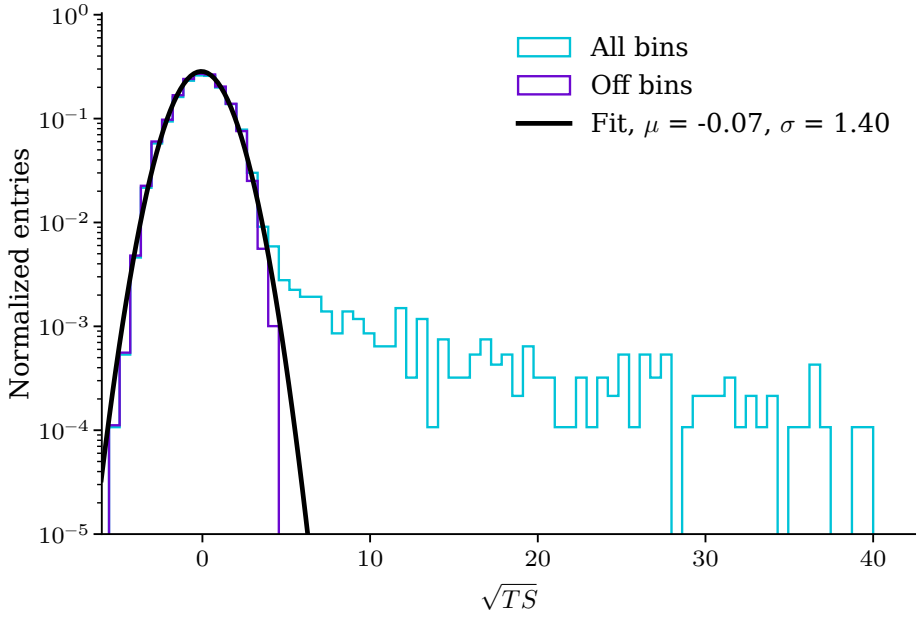

Figure 6.16: Histograms for the significance values of the stacked DL4 map in Figure 6.15, outside the exclusion region, *Off* bins, and within in the complete map, *All* bins. A normal distribution is fitted to the *Off* bins.

Parameter	Fit	MAGIC reference
ϕ_0 / TeVcm^{2}s	3.08±0.06 $\times 10^{-11}$	3.39±0.09 $\times 10^{-11}$
α	2.52±0.03	2.51±0.02
β	0.09±0.01	0.21±0.03

Table 6.5: Parameters of the fitted `LogParabolaSpectralModel` and the MAGIC reference, taken from [185], for the stacked Crab Nebula data.

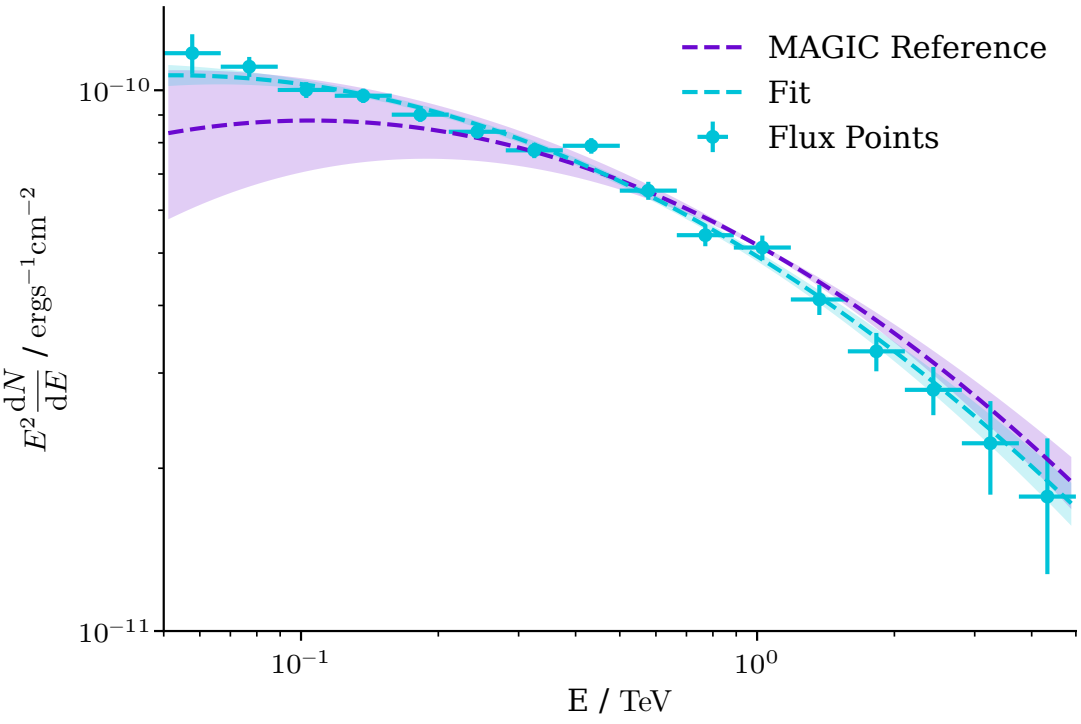

Figure 6.17: Fitted SED and flux points of the Crab Nebula inferred from the stacked DL4 data. The MAGIC reference curve is taken from [185]. The parameters of the curves are listed in Table 6.5

.

7 Does it Matter in CBe dsph?

The novel *exclusion-rotation* background model, generated and validated in the preceding chapter, is applied to search for annihilating DM in CBe dSph. In the absence of a signal in the observed region, ULs are computed for two datasets: the 3D DL4 cube and the 1D reduced cube. The latter enables a comparison to limits published by MAGIC and is generated according to Section 5.4.
Two distinct UL methods are applied: the *classical* method, which is based on Wilks' theorem and detailed in Section 5.6, and the novel *Asimov* method, which is based on the approximations by Cowan et al. and detailed in Section 5.7. Finally, the CL_s method is applied to compute the Asimov bands under the physical constraint $\mu_{\mathrm{UL}} > 0$, as introduced in Section 5.8.
This chapter presents a comprehensive comparison of all methods, thereby illustrating the capabilities of the 3D Asimov UL in comparison to the MAGIC reference investigated in this chapter.

7.1 In Search for a Signal

Following the verification of the novel *exclusion-rotation* method on Crab Nebula observations, as detailed in Section 6.3, the DL4 data of CBe dSph is now subject to a more detailed investigation.

The DL4 cube of an arbitrary observation, integrated along the energy axis, is presented in Figure 7.1. In comparison to the sky map of the Crab Nebula for a single observation, as illustrated in Figure 6.12, no signal is discernible within the exclusion region. Furthermore, the sky maps of all observations can be found in Appendix C.1. This initial indication is further strengthened by a more detailed examination of the significance map, as displayed in Figure 7.2. The significance values are calculated by Equation 6.3, as implemented in the `Gammapy` `ExcessMapEstimator`. Moreover, Appendix C.2 provides the TS maps of all CBe dSph observations. The distribution of the significance values within *All* bins and

outside the exclusion region, *Off* bins, is constructed, as illustrated in Figure 7.3, and in a similar manner to that in Figure 6.13. The fit of a normal distribution to the *Off* bins indicates that the background model exhibits a minimal systematic uncertainty, with values of $\mu = -0.05$ and $\sigma = 1.00$. The distribution of the significance within the complete map is in close agreement with the distribution of the *Off* bins. Appendix C.3 illustrates the distributions of all observations accordingly. Consequently, no signal is claimed.

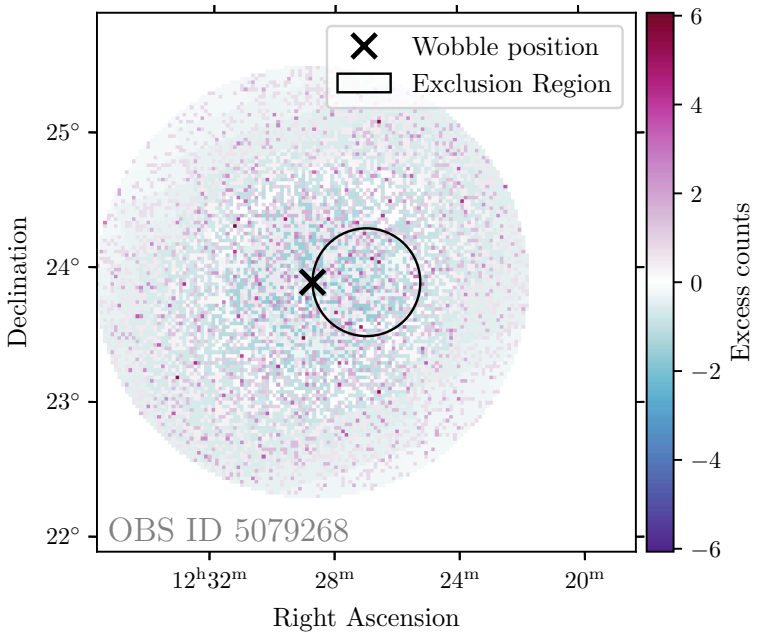

Figure 7.1: Excess counts of an arbitrary CBe dSph observation integrated over the energy axis. The map is centered on the coordinates of the source. The black circle illustrates the exclusion region used for the background modelling, whereas the black cross denotes the Wobble position of the observation.

To enhance statistics and thereby identify potential flux in the region of interest, all data from the CBe dSph DL4 cubes is stacked. Once more, the excess map and the significance map are computed. Figure 7.4 and Figure 7.5 illustrate these findings. A tension of 4σ is evident at the upper boundary of the exclusion region depicted in Figure 7.5. The distribution of significance values within the spatial bins is evaluated in Figure 7.6. The normal distribution fitted to the *Off* bins yields a mean of $\mu = 0.00$ and a standard deviation of $\sigma = 1.11$. Accordingly, the value of σ_{sys} is determined to be $\sigma_{\text{sys}} = 0.48$. As with the analysis of the Crab Nebula, which is illustrated in Figure 6.16, the stacking procedure has the effect of enhancing the systematic uncertainties. Moreover, the histogram encompassing

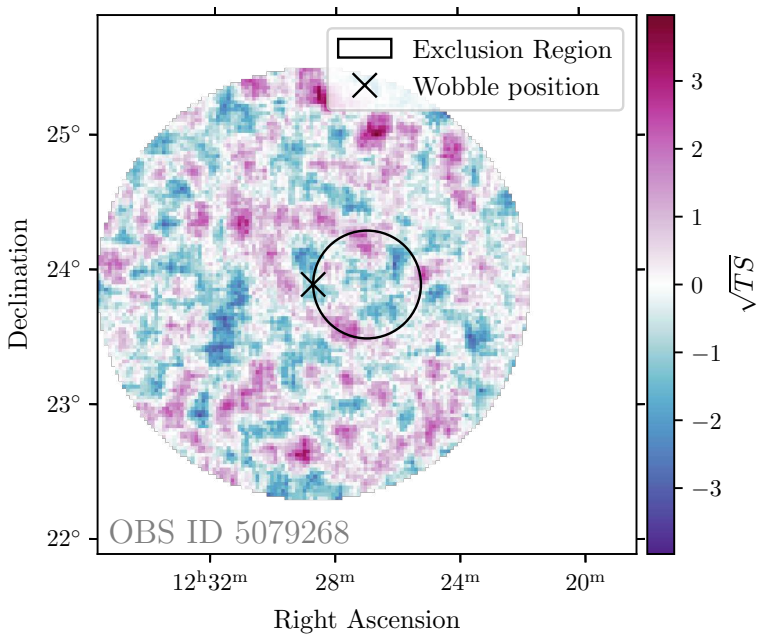

Figure 7.2: Significance map of an arbitrary CBe dSph observation, based on the data in Figure 7.1, integrated over the energy axis. The map is centered on the coordinates of the source. The black circle illustrates the exclusion region used for the background modelling, whereas the black cross denotes the Wobble position of the observation.

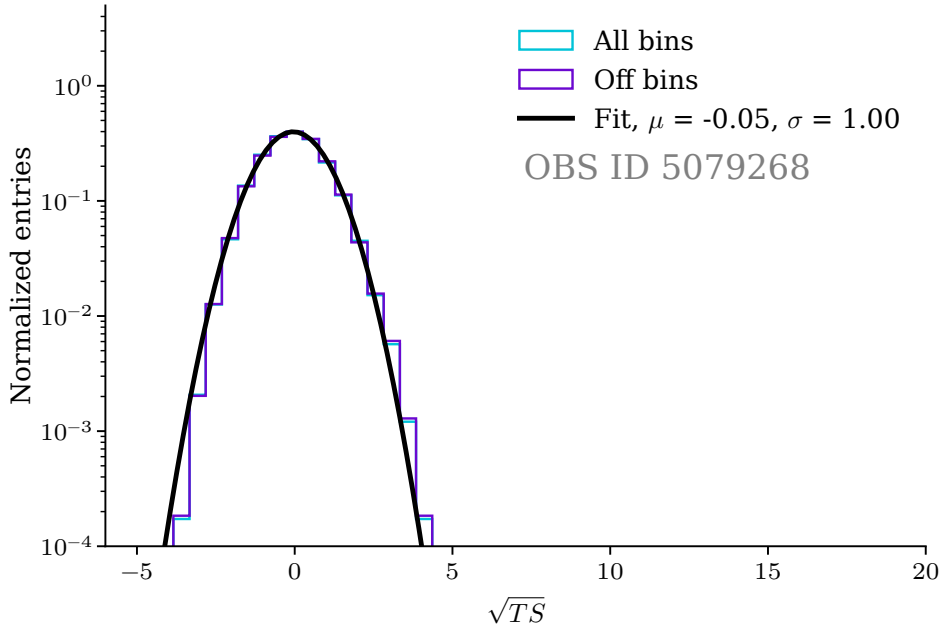

Figure 7.3: Histograms for the significance values of Figure 7.2 outside the exclusion region, *Off* bins, and within the complete map, *All* bins. A normal distribution is fitted to the *Off* bins.

the entire significance map demonstrates a similar region of 4σ. In light of the observed facts, namely the location of the increase of excess on the edge of the exclusion region and the predominance of its structural morphology in the *Off* bins, it can be posited that the observed tension may be attributed to a systematic error in the construction of the model. Furthermore, the presence of another region with a higher significance in the bins, which are utilised for the background model, is evident. Consequently, no detection of a source is claimed.

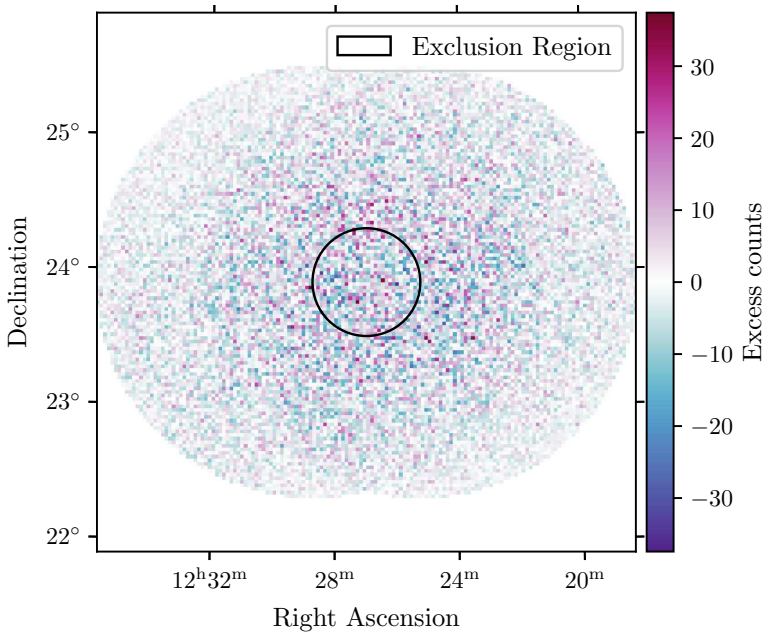

Figure 7.4: Excess map of the stacked DL4 CBe dSph observations, integrated over the energy axis. The map is centered on the coordinates of the source. The black circle illustrates the exclusion region used for the background modelling.

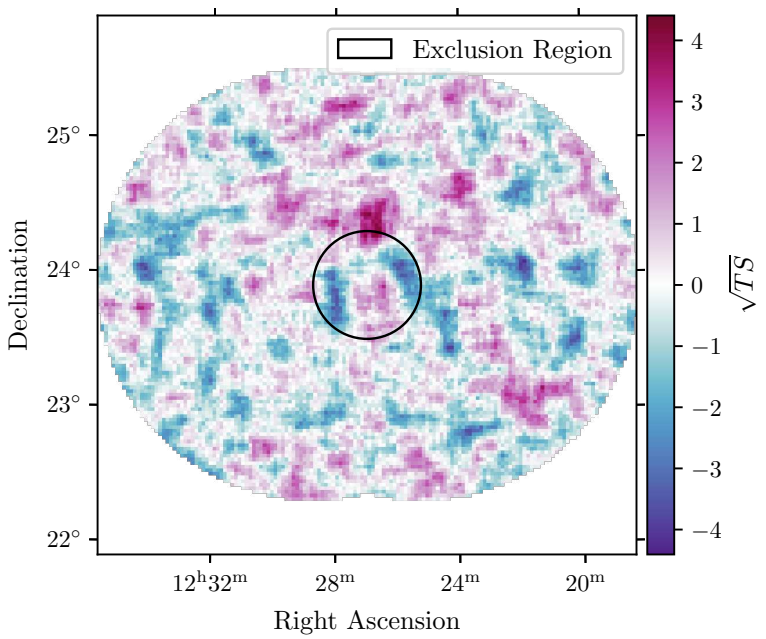

Figure 7.5: Significance map of the stacked DL4 CBe dSph observations, integrated over the energy axis. The map is centered on the coordinates of the source. The black circle illustrates the exclusion region used for the background modelling.

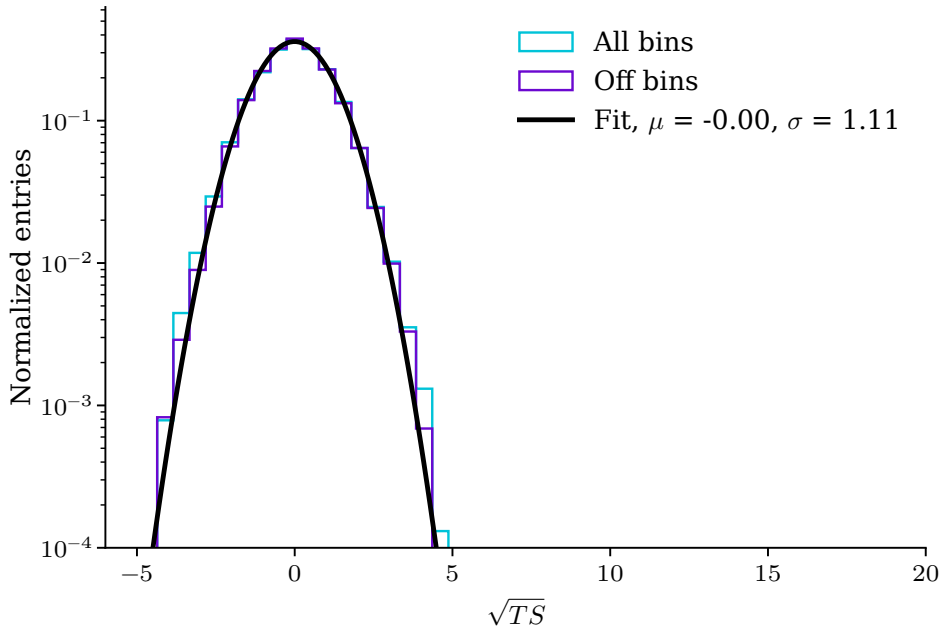

Figure 7.6: Histograms for the significance values of the stacked DL4 map in Figure 7.5, outside the exclusion region, *Off* bins, and within the complete map, *All* bins. A normal distribution is fitted to the *Off* bins.

7.2 Modelling the J-Factor

For the further analysis, ULs on the thermally averaged cross-section for annihilating DM are calculated, given that no detection was claimed in the preceding section.
As outlined in Section 2.4, the DM flux for annihilation present in CBe dSph is given by Equation 2.13, which is restated here in its abstract form

$$\frac{\mathrm{d}\Phi(\Delta\Omega)}{\mathrm{d}E} = \text{PP factor} \times \text{AP factor}, \tag{7.1}$$

where the PP factor is the primary spectrum of the DM-induced secondaries. The AP factor or J-factor describes the content of the DM inside the galaxy.

In the following section, ULs are calculated for annihilation of DM to $b\bar{b}$, W^+W^-, $\mu^+\mu^-$, and $\tau^+\tau^-$. The primary spectra for the PP factor are provided by the PPPC4DM [84]. To calculate the J-factor, a Zhao profile[1], as described in Equation 2.23, with parameters from Table 7.1, is used. The values for the parameters are extracted from the work of Geringer-Sameth et al. [186], representing the mean density parameters. The J-factor distribution is calculated using `Gammapy`'s `JFactory`, in accordance with the methodology outlined in Equation 2.15. The resulting J-factor map is presented in Figure 7.7. In the context of the 1D analysis, the map is integrated within a specified *ON* region with radius r, as outlined in Section 5.4. Here, the term ON region arises from the *reflected regions* method outlined in Section 4.9. To allow for an accurate comparison of the results in the subsequent section, $r = 0.17$ deg is chosen, as given by the most recent publication by the MAGIC [14]. The integration yields a value that is approximately one order of magnitude smaller than the J-factor employed in the publication, with $\log_{10} J \approx 17.81\,\mathrm{GeV}^2/\mathrm{cm}^5$. This discrepancy can be attributed to the fact that the J-factor employed by the MAGIC collaboration is taken from Geringer-Sameth et al. for the mean J-factor profile, rather than the J-factor generated by the mean density parameters. As the two-dimensional J-factor map is not published by Geringer-Sameth et al., and a re-computation of the J-factors is not within the scope of this thesis, the analysis will continue with the J-factor given by the parameters in Table 7.1 to maintain coherence throughout the analyses presented in this thesis.

The following sections present the results of two dedicated sets of UL computations. Firstly, a 1D analysis is presented, which is comparable to the published analysis by the MAGIC collaboration for CBe dSph [14].

[1] An implementation of this profile was added to `Gammapy` by the author.

Table 7.1: Parameters of the Zhao profile used to model the DM distribution in CBe dSph, taken from [186].

Parameter	Value
ρ_s / $m_{sun}{}^{-1}pc^{-3}$	$10^{-0.9884}$
r / pc	44
r_s / pc	$10^{3.7104}$
α	1.9942
β	6.4440
γ	0.4300

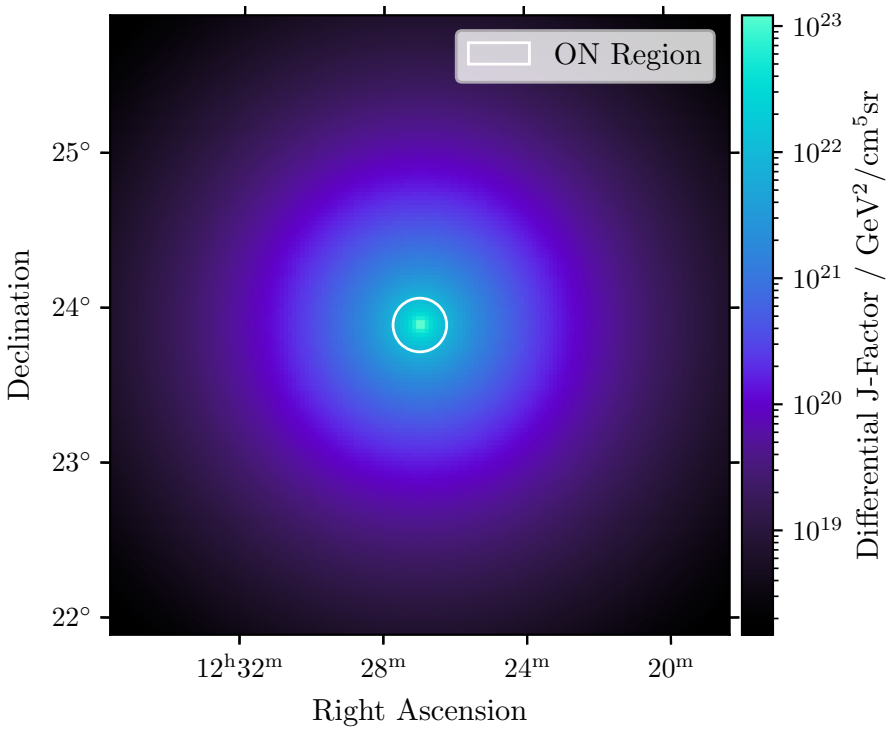

Figure 7.7: J-factor map for CBe dSph computed with `Gammapy`'s `JFactory`, based on the Zhao profile given in Table 7.1. The *ON* region of the analysis published in [14] is indicated as a white circle.

Following the findings of this analysis, a novel approach to DM search with MAGIC observations is established by repeating the analysis in 3D.
All ULs are calculated with $CL_{\mathrm{s+b}} = 0.95$ and based on $\tilde{q}_\mu$, as detailed in Section 5.6, to avoid $\hat{\mu} < 0$. Furthermore, the ULs are calculated twice, based on the *classical* Wilks' theorem and the *Asimov* approximation, as detailed in Section 5.7. The limits are recalculated using the CL_s method, as outlined in Section 5.8, which represents the final stage of the CBe dSph analysis.

7.3 Upper Limits on DM - 1D Reduction

In accordance with Section 5.4, a 1D reduction of the stacked DL4 cube is initially conducted, resulting in the generation of a `Gammapy SpectrumDataset`, also referred to as the *measurement* dataset. This dataset is computed by integrating the reconstructed events of CBe dSph inside the defined *ON* region with $r = 0.17°$, as introduced in the preceding section. The counts within the *OFF* region are calculated from the background model by performing the same integration. This simplification results in the loss of spatial information present in both the DL4 cube and the J-factor map, as indicated in Figure 7.7.
The constructed dataset exhibits properties similar to those of the dataset used in the published analysis of CBe dSph by MAGIC [14], which is based on the estimation of the background using the *reflection regions* method, as detailed in Section 4.9.

The ULs are computed in line with Equation 5.13. In the context of the MAGIC standard analysis, the distribution of the TS is assumed to follow a χ^2 distribution, provided that Wilk's theorem is applicable. This describes the aforementioned *classical* limits. In practice, the strength parameter μ, which scales the thermally averaged cross-section, is found by numerically calculating the p-value for $CL_{\mathrm{s+b}} = 0.95$, i.e.

$$p = \int_{\tilde{q}_{\mu,\mathrm{obs}}}^{\infty} \chi^2(\tilde{q}_\mu)\, d\tilde{q}_\mu$$
$$\stackrel{!}{=} 1 - CL_{\mathrm{s+b}} = 0.05 \tag{7.2}$$
$$\Leftrightarrow \sqrt{\tilde{q}_{\mu,\mathrm{obs}}} \stackrel{!}{=} 2.71. \tag{7.3}$$

Here, $\tilde{q}_{\mu,\mathrm{obs}}$ represents the TS, as detailed in Section 5.7, that is evaluated on the `SpectrumDataset` of the stacked observations. Here, the NP vector $\vec{\theta}$ is one-dimensional and contains a single normalisation parameter for the background model θ_{bkg}. This approach is preferable to a `PiecewiseNormSpectralModel` with

a normalisation parameter for each energy bin of the background model, to avoid modifying the inferred spectral shape outside the exclusion region, as detailed in Section 6.2.

Figure 7.8 and Figure 7.9 display the ULs on the thermally averaged cross-section for the annihilation channels $b\bar{b}$, W^+W^-, $\mu^+\mu^-$, and $\tau^+\tau^-$ for 30 assumed DM masses between 0.17 TeV and 100 TeV, as derived from Equation 7.3. This minimum mass of 0.17 TeV is selected to be marginally larger than twice the mass of the W boson, to circumvent numerical instability in the vicinity of the energy edges of the primary spectrum. The maximum value for the mass is in alignment with the MAGIC convention.
Furthermore, the ULs for the null hypothesis H_0 are calculated in addition to those for the measurement dataset. The median, 1σ, and 2σ region of H_0 are computed using 300 MC simulations for each channel. The NP θ_{bkg} is profiled on the `SpectrumDataset` of the observations for the case $\mu = 0$, with the objective to produce simulation parameters that are as close as possible to the conditions of the measurement. In total, the computation of the null hypothesis on the MCs required approximately 100 h of single-core CPU time on LiDO3. For the calculation of the *Asimov* ULs, the newly developed `TITRATE` package [12], as detailed in Section 5.9, is used to enable a first-ever computation of limits using the approximation by Cowan et al. with `Gammapy` and MAGIC observations. The feasibility of the asymptotic limits, introduced in Section 5.7, is initially investigated. Validation is conducted using the `AsymptoticValidator` of `TITRATE`, which simulates 1000 MC datasets under two scenarios: $\mu = \mu'$ and $\mu \neq \mu'$. Once more, the profiled NP θ_{bkg} is calculated from the `SpectrumDataset` of the observations, assuming μ', to simulate datasets that are close to the conditions of the real data. The distribution of the TS, $f(\tilde{q}_\mu|\mu', \hat{\hat{\theta}}_{\mu'})$, is calculated for the aforementioned two sets of MC, assuming $\mu' = 0$ and $\mu = \mathcal{O}(\mu_{UL,H_0})$, as well as $\mu' = \mu = \mathcal{O}(\mu_{UL,H_0})$. Here $\mathcal{O}(\mu_{UL,H_0})$ denotes the order of magnitude of the H_0 UL inferred in Figure 7.8 and Figure 7.9 for the respective models. This therefore validates the cases of calculating p_μ, which is required for $CL_{\text{s+b}}$, and p_b, which is required for CL_{s} limits, as detailed in Section 5.7 and Section 5.8. For valid ULs, the non-central-χ^2 distribution provides a close approximation for the simulated distribution of the TS. Figure 7.10 illustrates the binned TS values of the simulations for a model with annihilation to $b\bar{b}$ and a mass of 0.17 TeV. The asymptotic limits demonstrate a χ^2 and non-central χ^2 distribution in accordance with the expectation. Comprehensive validation is performed for models with DM masses of 0.17 TeV, 1.53 TeV, 13.82 TeV, and 100 TeV, and encompasses the channels presented in Figure 7.8 and Figure 7.9. The 16 validation plots can be found in Appendix E.1.

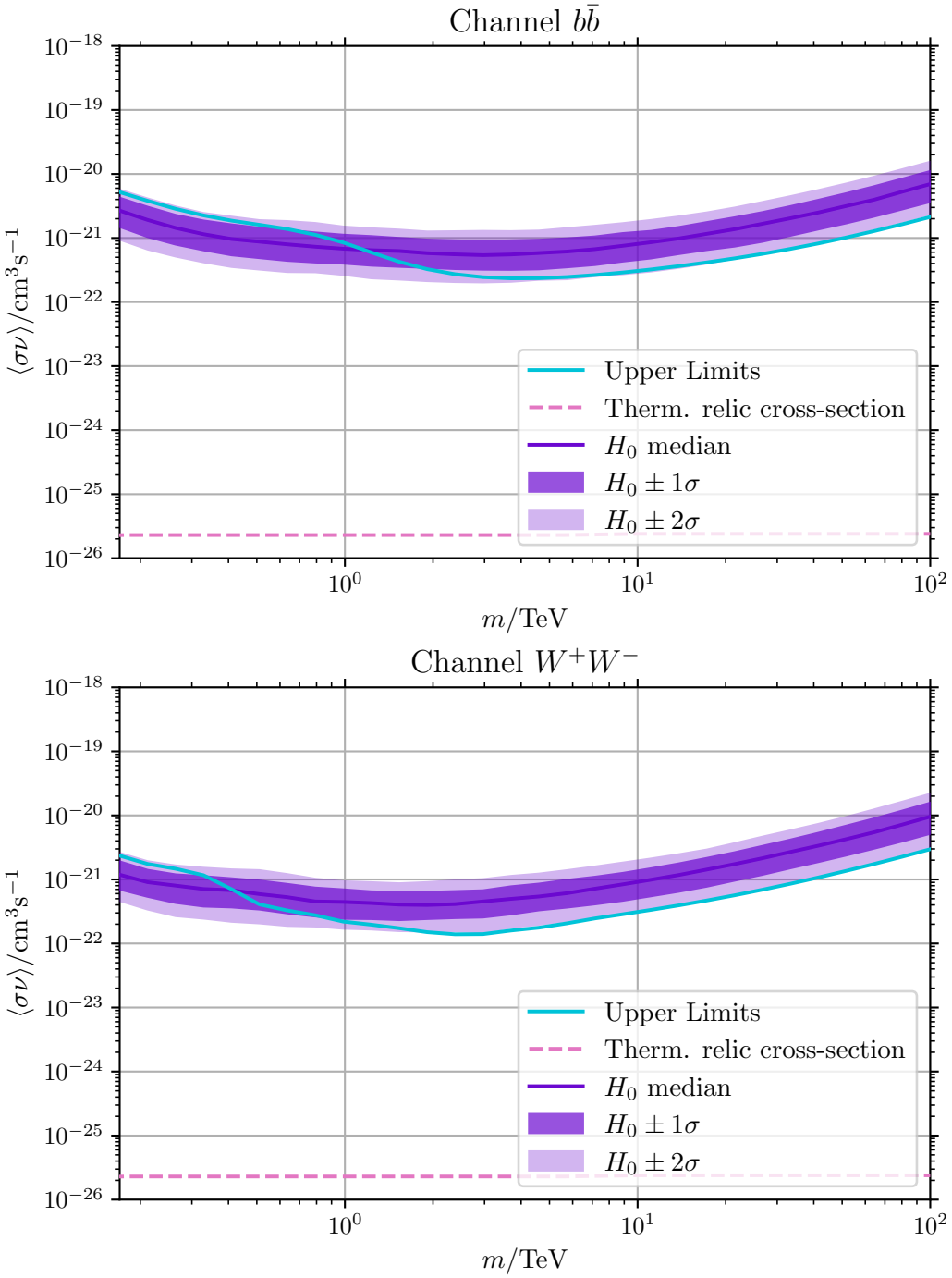

Figure 7.8: ULs on the thermally averaged cross-section for annihilating DM into $b\bar{b}$ and W^+W^- from $m_\chi = 0.17\,\mathrm{TeV}$ to $m_\chi = 100\,\mathrm{TeV}$. The limits are calculated using Wilks theorem on the 1D reduced CBe dSph observations. The ULs for the null hypothesis H_0 are calculated with 300 background-only MC sets. Thermal relic cross-section taken from [57].

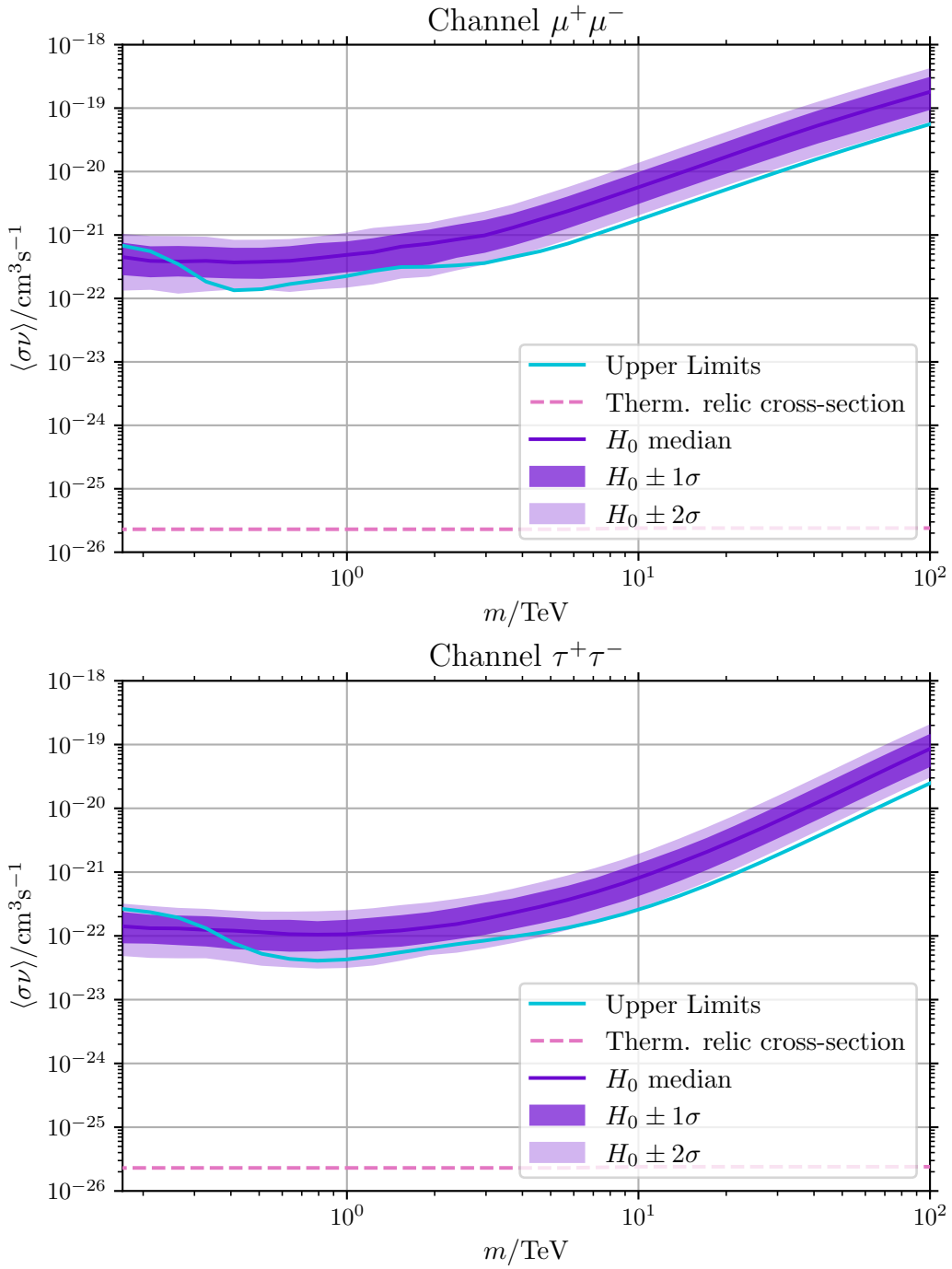

Figure 7.9: ULs on the thermally averaged cross-section for annihilating DM into $\mu^+\mu^-$ and $\tau^+\tau^-$ from $m_\chi = 0.17\,\mathrm{TeV}$ to $m_\chi = 100\,\mathrm{TeV}$. The limits are calculated using Wilks' theorem on the 1D reduced CBe dSph observations. The ULs for the null hypothesis H_0 are calculated with 300 background-only MC sets. Thermal relic cross-section taken from [57].

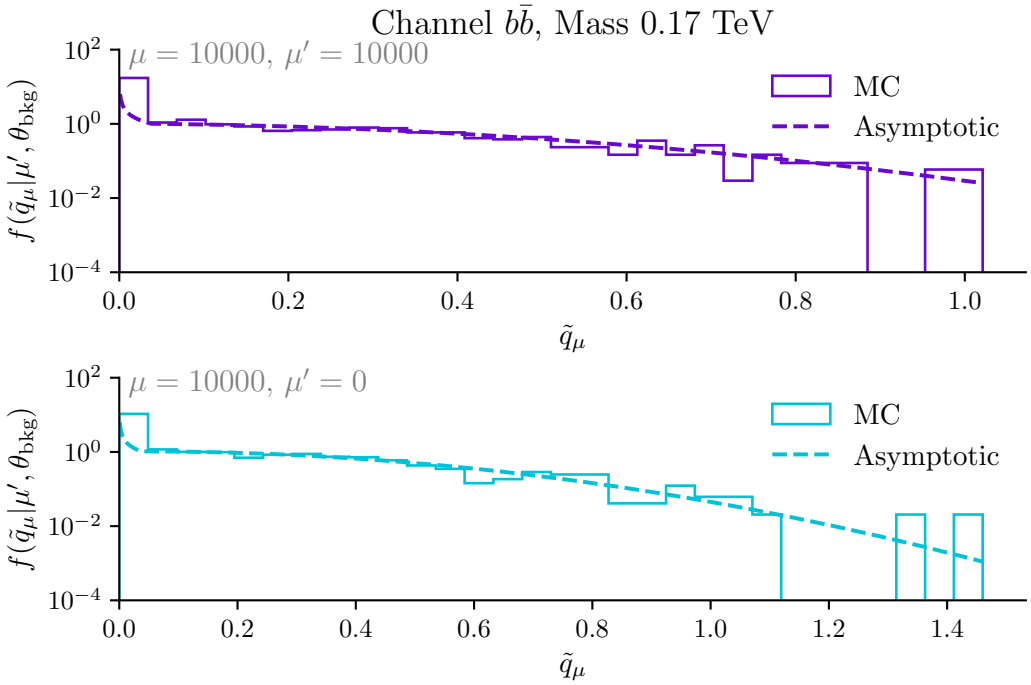

Figure 7.10: Distribution of the TS, derived from computation of $\tilde{q}_\mu$ on 1000 1D MCs using `TITRATE`. The asymptotic limits, based on Cowan et al., are shown to display the approximation. $\tilde{q}_\mu$ is calculated for a DM model with mass 0.17 TeV and annihilation into $b\bar{b}$.

Moreover, the ULs based on the Asimov datasets, as detailed in Section 5.7, are displayed in Figure 7.11 and Figure 7.12. The calculation of the null hypothesis bands H_0 is based on Equation 5.25 and Equation 5.26. The H_0 band for the 2σ region includes ULs that are smaller than zero, which is a consequence explained in Section 5.8 and illustrated in Figure 5.6.
In total, the Asimov-based computation required approximately 16 min of single-core CPU time for all masses and all channels, representing a significant reduction in computation time compared to the MC-based ULs. Furthermore, Figure 7.11 and Figure 7.12 illustrate the ULs for the null hypothesis published by MAGIC for CBe dSph. As the J-factor, calculated in Section 7.2 is based on the Zhao profile with median parameter values, the ULs calculated here show a significant deviation from the published values. Two allow for a more accurate comparison to be made, the ULs for med$[H_0]$ are scaled with the J-factor found by Geringer-Sameth et al. [186] through derivation from the containment profile. However, this is not suitable for the 3D analysis, since the J-factor map cannot be computed based on the profile. Overall the sensitivity is comparable to the MAGIC publication under these assumptions.

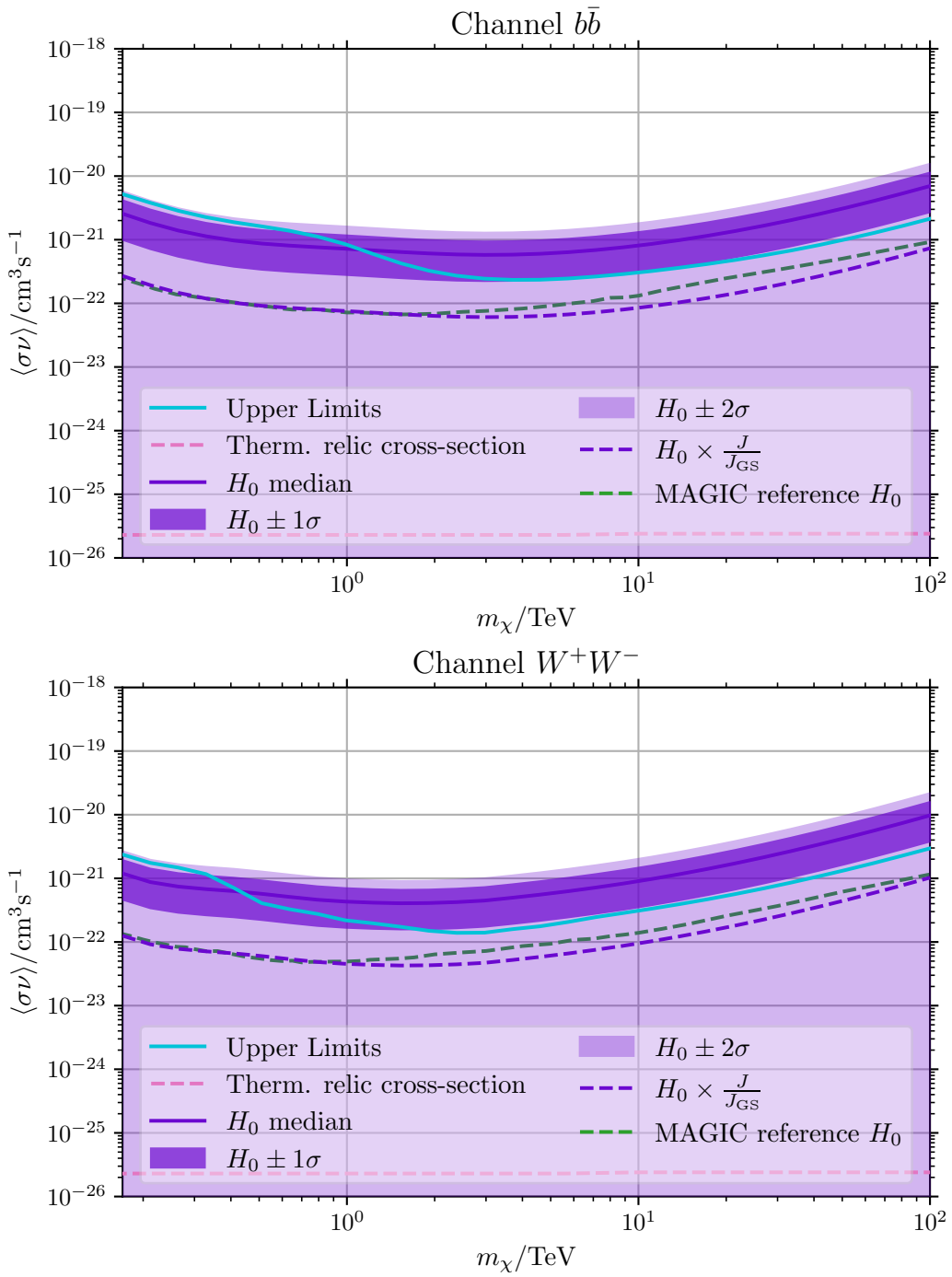

Figure 7.11: ULs on the thermally averaged cross-section for annihilating DM into $b\bar{b}$ and W^+W^- from $m_\chi = 0.17\,\mathrm{TeV}$ to $m_\chi = 100\,\mathrm{TeV}$. The limits are calculated using Asimov dataset on the 1D reduced CBe dSph observations. The ULs for the null hypothesis H_0 are calculated with one Asimov dataset per model. MAGIC reference taken from [14]. H_0 median scaled with the J-Factor from [186] is displayed as a dashed line.

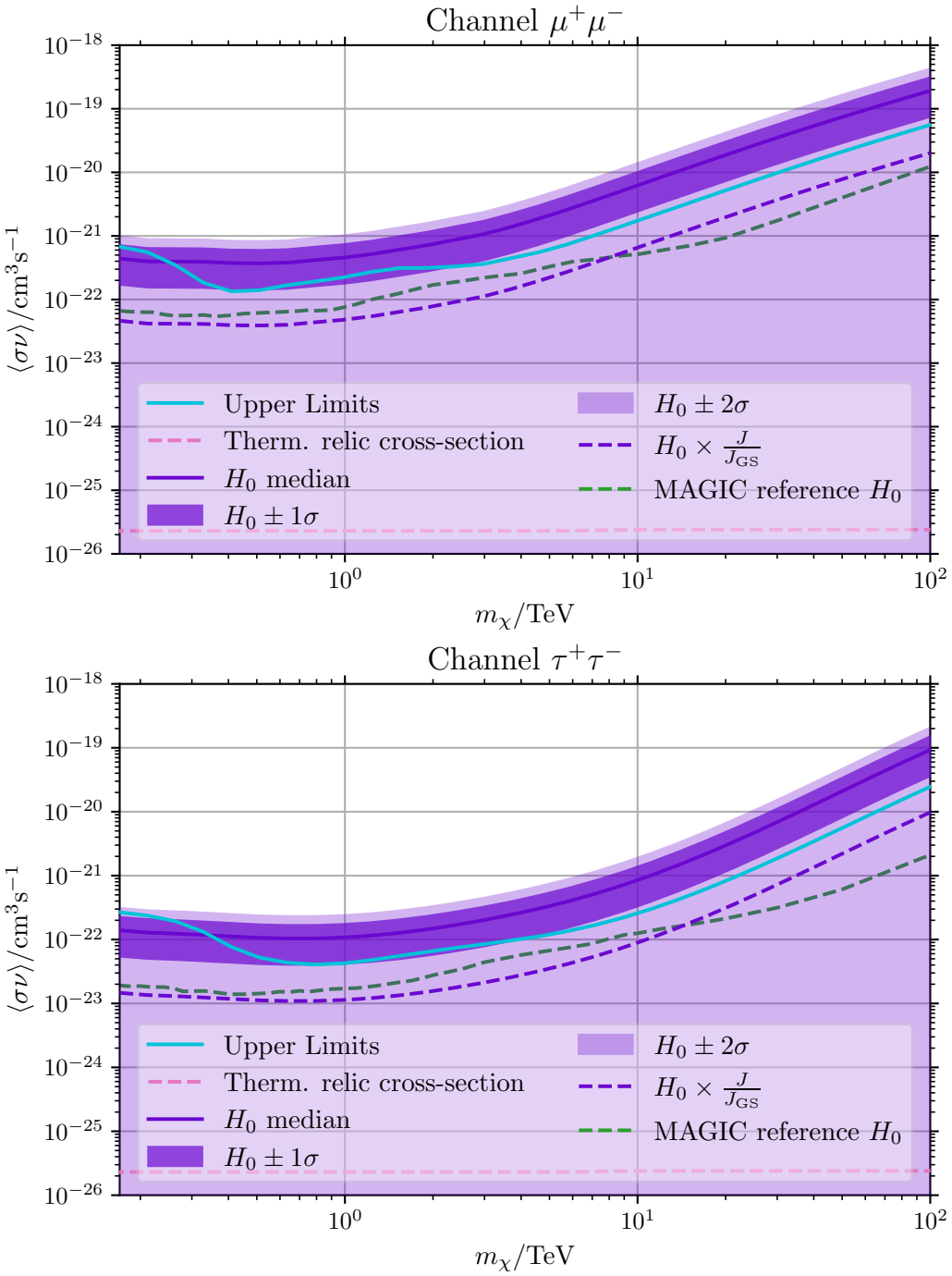

Figure 7.12: ULs on the thermally averaged cross-section for annihilating DM into $\mu^+\mu^-$ and $\tau^+\tau^-$ from $m_\chi = 0.17\,\mathrm{TeV}$ to $m_\chi = 100\,\mathrm{TeV}$. The limits are calculated using Asimov dataset on the 1D reduced CBe dSph observations. The ULs for the null hypothesis H_0 are calculated with one Asimov dataset per model. MAGIC reference taken from [14]. H_0 median scaled with the J-Factor from [186] is displayed as a dashed line.

7.4 Upper Limits on DM - 3D

Building upon the analysis presented in the preceding section, the full 3D analysis seeks to infer ULs for annihilating DM, with masses between 0.17 TeV and 100 TeV for each channel of $b\bar{b}$, W^+W^-, $\mu^+\mu^-$, and $\tau^+\tau^-$. This novel analysis presents the first 3D DM ULs for MAGIC, employing `Gammapy` and `TITRATE`.

In contrast to the 1D analysis, the complete J-factor map, as illustrated in Figure 7.7, is employed for modelling the DM content through the application of Equation 2.13. Therefore, the data regarding the morphology of the DM density is incorporated, in contrast to the approach taken in the preceding section. The strength parameter for $CL_{\mathrm{s+b}} = 0.95$ is found using the *classical* approximation given by Equation 7.3 and the *Asimov* approximation based on Section 5.7. The resulting limits for the former case are illustrated in Figure 7.13 and Figure 7.14.

Furthermore, to validate the usage of the approximation by Cowan et al., `TITRATE`'s `AsymptoticValidator` is employed to simulate 1000 MC `MapDataset`s for both $\mu' = 0$ and $\mu' = \mathcal{O}(\mu_{UL,H_0})$, which denotes the order of magnitude of the H_0 UL inferred in Figure 7.13 and Figure 7.14 for the respective models. The TS values of these datasets are calculated in a manner analog to that described in the preceding section, with $\mu = \mathcal{O}(\mu_{UL,H_0})$, based on Section 5.7. Figure 7.15 displays the binned TS values of the simulations for annihilation to $b\bar{b}$ and a mass of $m_\chi = 0.17$ TeV, together with the non-central χ^2 approximation. As with the 1D case, the validation sets for the 3D analysis demonstrate satisfactory agreement with the asymptotic limits. Comprehensive validation is performed for models with DM masses of 0.17 TeV, 1.53 TeV, 13.82 TeV, and 100 TeV, and encompassing the channels presented in Figure 7.13 and Figure 7.14. The 16 validation plots can be found in Appendix E.2.

The "Asimov"-based ULs are illustrated in Figure 7.16 and Figure 7.17. Similar to Figure 7.11 and Figure 7.12, negative values for the 2σ region of H_0 are evident, which arise from the $CL_{\mathrm{s+b}}$ method. A comprehensive comparison of the ULs for the 1D and 3D analysis is provided in the subsequent section.

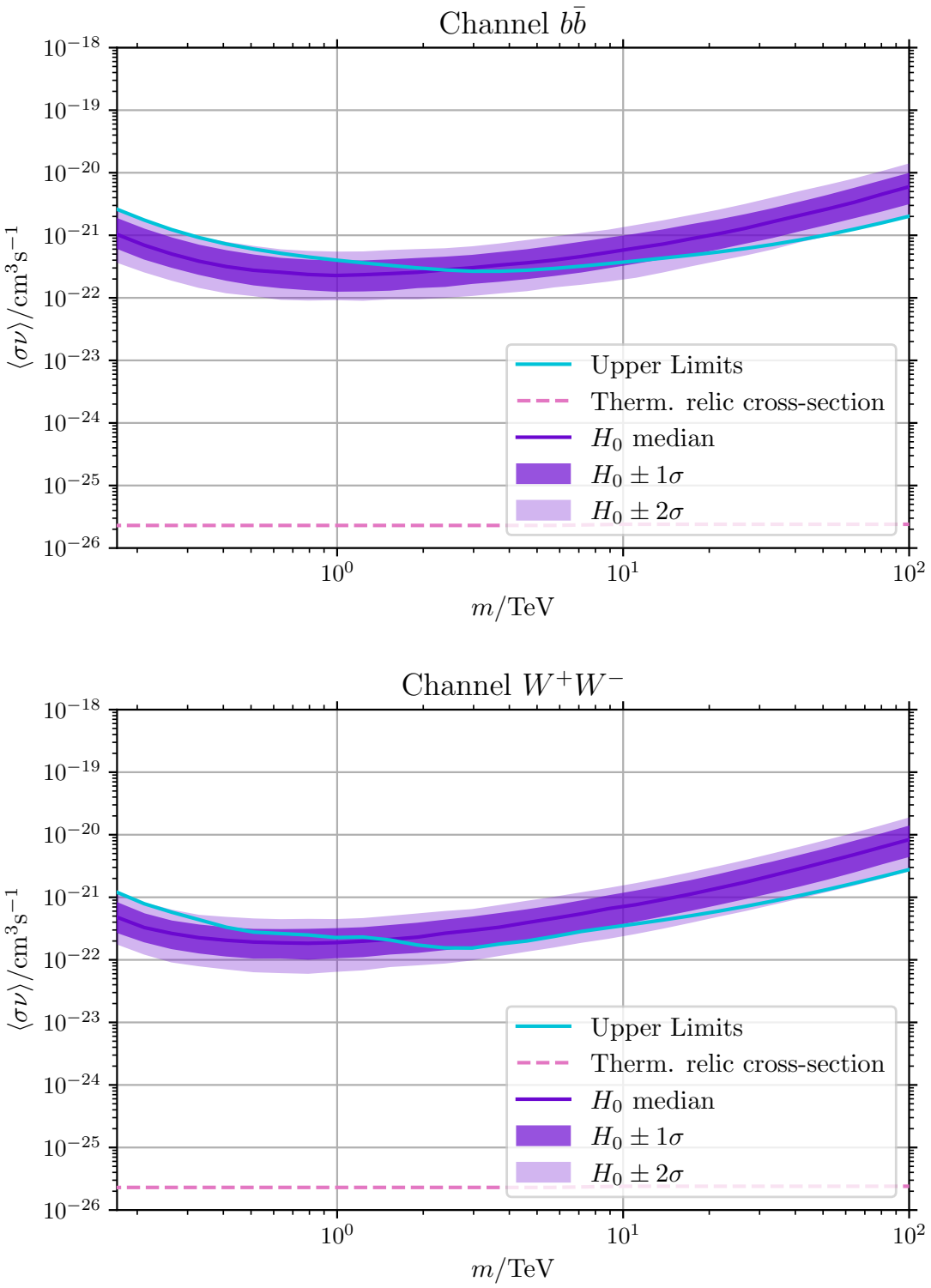

Figure 7.13: ULs on the thermally averaged cross-section for annihilating DM into $b\bar{b}$ and W^+W^- from $m_\chi = 0.17\,\mathrm{TeV}$ to $m_\chi = 100\,\mathrm{TeV}$. The limits are calculated using Wilks' theorem on the CBe dSph DL4 cube. The ULs for the null hypothesis H_0 are calculated with 300 background-only MC sets. Thermal relic cross-section taken from [57].

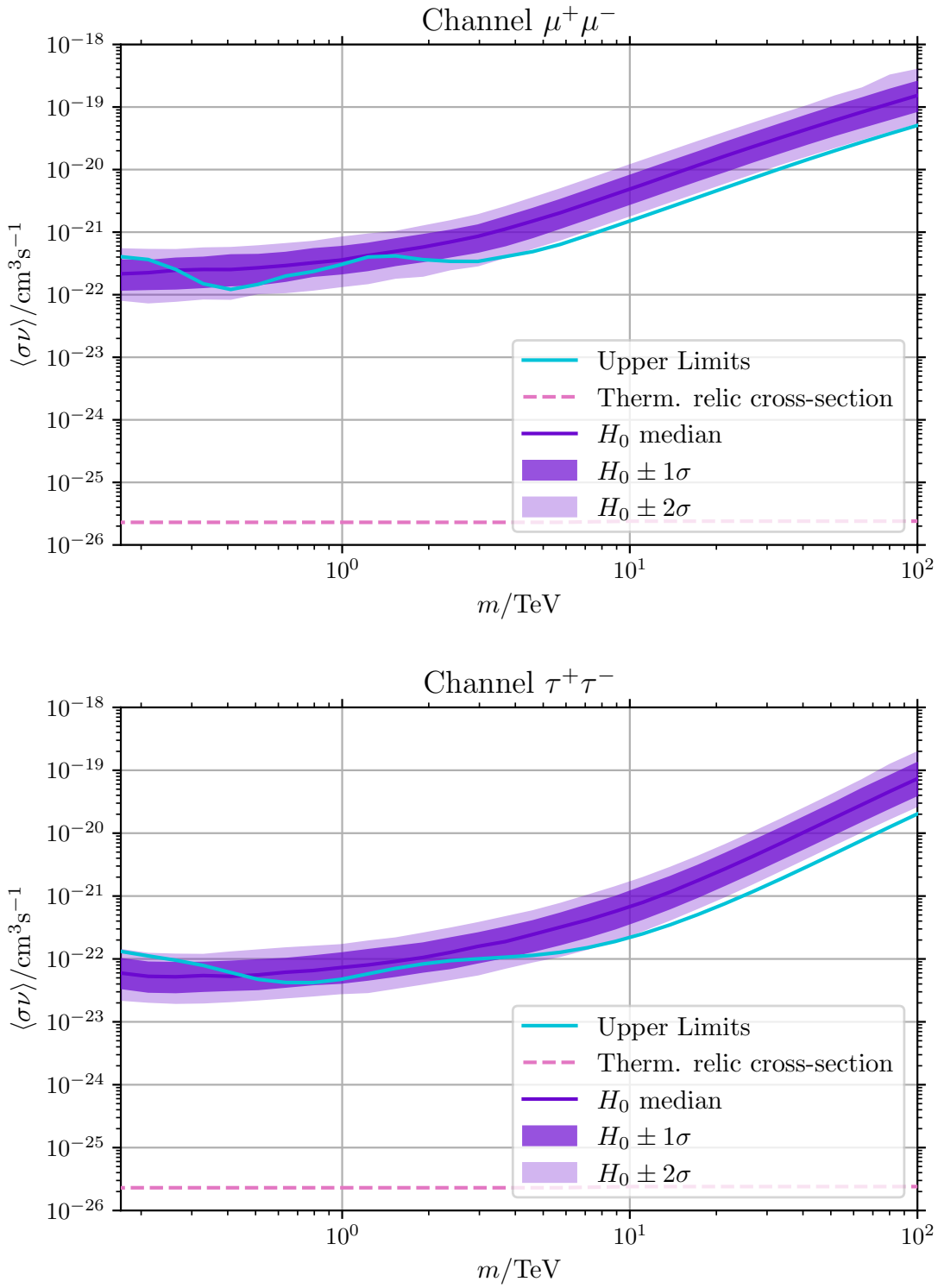

Figure 7.14: ULs on the thermally averaged cross-section for annihilating DM into $\mu^+\mu^-$ and $\tau^+\tau^-$ from $m_\chi = 0.17\,\mathrm{TeV}$ to $m_\chi = 100\,\mathrm{TeV}$. The limits are calculated using Wilks' theorem on the CBe dSph DL4 cube. The ULs for the null hypothesis H_0 are calculated with 300 background-only MC sets. Thermal relic cross-section taken from [57].

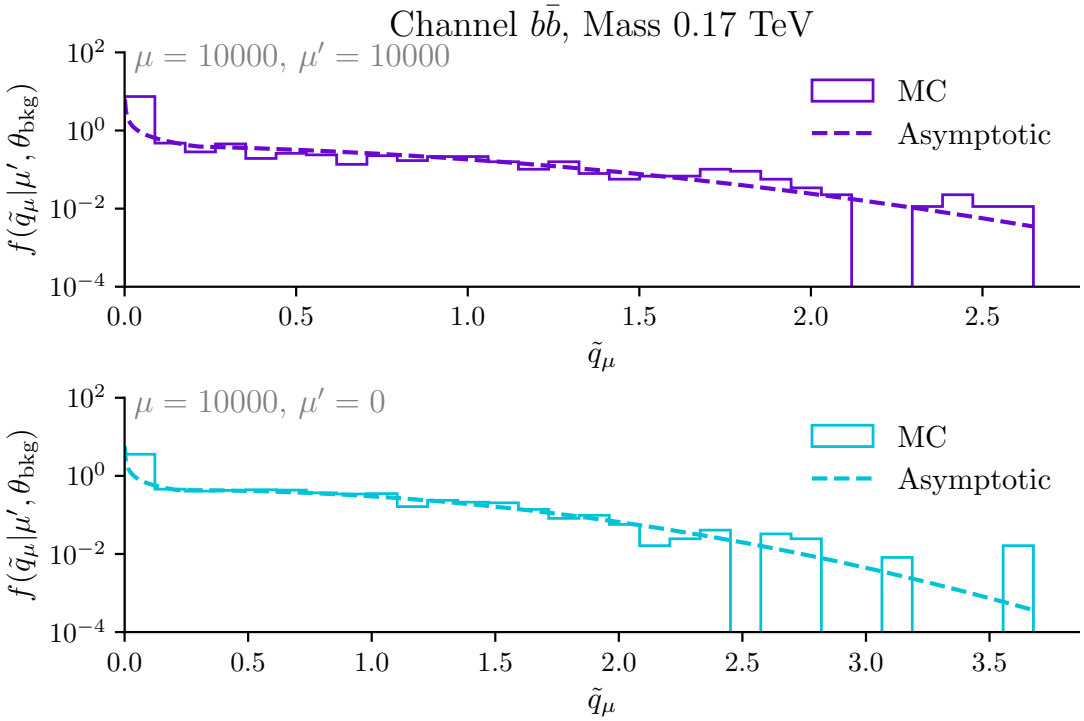

Figure 7.15: Distribution of the TS, derived from computation of $\tilde{q}_\mu$ on 1000 3D MCs, The asymptotic limits, based on Cowan et al., are shown to display the approximation. $\tilde{q}_\mu$ is calculated for a DM model with mass 0.17 TeV and annihilation into $b\bar{b}$.

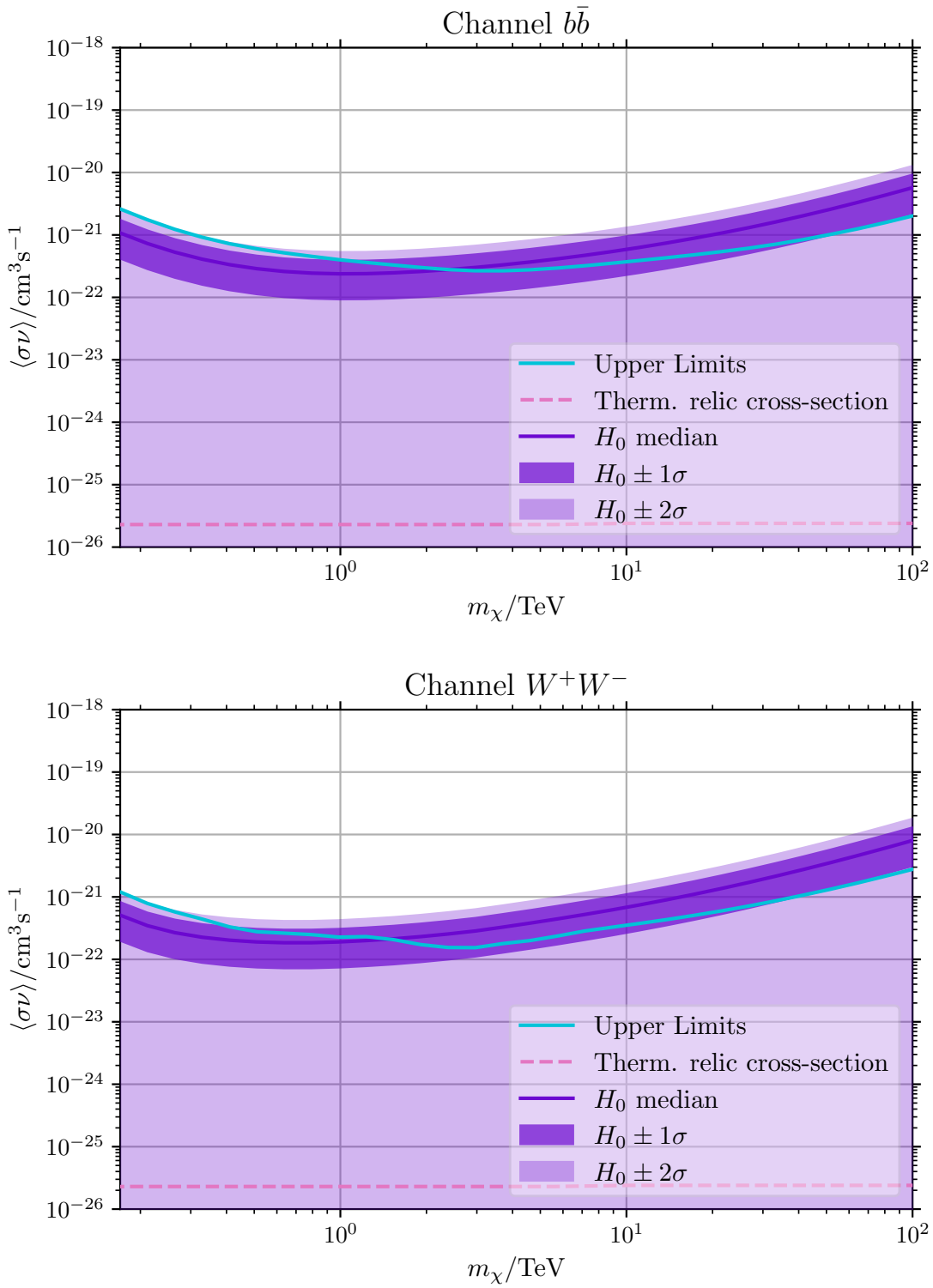

Figure 7.16: ULs on the thermally averaged cross-section for annihilating DM into $b\hat{b}$ and W^+W^- from $m_\chi = 0.17\,\mathrm{TeV}$ to $m_\chi = 100\,\mathrm{TeV}$. The limits are calculated using Asimov dataset on the CBe dSph DL4 cube. The ULs for the null hypothesis H_0 are calculated with one Asimov dataset per model.

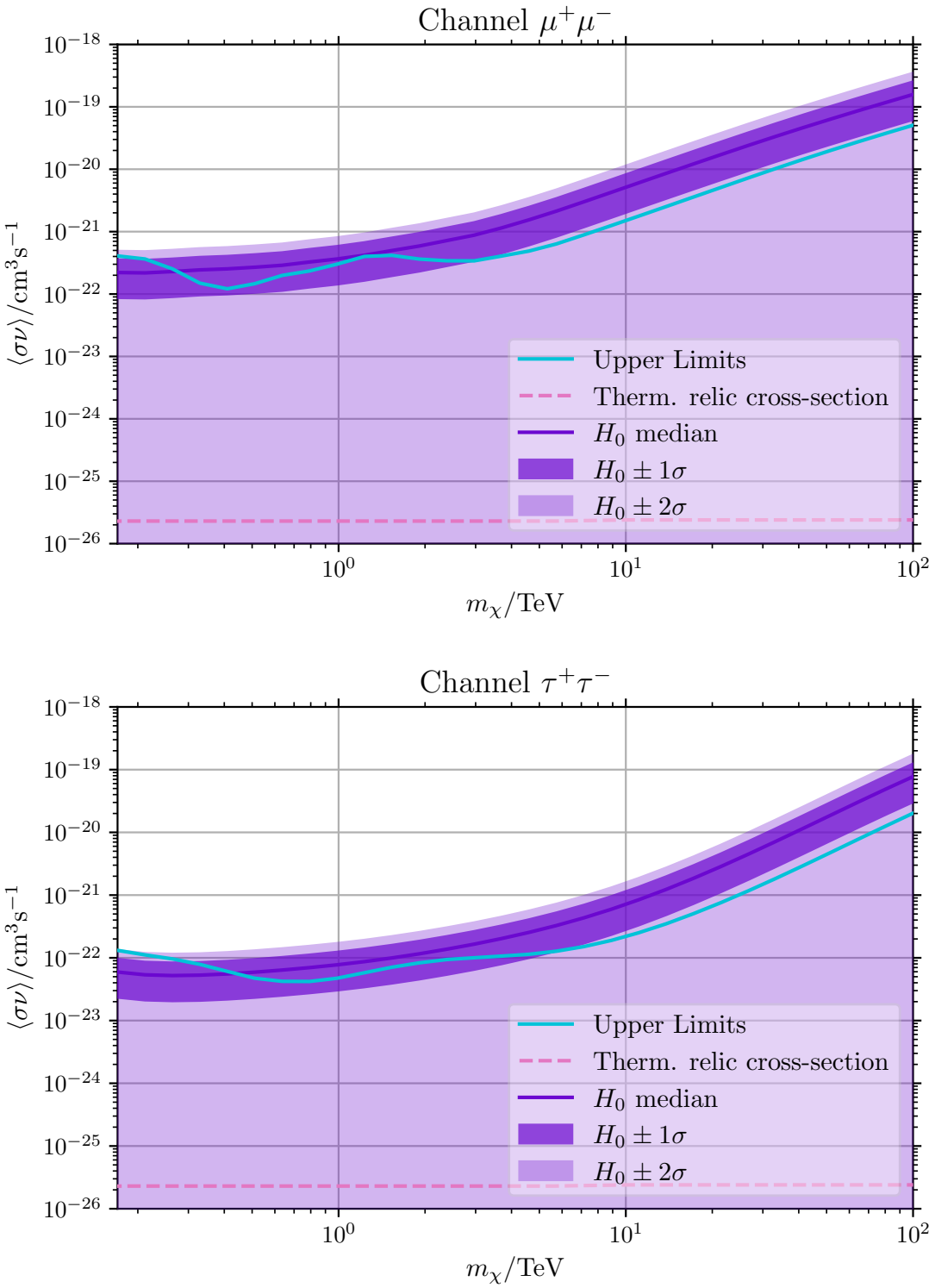

Figure 7.17: ULs on the thermally averaged cross-section for annihilating DM into $\mu^+\mu^-$ and $\tau^+\tau^-$ from $m_\chi = 0.17\,\mathrm{TeV}$ to $m_\chi = 100\,\mathrm{TeV}$. The limits are calculated using Asimov dataset on the CBe dSph DL4 cube. The ULs for the null hypothesis H_0 are calculated with one Asimov dataset per model.

7.5 Asimov Limits Across Dimensions - A detailed Comparison

To gain further insight into the potential advantages of the novel 3D analysis for annihilating DM over a classical 1D analysis, a detailed comparison is presented in this section. Furthermore, the *Asimov* ULs, based on the proposed approximations by Cowan et al., are compared to the *classical* ULs, which are based on Wilks' theorem. Figure 7.18 and Figure 7.19 display multi-views of the different ratios between the 1D and 3D ULs and their asymptotic approximations. The former figure illustrates the ULs calculated on the DL4 cube of the observations, while the latter figure presents the median ULs for the null hypothesis H_0.

Figure 7.18 demonstrates that the ratios of the Asimov and classical ULs are in perfect agreement with a value of one for both the 1D and 3D analysis. This is due to the fact that the calculation based on Wilks' theorem and the approximation by Cowan et al. lead to the same UL for $CL_{\mathrm{s+b}}$. Consequently, the ratios between 1D and 3D are identical, i.e. ${}^{UL_{\mathrm{3D,Asimov}}}/_{UL_{\mathrm{1D,Asimov}}} = {}^{UL_{\mathrm{3D}}}/_{UL_{\mathrm{1D}}}$. While the ratio varies for each channel, it also differs for different masses. This effect is also evident in the ratio pertaining to the null hypothesis, displayed in Figure 7.19, wherein a global enhancement of the 3D ULs over the 1D ULs is observed. This improvement deviates from that of the UL on the *measurement* cube, due to the influence of the 4σ region, which plays a dominant role in the calculation of the ULs in both the 1D and 3D scenarios.
To further investigate and understand this behaviour, it is necessary to evaluate a number of key properties associated with the calculation. In the following section, the ratio ${}^{UL_{\mathrm{3D}}}/_{UL_{\mathrm{1D}}}$ for H_0 will be considered.

The TS depends on the evaluation of the likelihood, as given by the Cash statistic and introduced in Equation 5.3. Comparing the 1D and the 3D datasets reveals that the number of bins changes, as spatial bins are now included. The impact of the newly contributing bins is most significant when comparing models whose spectra have not yet reached the maximum energy of the DL4 cube, which mainly arises from the effects present at the energetic boundary of the models, as displayed in Figure 2.7. This is the case for all models with a mass of $m_\chi < m_{\mathrm{th}} = E_{\mathrm{max}}$. For masses beyond m_{th}, the total flux integrated over the entire energy axis up to E_{max} of the models remains relatively constant. Consequently, this mass range does not exhibit the aforementioned effect for $m_\chi < m_{\mathrm{th}}$. Figure 7.20 displays the gradient of the integrated DM flux with respect to the DM mass. As expected, this gradient provides an approximation of the aforementioned effect, given that the flux directly relates to the ULs.

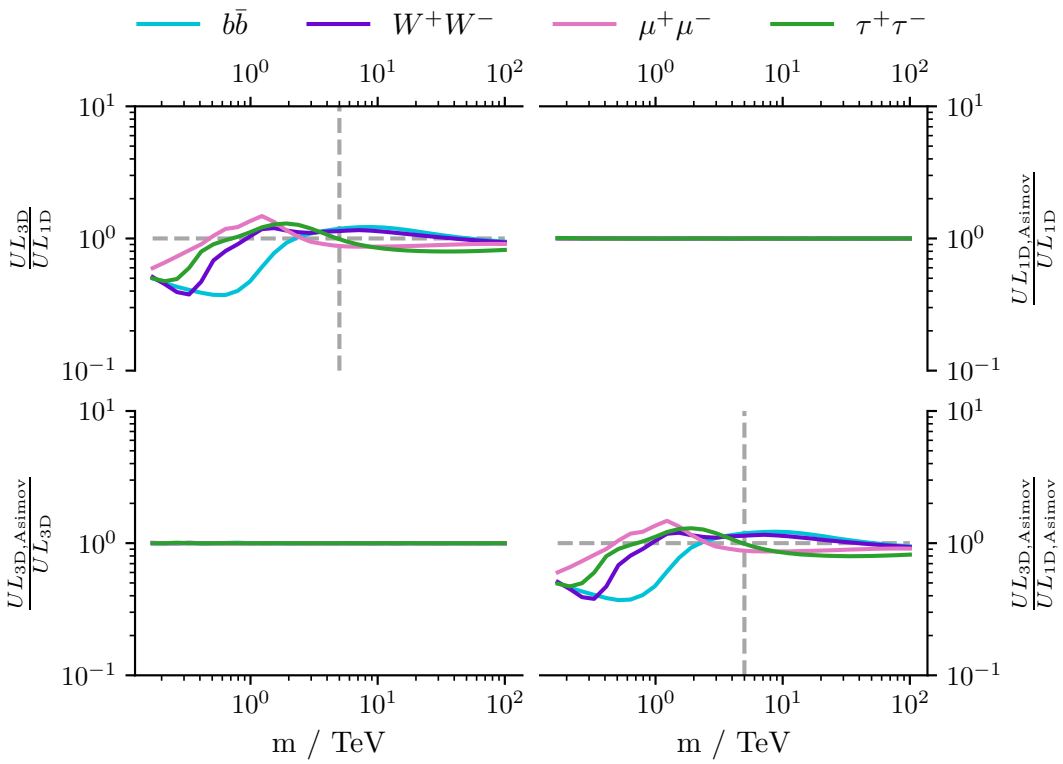

Figure 7.18: Ratio of ULs on the measured datasets. 3D denotes the UL on the DL4 cube, whereas 1D denotes the ULs on the spatially reduced DL4. *Asimov* denotes the ULs calculated with the Cowan et al. approximation.

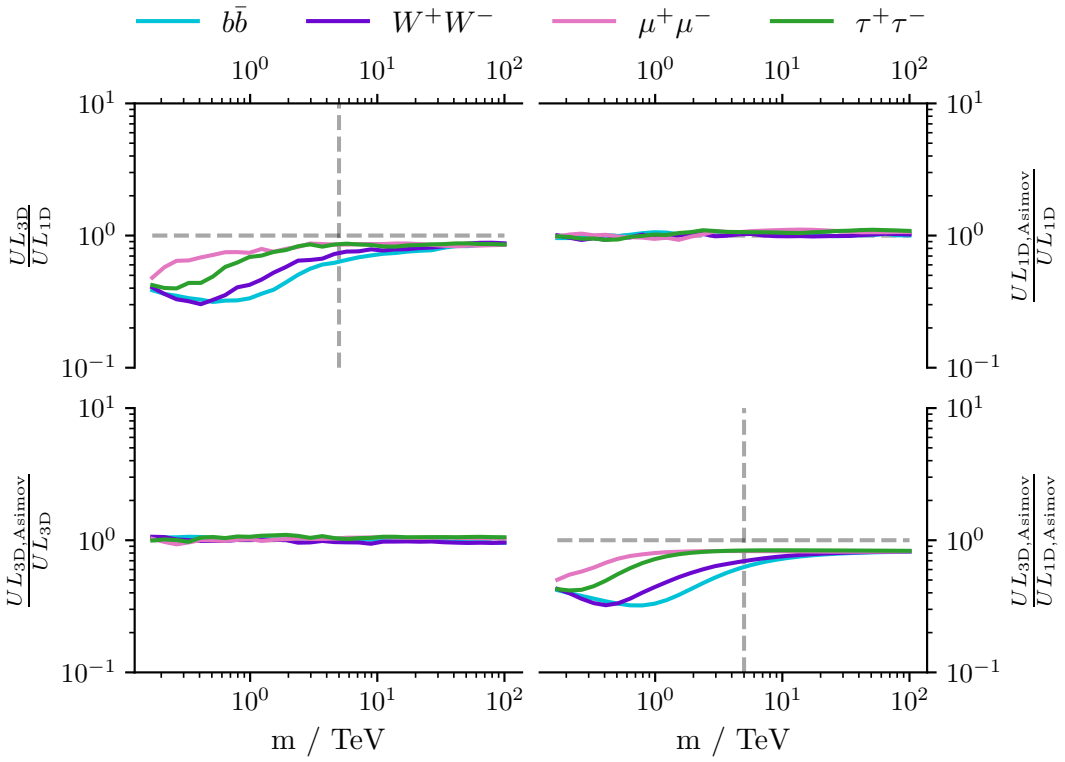

Figure 7.19: Ratio of median ULs on the MC for the classical case and on the Asimov datasets for the Cowan et al. approximation. 3D denotes the ULs on the DL4 cube, whereas 1D denotes the ULs on the spatially reduced DL4 cube.

It is evident that an overall constant improvement of the ULs for the 3D over the 1D case is present.

The ratios of the Asimov ULs over the classical ULs are approximately one, which indicates the validity of the Cowan et al. approximations. Therefore, the fraction $UL_{\mathrm{3D}}/UL_{\mathrm{1D}}$ is approximately $UL_{\mathrm{3D,Asimov}}/UL_{\mathrm{1D,Asimov}}$. Although the Asimov ratio appears to be more gradual, this is largely due to the limited amount of MC samples used for the classical case.

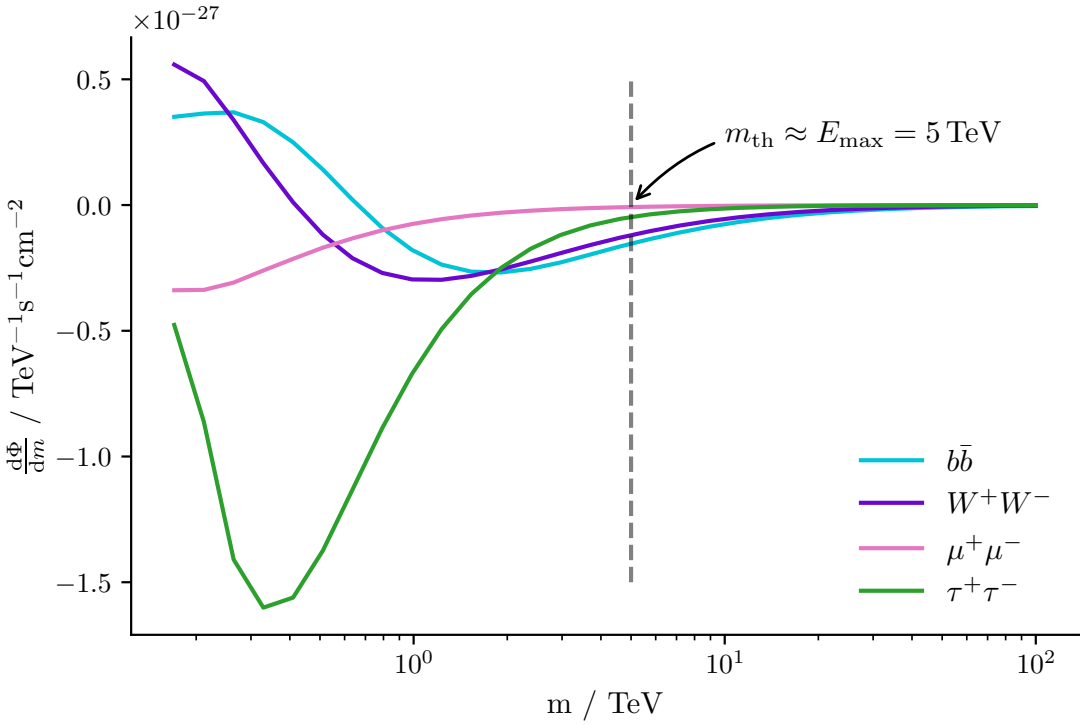

Figure 7.20: Gradient of the integrated flux $\frac{\mathrm{d}\Phi}{\mathrm{d}m}$ of the DM model with respect to the model mass. The integration bounds are defined by the energy range of the analysis.

7.6 Avoiding the Negative - The CL_s method

The unphysical values for the ULs, $\langle\sigma v\rangle < 0$, present a major issue for the goal of constraining theoretical models. A case in point is provided by the null hypothesis bands calculated from the Asimov datasets, which are illustrated in Figure 7.11, Figure 7.12, Figure 7.16, and Figure 7.17. This issue arises from the UL calculation based on the CL for signal and background, $CL_{\mathrm{s+b}}$. One method to circumvent $\mu_{\mathrm{UL}} \leq 0$ is to calculate the signal-only CL_{s} instead, as detailed in

Section 5.8. This calculation requires the use of Asimov datasets and is not possible with the classical approach without a challenging amount of MC simulations. The ULs for the 1D case, based on the Asimov datasets, are illustrated in Figure 7.21 and Appendix E.3, respectively. It is evident that the 2σ band for the null hypothesis H_0 no longer includes unphysical results.

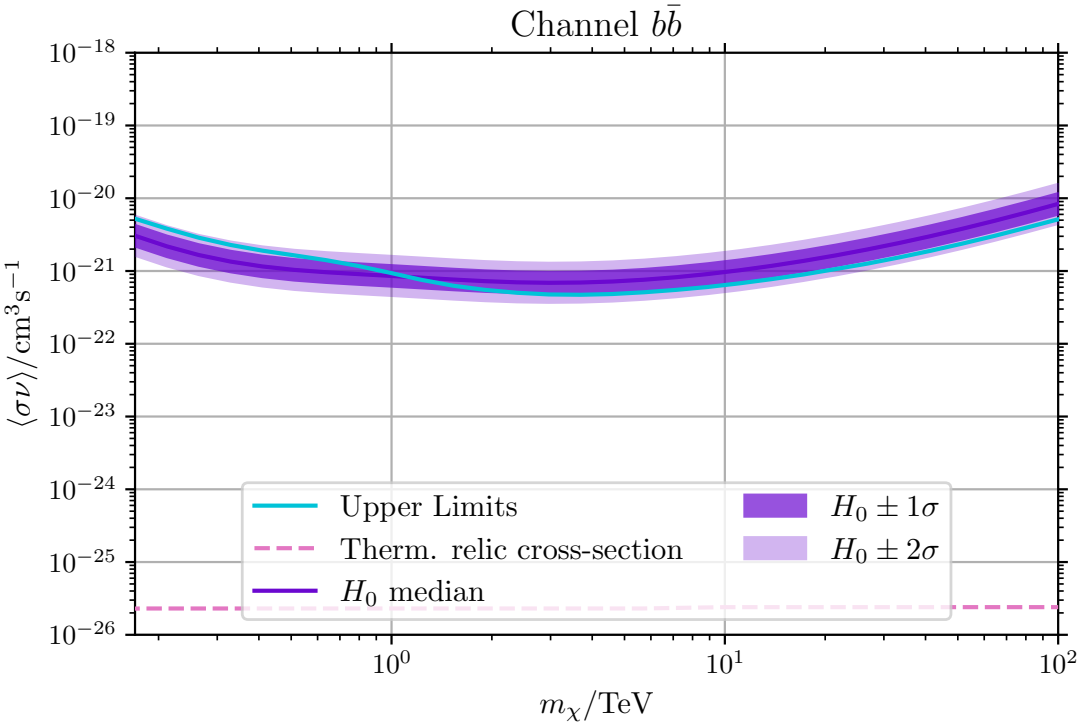

Figure 7.21: CL_s ULs on the thermally averaged cross-section for annihilating DM into $b\bar{b}$ from $m_\chi = 0.17\,\mathrm{TeV}$ to $m_\chi = 100\,\mathrm{TeV}$. The limits are calculated using Asimov datasets on the 1D reduced CBe dSph observations. The ULs for the null hypothesis H_0 are calculated with one Asimov dataset per model.

Figure 7.22 and Figure 7.23 display the CL_s ULs for the DL4 cube together with the MAGIC reference introduced in Section 7.3. The J_{GS} scaled sensitivity outperforms the 1D classical $CL_{\mathrm{s+b}}$ limits except for the $\mu^+\mu^-$ and $\tau^+\tau^-$ channel above $m_\chi > 8\,\mathrm{TeV}$ and $m_\chi > 13\,\mathrm{TeV}$, respectively. It is noted that the stacked DL4 cube encompasses half of the events in comparison to the reference, due to the strict quality cuts applied in Section 6.1.

Furthermore, the ratios between the CL_{s} and $CL_{\mathrm{s+b}}$ limits are displayed in Figure 7.24. The ratios for the null hypothesis H_0 in both the 1D and 3D cases demonstrate a constant shift of the ULs, resulting in more conservative limits.

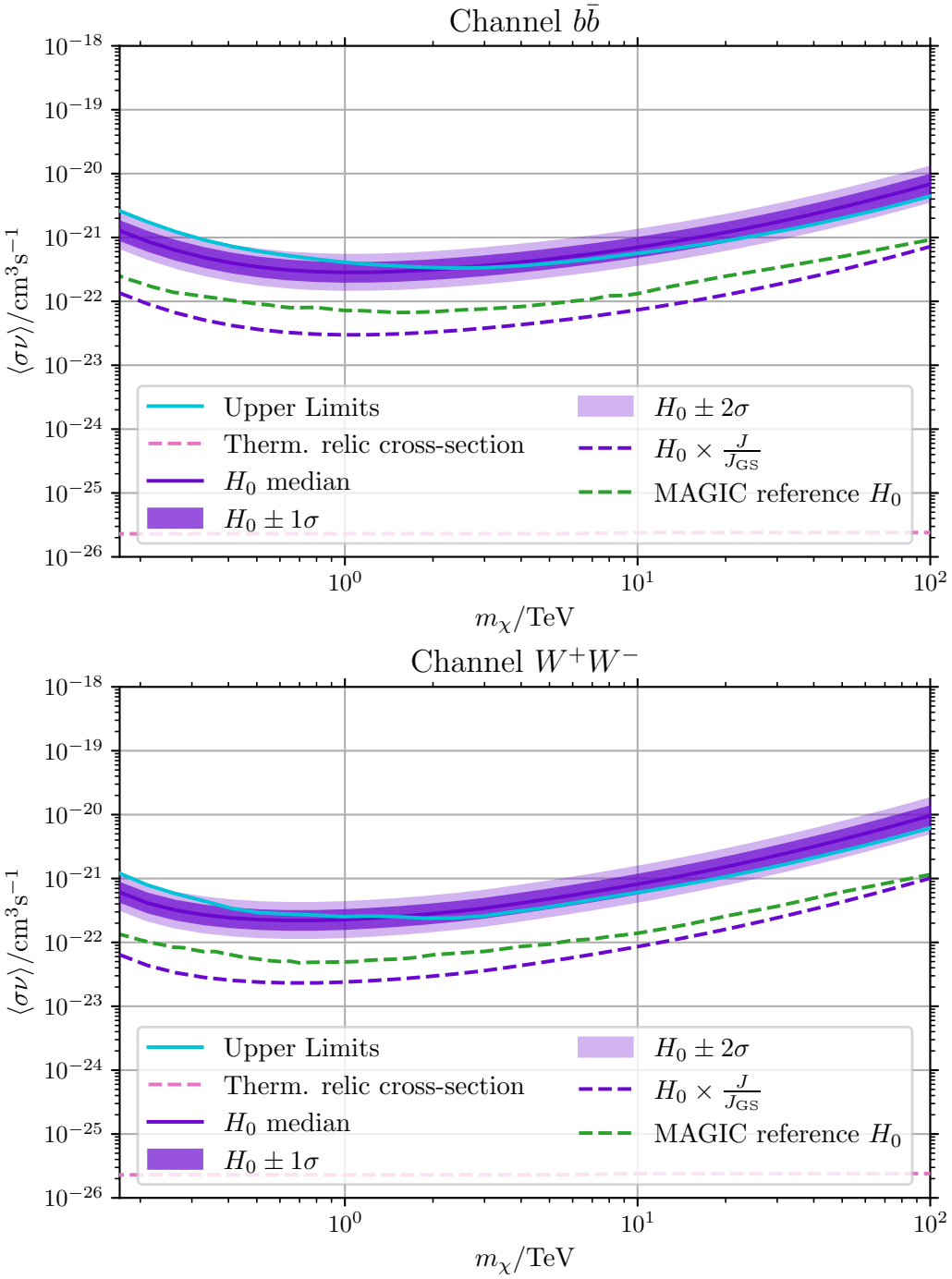

Figure 7.22: CL_s ULs on the thermally averaged cross-section for annihilating DM into $b\bar{b}$ and W^+W^- from $m_\chi = 0.17\,\mathrm{TeV}$ to $m_\chi = 100\,\mathrm{TeV}$. The limits are calculated using Asimov datasets on the CBe dSph DL4 cube. MAGIC reference taken from [14]. H_0 median scaled with the J-Factor from [186] is displayed as a dashed line.

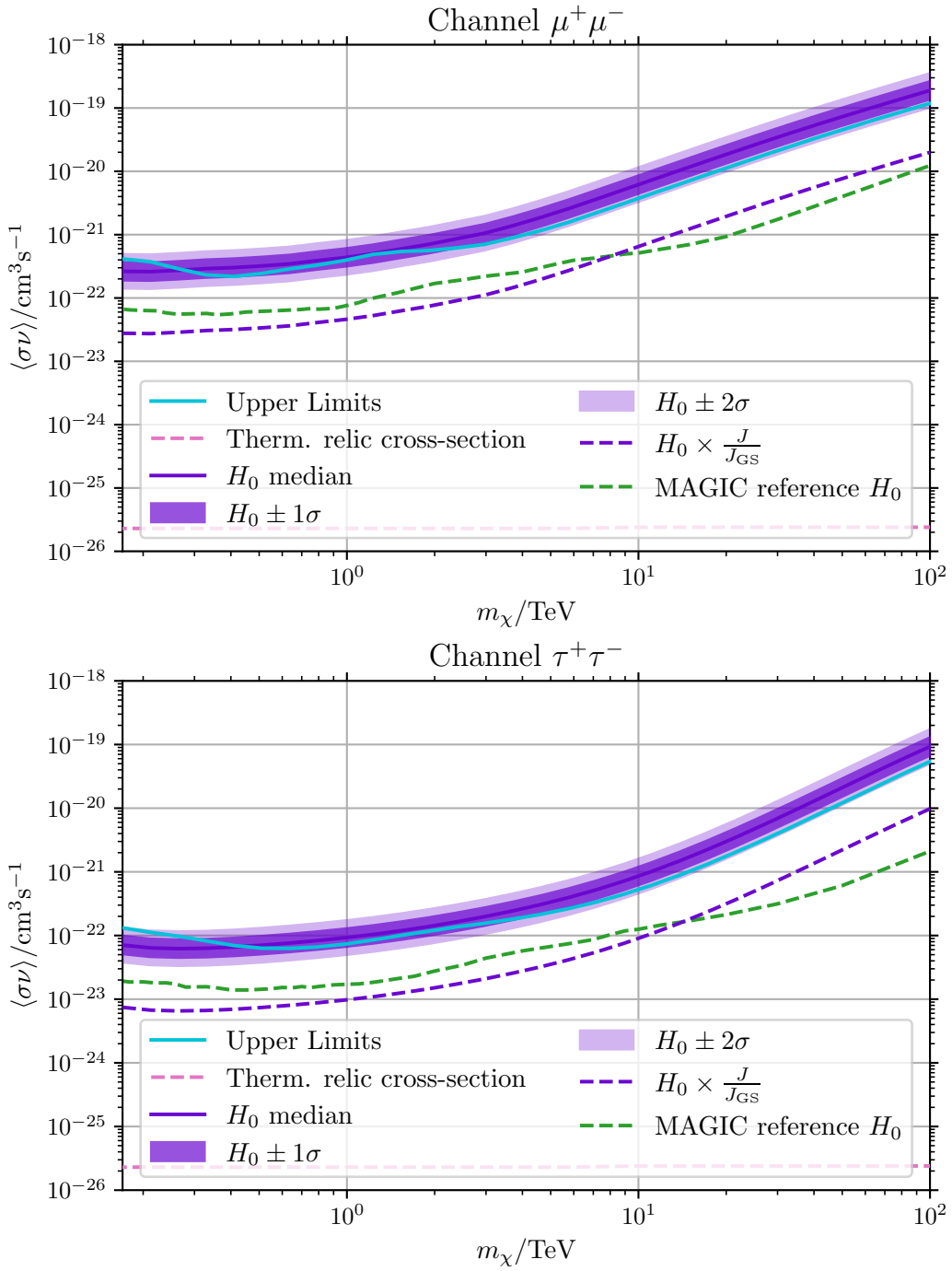

Figure 7.23: CL_s ULs on the thermally averaged cross-section for annihilating DM into $\mu^+\mu^-$ and $\tau^+\tau^-$ from $m_\chi = 0.17\,\mathrm{TeV}$ to $m_\chi = 100\,\mathrm{TeV}$. The limits are calculated using Asimov datasets on the CBe dSph DL4 cube. MAGIC reference taken from [14]. H_0 median scaled with the J-Factor from [186] is displayed as a dashed line.

Additionally, a correction of the ULs is observed on the DL4 cube for all channels and masses. Overall, this indicates a smaller sensitivity for the signal model in this region, arising from p_b being larger than zero, i.e. the distributions of the TS in the signal plus background case and the background-only case are closer together.

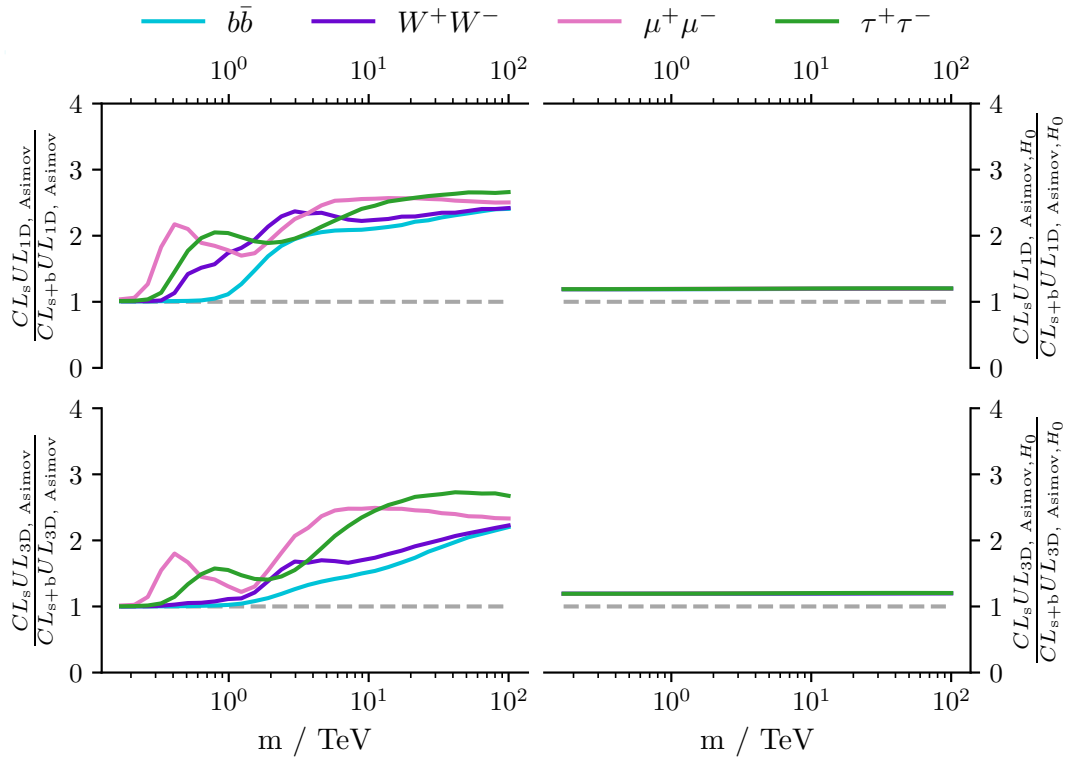

Figure 7.24: Ratios of the CL_{s} and $CL_{\mathrm{s+b}}$ Asimov ULs. **Top/Bottom:** Ratio calculated on 1D reduced observations and DL4 cube. **Left/Right**: Ratio calculated on measured datasets and null hypothesis H_0 datasets.

8 Conclusion and Future Prospects

Gamma-ray signals induced by high-density DM regions, such as dwarf galaxies, offer insights into the particles that shaped the structure of our universe. These signals traverse the cosmos to potentially reach Earth, where they deposit their energy in the atmosphere, which acts as a large calorimeter observable by IACTs. The presented thesis utilizes approximately 50 h of CBe dSph observations taken by MAGIC between 30/01/2019 and 04/06/2019, to search for annihilating WIMP DM.

For the first time, a three-dimensional analysis of DL3 data has been performed for a MAGIC dwarf galaxy target. This analysis required the development of novel methods to access and leverage the information contained in the additional spatial dimensions of the data.
First, the *exclusion-rotation* method is proposed for background modelling to generate full-enclosure IRFs. To validate this method, a new cross-check on Crab Nebula data is introduced, going beyond the MAGIC requirements of a reproducible SED from one-dimensional (energy-only) data.
The new set of full-enclosure IRFs is employed to model and fit the DM signal arising from CBe dSph. With the DL4 cube containing 180000 bins, a fast, efficient, and robust method for statistical testing has to be adopted. In this first-ever three-dimensional search for DM on MAGIC data, *Asimov* datasets are utilized to approximate the TS, and the implemented methods are made available to the gamma-ray community through the open-source Python package `TITRATE`. Moreover, for the first time, the CL_s method is performed for UL calculation on the thermally averaged cross-section in the context of MAGIC analyses.

The presented analysis does not find evidence for gamma rays induced by DM in CBe dSph. ULs on the thermally averaged cross-section for WIMPs masses between 0.17 TeV and 100 TeV annihilating to $b\bar{b}$, W^+W^-, $\mu^+\mu^-$, and $\tau^+\tau^-$ are set. Notably, the three-dimensional sensitivity outperforms the one-dimensional sensitivity. The Asimov datasets exhibit comparable performance to the approx-

imation by Wilks' theorem while requiring significantly fewer computational resources. The ULs on the stacked DL4 cube do not exclude any DM models and deviate from the expected limits due to systematic effects in the background model. The use of the CL_s method provides more conservative ULs on the thermally averaged cross-section and its three-dimensional exclusion sensitivity outperforms the published sensitivity for all channels and masses, except for the annihilation to $\mu^+\mu^-$ and $\tau^+\tau^-$ above $m_\chi > 8\,\mathrm{TeV}$ and $m_\chi > 13\,\mathrm{TeV}$, respectively, when scaled to the J-Factor used in the previous study by MAGIC [14].

The analysis at hand achieved multiple milestones in modern gamma-ray astronomy by advancing background modelling techniques necessary for the search for faint signals, and employing novel methods – Asimov datasets – for statistical testing while benefiting from efficient computation for sustainability.
Nevertheless, three key avenues for refining this analysis are identified:

J-Factor The three-dimensional ULs presented in this work rely on the J-Factor map computed from the median profile parameters provided by [186]. A comparison to the median J-Factor in the one-dimensional analysis published by MAGIC [14] is achievable through a linear scaling of the ULs, which naturally introduces a bias. In future work, this bias could be mitigated by conducting an extensive study of the DM content in CBe dSph to improve the modelling of the J-Factor.

Systematics The DM analysis chain presented does not incorporate systematic uncertainties arising from the measurement process, gamma-ray reconstruction, background modelling, or theoretical uncertainties of the DM spectra. Future extensions of this work should include a detailed investigation of these effects and the modification of the fitting procedure to account for the additional NPs.

Multi-channel analysis Although the sensitivity for DM searches has improved, the exclusion of DM models was not achieved in this work. Expanding the dataset with additional observations of other dwarf galaxies observed by MAGIC and other instruments such as Fermi-LAT or the future CTAO could significantly enhance the sensitivity. Furthermore, incorporating multiple channels of WIMP annihilation products, for example radio signals and neutrino signals, is particularly promising for advancing the field in the context of MMA. With the Asimov approximations at hand, the computational effort required for such a complex analysis is brought to a minimum.

Bibliography

[1] F. Zwicky. "Die Rotverschiebung von extragalaktischen Nebeln". In: *Helv. Phys. Acta* 6 (1933). DOI: 10.1007/s10714-008-0707-4.

[2] F. Zwicky. "On the Masses of Nebulae and of Clusters of Nebulae". In: *Astrophys. J.* 86 (1937). DOI: 10.1086/143864.

[3] V. C. Rubin, W. K. Ford Jr., and N. Thonnard. "Extended rotation curves of high-luminosity spiral galaxies. IV. Systematic dynamical properties, Sa through Sc". In: *Astrophys. J. Lett.* 225 (1978). DOI: 10.1086/182804.

[4] G. Jungman, M. Kamionkowski, and K. Griest. "Supersymmetric dark matter". In: *Phys. Rept.* 267 (1996). DOI: 10.1016/0370-1573(95)00058-5.

[5] L. Bergström. "Nonbaryonic dark matter: Observational evidence and detection methods". In: *Rept. Prog. Phys.* 63 (2000). DOI: 10.1088/0034-4885/63/5/2r3.

[6] V. F. Hess. "Über Beobachtungen der durchdringenden Strahlung bei sieben Freiballonfahrten". In: *Phys. Z.* 13 (1912).

[7] T. Inada et al. "Search for gamma-ray line emission from Dark Matter annihilation in the Galactic Centre with the MAGIC telescopes". In: *J. Phys. Conf. Ser.* 2156 (2021). DOI: 10.1088/1742-6596/2156/1/012063.

[8] T. Miener et al. "Combined search in dwarf spheroidal galaxies for branon dark matter annihilation signatures with the MAGIC Telescopes". In: *PoS* Gamma 2022 (2024). DOI: 10.22323/1.417.0196.

[9] V. A. Acciari et al. "Constraining Dark Matter lifetime with a deep gamma-ray survey of the Perseus Galaxy Cluster with MAGIC". In: *Phys. Dark Univ.* 22 (2018). DOI: 10.1016/j.dark.2018.08.002.

[10] L. M. Linhoff. "Multiwavelength analysis of the TeV-radio galaxy 3C 84/NGC 1275". PhD thesis. TU Dortmund University, 2021. DOI: 10.17877/DE290R-22408.

[11] A. Donath et al. "Gammapy: A Python package for gamma-ray astronomy". In: *A&A* 678 (2023). DOI: 10.1051/0004-6361/202346488. URL: https://doi.org/10.1051/0004-6361/202346488.

[12] S. Fröse. *TITRATE v0.5.1*. Version v0.5.1. 2025. DOI: 10.5281/zenodo.14749273.

[13] C. Nigro, T. Hassan, and L. Olivera-Nieto. "Evolution of Data Formats in Very-High-Energy Gamma-Ray Astronomy". In: *Universe* 7 (2021). DOI: 10.3390/universe7100374.

[14] V. A. Acciari et al. "Combined searches for dark matter in dwarf spheroidal galaxies observed with the MAGIC telescopes, including new data from Coma Berenices and Draco". In: *Phys. Dark Univ.* 35 (2022). DOI: 10.1016/j.dark.2021.100912.

[15] *Cosmic History*. NASA. 2025. URL: https://science.nasa.gov/universe/overview/ (visited on 2025-01-02).

[16] N. Deruelle, J.-P. Uzan, and P. de Forcrand-Millard. *Relativity in Modern Physics*. Oxford University Press, 2018. DOI: 10.1093/oso/9780198786399.001.0001.

[17] A. R. Liddle and D. H. Lyth. *Cosmological Inflation and Large-Scale Structure*. Cambridge University Press, 2000.

[18] A. H. Guth. "Inflationary universe: A possible solution to the horizon and flatness problems". In: *Phys. Rev. D* 23 (1981). DOI: 10.1103/PhysRevD.23.347.

[19] E. W. Kolb and M. S. Turner. "The early Universe". In: *Nature* 294 (1981). DOI: https://doi.org/10.1038/294521a0.

[20] E. W. Kolb and M. S. Turner. "Grand Unified Theories and the Origin of the Baryon Asymmetry". In: *Annual Review of Nuclear and Particle Science* 33 (1983). DOI: https://doi.org/10.1146/annurev.ns.33.120183.003241.

[21] B. Ryden. *Introduction to Cosmology*. Cambridge University Press, 2017.

[22] M. S. Turner. "Dark Matter and Dark Energy in the Universe". In: *Physica Scripta Volume T* 85 (2000). DOI: 10.1238/Physica.Topical.085a00210.

[23] C. W. Misner et al. *Gravitation*. Princeton University Press, 2018.

[24] A. G. Riess et al. "Observational Evidence from Supernovae for an Accelerating Universe and a Cosmological Constant". In: *Astron. J.* 116 (1998). DOI: 10.1086/300499.

[25] P. J. Steinhardt. "A quintessential introduction to dark energy". In: *Phil. Trans. Roy. Soc. Lond. A* 361 (2003). DOI: 10.1098/rsta.2003.1290.

[26] N. Straumann. "Dark Energy: Recent Developments". In: *Mod. Phys. Lett. A* 21 (2006). DOI: 10.1142/S0217732306020573.

[27] A. A. Penzias and R. W. Wilson. "A Measurement of Excess Antenna Temperature at 4080 Mc/s". In: *Astrophys J.* 142 (1965). DOI: 10.1086/148307.

[28] G. F. Smoot et al. "Structure in the COBE differential microwave radiometer first year maps". In: *Astrophys. J. Lett.* 396 (1992). DOI: 10.1086/186504.

[29] R. K. Sachs and A. M. Wolfe. "Perturbations of a cosmological model and angular variations of the microwave background". In: *Astrophys. J.* 147 (1967). DOI: 10.1007/s10714-007-0448-9.

[30] C. L. Bennett et al. "Nine-Year Wilkinson Microwave Anisotropy Probe (WMAP) Observations: Final Maps and Results". In: *Astrophys. J. Suppl.* 208 (2013). DOI: 10.1088/0067-0049/208/2/20.

[31] Y. Akrami et al. "Planck 2018 results. IV. Diffuse component separation". In: *A&A* 641 (2020). DOI: 10.1051/0004-6361/201833881.

[32] R. Laureijs et al. *Euclid Definition Study Report*. 2011. arXiv: 1110.3193 [astro-ph.CO].

[33] M. Bartelmann and P. Schneider. "Weak gravitational lensing". In: *Phys. Rept.* 340 (2001). DOI: 10.1016/S0370-1573(00)00082-X.

[34] K. Umetsu et al. "The Mass Structure of the Galaxy Cluster Cl0024+1654 from a Full Lensing Analysis of Joint Subaru and ACS/NIC3 Observations". In: *Astrophys. J.* 714 (2010). DOI: 10.1088/0004-637X/714/2/1470.

[35] M. Milgrom. "A Modification of the Newtonian dynamics as a possible alternative to the hidden mass hypothesis". In: *Astrophys. J.* 270 (1983). DOI: 10.1086/161130.

[36] D. Clowe et al. "A direct empirical proof of the existence of dark matter". In: *Astrophys. J. Lett.* 648 (2006). DOI: 10.1086/508162.

[37] J. M. Oschmann and L. M. Stepp, eds. *The Magellan Telescopes*. Vol. 4837. SPIE Conference Series. 2003. DOI: 10.1117/12.457909.

[38] *The Hubble Space Telescope*. NASA. 2025. URL: https://science.nasa.gov/mission/hubble/ (visited on 2025-01-06).

[39] M. C. Weisskopf. "The Chandra X-Ray Observatory: Progress Report and Highlights". In: *Proc. SPIE Int. Soc. Opt. Eng.* 8443 (2012). Ed. by T. Takahashi, S. S. Murray, and J.-W. A. den Herder. DOI: 10.1117/12.929670.

[40] D. Baade et al. "The Wide Field Imager at the 2.2-m MPG/ESO telescope: first views with a 67-million-facette eye." In: *The Messenger* 95 (1999).

[41] *The Bullet Cluster*. X-ray: NASA/CXC/CfA/M.Markevitch, Optical and lensing map: NASA/STScI, Magellan/U.Arizona/D.Clowe, Lensing map: ESO WFI. 2025. URL: https://www.esa.int/ESA_Multimedia/Images/2007/07/The_Bullet_Cluster2 (visited on 2025-01-03).

[42] J. E. Kim and G. Carosi. "Axions and the Strong CP Problem". In: *Rev. Mod. Phys.* 82 (2010). [Erratum: *Rev. Mod. Phys.* 91, 049902 (2019)]. DOI: 10.1103/RevModPhys.82.557.

[43] R. D. Peccei and H. R. Quinn. "CP Conservation in the Presence of Pseudoparticles". In: *Phys. Rev. Lett.* 38 (1977). DOI: 10.1103/PhysRevLett.38.1440. URL: https://link.aps.org/doi/10.1103/PhysRevLett.38.1440.

[44] J. E. Kim. "Weak Interaction Singlet and Strong CP Invariance". In: *Phys. Rev. Lett.* 43 (1979). DOI: 10.1103/PhysRevLett.43.103.

[45] M. A. Shifman, A. I. Vainshtein, and V. I. Zakharov. "Can Confinement Ensure Natural CP Invariance of Strong Interactions?" In: *Nucl. Phys. B* 166 (1980). DOI: 10.1016/0550-3213(80)90209-6.

[46] P. Svrcek and E. Witten. "Axions In String Theory". In: *JHEP* 06 (2006). DOI: 10.1088/1126-6708/2006/06/051.

[47] C. O'HARE. *cajohare/AxionLimits: AxionLimits*. Version v1.0. 2020. DOI: 10.5281/zenodo.3932430.

[48] P. F. Depta, M. Hufnagel, and K. Schmidt-Hoberg. "Robust cosmological constraints on axion-like particles". In: *JCAP* 05 (2020). DOI: 10.1088/1475-7516/2020/05/009.

[49] K. Langhoff, N. J. Outmezguine, and N. L. Rodd. "Irreducible Axion Background". In: *Phys. Rev. Lett.* 129 (2022). DOI: 10.1103/PhysRevLett.129.241101.

[50] P. Arias et al. "WISPy Cold Dark Matter". In: *JCAP* 06 (2012). DOI: 10.1088/1475-7516/2012/06/013.

[51] J. W. Brockway, E. D. Carlson, and G. G. Raffelt. "SN1987A gamma-ray limits on the conversion of pseudoscalars". In: *Phys. Lett. B* 383 (1996). DOI: 10.1016/0370-2693(96)00778-2.

[52] J. A. Grifols, E. Masso, and R. Toldra. "Gamma-rays from SN1987A due to pseudoscalar conversion". In: *Phys. Rev. Lett.* 77 (1996). DOI: 10.1103/PhysRevLett.77.2372.

[53] M. Meyer and T. Petrushevska. "Search for Axionlike-Particle-Induced Prompt γ-Ray Emission from Extragalactic Core-Collapse Supernovae with the *Fermi* Large Area Telescope". In: *Phys. Rev. Lett.* 124 (2020). [Erratum: *Phys. Rev. Lett.* 125, 119901 (2020)]. DOI: 10.1103/PhysRevLett.124.231101.

[54] H. Abe et al. "Constraints on axion-like particles with the Perseus Galaxy Cluster with MAGIC". In: *Phys. Dark Univ.* 44 (2024). DOI: 10.1016/j.dark.2024.101425.

[55] E. Dwek and F. Krennrich. "The Extragalactic Background Light and the Gamma-ray Opacity of the Universe". In: *Astropart. Phys.* 43 (2013). DOI: 10.1016/j.astropartphys.2012.09.003.

[56] P. Gondolo and G. Gelmini. "Cosmic abundances of stable particles: Improved analysis". In: *Nucl. Phys. B* 360 (1991). DOI: 10.1016/0550-3213(91)90438-4.

[57] G. Steigman, B. Dasgupta, and J. F. Beacom. "Precise Relic WIMP Abundance and its Impact on Searches for Dark Matter Annihilation". In: *Phys. Rev. D* 86 (2012). DOI: 10.1103/PhysRevD.86.023506.

[58] N. Aghanim et al. "Planck 2018 results. VI. Cosmological parameters". In: *A&A* 641 (2020). [Erratum: *A&A* 652, C4 (2021)]. DOI: 10.1051/0004-6361/201833910.

[59] J. L. Feng. "The WIMP paradigm: Theme and variations". In: *SciPost Phys. Lect. Notes* 71 (2023). DOI: 10.21468/SciPostPhysLectNotes.71.

[60] C. Csaki. "The Minimal supersymmetric standard model (MSSM)". In: *Mod. Phys. Lett. A* 11 (1996). DOI: 10.1142/S021773239600062X.

[61] H. Abe et al. “Search for Gamma-Ray Spectral Lines from Dark Matter Annihilation up to 100 TeV toward the Galactic Center with MAGIC”. In: *Phys. Rev. Lett.* 130 (2023). DOI: 10.1103/PhysRevLett.130.061002.

[62] H. Abdallah et al. “Search for γ-Ray Line Signals from Dark Matter Annihilations in the Inner Galactic Halo from 10 Years of Observations with H.E.S.S.” In: *Phys. Rev. Lett.* 120 (2018). DOI: 10.1103/PhysRevLett.120.201101.

[63] M. Ackermann et al. “Fermi LAT Search for Dark Matter in Gamma-ray Lines and the Inclusive Photon Spectrum”. In: *Phys. Rev. D* 86 (2012). DOI: 10.1103/PhysRevD.86.022002.

[64] J. W. Foster et al. “Search for dark matter lines at the Galactic Center with 14 years of Fermi data”. In: *Phys. Rev. D* 107 (2023). DOI: 10.1103/PhysRevD.107.103047.

[65] F. Ferrer, L. M. Krauss, and S. Profumo. “Indirect detection of light neutralino dark matter in the NMSSM”. In: *Phys. Rev. D* 74 (2006). DOI: 10.1103/PhysRevD.74.115007.

[66] L. Bergstrom and P. Ullio. “Full one loop calculation of neutralino annihilation into two photons”. In: *Nucl. Phys. B* 504 (1997). DOI: 10.1016/S0550-3213(97)00530-0.

[67] T. Bringmann and C. Weniger. “Gamma Ray Signals from Dark Matter: Concepts, Status and Prospects”. In: *Phys. Dark Univ.* 1 (2012). DOI: 10.1016/j.dark.2012.10.005.

[68] T. R. Slatyer. “Indirect detection of dark matter.” In: *Theoretical Advanced Study Institute in Elementary Particle Physics: Anticipating the Next Discoveries in Particle Physics*. 2018. DOI: 10.1142/9789813233348_0005.

[69] J. Billard et al. “Direct detection of dark matter—APPEC committee report*”. In: *Rept. Prog. Phys.* 85 (2022). DOI: 10.1088/1361-6633/ac5754.

[70] R. F. Lang. “The CRESST-II Experiment”. In: *43rd Rencontres de Moriond on Electroweak Interactions and Unified Theories*. 2008. arXiv: 0805.4705 [astro-ph].

[71] M. Mancuso et al. “Searches for Light Dark Matter with the CRESST-III Experiment”. In: *J. Low Temp. Phys.* 199 (2020). DOI: 10.1007/s10909-020-02343-3.

[72] E. Aprile et al. “The XENON1T Dark Matter Experiment”. In: *Eur. Phys. J. C* 77 (2017). DOI: 10.1140/epjc/s10052-017-5326-3.

[73] E. Aprile et al. “The XENONnT dark matter experiment”. In: *Eur. Phys. J. C* 84 (2024). DOI: 10.1140/epjc/s10052-024-12982-5.

[74] V. Sanglard. “The EDELWEISS experiment and Dark Matter Direct Detection”. In: 2003. arXiv: astro-ph/0306233.

[75] E. Armengaud et al. “Performance of the EDELWEISS-III experiment for direct dark matter searches”. In: *JINST* 12 (2017). DOI: 10.1088/1748-0221/12/08/P08010.

[76] E. Aprile et al. “First Search for Light Dark Matter in the Neutrino Fog with XENONnT”. In: (Sept. 2024). arXiv: 2409.17868 [hep-ex].

[77] A. Vartak. *Dark matter search in CMS. Dark matter searches at the CMS experiment*. Tech. rep. 2017. URL: https://cds.cern.ch/record/2271096.

[78] A. Elliot. “Dark matter searches with the ATLAS detector”. In: *EPJ Web Conf.* 158 (2017). Ed. by P. Mandrik. DOI: 10.1051/epjconf/201715801007.

[79] T. Mombächer. “Dark matter searches at LHCb”. In: *PoS* EPS-HEP2021 (2022). DOI: 10.22323/1.398.0185. arXiv: 2111.00306 [hep-ex].

[80] A. W. McConnachie. “The observed properties of dwarf galaxies in and around the Local Group”. In: *Astron. J.* 144 (2012). DOI: 10.1088/0004-6256/144/1/4.

[81] J. Grcevich and M. E. Putman. “HI in Local Group Dwarf Galaxies and Stripping by the Galactic Halo”. In: *Astrophys. J.* 696 (2009). [Erratum: *Astrophys. J.* 721, 922 (2010)]. DOI: 10.1088/0004-637X/721/1/922.

[82] A. Dominguez et al. “Extragalactic Background Light Inferred from AEGIS Galaxy SED-type Fractions”. In: *Mon. Not. Roy. Astron. Soc.* 410 (2011). DOI: 10.1111/j.1365-2966.2010.17631.x.

[83] A. Charbonnier et al. “Dark matter profiles and annihilation in dwarf spheroidal galaxies: prospectives for present and future gamma-ray observatories - I. The classical dSphs”. In: *Mon. Not. Roy. Astron. Soc.* 418 (2011). DOI: 10.1111/j.1365-2966.2011.19387.x.

[84] M. Cirelli et al. “PPPC 4 DM ID: A Poor Particle Physicist Cookbook for Dark Matter Indirect Detection”. In: *JCAP* 03 (2011). [Erratum: *JCAP* 10, E01 (2012)]. DOI: 10.1088/1475-7516/2012/10/E01.

[85] C. W. Bauer, N. L. Rodd, and B. R. Webber. “Dark matter spectra from the electroweak to the Planck scale”. In: *JHEP* 06 (2021). DOI: 10.1007/JHEP06(2021)121.

[86] C. Arina et al. “CosmiXs: cosmic messenger spectra for indirect dark matter searches”. In: *JCAP* 03 (2024). DOI: 10.1088/1475-7516/2024/03/035.

[87] J. Binney and S. Tremaine. *Galactic Dynamics*. Princeton University Press, 2008.

[88] K. G. Begeman, A. H. Broeils, and R. H. Sanders. “Extended rotation curves of spiral galaxies: Dark haloes and modified dynamics”. In: *Mon. Not. Roy. Astron. Soc.* 249 (1991). DOI: 10.1093/mnras/249.3.523.

[89] A. Burkert. “The Structure of dark matter halos in dwarf galaxies”. In: *Astrophys. J. Lett.* 447 (1995). DOI: 10.1086/309560.

[90] J. F. Navarro, C. S. Frenk, and S. D. M. White. “A Universal density profile from hierarchical clustering”. In: *Astrophys. J.* 490 (1997). DOI: 10.1086/304888.

[91] J. Einasto. “On the Construction of a Composite Model for the Galaxy and on the Determination of the System of Galactic Parameters”. In: *Trudy Astrofizicheskogo Instituta Alma-Ata* 5 (1965).

[92] A. W. Graham et al. “Empirical models for Dark Matter Halos. I. Nonparametric Construction of Density Profiles and Comparison with Parametric Models”. In: *Astron. J.* 132 (2006). DOI: 10.1086/508988.

[93] J. Diemand, B. Moore, and J. Stadel. “Convergence and scatter of cluster density profiles”. In: *Mon. Not. Roy. Astron. Soc.* 353 (2004). DOI: 10.1111/j.1365-2966.2004.08094.x.

[94] H. Zhao. “Analytical models for galactic nuclei”. In: *Mon. Not. Roy. Astron. Soc.* 278 (1996). DOI: 10.1093/mnras/278.2.488.

[95] W. J. G. de Blok. “The Core-Cusp Problem”. In: *Adv. Astron.* 2010 (2010). DOI: 10.1155/2010/789293.

[96] B. Moore et al. “Dark matter substructure within galactic halos”. In: *Astrophys. J. Lett.* 524 (1999). DOI: 10.1086/312287.

[97] A. Knierim. *aknierim/TikZ_assortment: Published version of TikZ graphics/source code*. Version v1.1. 2024. DOI: 10.5281/zenodo.11092754.

[98] M. G. Aartsen et al. “The IceCube Neutrino Observatory: Instrumentation and Online Systems”. In: *JINST* 12 (2017). [Erratum: *JINST* 19, E05001 (2024)]. DOI: 10.1088/1748-0221/12/03/P03012.

[99] B. P. Abbott et al. “Multi-messenger Observations of a Binary Neutron Star Merger”. In: *Astrophys. J. Lett.* 848 (2017). DOI: 10.3847/2041-8213/aa91c9.

[100] H. P. Dembinski et al. “Data-driven model of the cosmic-ray flux and mass composition from 10 GeV to 10^{11} GeV”. In: *PoS* International Cosmic Ray Conference (2017). DOI: 10.22323/1.301.0533. arXiv: 1711.11432 [astro-ph.HE].

[101] P. N. Best and T. M. Heckman. “On the fundamental dichotomy in the local radio-AGN population: accretion, evolution, and host galaxy properties”. In: *Mon. Not. Roy. Astron. Soc.* 421 (2012). DOI: 10.1111/j.1365-2966.2012.20414.x.

[102] K. Akiyama et al. “First M87 Event Horizon Telescope Results. I. The Shadow of the Supermassive Black Hole”. In: *Astrophys. J. Lett.* 875 (2019). DOI: 10.3847/2041-8213/ab0ec7.

[103] B. S. Acharya et al. *Science with the Cherenkov Telescope Array*. WSP, 2018. DOI: 10.1142/10986.

[104] W. B. Atwood et al. “The Large Area Telescope on the Fermi Gamma-ray Space Telescope Mission”. In: *Astrophys. J.* 697 (2009). DOI: 10.1088/0004-637X/697/2/1071.

[105] H. Abdalla et al. “The H.E.S.S. Galactic plane survey”. In: *A&A* 612 (2018). DOI: 10.1051/0004-6361/201732098.

[106] J. Aleksić et al. “The major upgrade of the MAGIC telescopes, Part II: A performance study using observations of the Crab Nebula”. In: *Astropart. Phys.* 72 (2016). DOI: 10.1016/j.astropartphys.2015.02.005.

[107] F. Jansen et al. “XMM-Newton observatory. I. The spacecraft and operations.” In: *A&A* 365 (2001). DOI: 10.1051/0004-6361:20000036.

[108] J. P. Gardner et al. “The James Webb Space Telescope”. In: *Space Sci. Rev.* 123 (2006). DOI: 10.1007/s11214-006-8315-7.

[109] J. Tauber et al., eds. *The Scientific programme of Planck*. 2006. arXiv: astro-ph/0604069.

[110] T. K. Gaisser, T. Stanev, and S. Tilav. “Cosmic Ray Energy Spectrum from Measurements of Air Showers”. In: *Front. Phys. (Beijing)* 8 (2013). DOI: 10.1007/s11467-013-0319-7.

[111] J. C. Arteaga Velazquez et al. “The Pierre Auger Observatory”. In: *AIP Conf. Proc.* 670 (2003). Ed. by L. Villasenor and V. Villanueva. DOI: 10.1063/1.1594374.

[112] H. Kawai et al. “Telescope array experiment”. In: *Nucl. Phys. B Proc. Suppl.* 175-176 (2008). Ed. by K. S. Cheng et al. DOI: 10.1016/j.nuclphysbps.2007.11.002.

[113] M. G. Aartsen et al. “Multimessenger observations of a flaring blazar coincident with high-energy neutrino IceCube-170922A”. In: *Science* 361 (2018). DOI: 10.1126/science.aat1378.

[114] R. Abbasi et al. “Evidence for neutrino emission from the nearby active galaxy NGC 1068”. In: *Science* 378 (2022). DOI: 10.1126/science.abg3395.

[115] A. Einstein. “Näherungsweise Integration der Feldgleichungen der Gravitation”. In: *Sitzungsberichte der Königlich Preussischen Akademie der Wissenschaften* (1916).

[116] A. Einstein. “Über Gravitationswellen”. In: *Sitzungsberichte der Königlich Preussischen Akademie der Wissenschaften* (1918).

[117] B. P. Abbott et al. “Observation of Gravitational Waves from a Binary Black Hole Merger”. In: *Phys. Rev. Lett.* 116 (2016). DOI: 10.1103/PhysRevLett.116.061102.

[118] P. Amaro-Seoane et al. “Laser Interferometer Space Antenna”. In: (2017). arXiv: 1702.00786 [astro-ph.IM].

[119] M. Maggiore et al. “Science Case for the Einstein Telescope”. In: *JCAP* 03 (2020). DOI: 10.1088/1475-7516/2020/03/050.

[120] J. Matthews. “A Heitler model of extensive air showers”. In: *Astropart. Phys.* 22 (2005). DOI: 10.1016/j.astropartphys.2004.09.003.

[121] K.-H. Kampert and A. A. Watson. "Extensive Air Showers and Ultra High-Energy Cosmic Rays: A Historical Review". In: *Eur. Phys. J. H* 37 (2012). DOI: 10.1140/epjh/e2012-30013-x.

[122] W. Heitler. *The quantum theory of radiation*. Oxford: Oxford University Press, 1954.

[123] R. M. Wagner. "Measurement of Very High Energy Gamma-Ray Emission from Four Blazars Using the MAGIC Telescope and a Comparative Blazar Study". PhD thesis. Munich, Tech. U., 2006.

[124] P. A. Cherenkov. "Visible luminescence of pure liquids under the influence of γ-radiation". In: *Dokl. Akad. Nauk SSSR* 2 (1934). DOI: 10.3367/UFNr.0093.196710n.0385.

[125] I. M. Frank and I. E. Tamm. "Coherent visible radiation of fast electrons passing through matter". In: *Compt. Rend. Acad. Sci. URSS* 14 (1937). Ed. by V. L. Ginzburg, B. M. Bolotovsky, and I. M. Dremin. DOI: 10.3367/UFNr.0093.196710o.0388.

[126] T. M. Shaffer, E. C. Pratt, and J. Grimm. "Utilizing the power of Cerenkov light with nanotechnology". In: *Nature Nanotechnology* 12 (2017). DOI: 10.1038/nnano.2016.301.

[127] C. Baixeras et al. "Commissioning and first tests of the MAGIC telescope". In: *Nucl. Instrum. Meth. A* 518 (2004). Ed. by G. Batignani et al. DOI: 10.1016/j.nima.2003.10.057.

[128] J. Cortina. "Status and First Results of the MAGIC Telescope". In: *Astrophys. Space Sci.* 297 (2005). DOI: 10.1007/s10509-005-7627-5.

[129] P. Colin et al. "Performance of the MAGIC telescopes in stereoscopic mode". In: (2009). arXiv: 0907.0960 [astro-ph.IM].

[130] J. Aleksić et al. "The major upgrade of the MAGIC telescopes, Part I: The hardware improvements and the commissioning of the system". In: *Astropart. Phys.* 72 (2016). DOI: 10.1016/j.astropartphys.2015.04.004.

[131] C.-C. Hsu et al. "The Camera of the MAGIC-II Telescope". In: *International Cosmic Ray Conference*. Vol. 3. 2007. arXiv: 0709.2474 [astro-ph].

[132] S. Mender. "Spectral and spatial analysis of MAGIC telescope data in a standardized format". PhD thesis. TU Dortmund University, 2023. DOI: 10.17877/DE290R-24082.

[133] V. P. Fomin et al. “New methods of atmospheric Cherenkov imaging for gamma-ray astronomy. 1: The False source method”. In: *Astropart. Phys.* 2 (1994). DOI: 10.1016/0927-6505(94)90036-1.

[134] C. Fruck et al. “A novel LIDAR-based Atmospheric Calibration Method for Improving the Data Analysis of MAGIC”. In: *International Cosmic Ray Conference*. 2014. arXiv: 1403.3591 [astro-ph.IM].

[135] G. Lombardi et al. “El Roque de Los Muchachos Site Characteristics. III. Analysis of Atmospheric Dust and Aerosol Extinction”. In: *A&A* 483 (2008). DOI: 10.1051/0004-6361:20078372.

[136] M. Gaug et al. “Atmospheric Monitoring for the MAGIC Telescopes”. In: *International Workshop on Atmospheric Monitoring for High-Energy Astroparticle Detectors*. 2014. arXiv: 1403.5083 [astro-ph.IM].

[137] J. Albert et al. “FADC signal reconstruction for the MAGIC Telescope”. In: *Nucl. Instrum. Meth. A* 594 (2008). DOI: 10.1016/j.nima.2008.06.043.

[138] R. Mirzoyan. “On the Calibration Accuracy of Light Sensors in Atmospheric Cherenkov Fluorescence and Neutrino Experiments”. In: *International Cosmic Ray Conference*. Vol. 7. 1997.

[139] T. Schweizer et al. “The optical calibration of the MAGIC telescope camera”. In: *IEEE Trans. Nucl. Sci.* 49 (2002). Ed. by J. D. Valentine. DOI: 10.1109/TNS.2002.803867.

[140] Y. Kobayashi et al. “Camera Calibration of the CTA-LST prototype”. In: *PoS* International Cosmic Ray Conference (2021). DOI: 10.22323/1.395.0720.

[141] J. Aleksić. “The MAGIC Telescopes”. In: *Optimized Dark Matter Searches in Deep Observations of Segue 1 with MAGIC*. Springer International Publishing, 2016. DOI: 10.1007/978-3-319-23123-5_3.

[142] A. M. Hillas. “Cerenkov Light Images of EAS Produced by Primary Gamma Rays and by Nuclei”. In: *International Cosmic Ray Conference*. Vol. 3. 1985.

[143] J. Albert et al. “Implementation of the Random Forest Method for the Imaging Atmospheric Cherenkov Telescope MAGIC”. In: *Nucl. Instrum. Meth. A* 588 (2008). DOI: 10.1016/j.nima.2007.11.068.

[144] K. Ishio and D. Paneque. "A novel energy reconstruction method for the MAGIC stereoscopic observation". In: *Astropart. Phys.* 158 (2024). DOI: 10.1016/j.astropartphys.2024.102937.

[145] D. Heck et al. *CORSIKA: A Monte Carlo code to simulate extensive air showers*. 1998.

[146] P. Majumdar et al. "Monte Carlo simulation for the MAGIC telescope". In: *International Cosmic Ray Conference*. 2005.

[147] F. Goebel et al. "Absolute energy scale calibration of the MAGIC telescope using muon images". In: *7th Workshop on Towards a Network of Atmospheric Cherenkov Detectors*. 2005.

[148] R. W. Lessard et al. "A New analysis method for reconstructing the arrival direction of TeV gamma-rays using a single imaging atmospheric Cherenkov telescope". In: *Astropart. Phys.* 15 (2001). DOI: 10.1016/S0927-6505(00)00133-X.

[149] A. Moralejo et al. *MARS, the MAGIC Analysis and Reconstruction Software*. 2009. arXiv: 0907.0943 [astro-ph.IM].

[150] R. Zanin. "MARS, the MAGIC analysis and reconstruction software". In: *International Cosmic Ray Conference*. 2013.

[151] J. L. Schubert. "Pulsar analyses with the MAGIC experiment". PhD thesis. TU Dortmund University, 2024. DOI: 10.17877/DE290R-24588.

[152] S. Abe et al. "Standardised formats and open-source analysis tools for the MAGIC telescopes data". In: *JHEAp* 44 (2024). DOI: 10.1016/j.jheap.2024.09.011.

[153] B. S. Acharya et al. "Introducing the CTA concept". In: *Astropart. Phys.* 43 (2013). DOI: 10.1016/j.astropartphys.2013.01.007.

[154] R. A. Ong. "The Cherenkov Telescope Array: Science Goals and Current Status". In: *EPJ Web Conf.* 209 (2019). Ed. by M. De Vincenzi, A. Capone, and A. Morselli. DOI: 10.1051/epjconf/201920901038.

[155] C. Nigro. "Establishing the MAGIC data legacy: adopting standardised data formats and open-source analysis tools". In: *PoS* Gamma 2022 (2023). DOI: 10.22323/1.417.0122.

[156] B. Bruers et al. "Resource-aware research on Universe and Matter: call-to-action in digital transformation". In: *The European Physical Journal Special Topics* (2024). DOI: 10.1140/epjs/s11734-024-01436-4.

[157] D. Berge, S. Funk, and J. Hinton. "Background Modelling in Very-High-Energy gamma-ray Astronomy". In: *A&A* 466 (2007). DOI: 10.1051/0004-6361:20066674.

[158] I. Vovk, M. Strzys, and C. Fruck. "Spatial likelihood analysis for MAGIC telescope data - From instrument response modelling to spectral extraction". In: *A&A* 619 (2018). DOI: 10.1051/0004-6361/201833139.

[159] S. Mender et al. "Computing sky maps using the open-source package Gammapy and MAGIC data in a standardized format". In: *PoS* Gamma 2022 (2023). DOI: 10.22323/1.417.0215.

[160] L. Mohrmann et al. "Validation of open-source science tools and background model construction in γ-ray astronomy". In: *A&A* 632 (2019). DOI: 10.1051/0004-6361/201936452.

[161] T. C. Weekes et al. "VERITAS: The Very energetic radiation imaging telescope array system". In: *Astropart. Phys.* 17 (2002). DOI: 10.1016/S0927-6505(01)00152-9.

[162] G. Maier. *V2DL5-Binary-Analysis - High-level analysis for binary light curves for VERITAS*. Version v0.4.0. DOI: 10.5281/zenodo.12903920.

[163] T. DeYoung. "The HAWC observatory". In: *Nucl. Instrum. Meth. A* 692 (2012). Ed. by A. Capone et al. DOI: 10.1016/j.nima.2012.01.026.

[164] A. Albert et al. "Validation of standardized data formats and tools for ground-level particle-based gamma-ray observatories". In: *A&A* 667 (2022). DOI: 10.1051/0004-6361/202243527.

[165] *How to compute a 3D cube*. Gammapy. 2025. URL: https://docs.gammapy.org/1.3/getting-started/index.html#getting-started (visited on 2025-01-14).

[166] W. Cash. "Parameter estimation in astronomy through application of the likelihood ratio". In: *Astrophys. J.* 228 (1979). DOI: 10.1086/156922.

[167] R. M. Dominik et al. "Interpolation of Instrument Response Functions for the Cherenkov Telescope Array in the Context of pyirf". In: *PoS* International Cosmic Ray Conference (2023). DOI: 10.22323/1.444.0618.

[168] J. Neyman and E. S. Pearson. "On the Problem of the Most Efficient Tests of Statistical Hypotheses". In: *Phil. Trans. Roy. Soc. Lond. A* 231 (1933). DOI: 10.1098/rsta.1933.0009.

[169] S. S. Wilks. "The Large-Sample Distribution of the Likelihood Ratio for Testing Composite Hypotheses". In: *Annals Math. Statist.* 9 (1938). DOI: 10.1214/aoms/1177732360.

[170] G. Cowan et al. "Asymptotic formulae for likelihood-based tests of new physics". In: *Eur. Phys. J. C* 71 (2011). [Erratum: *Eur. Phys. J. C* 73, 2501 (2013)]. DOI: 10.1140/epjc/s10052-011-1554-0.

[171] E. Gross. "Practical Statistics for High Energy Physics". In: *CERN Yellow Rep. School Proc.* 3 (2018). Ed. by M. Mulders and G. Zanderighi. DOI: 10.23730/CYRSP-2018-003.199.

[172] A. L. Read. "Presentation of search results: The CL_s technique". In: *J. Phys. G* 28 (2002). Ed. by M. R. Whalley and L. Lyons. DOI: 10.1088/0954-3899/28/10/313.

[173] F. Acero et al. *Gammapy: Python toolbox for gamma-ray astronomy*. Version v1.2. 2024. DOI: 10.5281/zenodo.10726484.

[174] Astropy Collaboration et al. "The Astropy Project: Sustaining and Growing a Community-oriented Open-source Project and the Latest Major Release (v5.0) of the Core Package". In: *Astrophys. J.* 935 (2022). DOI: 10.3847/1538-4357/ac7c74.

[175] J. Rico et al. *gLike*. Version 00.10.03. 2022. DOI: 10.5281/zenodo.7342721.

[176] T. Miener and D. Nieto. *LklCom: Combining likelihoods from different experiments*. Version v0.5.3. 2021. DOI: 10.5281/zenodo.4597500.

[177] S. Abdollahi et al. "Incremental Fermi Large Area Telescope Fourth Source Catalog". In: *Astrophys. J. Supp.* 260 (2022). DOI: 10.3847/1538-4365/ac6751.

[178] J. Ballet et al. "Fermi Large Area Telescope Fourth Source Catalog Data Release 4 (4FGL-DR4)". In: (2023). arXiv: 2307.12546 [astro-ph.HE].

[179] L. Nickel. "We are number one". PhD thesis. TU Dortmund University, 2024. DOI: 10.17877/DE290R-24492.

[180] M. de Bony de Lavergne et al. *BAccMod*. 2025. URL: https://github.com/mdebony/BAccMod.

[181] T. Temim and J. DePasquale. *Crab Nebula (NIRCam and MIRI Image)*. NASA, ESA, CSA, STScI. 2025. URL: https://webbtelescope.org/contents/media/images/2023/137/01HBBMDH12APPEGB8DXVVEP8XA (visited on 2025-01-17).

[182] V. A. Acciari et al. "MAGIC very large zenith angle observations of the Crab Nebula up to 100 TeV". In: *A&A* 635 (2020). DOI: 10.1051/0004-6361/201936899.

[183] A. A. Abdo et al. "The First Fermi Large Area Telescope Catalog of Gamma-ray Pulsars". In: *Astrophys. J. Suppl.* 187 (2010). [Erratum: *Astrophys. J. Suppl.* 193, 22 (2011)]. DOI: 10.1088/0067-0049/187/2/460.

[184] J. Aleksic et al. "Phase-resolved energy spectra of the Crab Pulsar in the range of 50-400 GeV measured with the MAGIC Telescopes". In: *A&A* 540 (2012). DOI: 10.1051/0004-6361/201118166.

[185] J. Aleksić et al. "Measurement of the Crab Nebula spectrum over three decades in energy with the MAGIC telescopes". In: *JHEA* 5-6 (2015). DOI: 10.1016/j.jheap.2015.01.002.

[186] A. Geringer-Sameth, S. M. Koushiappas, and M. Walker. "Dwarf galaxy annihilation and decay emission profiles for dark matter experiments". In: *Astrophys. J.* 801 (2015). DOI: 10.1088/0004-637X/801/2/74.

Glossary

ADC Analog-to-Digital converter. 31, 32

AGN Active Galactic Nucleus. 19, 20

ALP Axion-Like Particle. 11, 12

Alt Altitude. 69

Alt-Az Altitude and Azimuth. 25, 26, 29, 68, 69, 71, 74

AMC Active Mirror Control. 26

AP Astrophysical. 15, 16, 90

autoMAGIC Automatic Analysis of MAGIC Data. 2, 3, 31, 47, 48, 53, 65, 78, 137

Az Azimuth. 69, 71–74, 78

CBe Coma Berenices. 2, 3, 65–68, 71, 74–76, 78, 82, 85–92, 94–98, 100, 101, 103, 104, 109–111, 113, 114, 137, 142–147, 151, 157, 169, 181, 208, 226

CDF cumulative density function. 58, 61

CDM Cold Dark Matter. 11, 13

CL confidence level. 59, 63, 85, 92, 93, 99, 105, 108–114, 208, 226

CMB Cosmic Microwave Background. 6, 8, 10, 13

coach Compressed Osteria Alias Computation of the Hadronness parameter. 46

COBE Cosmic Background Explorer. 8

CoG Center of Gravity. 36, 42

CORSIKA Cosmic Ray Simulations for Kascade. 38

CR Cosmic Ray. 2, 20–23, 33, 39

CRESST Cryogenic Rare Event Search with Superconducting Thermometers. 15

CTAO Cherenkov Telescope Array Observatory. 47, 53, 114

DAQ Data Acquisition System. 26, 28

DC Dark Current. 65

DEC Declination. 28, 75

DL3 Data Level 3. 3, 31, 45–50, 53–55, 65, 66, 68, 73, 75, 77, 78, 113

DL4 Data Level 4. 53–55, 57, 59–61, 73, 75, 77, 79, 81, 83–86, 88, 89, 92, 100, 101, 103–107, 109–114, 157, 193

DL5 Data Level 5. 54, 55, 77

DL6 Data Level 6. 54

DM Dark Matter. 1–3, 7–9, 11, 13–20, 53, 60, 64, 65, 85, 90–105, 108–111, 113, 114, 226

DRS4 Domino Ring Sampler 4. 27, 31, 32

dSph Dwarf Spheroidal Galaxy. 2, 3, 15, 19, 65–68, 71, 74–76, 78, 82, 85–92, 94–98, 100, 101, 103, 104, 109–111, 113, 114, 137, 142–147, 151, 157, 169, 181, 208, 226

EAS Extensive Air Shower. 19, 22–26, 31, 34, 35, 38–41

EBL Extragalactic Background Light. 12, 15

EDELWEISS Expérience pour détecter les WIMPs en site souterrain. 15

EHT Event Horizon Telescope. 19

ET Einstein Telescope. 21

Fermi-LAT Fermi-LAT. 19, 66, 114

FoV Field of View. 26, 41, 42, 44, 50–52, 68, 69, 71, 72

FWHM Full Width at Half Maximum. 10

GADF Gamma Astro Data Formats. 46, 54

GUT Grand Unified Theory. 6

HAWC High-Altitude Water Cherenkov Observatory. 53

HDU Header Data Unit. 73, 78

H.E.S.S. High Energy Stereoscopic System. 19, 53

IACT Imaging Air Cherenkov Telescope. 19, 20, 25, 26, 113

IF plate Interface plate. 25

IRF Instrument Response Function. 3, 31, 39–42, 46, 49, 56, 57, 113

JWST James Webb Space Telescope. 77

LHC Large Hadron Collider. 15

LIDAR Light Detection and Ranging. 28, 46, 65

LIGO Laser Interferometer Gravitational-Wave Observatory. 21

LISA Laser Interferometer Space Antenna. 21

l.o.s. line of sight. 17, 28

LSP Lightest Supersymmetric Particle. 13

LUT Look Up Table. 46

MAGIC Major Atmospheric Gamma-Ray Imaging Cherenkov Telescopes. 2, 3, 19, 25, 27, 29, 31, 33–36, 38, 39, 42, 43, 45–48, 53, 64, 65, 71, 73, 77, 82, 84, 85, 90, 92, 93, 96–99, 109–111, 113, 114, 142–149

MARS MAGIC Analysis and Reconstruction Software. 45–47, 77

MC Monte Carlo. 38–41, 46, 47, 51, 59, 60, 62, 77, 93–96, 99–102, 107–109, 208, 217

MLE maximum likelihood estimation. 55, 56, 60

MMA Multi-Messenger astronomy. 2, 19–21, 114

MOND Modified Newtonian Dynamics. 11

MSSM Minimal Supersymmetric Standard Model. 13, 14

NFW Navarro-Frenk-White. 17

NLL negative log-likelihood. 55, 56, 58

NN Next-Neighbour. 26, 34, 36

NP nuisance parameter. 57, 58, 92, 93, 114

NSB Night Sky Background. 26, 28, 34

PAO Pierre Auger Observatory. 21

PCA Principal Component Analysis. 36, 71–73

p.e. photo electrons. 28, 31, 32, 34, 36, 46

PIC Port d'Informació Científica. 45, 47, 48

pLLR profile log-likelihood ratio. 58, 61

PMT Photo Multiplier Tube. 26–28, 31–33

PP Particle Physics. 15, 16, 90

PSF Point Spread Function. 42, 44

QCD Quantum Chromodynamics. 11

RA Right Ascension. 28, 75

Ra-Dec Right Ascension and Declination. 55, 57, 68

RF Random Forest. 31, 38–42, 46, 77

SED Spectral Energy Density. 65, 77, 82, 84, 113

SM Standard Model. 1, 11, 13–16

sorcerer Simple, Outright Raw Calibration; Easy, Reliable Extraction Routines. 46

SSB Spontaneous Symmetry Breaking. 11

SUSY Super Symmetry. 13

TA Telescope Array. 21

TNG Telescopio Nazionale Galileo. 28, 65, 78, 142–149

TS test statistic. 3, 57–59, 61, 63, 79, 81, 85, 92, 93, 96, 99, 102, 105, 112, 113, 157, 193, 208, 217

UL upper limit. 2, 3, 53, 59–64, 85, 90, 92–101, 103–114, 208, 226

VERITAS Very Energetic Radiation Imaging Telescope Array System. 53

VHE Very-High Energy. 12

WIMP Weakly Interacting Massive Particle. 13, 14, 113, 114

WMAP Wilkinson Microwave Anisotropy Probe. 8

Zd Zenith distance. 71, 72, 74, 78

Appendix

A autoMAGIC Input Cards

This chapter displays the input cards that steer the processing of the CBe dSph and Crab Nebula observations with autoMAGIC.

A.1 CBe dSph

Listing A.1: analysis_coma_all_mcs.toml

```
mars_version = "Mars-V3-2-0"

[target]
source_name = "ComaBerenice"
start_date = 2019-01-30
stop_date = 2019-06-04

[data_selection]
L1Table = "L1_3NN"
L3Table = ""
transmission_9km_min_off = 0.8
transmission_9km_min = 0.85
transmission_9km_max = 1.2
zd_min = 5
zd_max = 50
dc_min = 0
dc_max = 2200
hv_setting = "NominalHV"
mola_threshold = 2
cloudiness_max_off = 20
cloudiness_max_on = 10
use_broken_lidar_data = true
calibrated_version_M1 = "current"
```

```
calibrated_version_M2 = "current"
force_take_pic_archive_mataju_files = false


[sorcerer]
ignore_mars_version_of_calibrated_file = true
force_take_pre_computed_calibrated_files = false


[star]
cleaning_method = "sum"
cl_lv1 = false
cl_lv2 = false
noise_lv_mean = false
noise_lv_rms = false
store_star_output = false


[superstar]
ignore_mars_version_of_superstar_file = true
mataju_start_on_superstar_files = true


[RF]
cleaning_survival_rate = 0.5
force_rf = true
only_one_RF = false
max_underpopulated_bins_RF_check = 25
check_off_data_for_current_calibrated_version = true
energy_estimation_method = "RFenStereo"
use_egal_off_if_not_enough_gal_off = true


[mc_parameters]
corsika_versions = ["mmcs699", "mmcs6500"]
view_cone = "diffuse2.5"
dont_care_view_cone = false
mc_trigger_type = "standard"
extension = ""
max_number_lowe_mc_runs = 2000

[melibea]
use_lidar_correction = true
```

```
forced_coach_job_ids = false
force_diffuse_mcs = false


[magicDL3]
dl3_converter_version = "v0.1.15"
irf_type = "full-enclosure"
az_bins = 1
hadronness_cut_from_efficiency = true
theta2_cut_from_efficiency = false
hadronness_cut = 0.3
theta2_cut = 0.02
quantile_hadronness_cut = 0.9
quantile_theta2_cut = 0.9
```

A.2 Crab Nebula

Listing A.2: analysis_coma_all_mcs_crabcheck.toml

```
mars_version = "Mars-V3-2-0"

[target]
source_name = "CrabNebula"
start_date = 2018-11-01
stop_date = 2019-09-15

[data_selection]
L1Table = "L1_3NN"
L3Table = ""
transmission_9km_min_off = 0.8
transmission_9km_min = 0.85
transmission_9km_max = 1.2
zd_min = 5
zd_max = 35
dc_min = 0
dc_max = 2200
hv_setting = "NominalHV"
mola_threshold = 2
cloudiness_max_off = 20
cloudiness_max_on = 10
use_broken_lidar_data = true
calibrated_version_M1 = "current"
calibrated_version_M2 = "current"
```

```
force_take_pic_archive_mataju_files = false


[sorcerer]
ignore_mars_version_of_calibrated_file = true
force_take_pre_computed_calibrated_files = false


[star]
cleaning_method = "sum"
cl_lv1 = false
cl_lv2 = false
noise_lv_mean = false
noise_lv_rms = false
store_star_output = false


[superstar]
ignore_mars_version_of_superstar_file = true
mataju_start_on_superstar_files = true


[RF]
cleaning_survival_rate = 0.5
force_rf = true
only_one_RF = false
max_underpopulated_bins_RF_check = 25
check_off_data_for_current_calibrated_version = true
energy_estimation_method = "RFenStereo"
use_egal_off_if_not_enough_gal_off = true


[mc_parameters]
corsika_versions = ["mmcs699", "mmcs6500"]
view_cone = "diffuse2.5"
dont_care_view_cone = false
mc_trigger_type = "standard"
extension = ""
max_number_lowe_mc_runs = 2000
ignore_mars_version_of_selectmc_file = true

[melibea]
use_lidar_correction = true
```

```
forced_coach_job_ids = [3235]
force_diffuse_mcs = false


[magicDL3]
dl3_converter_version = "v0.1.15"
irf_type = "full-enclosure"
az_bins = 1
hadronness_cut_from_efficiency = true
theta2_cut_from_efficiency = false
hadronness_cut = 0.3
theta2_cut = 0.02
quantile_hadronness_cut = 0.9
quantile_theta2_cut = 0.9
```

B Quality Parameters

This chapter displays the dust tables for CBe dSph and the Crab Nebula, the excluded observations of the Crab Nebula, and normalisation parameters of the fitted `FoVBackgroundModel` to the CBe dSph *exclusion-rotation* models.

B.1 Dust Table CBe dSph

This section displays the dust values taken by TNG for each observation of the CBe dSph.

Table B.1: Dust values measured by TNG taken from MAGIC Long Term Monitoring. The values are matched with the observations of CBe dSph.

Date	Dust / µg/m^3	OBS ID
2019-01-30	0.207135	5079268
2019-01-30	0.207135	5079269
2019-01-31	0.271823	5079316
2019-01-31	0.271823	5079317
2019-01-31	0.271823	5079318
2019-01-31	0.271823	5079319
2019-01-31	0.271823	5079320
2019-02-01	0.114465	5079362
2019-02-01	0.114465	5079363
2019-02-01	0.114465	5079364
2019-02-01	0.114465	5079365
2019-02-01	0.114465	5079366
2019-02-01	0.114465	5079367
2019-02-03	0.199275	5079426
2019-02-03	0.199275	5079427
2019-02-03	0.199275	5079428
2019-02-03	0.199275	5079429
2019-02-03	0.199275	5079441
2019-02-03	0.199275	5079442
2019-02-03	0.199275	5079443
2019-02-04	NaN	5079497
2019-02-04	NaN	5079498
2019-02-04	NaN	5079499
2019-02-05	24.269176	5079530
2019-02-05	24.269176	5079531

Continued on next page

Table B.1: Dust values measured by TNG taken from MAGIC Long Term Monitoring. The values are matched with the observations of CBe dSph.

Date	Dust / µg/m^3	OBS ID
2019-02-05	24.269176	5079532
2019-02-05	24.269176	5079533
2019-02-05	24.269176	5079534
2019-02-05	24.269176	5079535
2019-02-06	8.326719	5079590
2019-02-06	8.326719	5079591
2019-02-06	8.326719	5079592
2019-02-06	8.326719	5079601
2019-02-06	8.326719	5079602
2019-02-06	8.326719	5079603
2019-02-07	1.456023	5079668
2019-02-07	1.456023	5079669
2019-02-07	1.456023	5079670
2019-02-08	0.814751	5079703
2019-02-08	0.814751	5079704
2019-02-08	0.814751	5079705
2019-02-08	0.814751	5079706
2019-02-08	0.814751	5079707
2019-02-08	0.814751	5079708
2019-02-08	0.814751	5079709
2019-02-08	0.814751	5079716
2019-02-08	0.814751	5079717
2019-02-09	0.488108	5079763
2019-02-09	0.488108	5079764
2019-02-09	0.488108	5079765
2019-02-09	0.488108	5079766
2019-02-10	0.655209	5079831
2019-02-10	0.655209	5079832
2019-02-10	0.655209	5079840
2019-02-10	0.655209	5079841
2019-02-11	5.458758	5079872
2019-02-11	5.458758	5079879
2019-02-11	5.458758	5079880
2019-02-12	6.103302	5079903
2019-02-12	6.103302	5079904
2019-02-12	6.103302	5079905
2019-02-13	3.585819	5079957

Continued on next page

Table B.1: Dust values measured by TNG taken from MAGIC Long Term Monitoring. The values are matched with the observations of CBe dSph.

Date	Dust / µg/m^3	OBS ID
2019-02-13	3.585819	5079958
2019-02-13	3.585819	5079969
2019-02-26	NaN	5080161
2019-02-26	NaN	5080162
2019-02-26	NaN	5080163
2019-02-28	NaN	5080263
2019-02-28	NaN	5080264
2019-02-28	NaN	5080265
2019-02-28	NaN	5080266
2019-02-28	NaN	5080267
2019-02-28	NaN	5080268
2019-02-28	NaN	5080269
2019-02-28	NaN	5080270
2019-03-01	NaN	5080335
2019-03-02	1.829935	5080384
2019-03-02	1.829935	5080385
2019-03-02	1.829935	5080386
2019-03-02	1.829935	5080391
2019-03-02	1.829935	5080392
2019-03-02	1.829935	5080393
2019-03-03	NaN	5080426
2019-03-03	NaN	5080427
2019-03-03	NaN	5080432
2019-03-03	NaN	5080433
2019-03-03	NaN	5080434
2019-03-03	NaN	5080439
2019-03-03	NaN	5080440
2019-03-04	0.090064	5080484
2019-03-04	0.090064	5080485
2019-03-04	0.090064	5080486
2019-03-04	0.090064	5080487
2019-03-04	0.090064	5080488
2019-03-04	0.090064	5080489
2019-03-05	0.157389	5080529
2019-03-05	0.157389	5080530
2019-03-05	0.157389	5080537
2019-03-05	0.157389	5080538

Continued on next page

Table B.1: Dust values measured by TNG taken from MAGIC Long Term Monitoring. The values are matched with the observations of CBe dSph.

Date	Dust / µg/m^3	OBS ID
2019-03-05	0.157389	5080539
2019-03-07	0.764508	5080595
2019-03-07	0.764508	5080596
2019-03-07	0.764508	5080597
2019-03-10	NaN	5080634
2019-03-11	NaN	5080635
2019-03-11	NaN	5080646
2019-03-11	NaN	5080647
2019-03-12	NaN	5080689
2019-03-12	NaN	5080690
2019-03-12	NaN	5080691
2019-03-12	NaN	5080692
2019-03-12	NaN	5080693
2019-03-12	NaN	5080694
2019-03-13	1.693025	5080729
2019-03-13	1.693025	5080730
2019-03-13	1.693025	5080731
2019-03-13	1.693025	5080732
2019-03-13	1.693025	5080733
2019-03-14	0.658721	5080780
2019-03-14	0.658721	5080781
2019-03-15	12.076678	5080817
2019-03-15	12.076678	5080818
2019-04-07	0.277732	5081024
2019-04-07	0.277732	5081025
2019-04-07	0.277732	5081026
2019-04-09	0.575788	5081164
2019-04-10	0.708416	5081165
2019-04-10	0.708416	5081166
2019-04-24	7.340000	5081422
2019-04-24	7.340000	5081423
2019-04-24	7.340000	5081424
2019-04-24	7.340000	5081425
2019-04-24	7.340000	5081426
2019-04-25	NaN	5081427
2019-04-25	NaN	5081471
2019-04-26	7.340000	5081472

Continued on next page

Table B.1: Dust values measured by TNG taken from MAGIC Long Term Monitoring. The values are matched with the observations of CBe dSph.

Date	Dust / µg/m^3	OBS ID
2019-04-26	7.340000	5081473
2019-04-26	7.340000	5081474
2019-04-26	7.340000	5081475
2019-05-01	7.340000	5081532
2019-05-01	7.340000	5081535
2019-05-01	7.340000	5081536
2019-05-01	7.340000	5081537
2019-05-02	NaN	5081538
2019-05-02	NaN	5081568
2019-05-02	NaN	5081569
2019-05-02	NaN	5081570
2019-05-02	NaN	5081571
2019-05-02	NaN	5081572
2019-05-02	NaN	5081573
2019-05-03	7.340000	5081574
2019-05-03	7.340000	5081575
2019-05-03	7.340000	5081608
2019-05-03	7.340000	5081609
2019-05-03	7.340000	5081617
2019-05-03	7.340000	5081618
2019-05-03	7.340000	5081619
2019-05-04	7.340000	5081649
2019-05-04	7.340000	5081650
2019-05-04	7.340000	5081651
2019-05-04	7.340000	5081652
2019-05-04	7.340000	5081653
2019-05-04	7.340000	5081654
2019-05-05	7.340000	5081692
2019-05-05	7.340000	5081693
2019-05-05	7.340000	5081694
2019-05-06	7.340000	5081697
2019-05-06	7.340000	5081736
2019-05-06	7.340000	5081737
2019-05-06	7.340000	5081738
2019-05-06	7.340000	5081739
2019-05-07	7.340000	5081776
2019-05-22	7.340000	5082062

Continued on next page

Table B.1: Dust values measured by TNG taken from MAGIC Long Term Monitoring. The values are matched with the observations of CBe dSph.

Date	Dust / µg/m^3	OBS ID
2019-05-28	7.340000	5082270
2019-05-31	7.340000	5082367
2019-05-31	7.340000	5082368

B.2 Dust Table Crab Nebula

This section displays the dust values taken by TNG for each observation of the Crab Nebula.

Table B.2: Dust values measured by TNG taken from MAGIC Long Term Monitoring. The values are matched with the observations of the Crab Nebula.

Date	Dust / µg/m^3	OBS ID
2018-11-08	0.152556	5076583
2018-11-08	0.152556	5076584
2018-11-08	0.152556	5076585
2018-11-09	4.514468	5076623
2018-11-09	4.514468	5076624
2018-11-09	4.514468	5076625
2018-11-11	0.161075	5076712
2018-11-11	0.161075	5076713
2018-11-11	0.161075	5076714
2018-12-08	1.081125	5077445
2019-01-01	0.144265	5078183
2019-01-01	0.144265	5078184
2019-01-01	0.144265	5078185
2019-01-04	0.078276	5078381
2019-01-04	0.078276	5078382
2019-01-04	0.078276	5078383
2019-01-05	0.075618	5078433
2019-01-05	0.075618	5078434
2019-01-05	0.075618	5078435
2019-01-11	0.156054	5078666
2019-01-13	0.872692	5078762
2019-01-13	0.872692	5078763
2019-01-26	0.215081	5079094
2019-01-26	0.215081	5079095
2019-01-26	0.215081	5079096
2019-01-26	0.215081	5079104
2019-02-05	24.269176	5079565
2019-02-05	24.269176	5079566
2019-02-22	NaN	5080038
2019-02-23	8.588312	5080060
2019-02-25	6.077396	5080149
2019-02-25	6.077396	5080150

Continued on next page

Table B.2: Dust values measured by TNG taken from MAGIC Long Term Monitoring. The values are matched with the observations of the Crab Nebula.

Date	Dust / µg/m^3	OBS ID
2019-02-25	6.077396	5080151
2019-02-25	6.077396	5080152
2019-02-27	NaN	5080255
2019-03-22	NaN	5080939

B.3 Excluded Observations Crab Nebula

This section displays the quality cuts for the Crab Nebula, as well as the excluded observations.

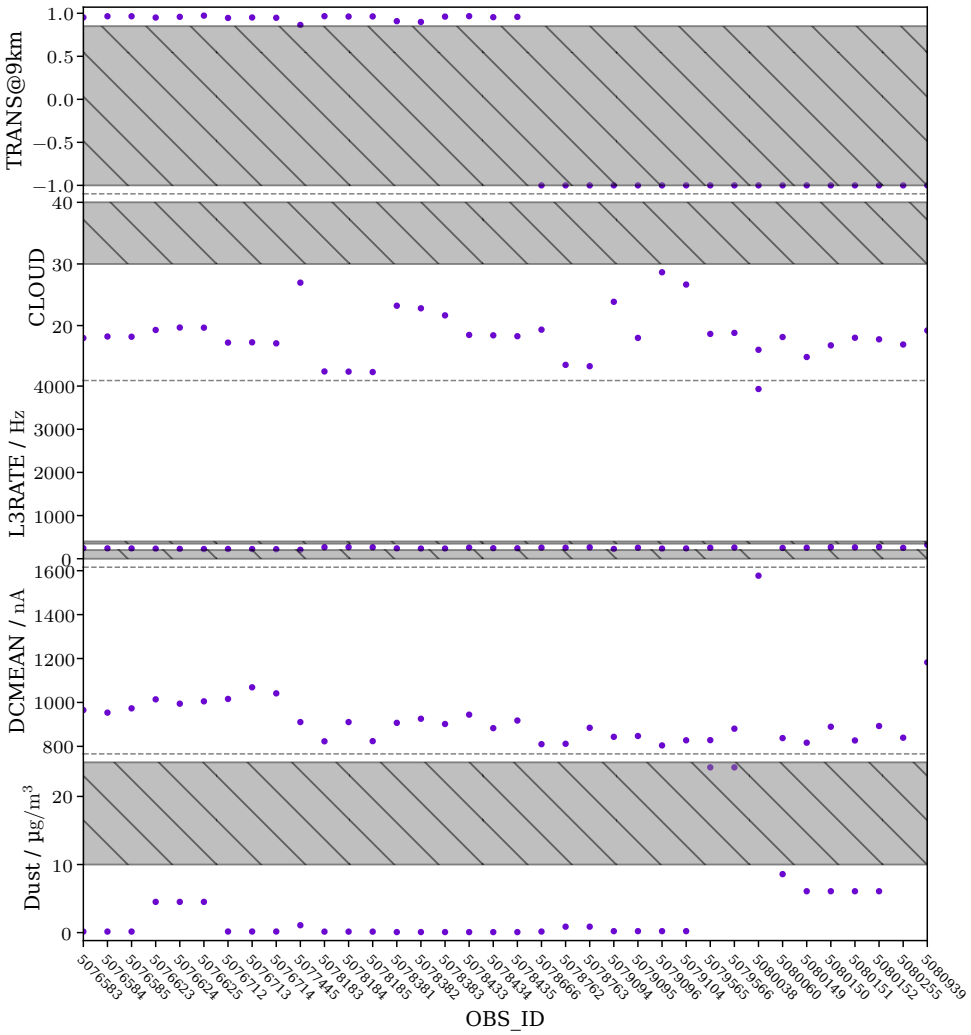

Figure B.1: Illustration of the applied quality cuts from Table 6.4 to the Crab nebula observations. The shaded regions indicate the exclusion of observations.

B.4 Normalisation Parameters CBe dSph

This section displays the normalisation parameters of the `FoVBackgroundModel` fitted to the CBe dSph *exclusion-rotation* models in dependence of the quality parameters `Tranmission`, `Cloudiness`, `L3 rate`, `DC mean`, and `Dust`. For each set of parameters a linear curve,

$$N = a \cdot Q + b \tag{B.1}$$

where N are the normalisation and Q are the quality parameters, is inferred. The Pearson correlation coefficient ρ is displayed in each Figure. A value of $\rho \geq 0.2$ hints for a linear correlation between the parameters. No correlation is found.

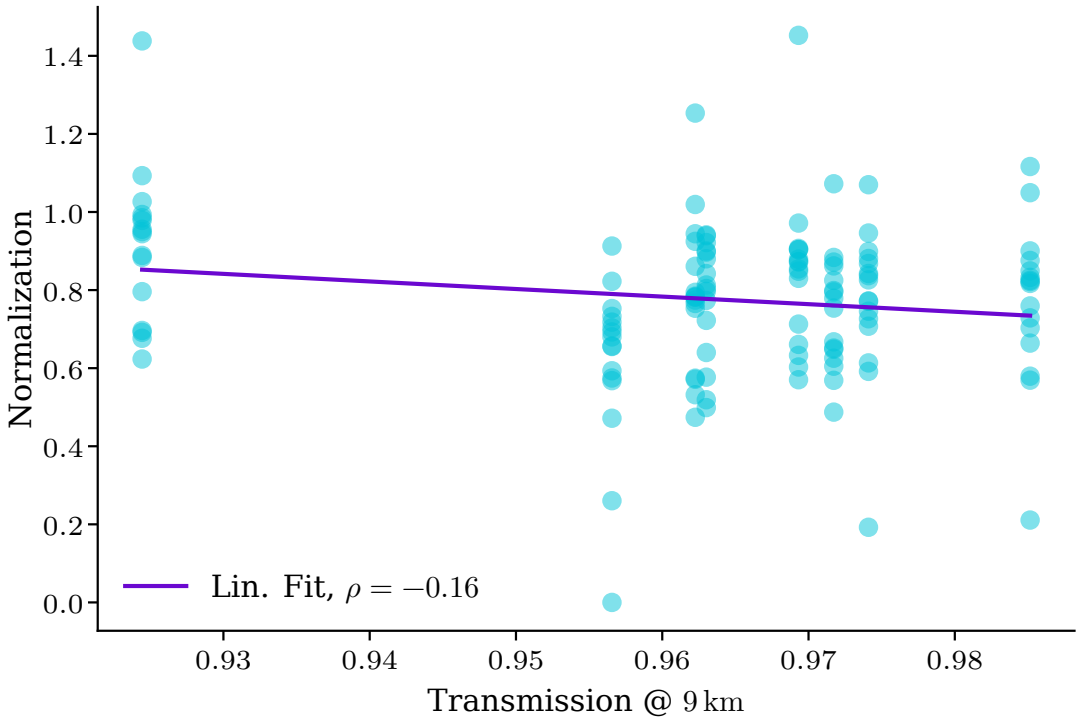

Figure B.2: Illustrations of the fitted normalisations parameters in dependence of the quality data for CBe dSph. Continued on following pages.

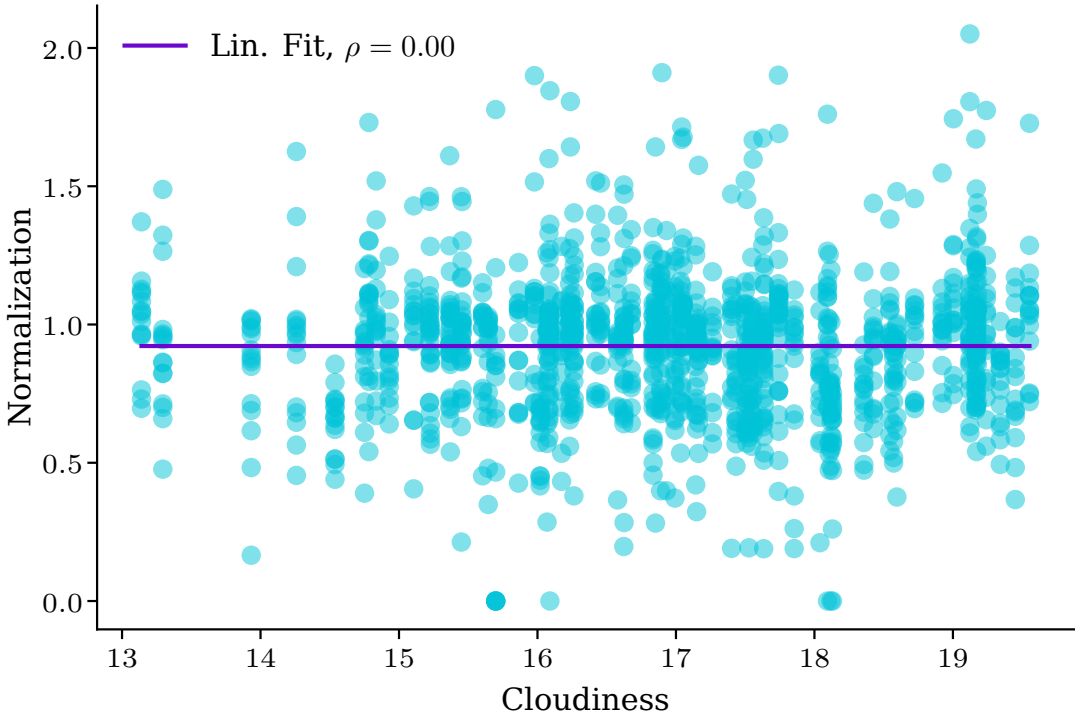

Figure B.3: (continued)

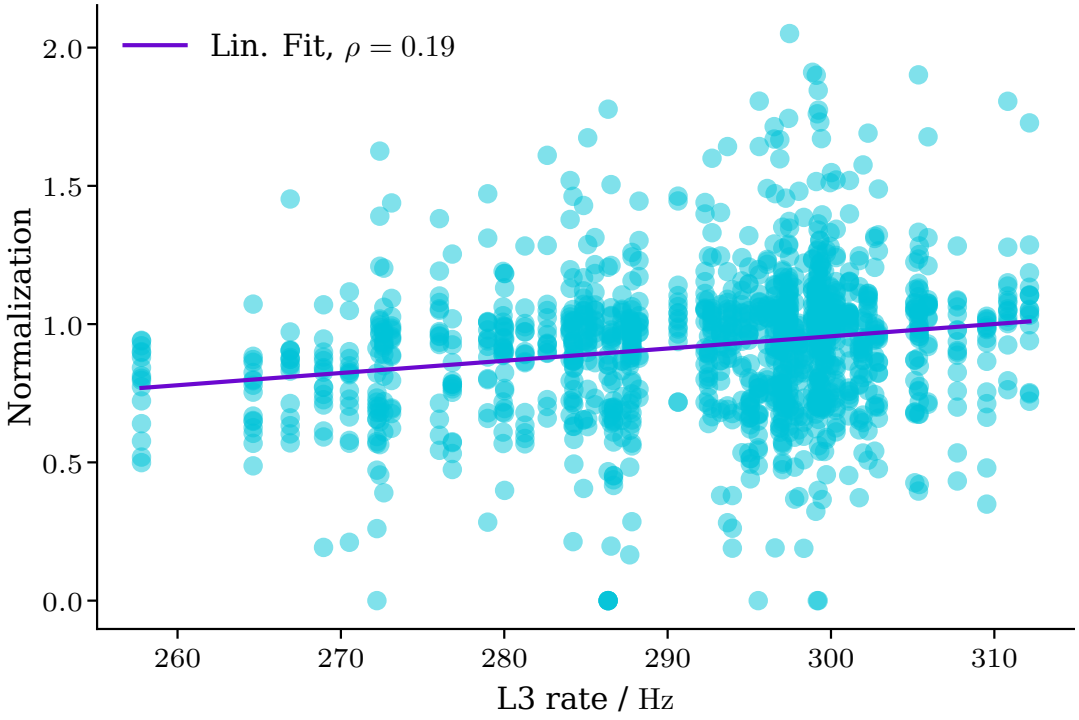

Figure B.3: (continued)

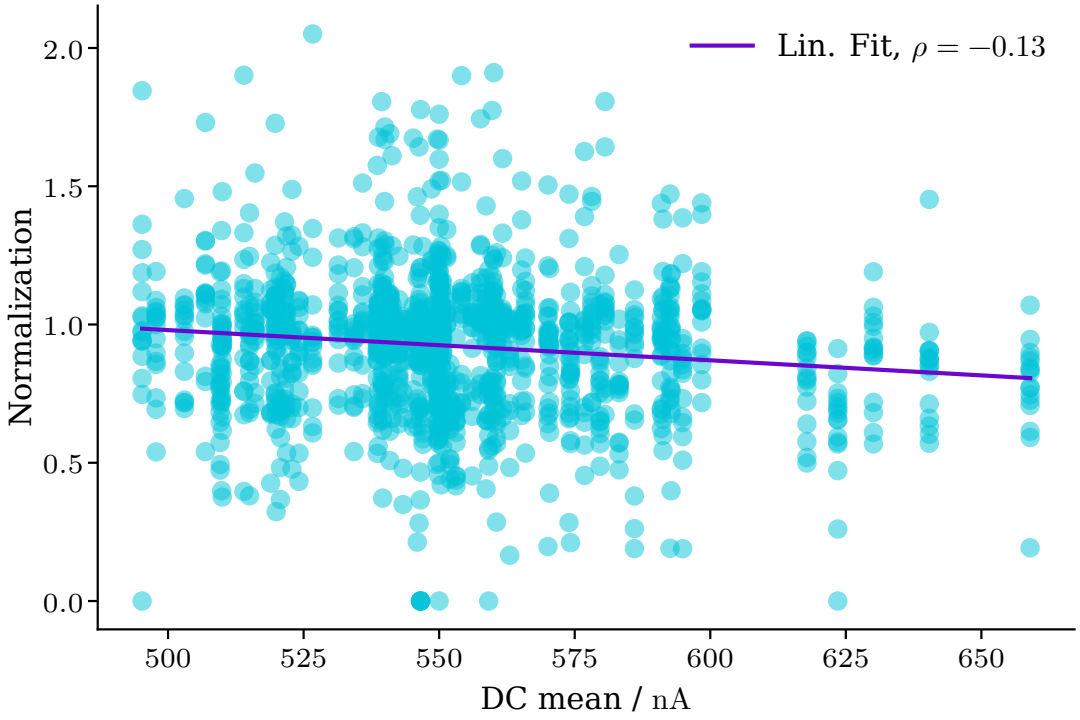

Figure B.3: (continued)

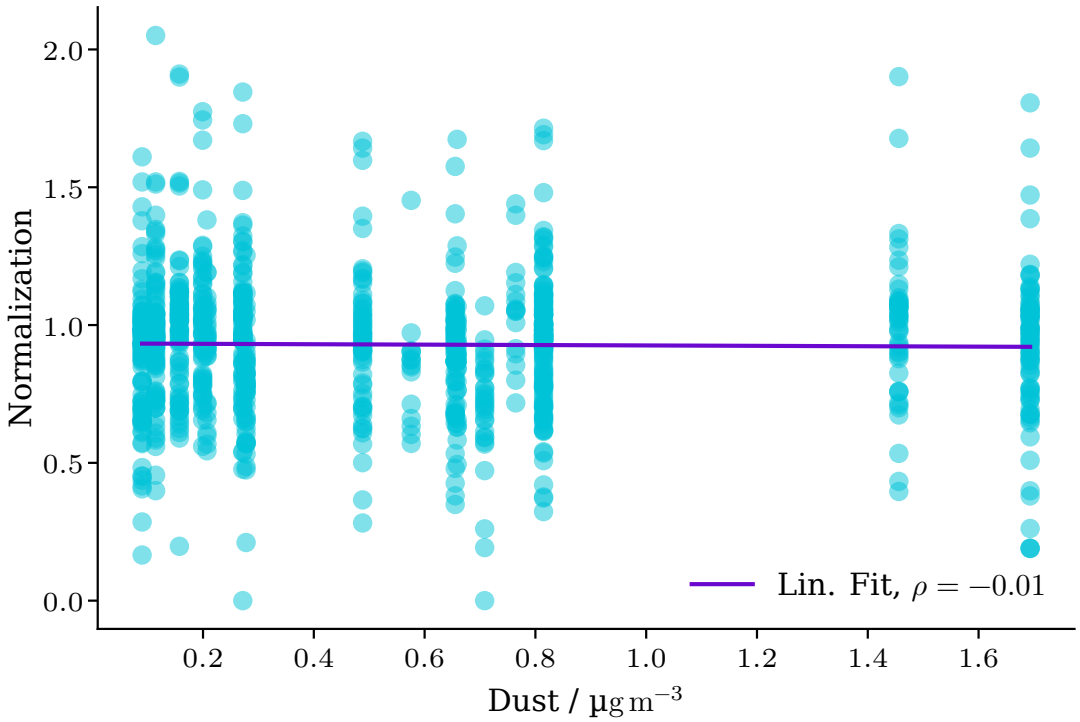

Figure B.3: (continued)

B.5 Normalisation Parameters Crab Nebula

This section displays the normalisation parameters of the `FoVBackgroundModel` fitted to the Crab Nebula *exclusion-rotation* models in dependence of the quality parameters `Tranmission`, `Cloudiness`, `L3 rate`, `DC mean`, and `Dust`. For each set of parameters a linear curve according to Equation B.1 is inferred. The Pearson correlation coefficient ρ is displayed in each Figure. A value of $\rho \geq 0.2$ hints for a linear correlation between the parameters. No correlation is found.

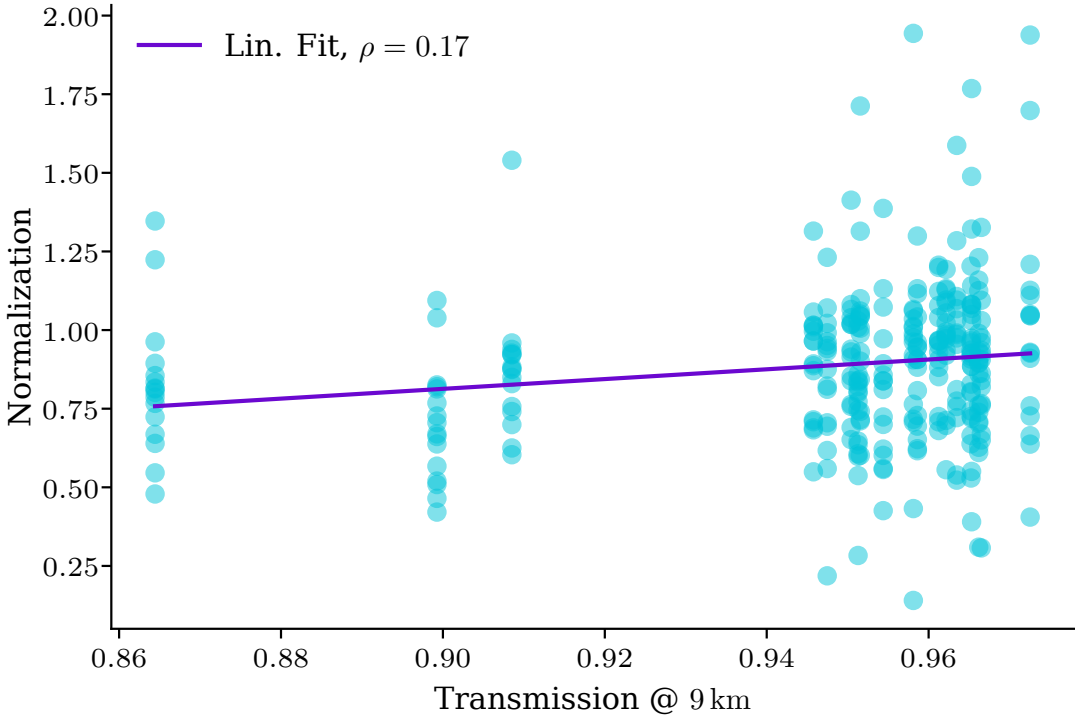

Figure B.3: Illustrations of the fitted normalisations parameters in dependence of the quality data for the Crab nebula. Continued on following pages.

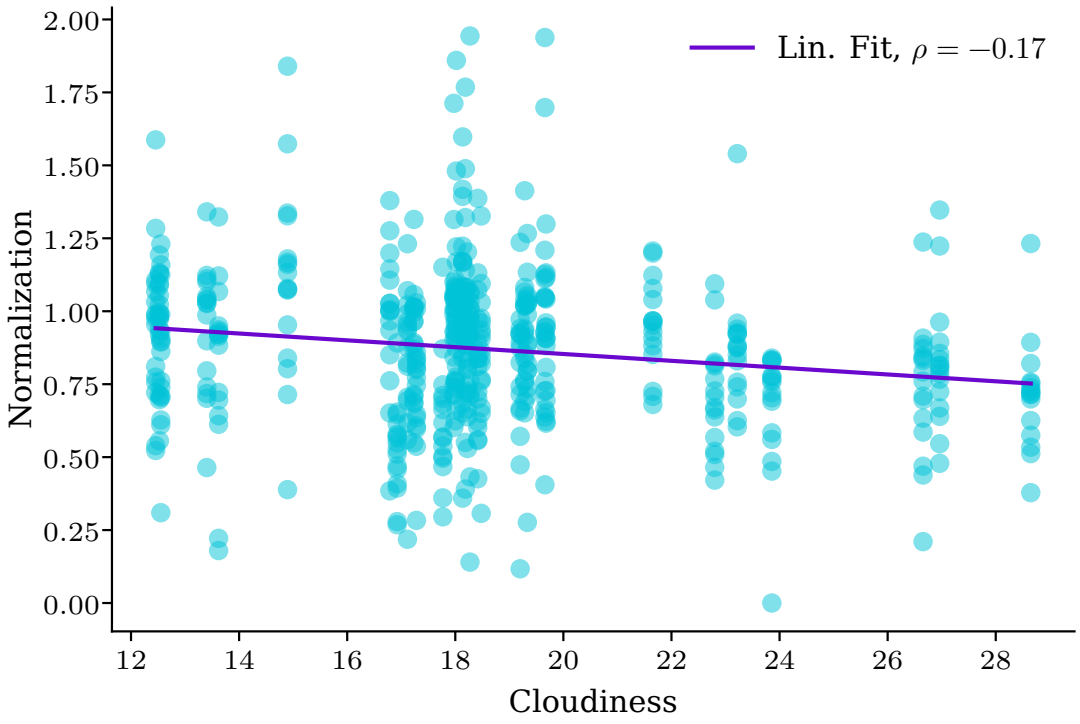

Figure B.3: (continued)

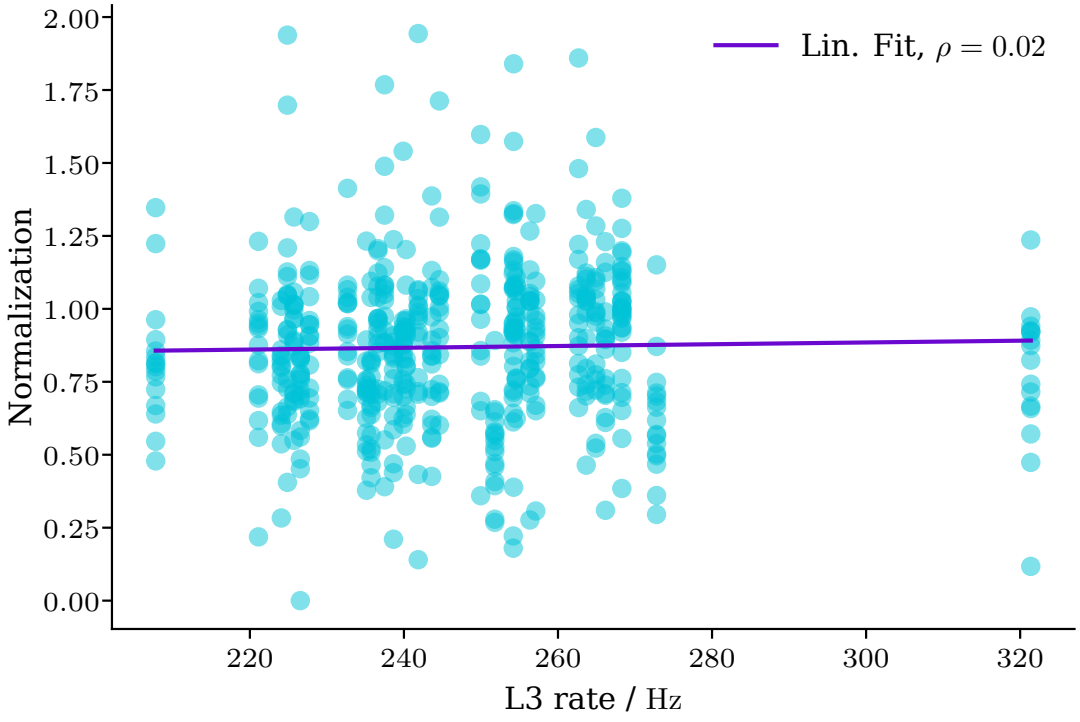

Figure B.3: (continued)

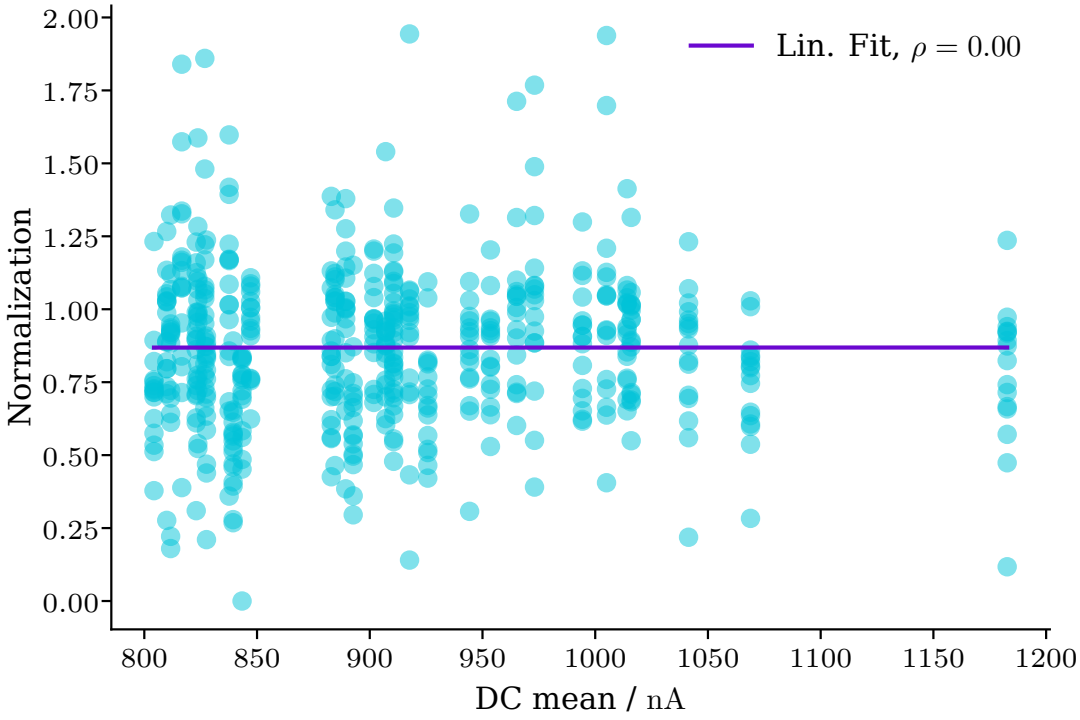

Figure B.3: (continued)

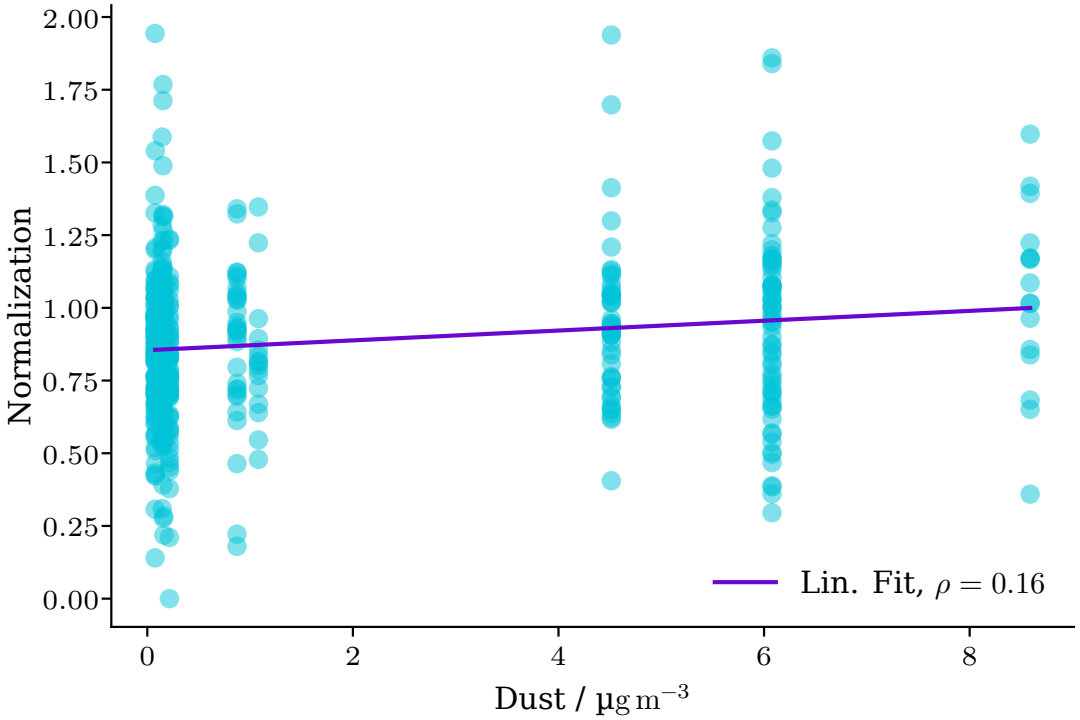

Figure B.3: (continued)

C DL4 Cubes CBe dSph

This chapter displays the excess maps, TS maps, and TS histograms for the CBe dSph DL4 cubes.

C.1 Excess Maps

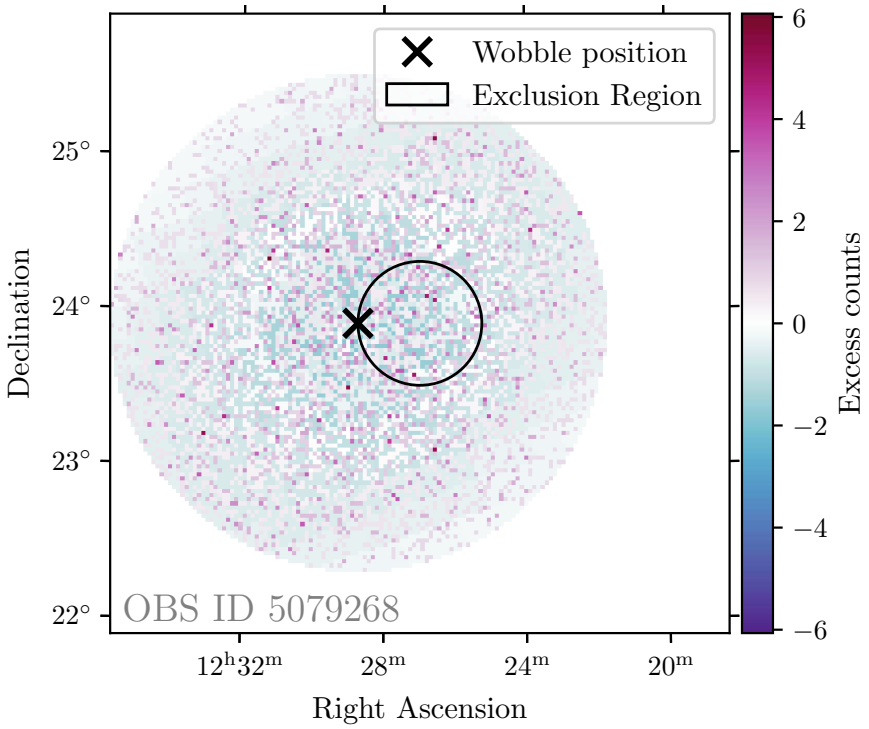

Figure C.4: Excess counts of all CBe dSph observations integrated over the energy axis. The map is centered on the coordinates of CBe dSph. The black circle illustrates the exclusion region used for the background modelling, whereas the black cross denotes the Wobble position of the observation. Continued on following pages.

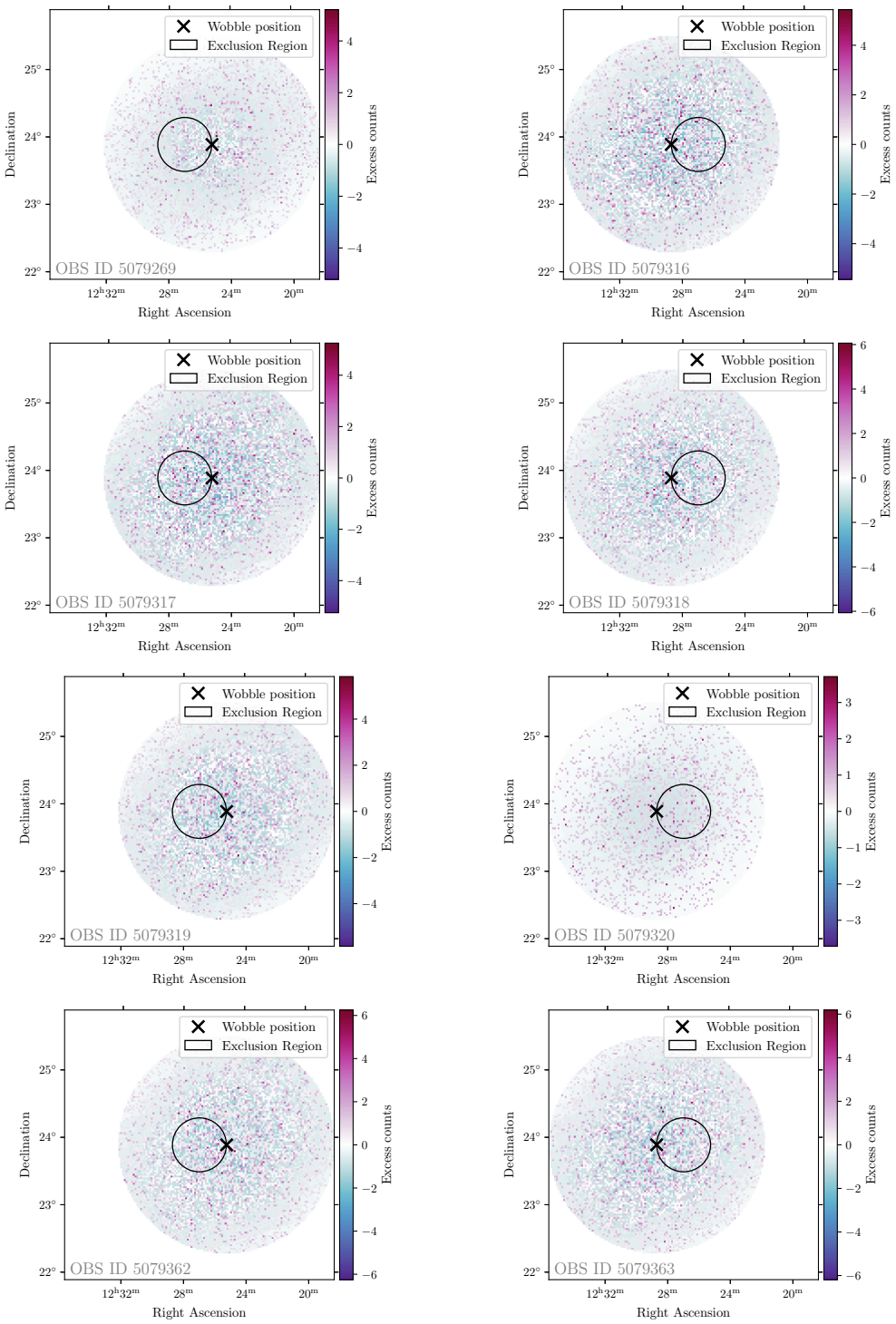

Figure C.4: (continued)

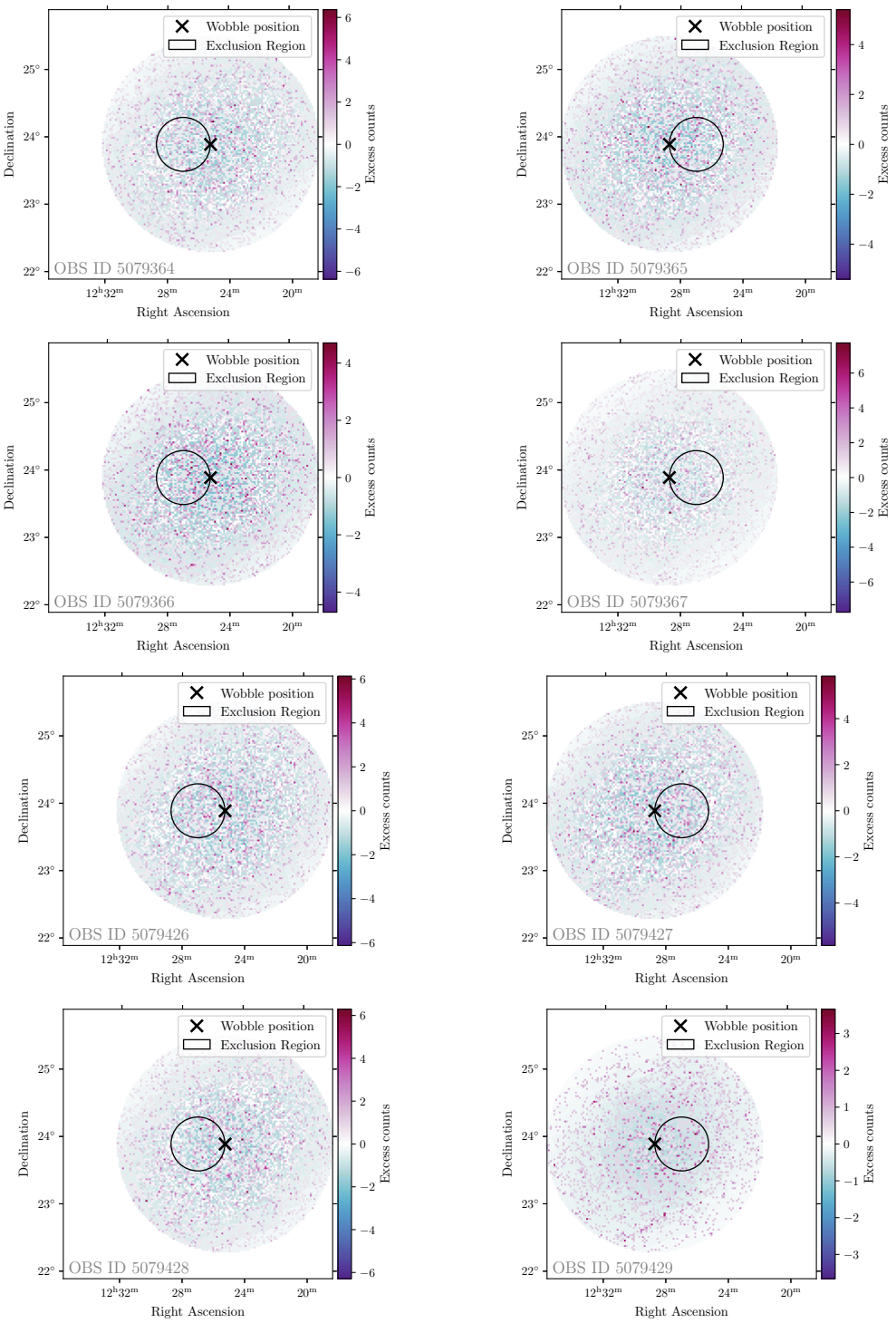

Figure C.4: (continued)

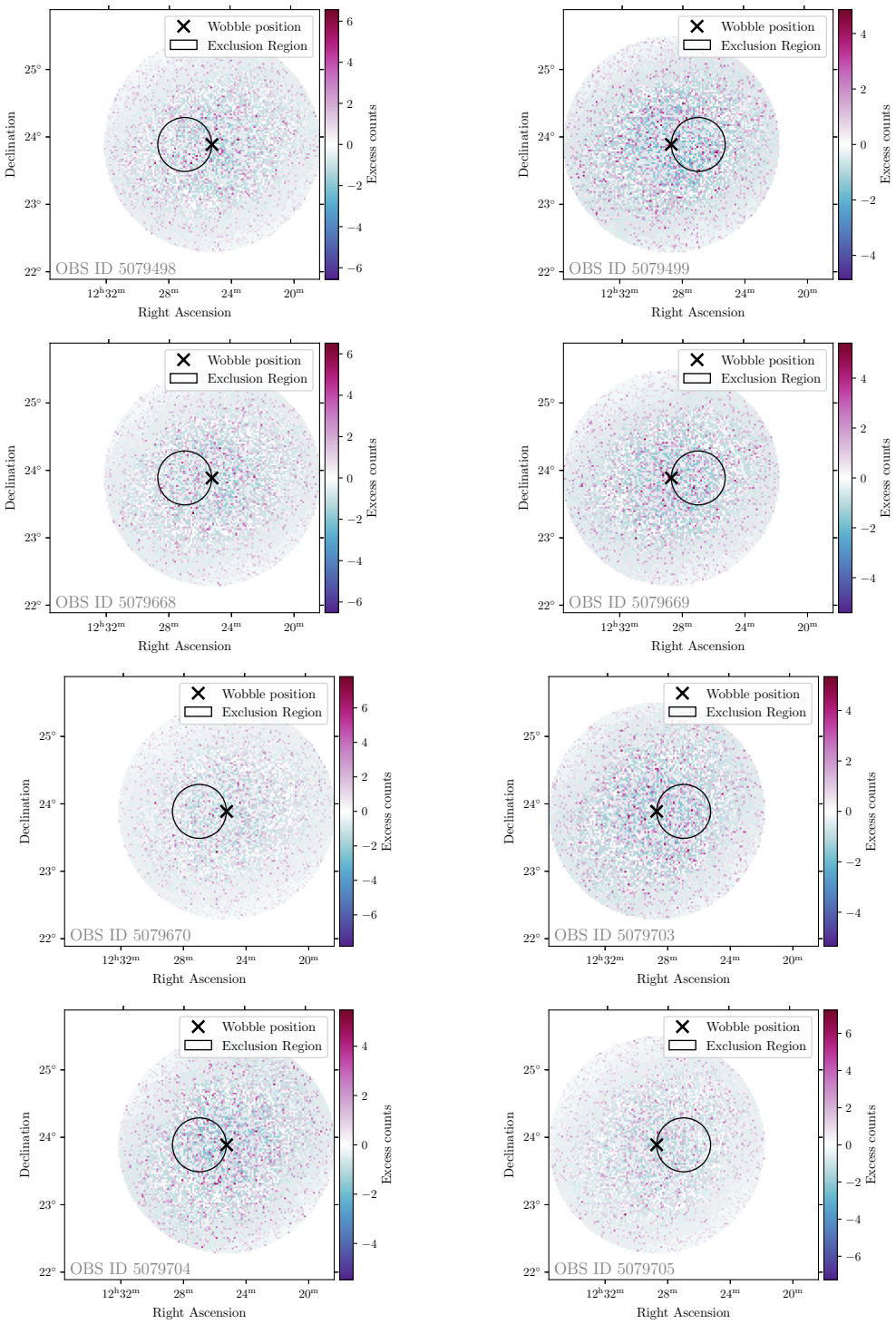

Figure C.4: (continued)

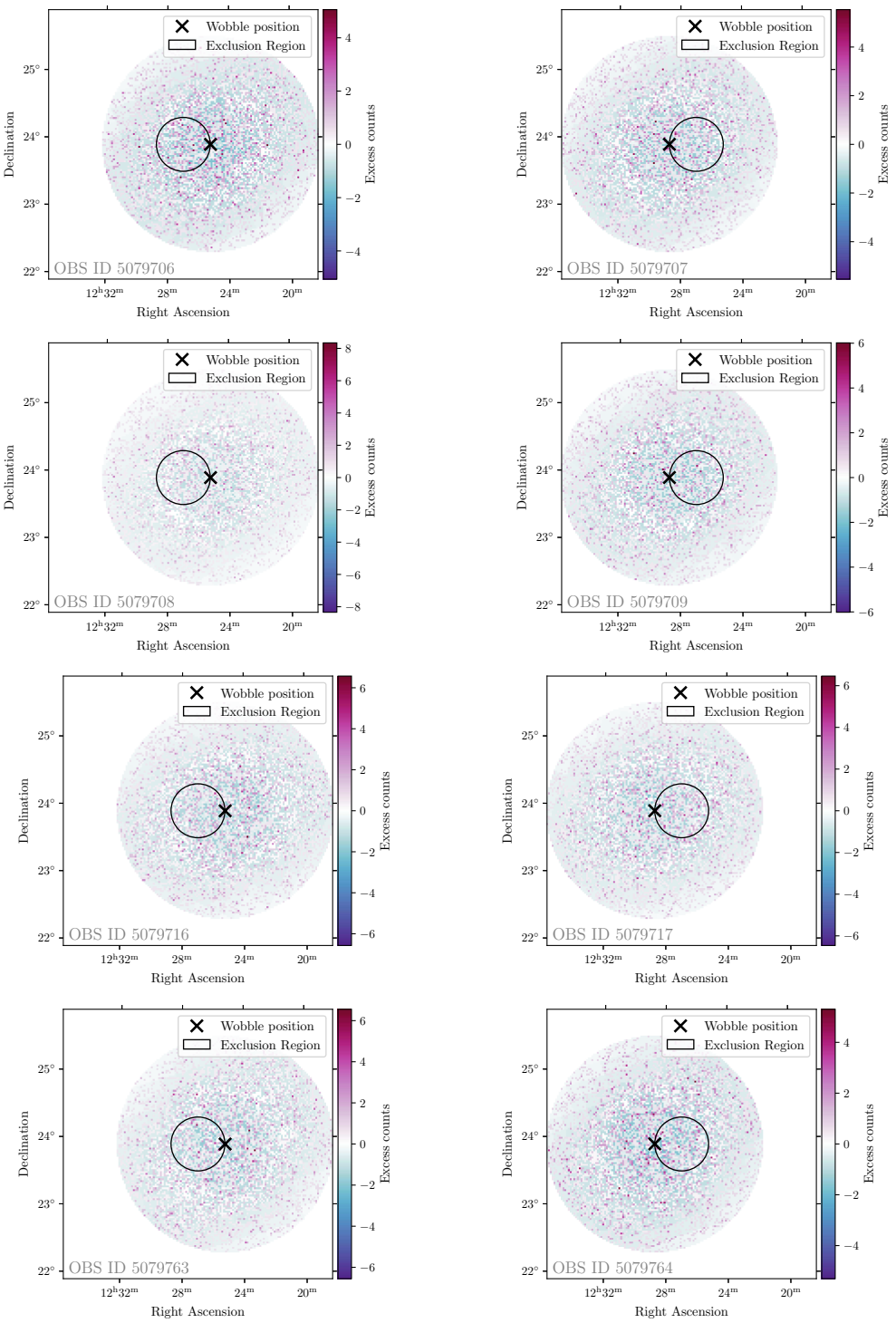

Figure C.4: (continued)

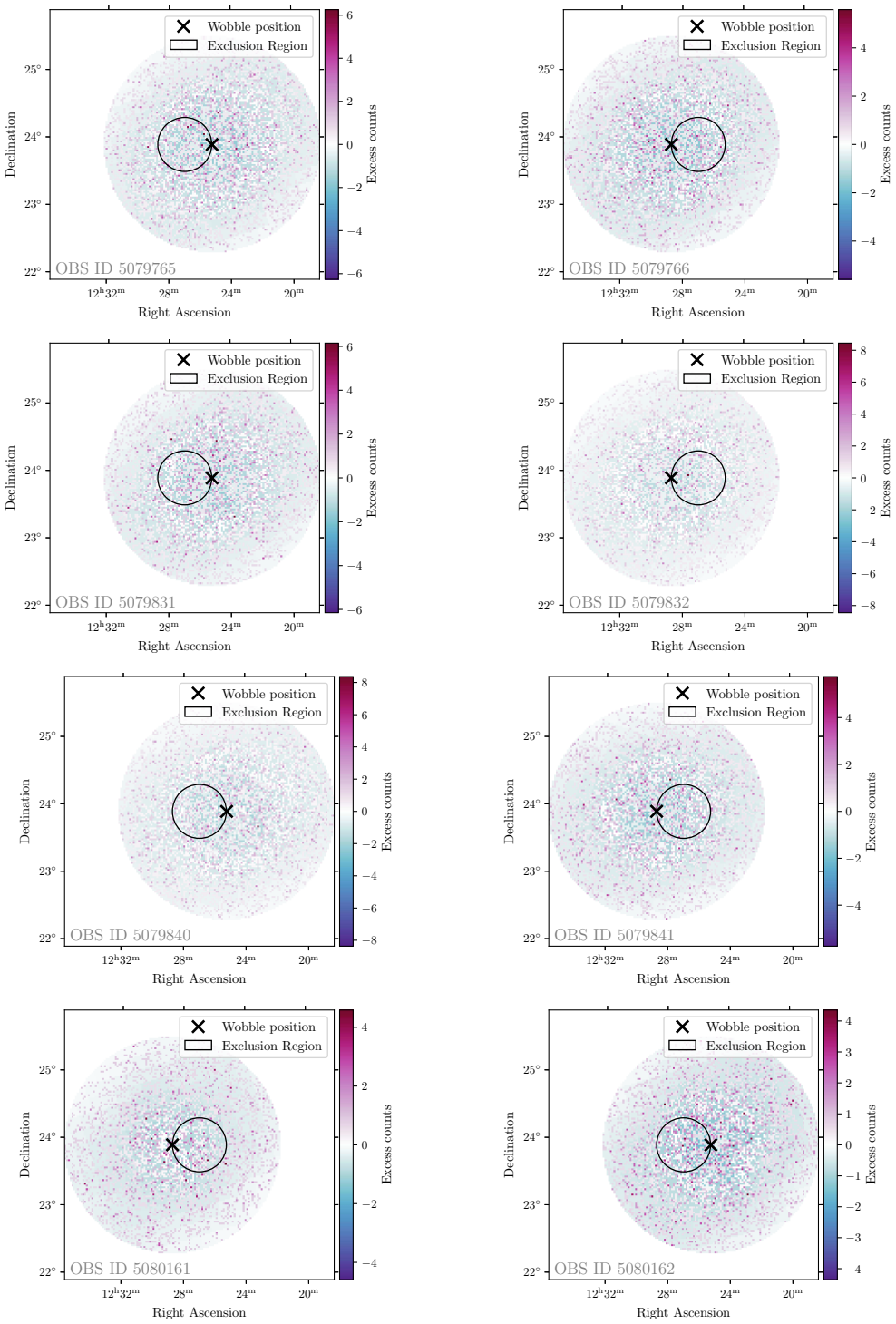

Figure C.4: (continued)

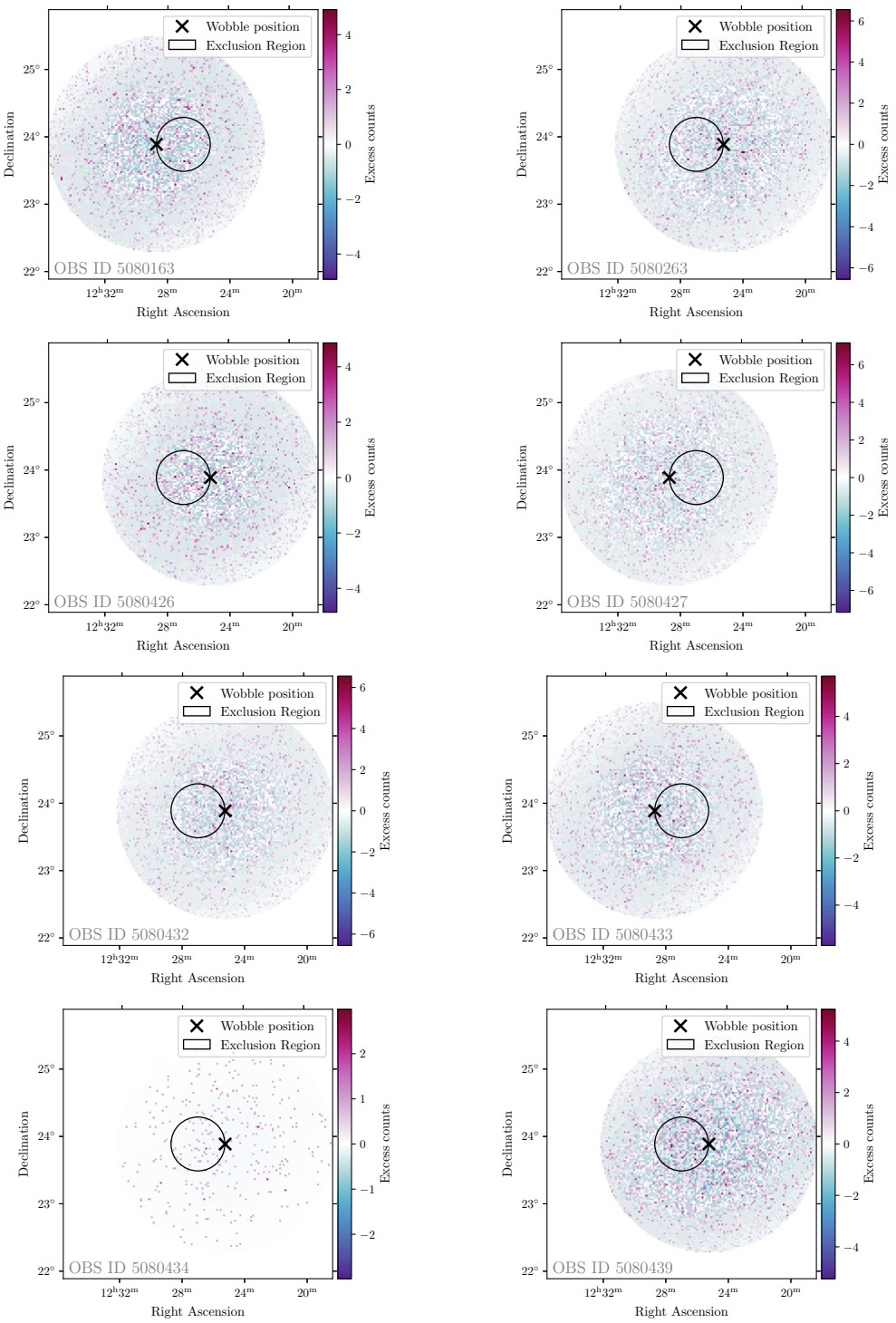

Figure C.4: (continued)

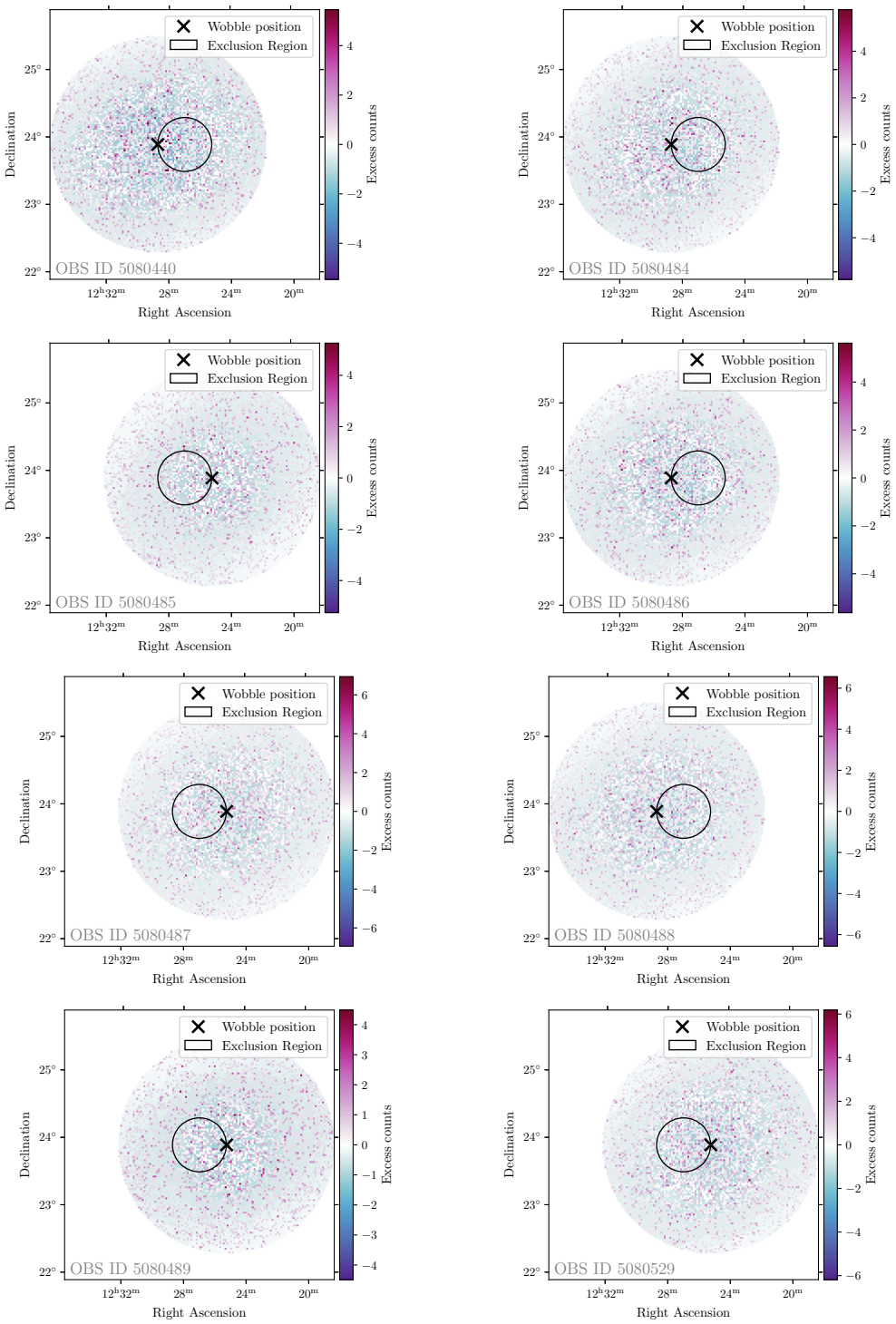

Figure C.4: (continued)

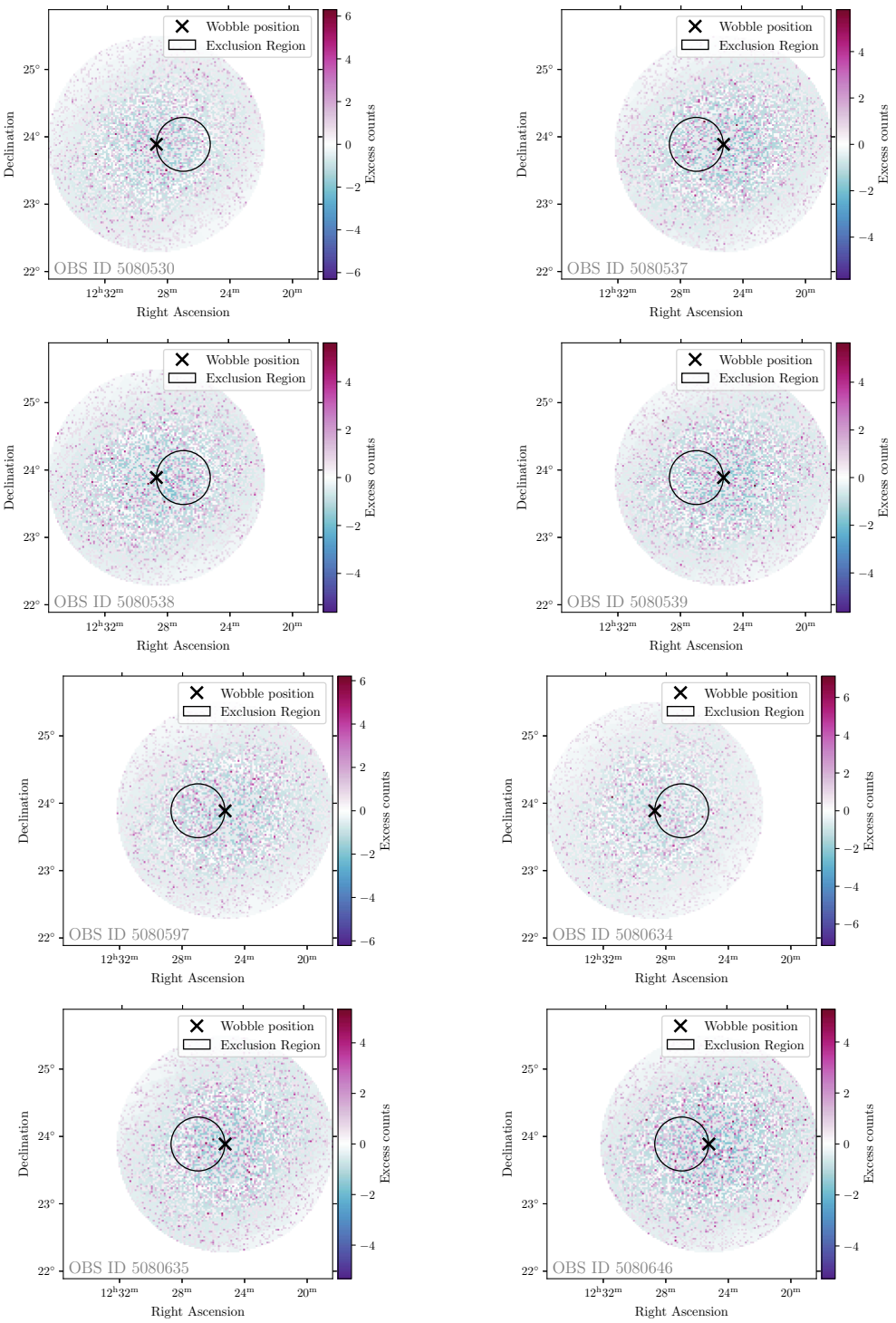

Figure C.4: (continued)

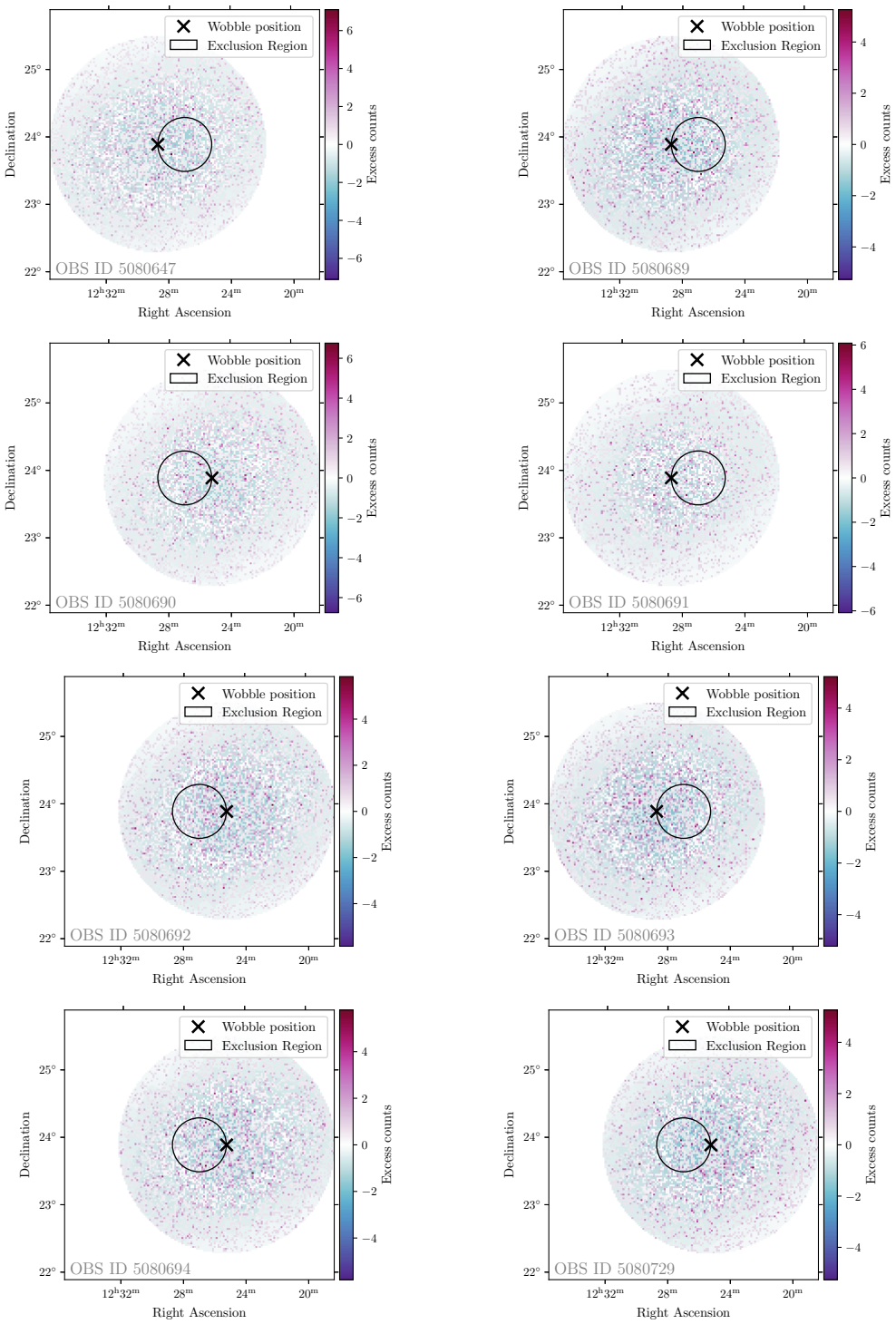

Figure C.4: (continued)

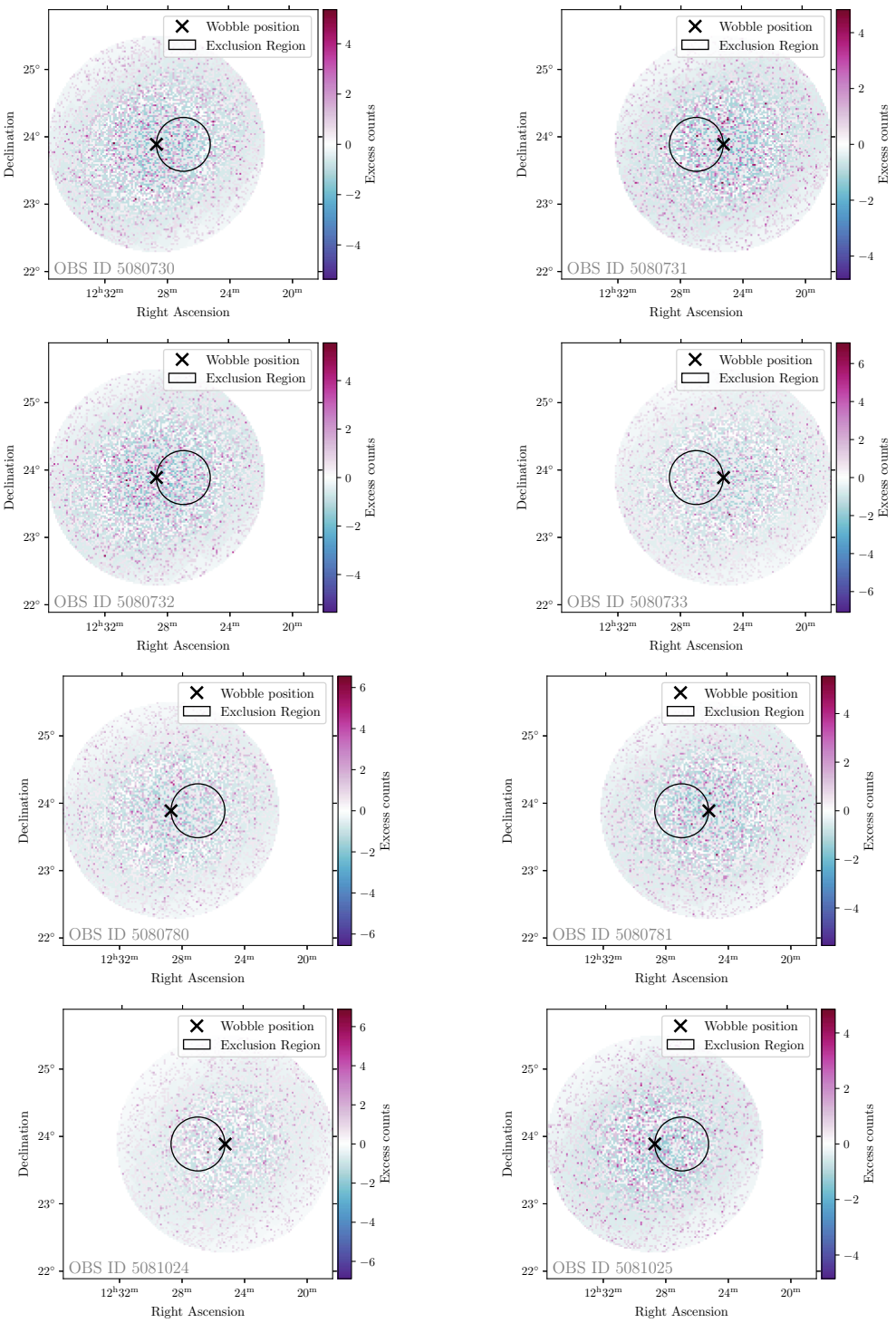

Figure C.4: (continued)

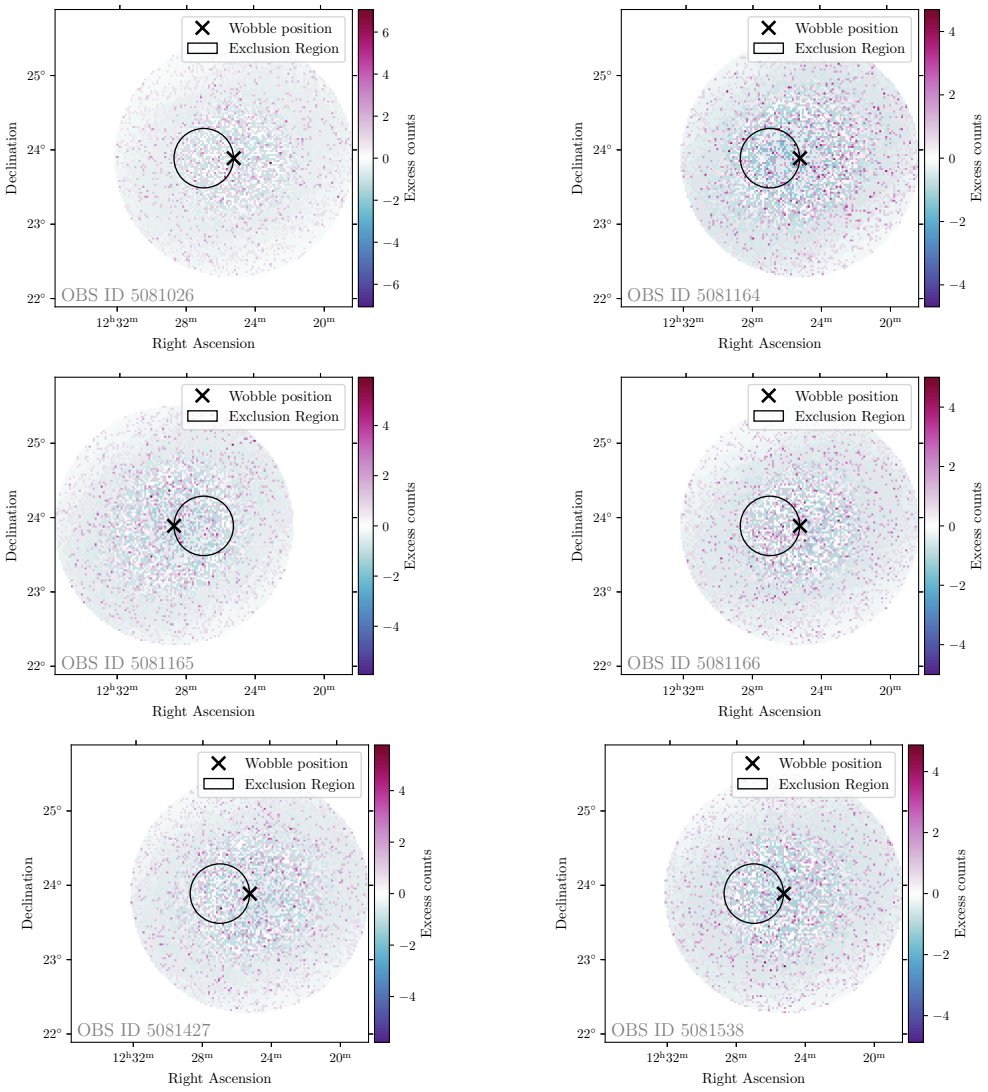

Figure C.4: (continued)

C.2 TS Maps

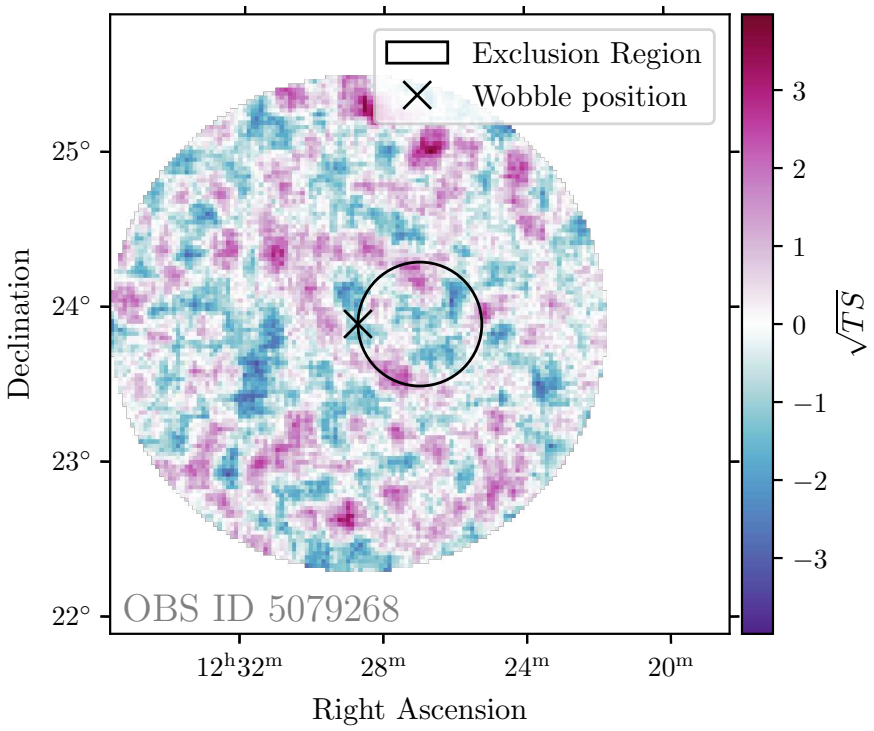

Figure C.5: Significance map of all CBe dSph observation, integrated over the energy axis. The map is centered on the coordinates of CBe dSph. The black circle illustrates the exclusion region used for the background modelling, whereas the black cross denotes the Wobble position of the observation. Continued on following pages.

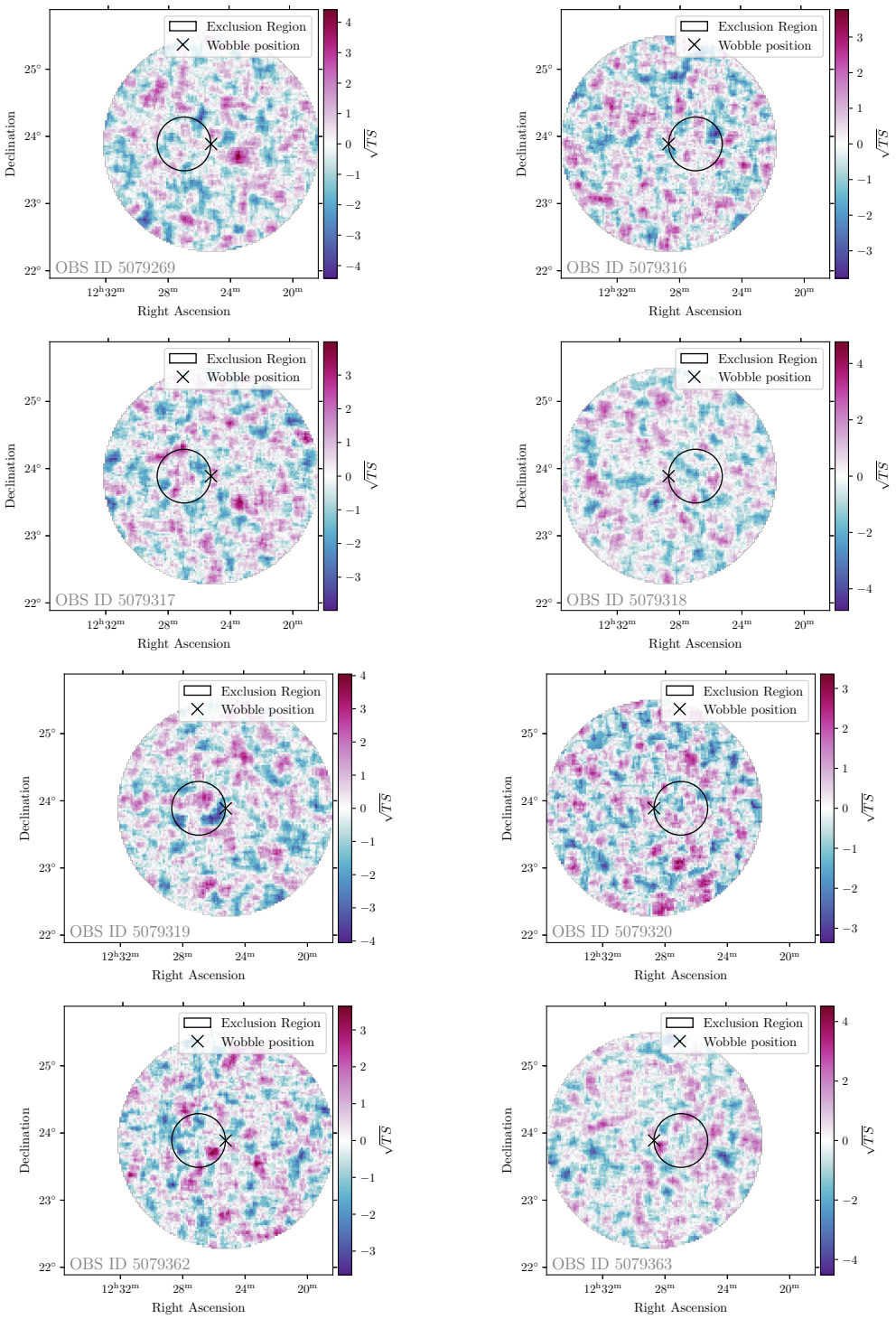

Figure C.5: (continued)

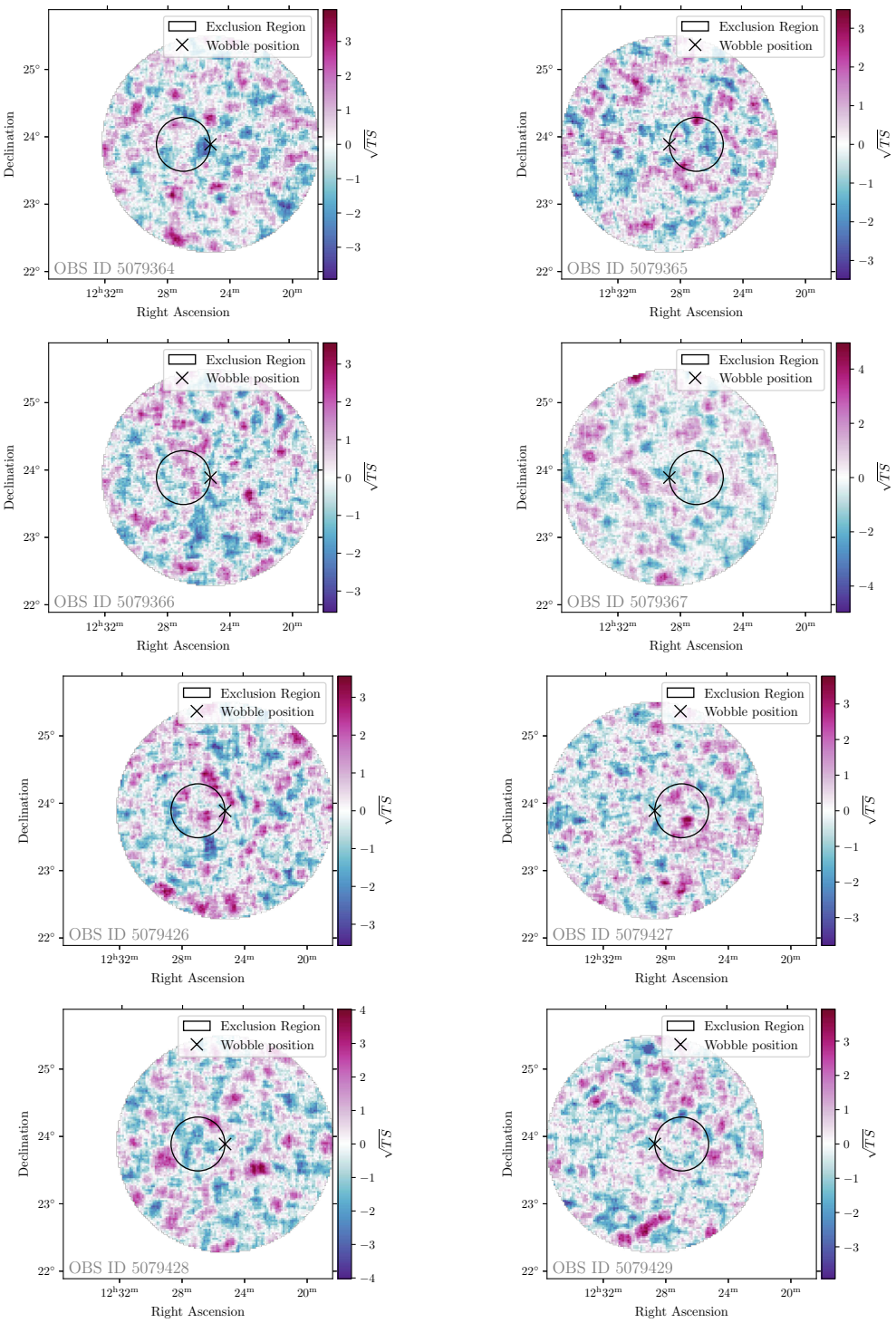

Figure C.5: (continued)

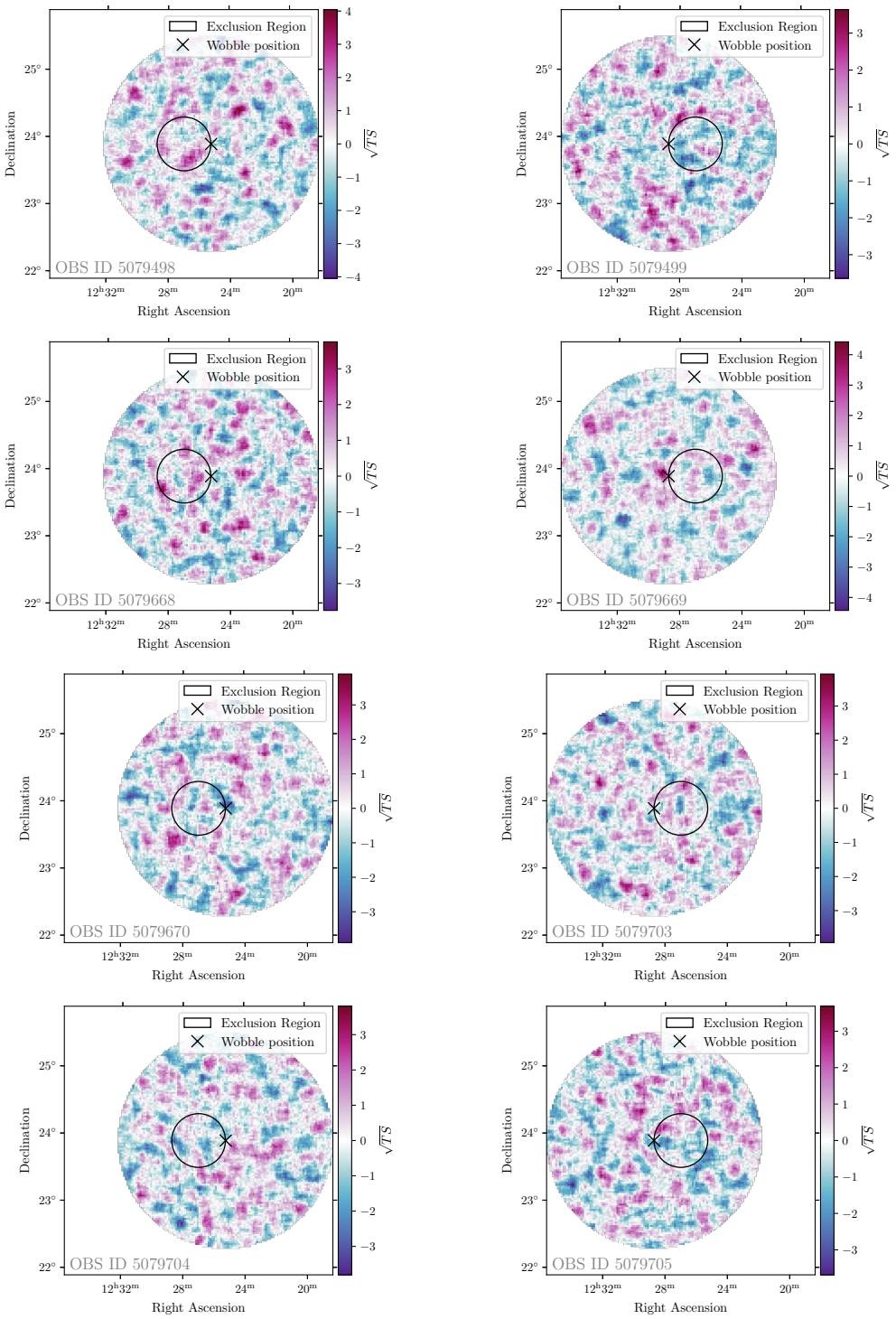

Figure C.5: (continued)

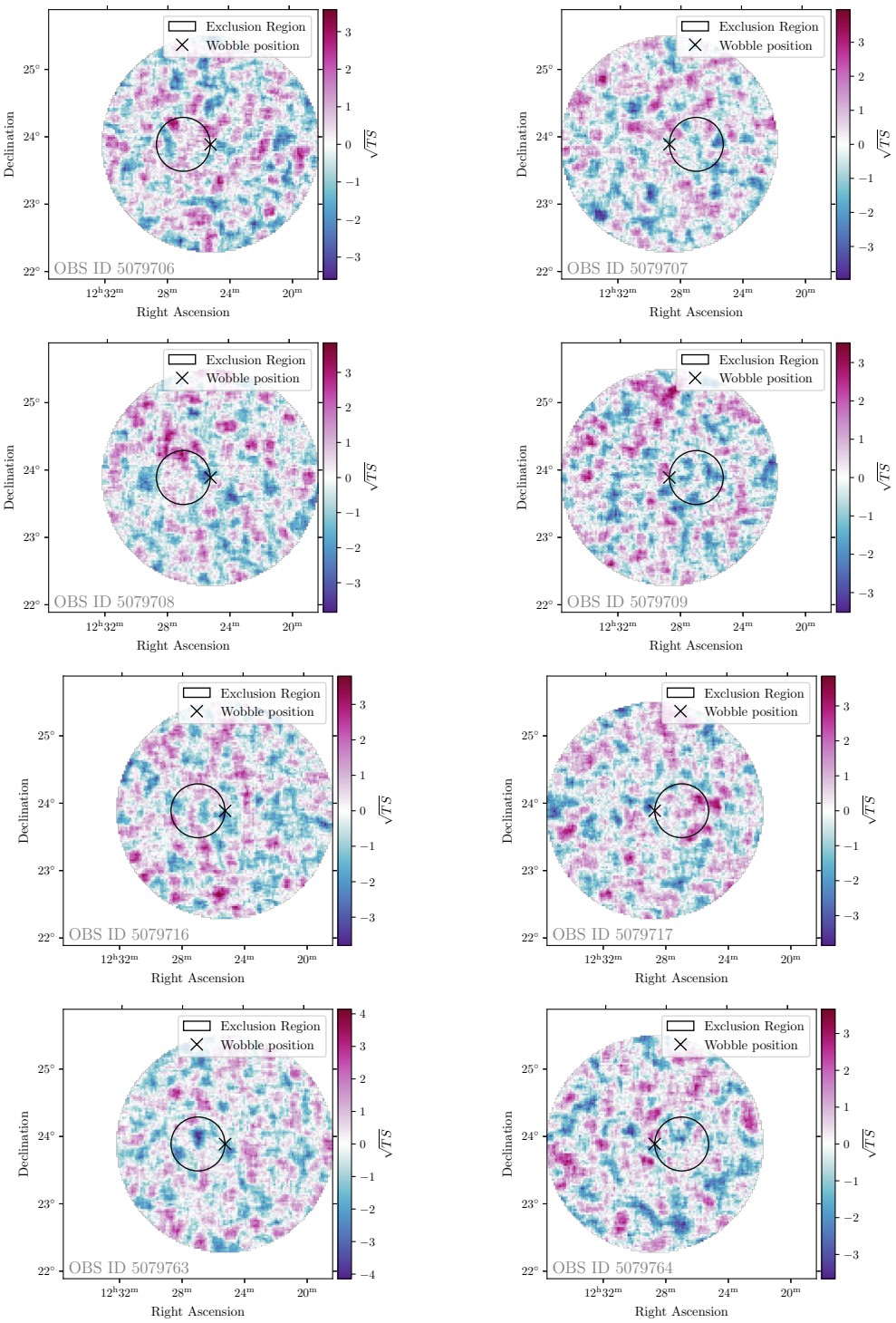

Figure C.5: (continued)

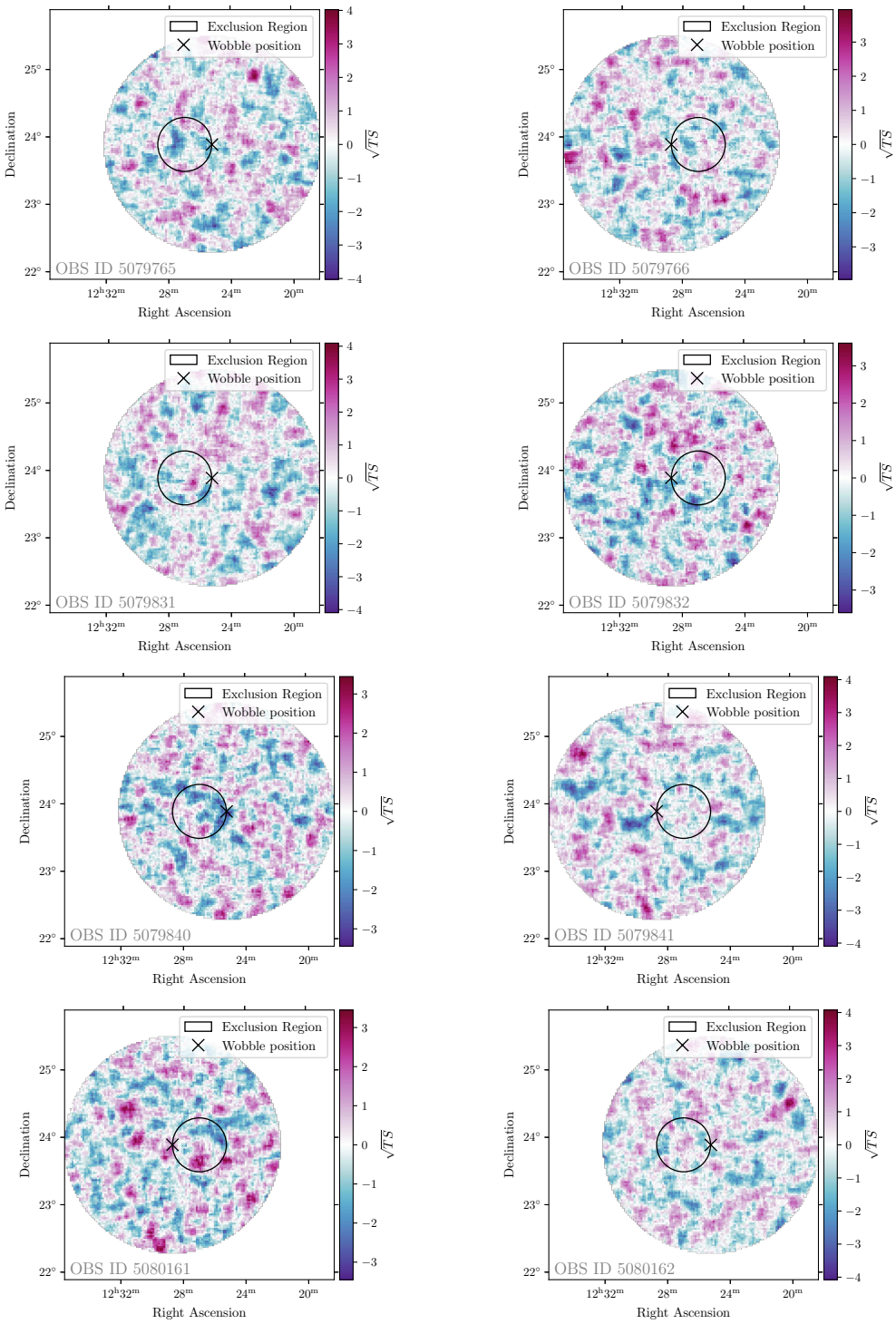

Figure C.5: (continued)

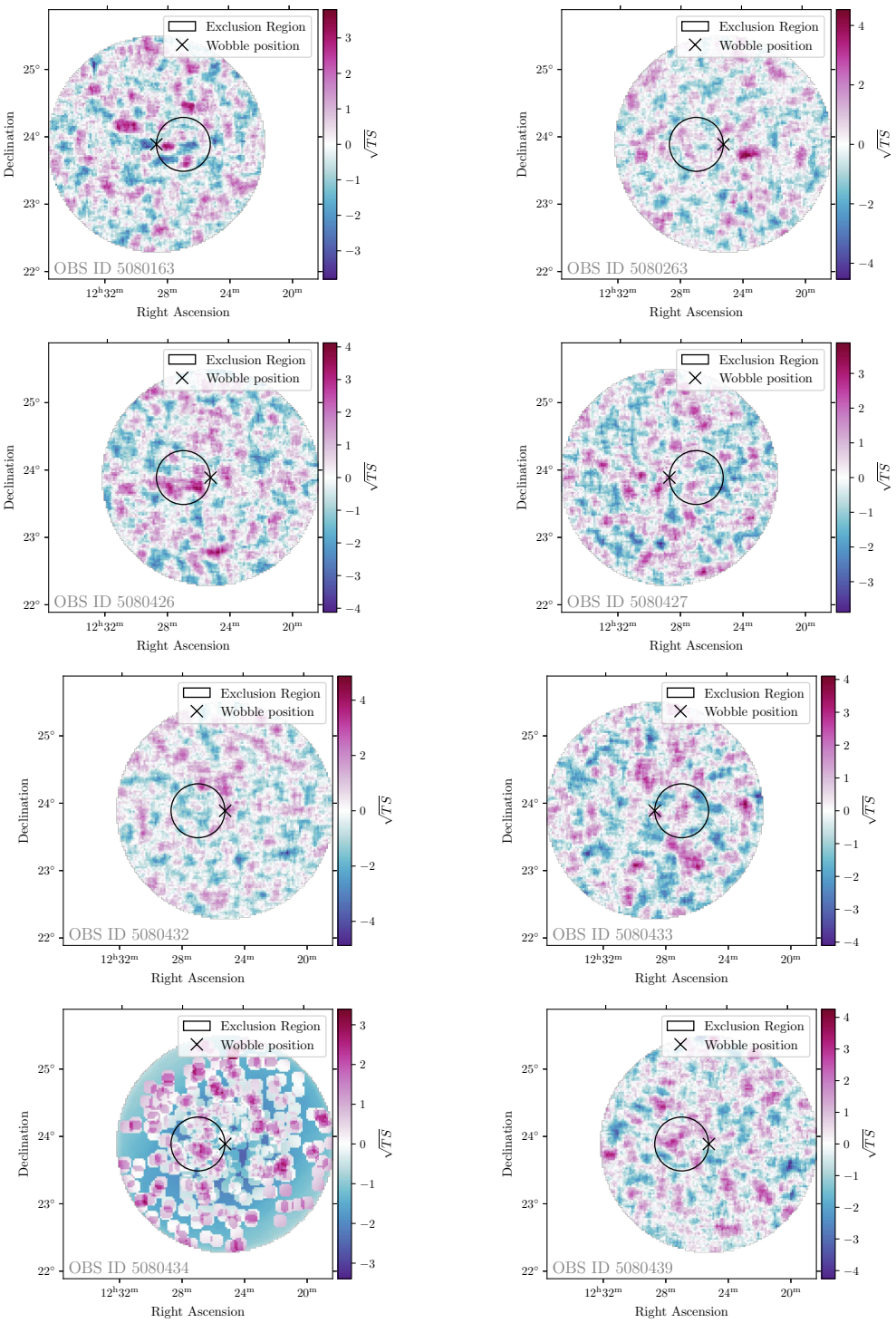

Figure C.5: (continued)

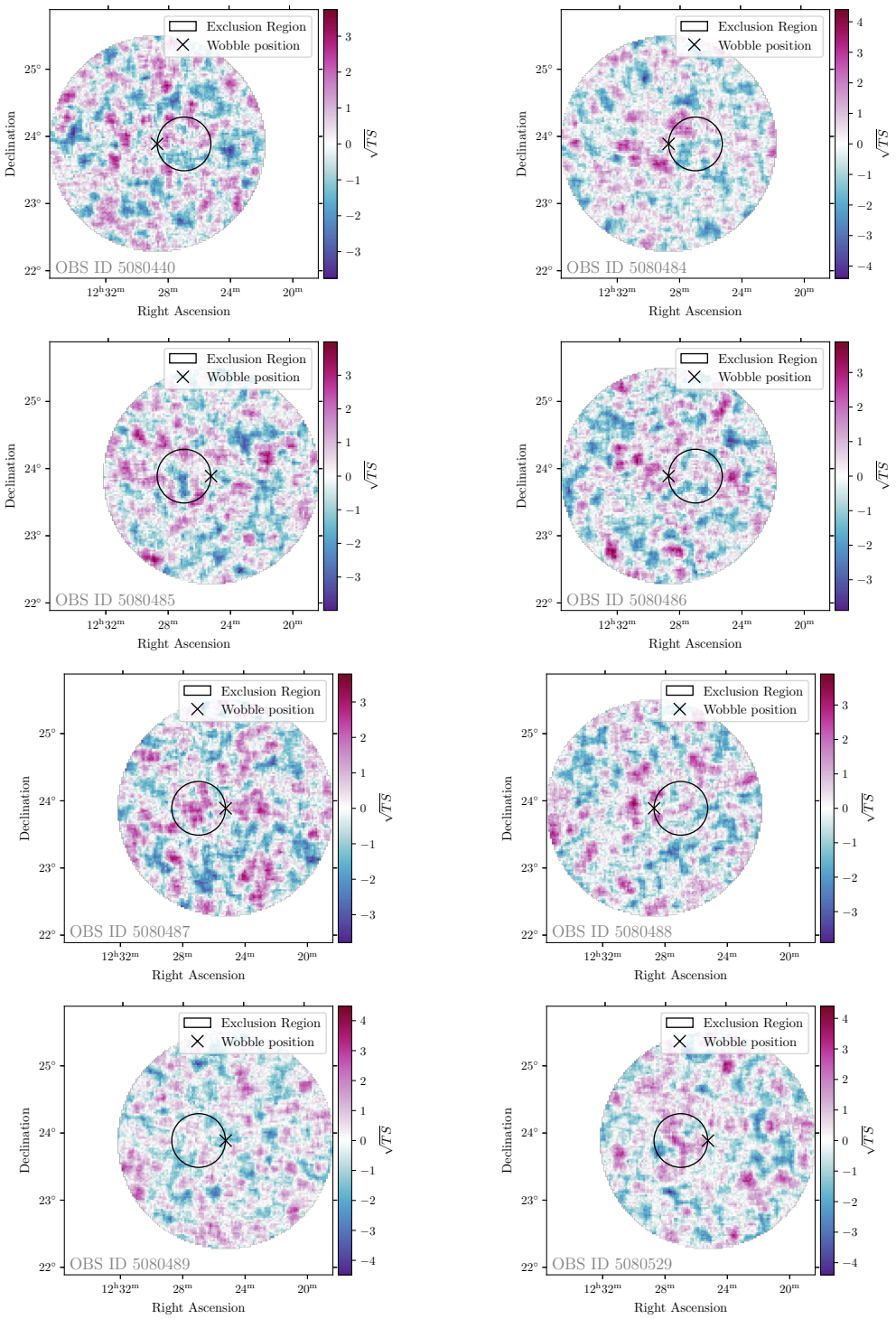

Figure C.5: (continued)

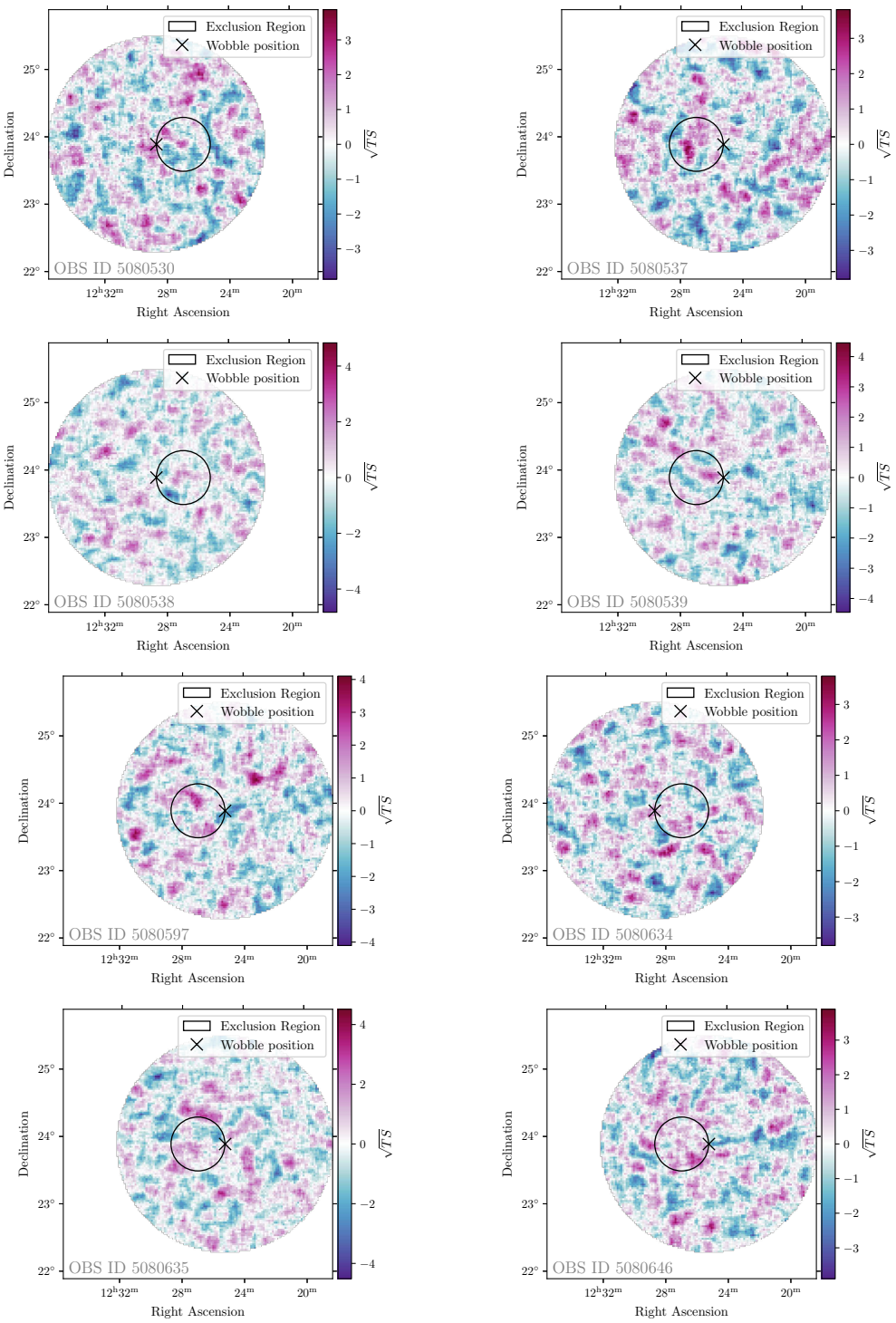

Figure C.5: (continued)

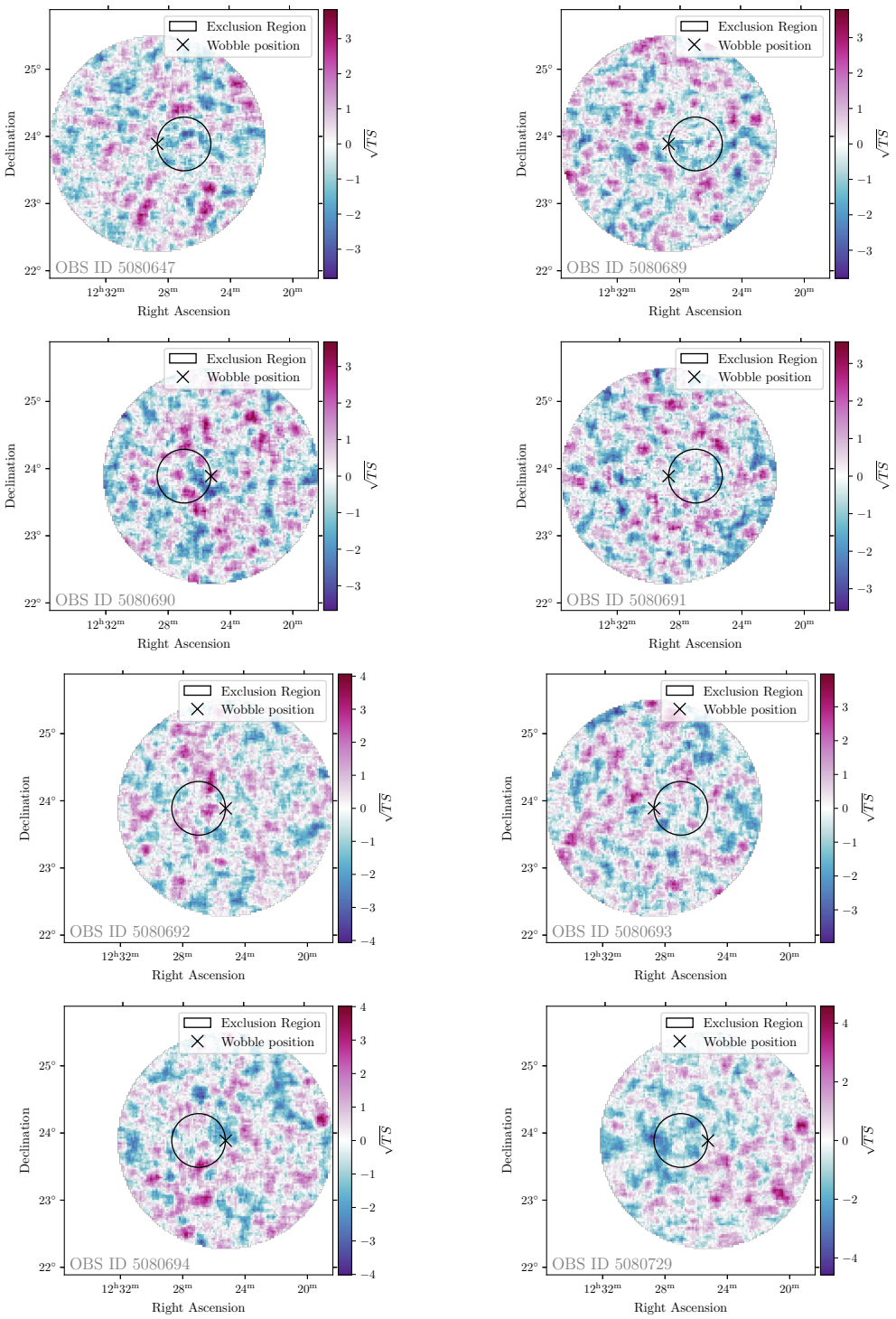

Figure C.5: (continued)

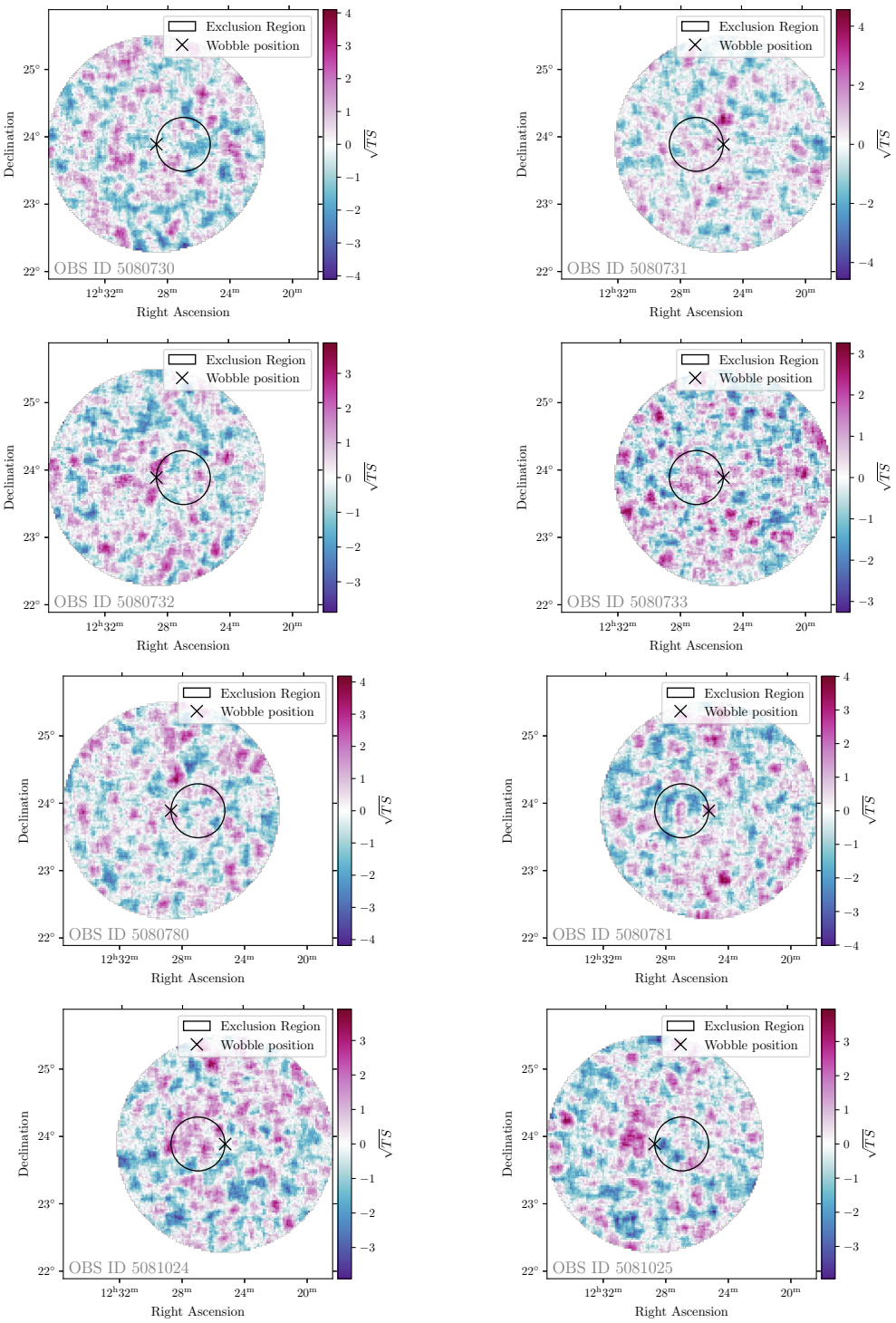

Figure C.5: (continued)

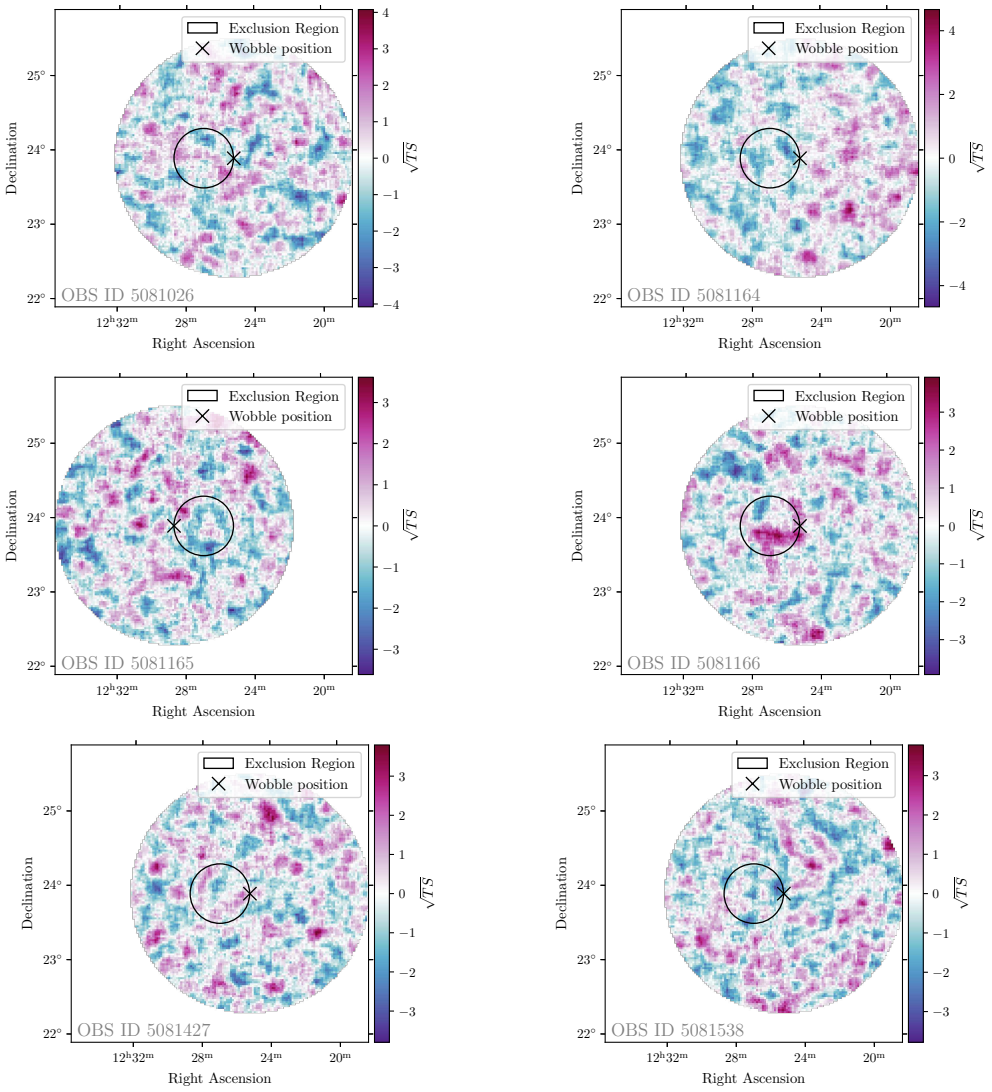

Figure C.5: (continued)

C.3 TS Histograms

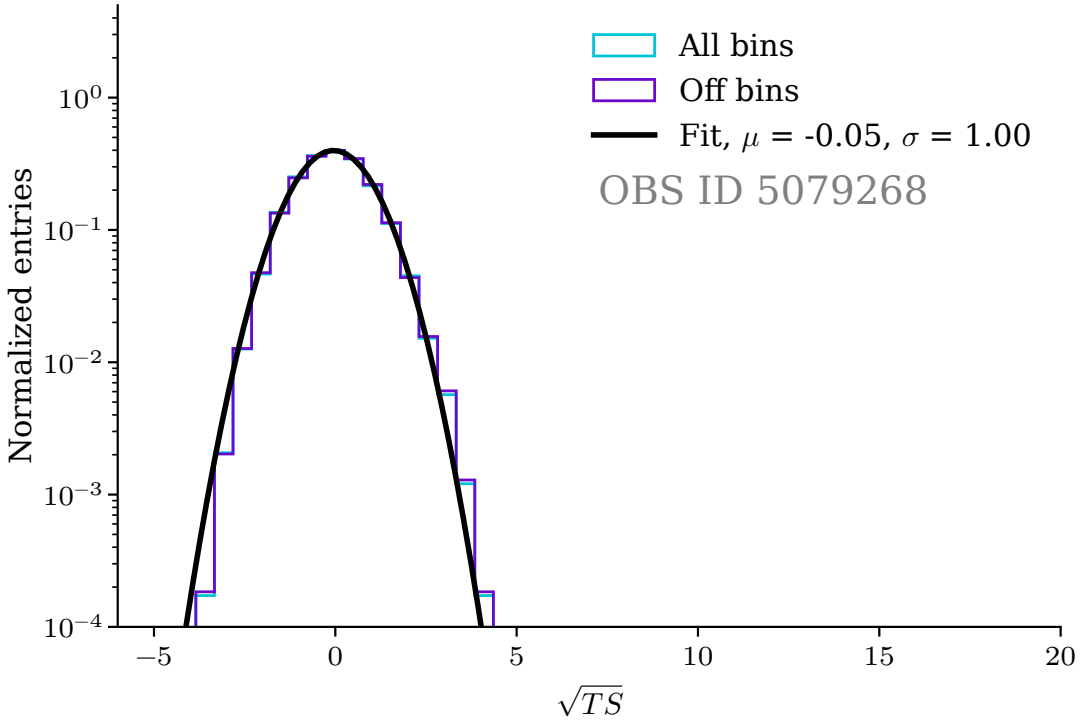

Figure C.6: Histograms for the significance values of for all CBe dSph observations, outside the exclusion regions, *Off* bins, and within the complete map, *All* bins. A normal distribution is fitted to the *Off* bins. Continued on following pages.

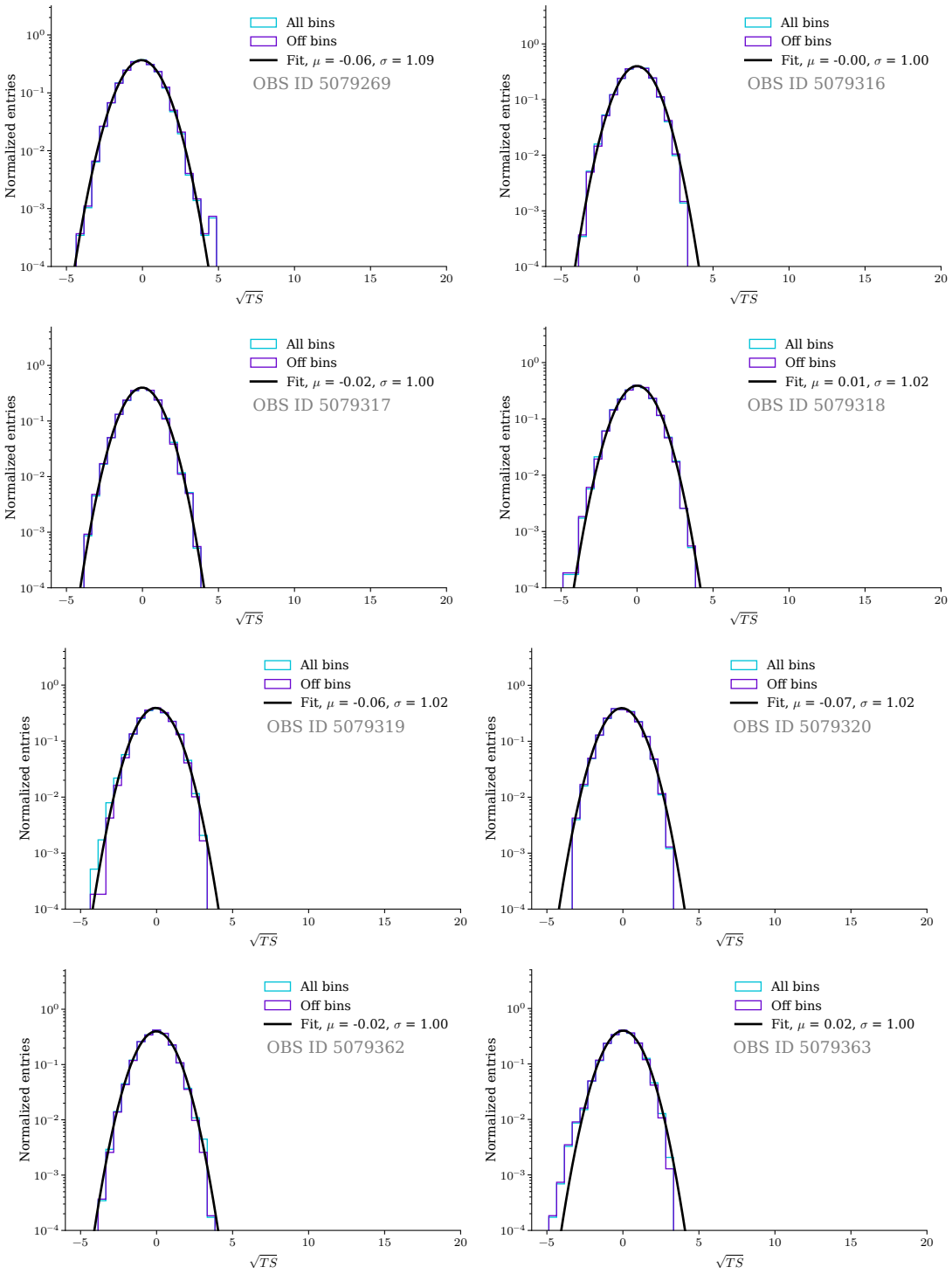

Figure C.6: (continued)

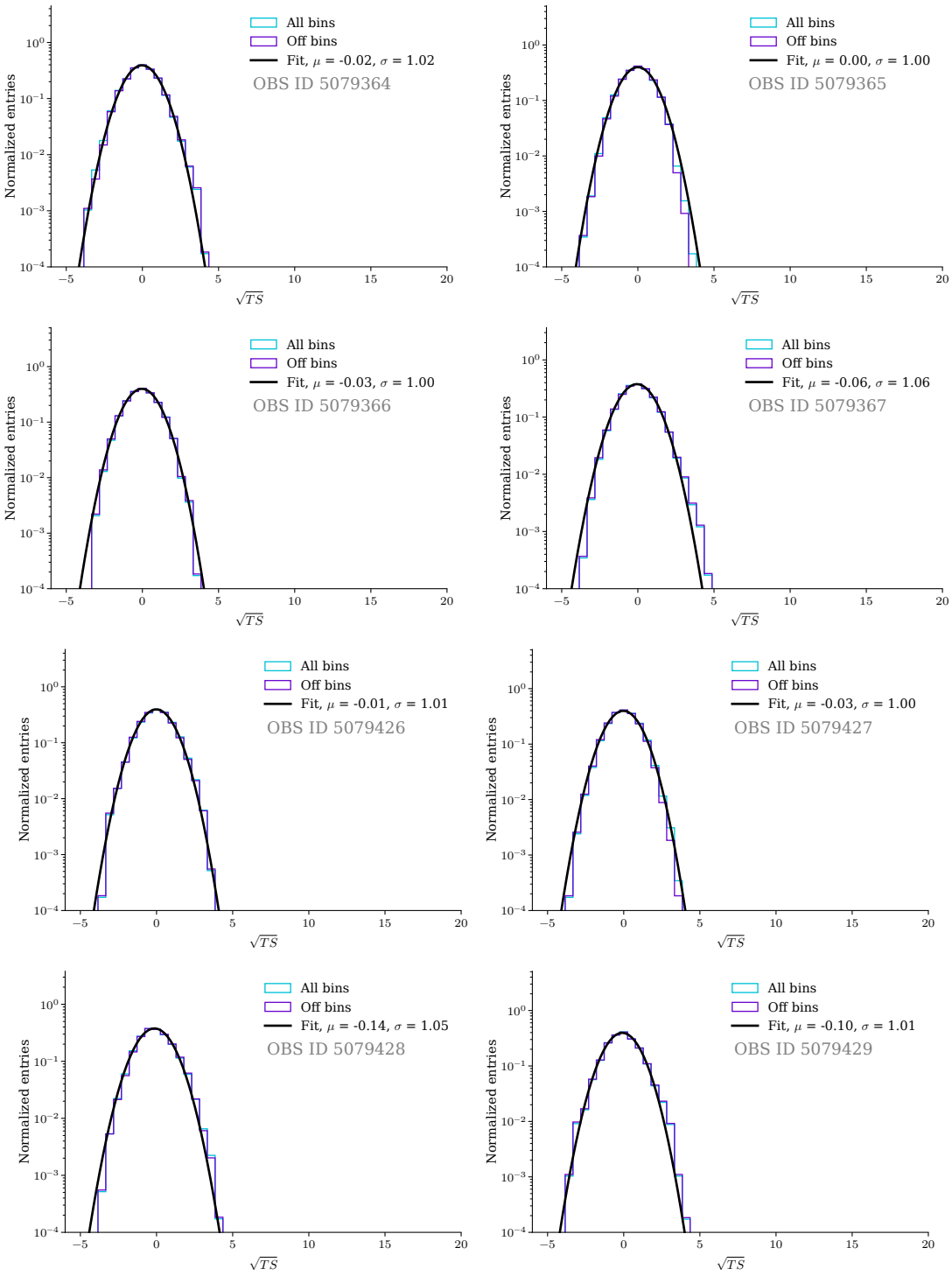

Figure C.6: (continued)

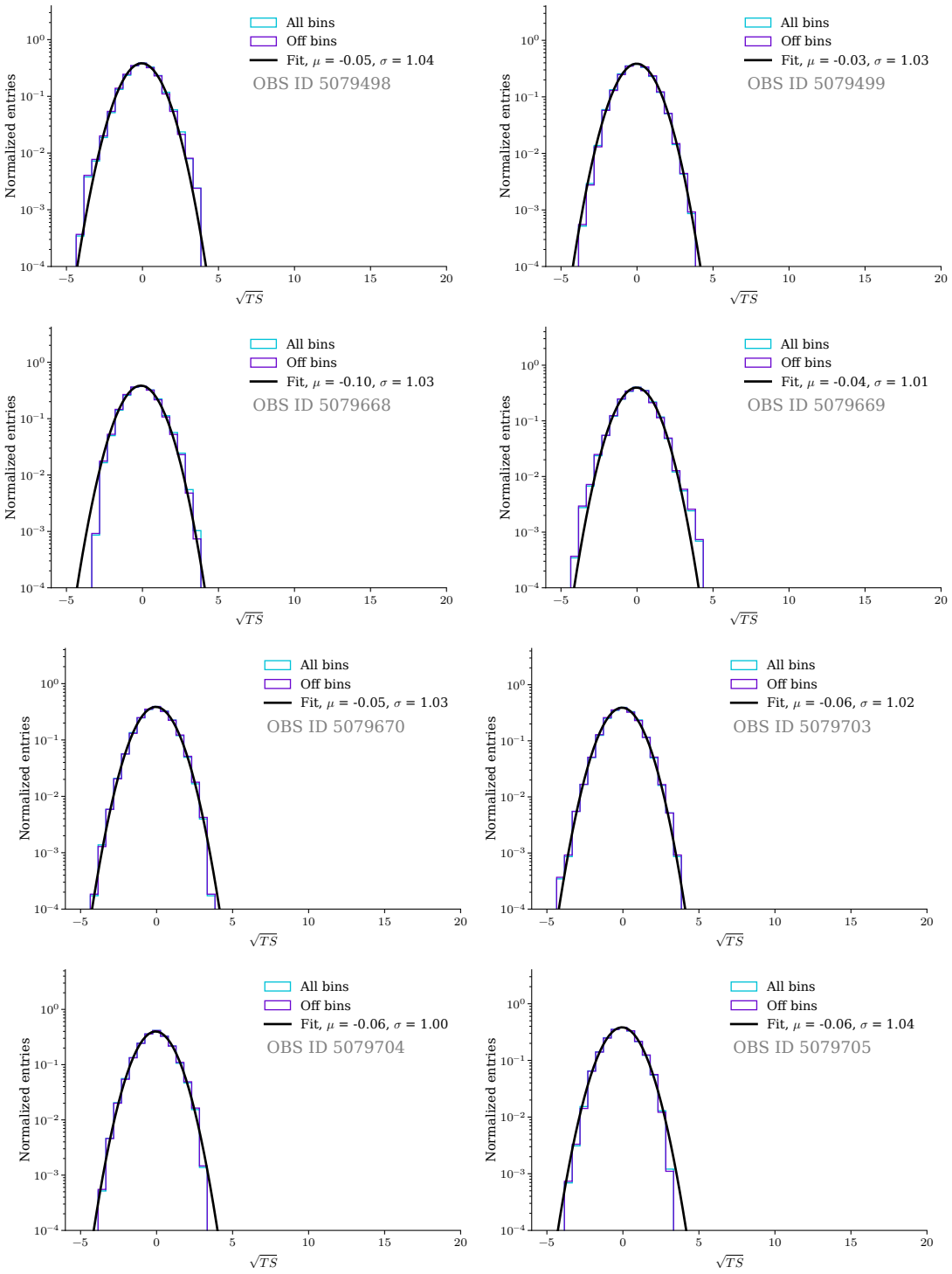

Figure C.6: (continued)

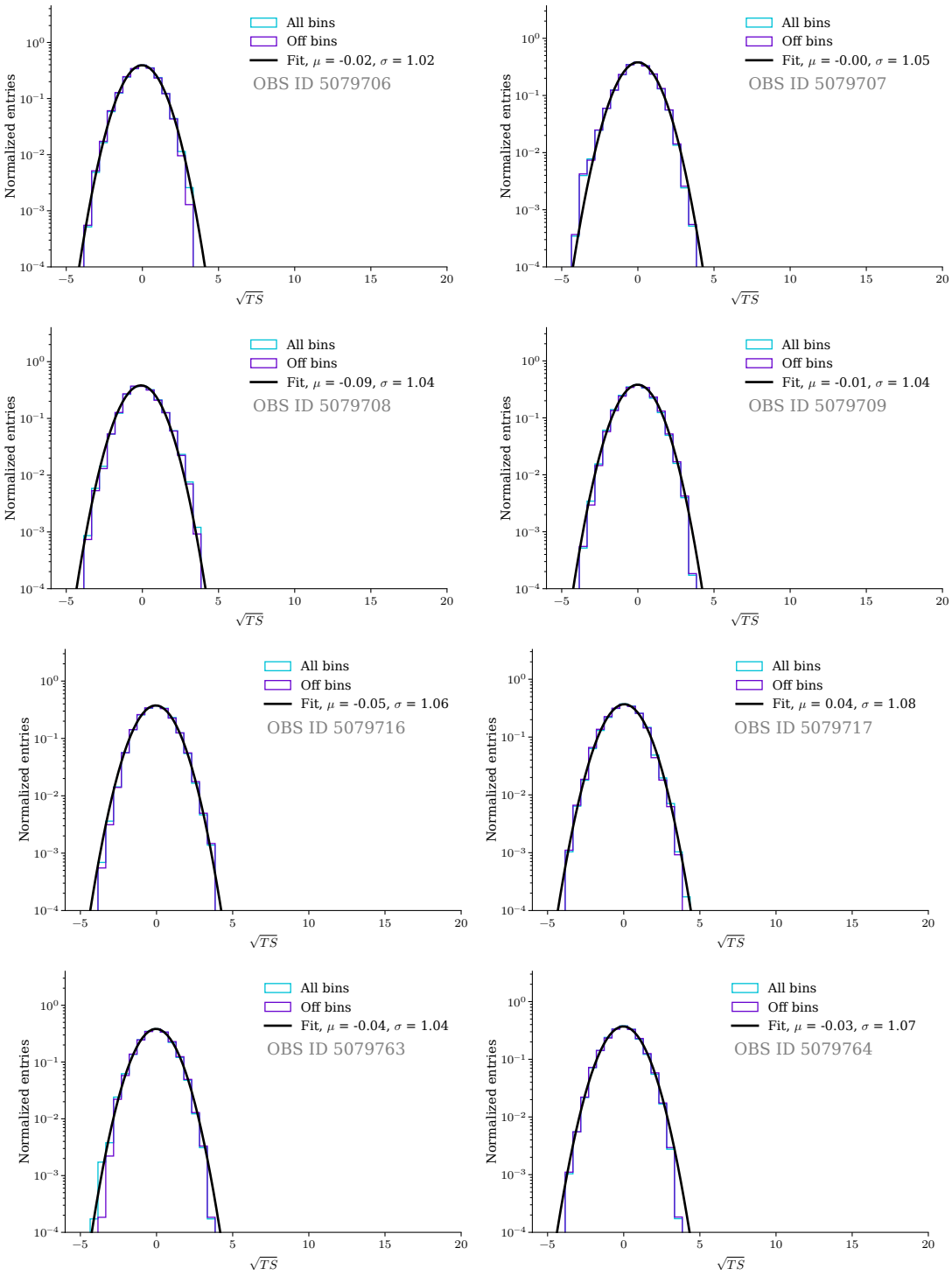

Figure C.6: (continued)

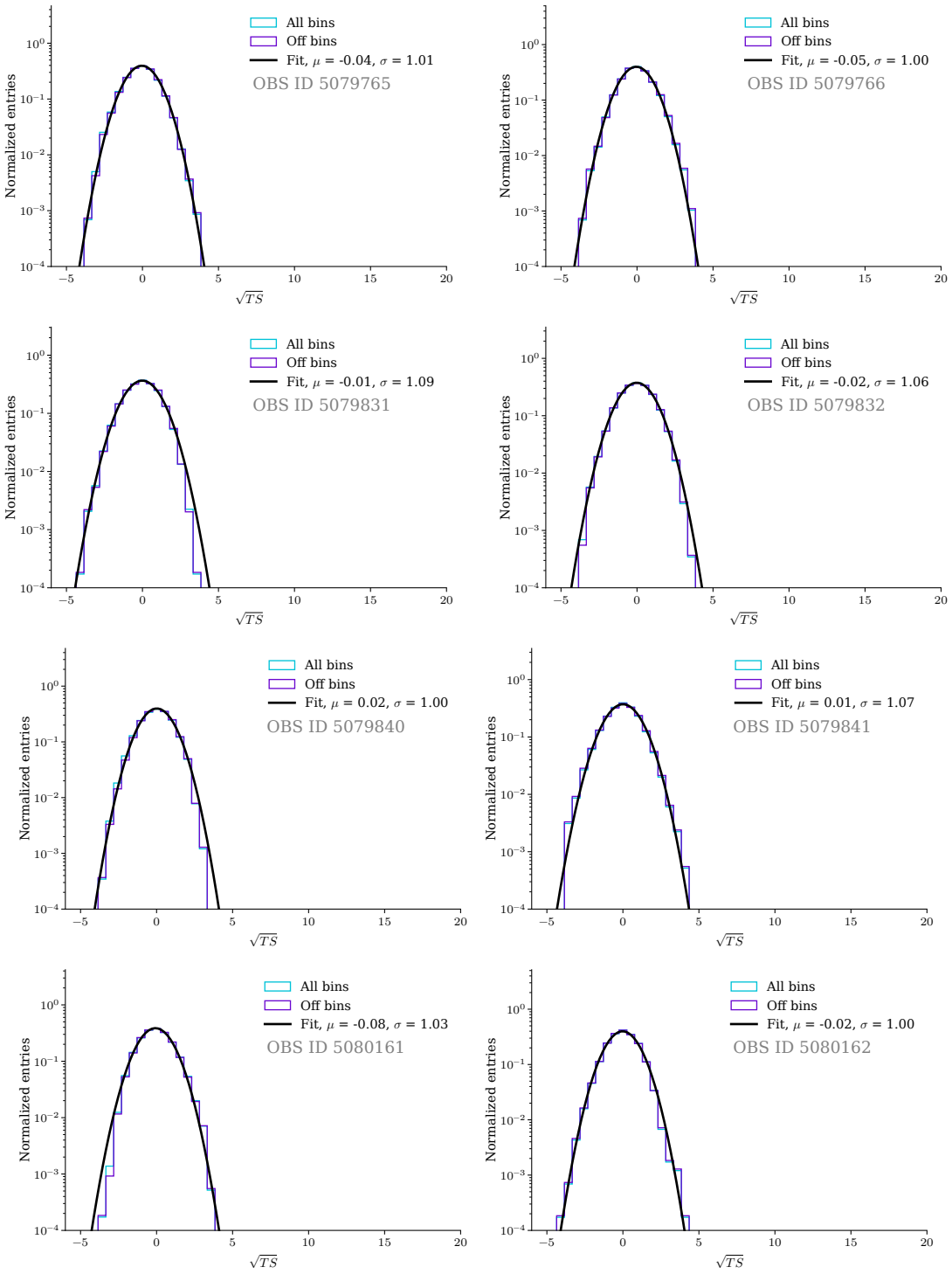

Figure C.6: (continued)

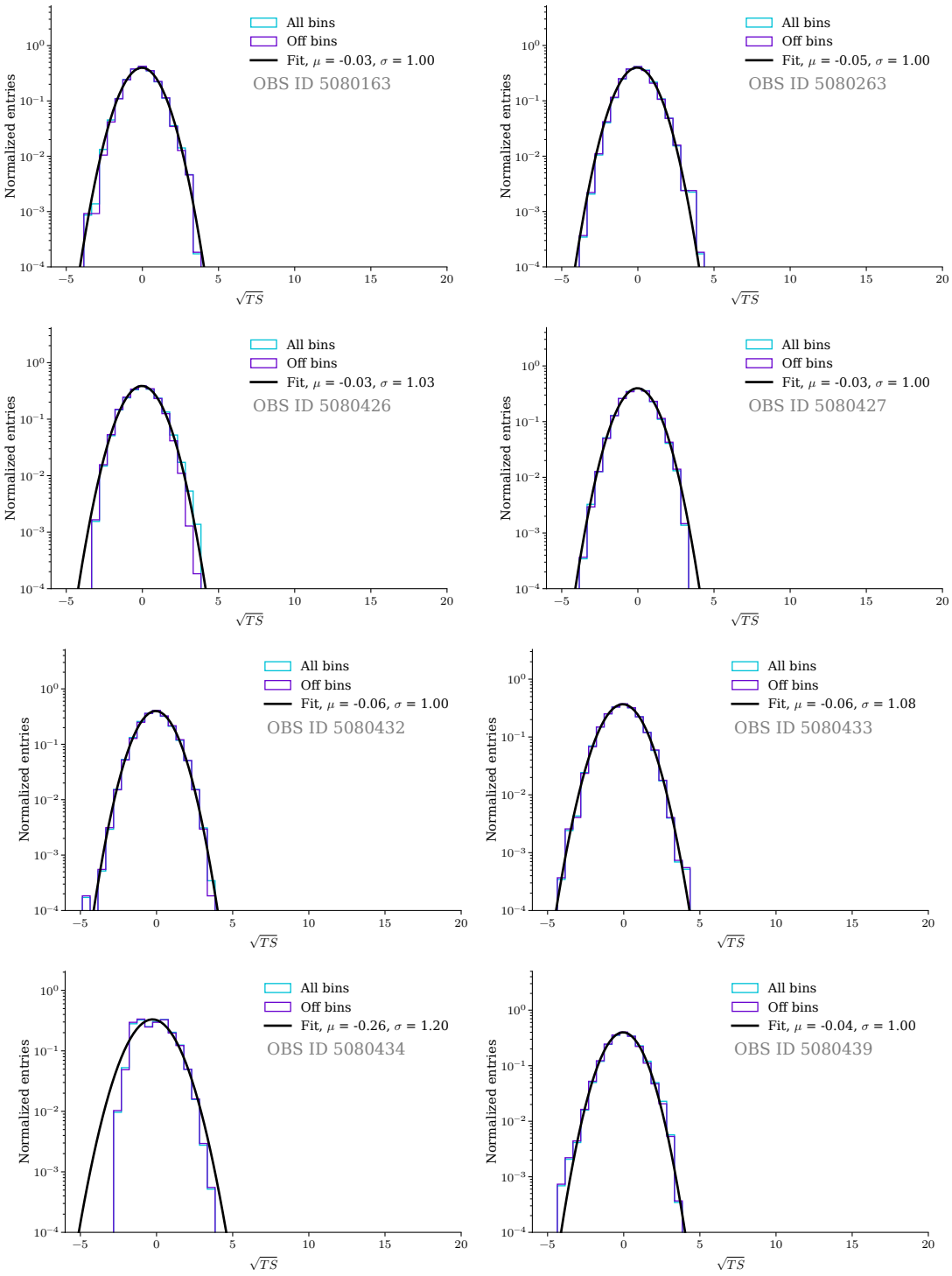

Figure C.6: (continued)

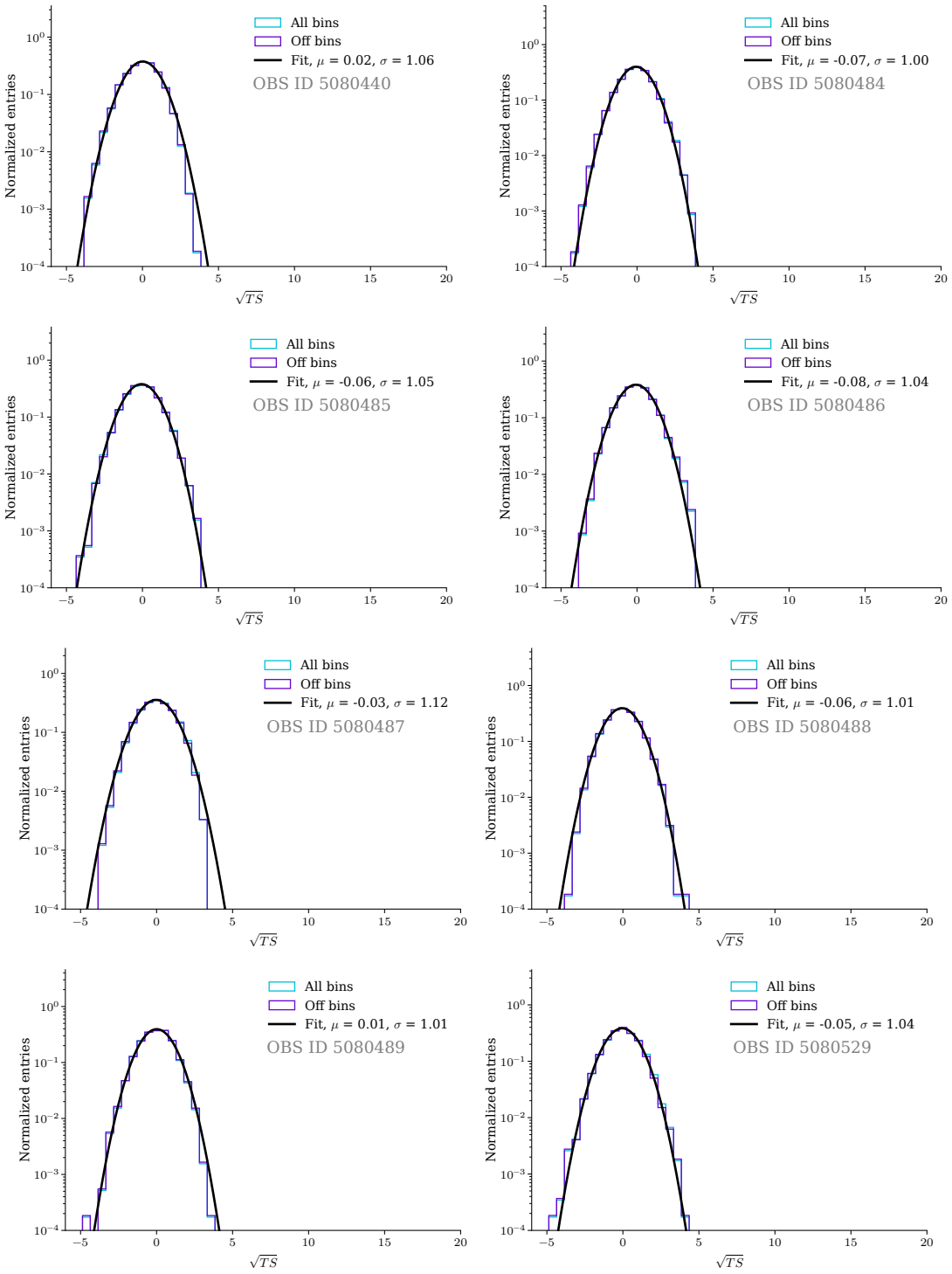

Figure C.6: (continued)

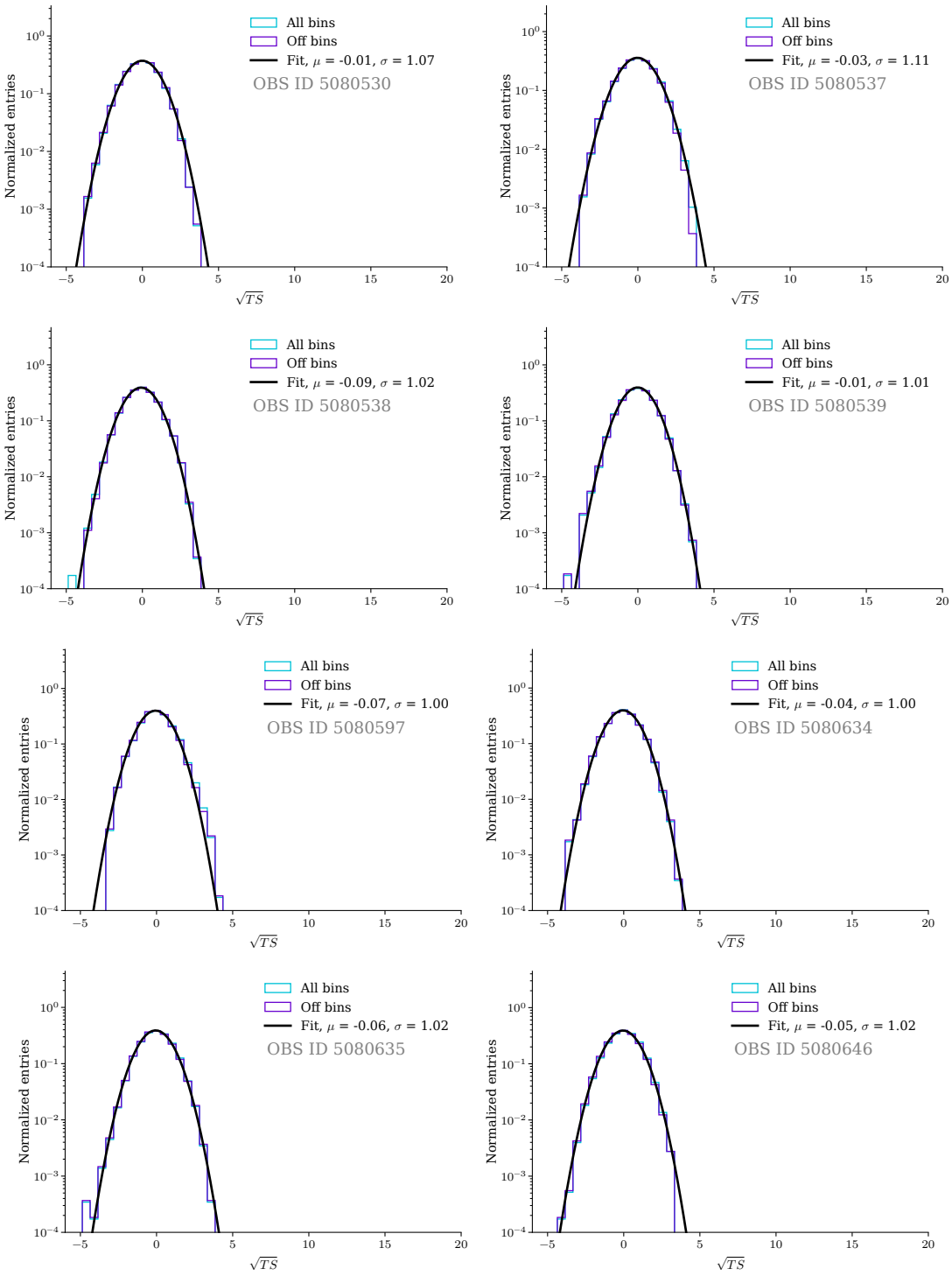

Figure C.6: (continued)

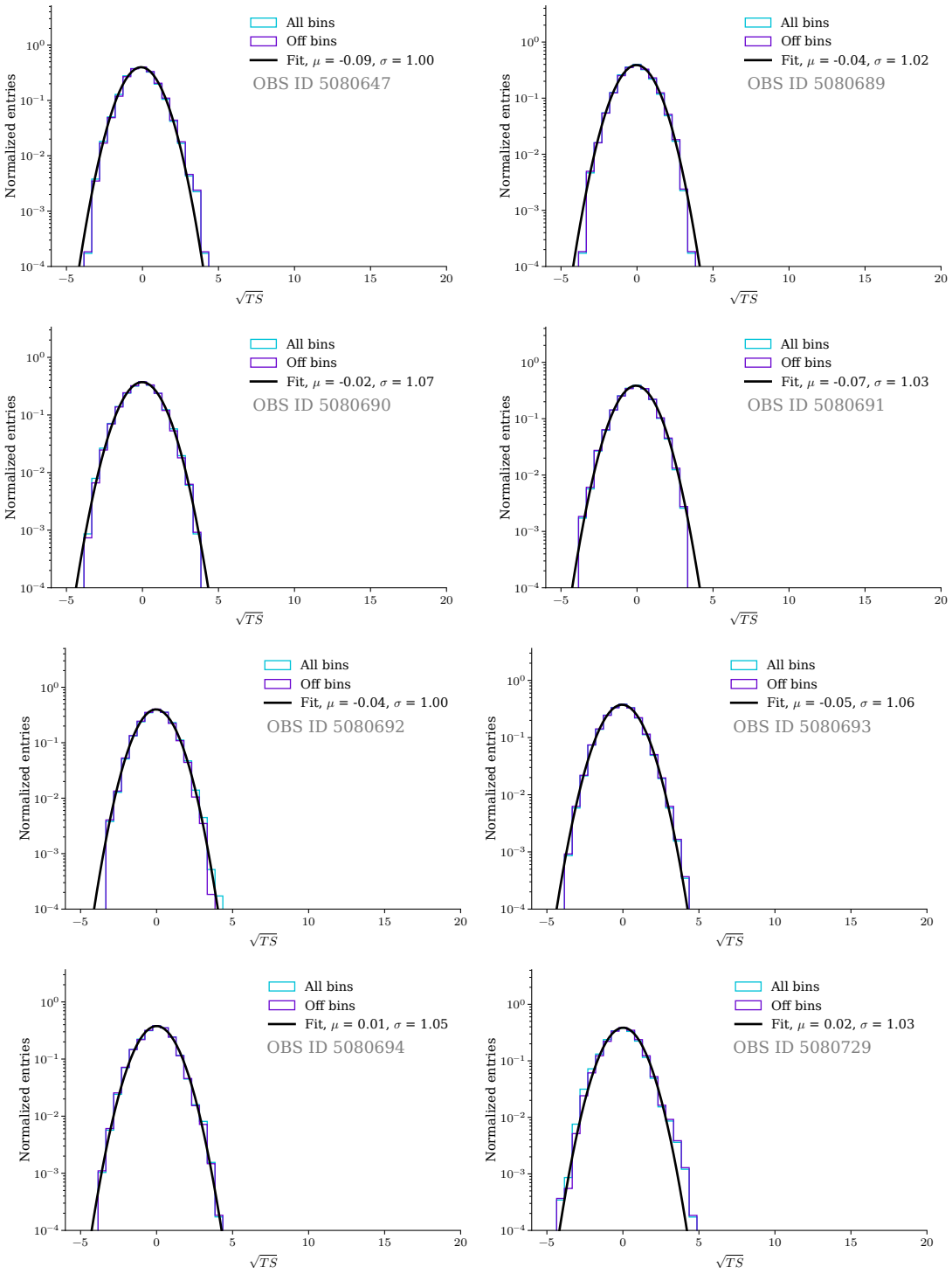

Figure C.6: (continued)

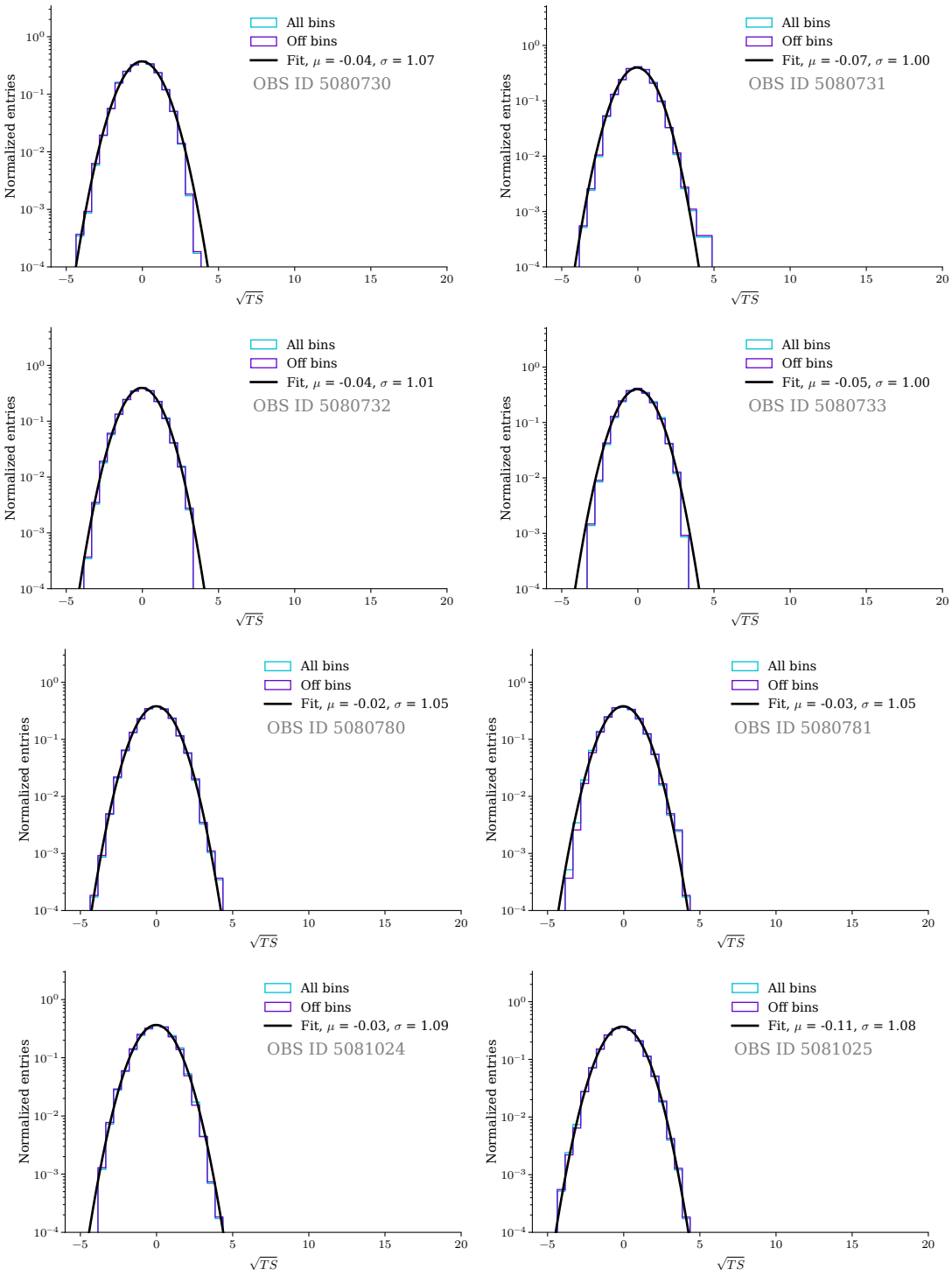

Figure C.6: (continued)

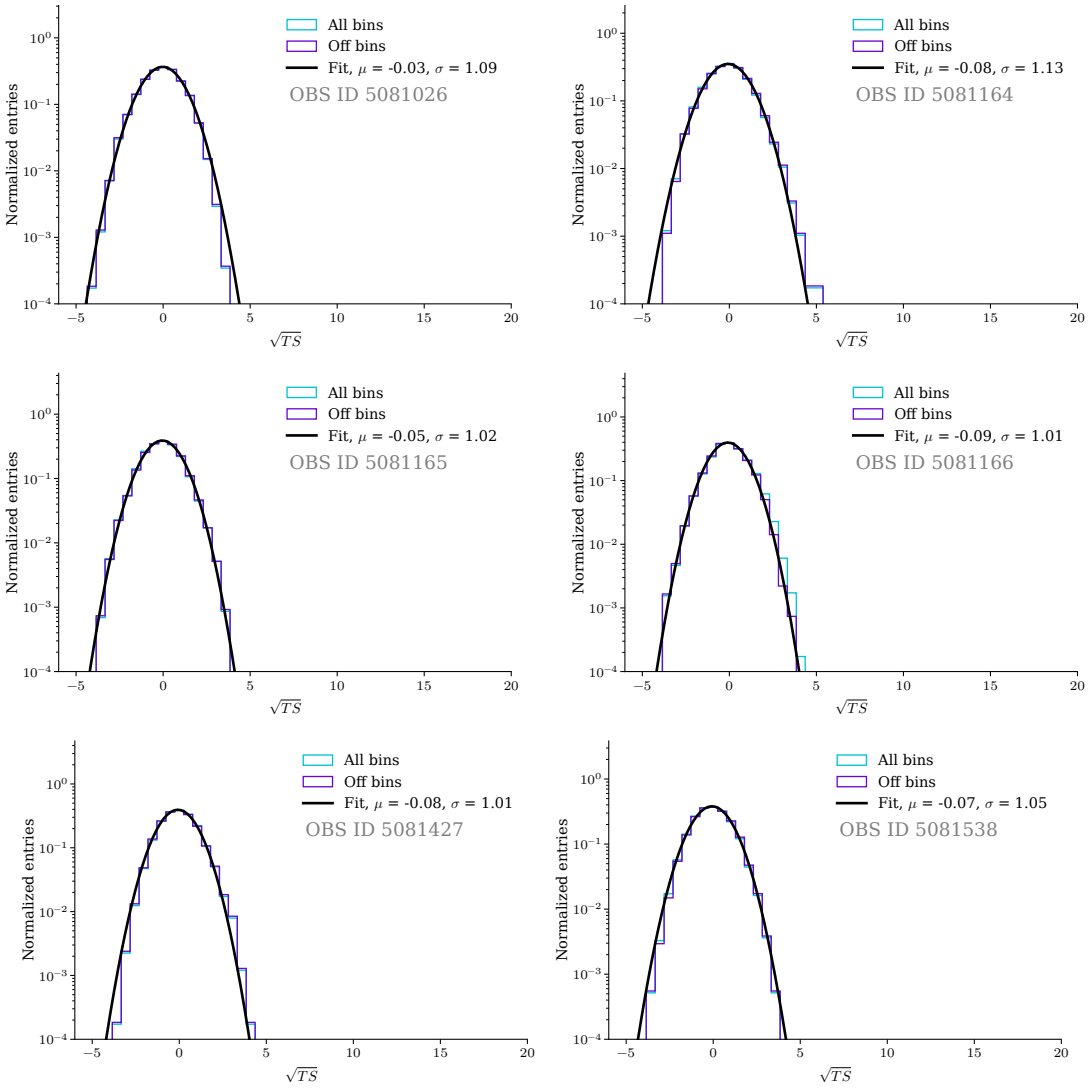

Figure C.6: (continued)

D DL4 Cubes Crab Nebula

This chapter displays the excess maps, TS maps, and TS histograms for the Crab Nebula DL4 cubes.

D.1 Excess Maps

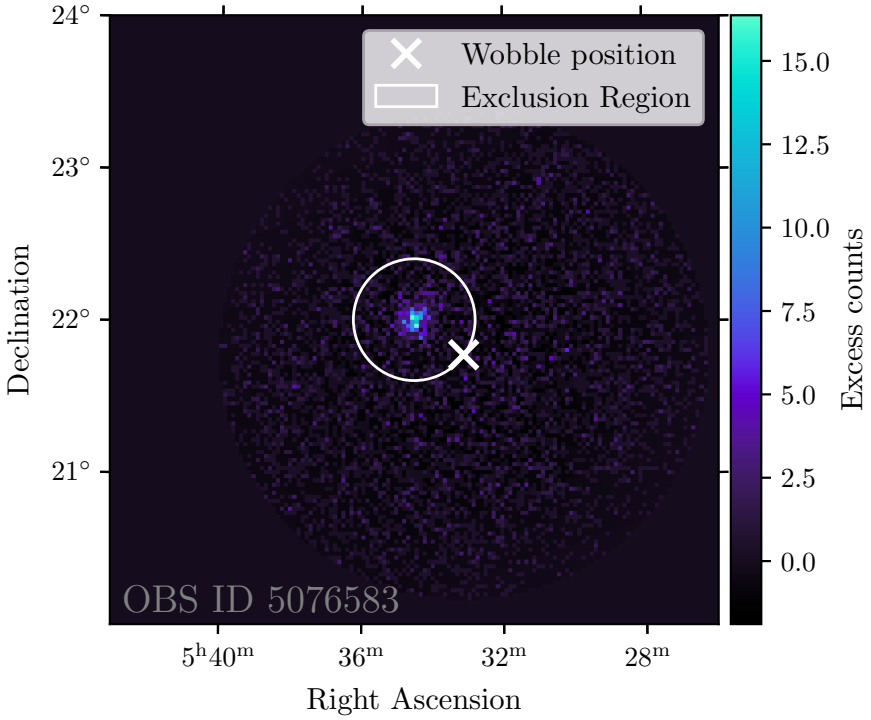

Figure D.7: Excess counts of all Crab Nebula observations integrated over the energy axis. The map is centered on the coordinates of the nebula. The white circle illustrates the exclusion region used for the background modelling, whereas the white cross denotes the Wobble position of the observation. Continued on following pages.

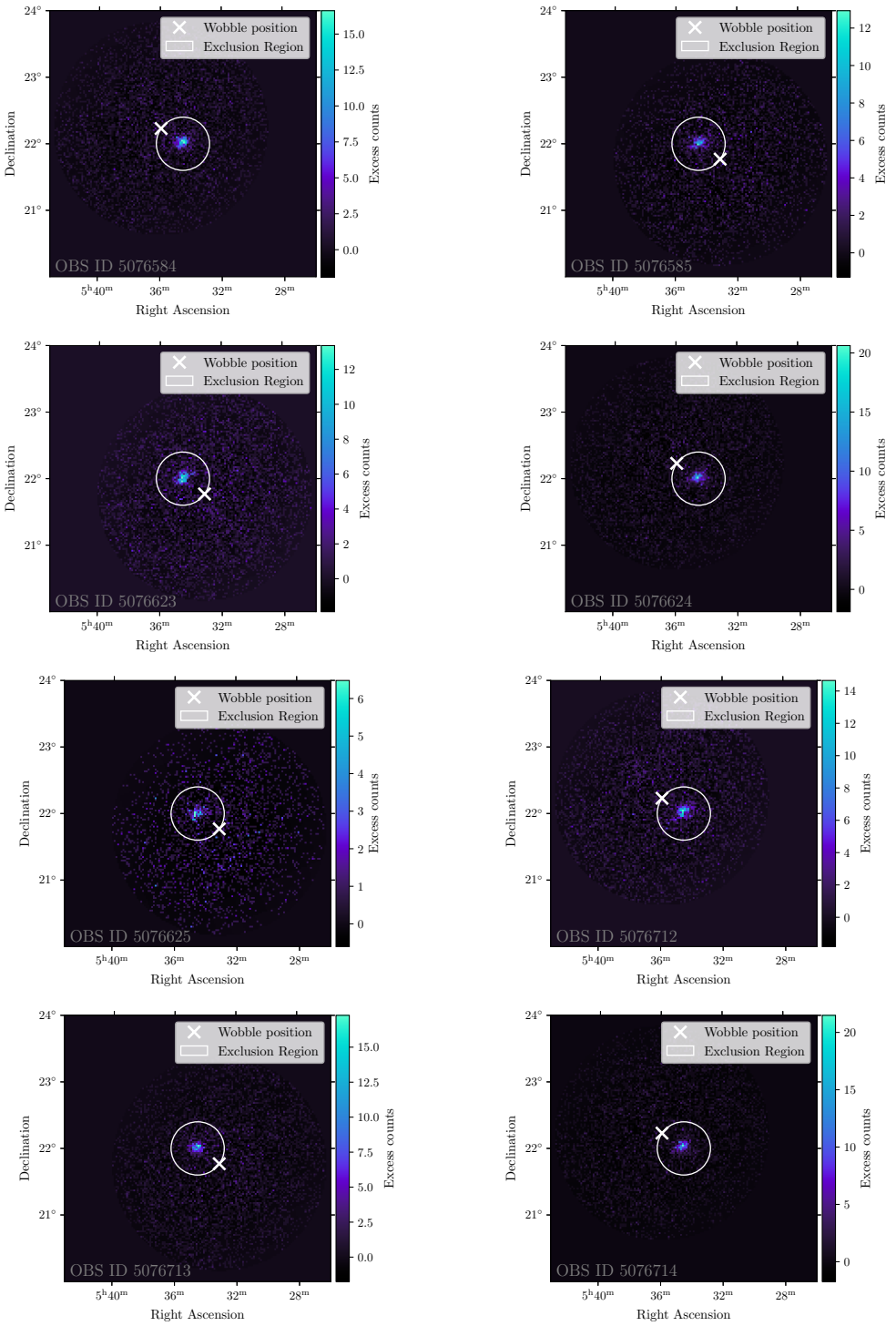

Figure D.7: (continued)

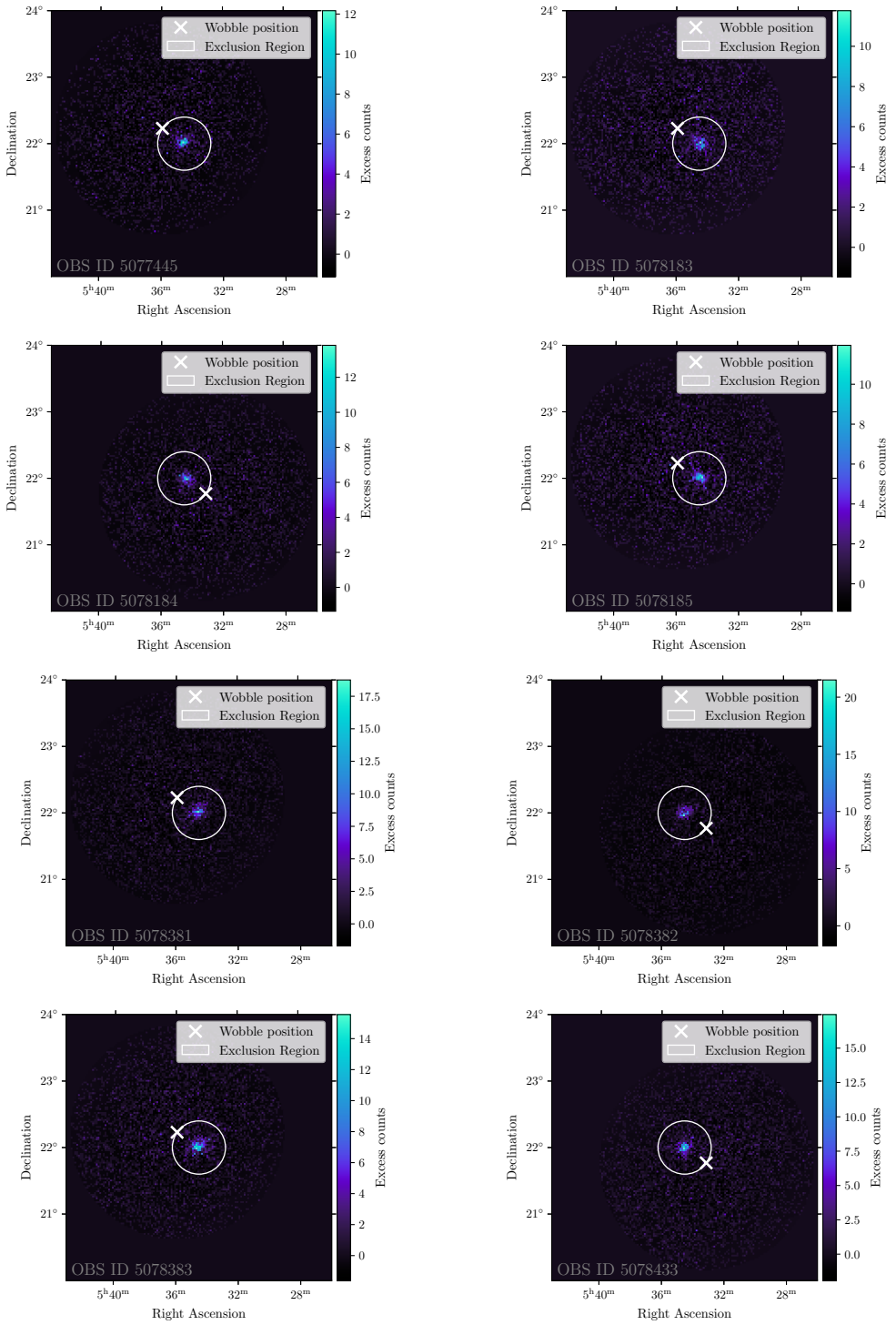

Figure D.7: (continued)

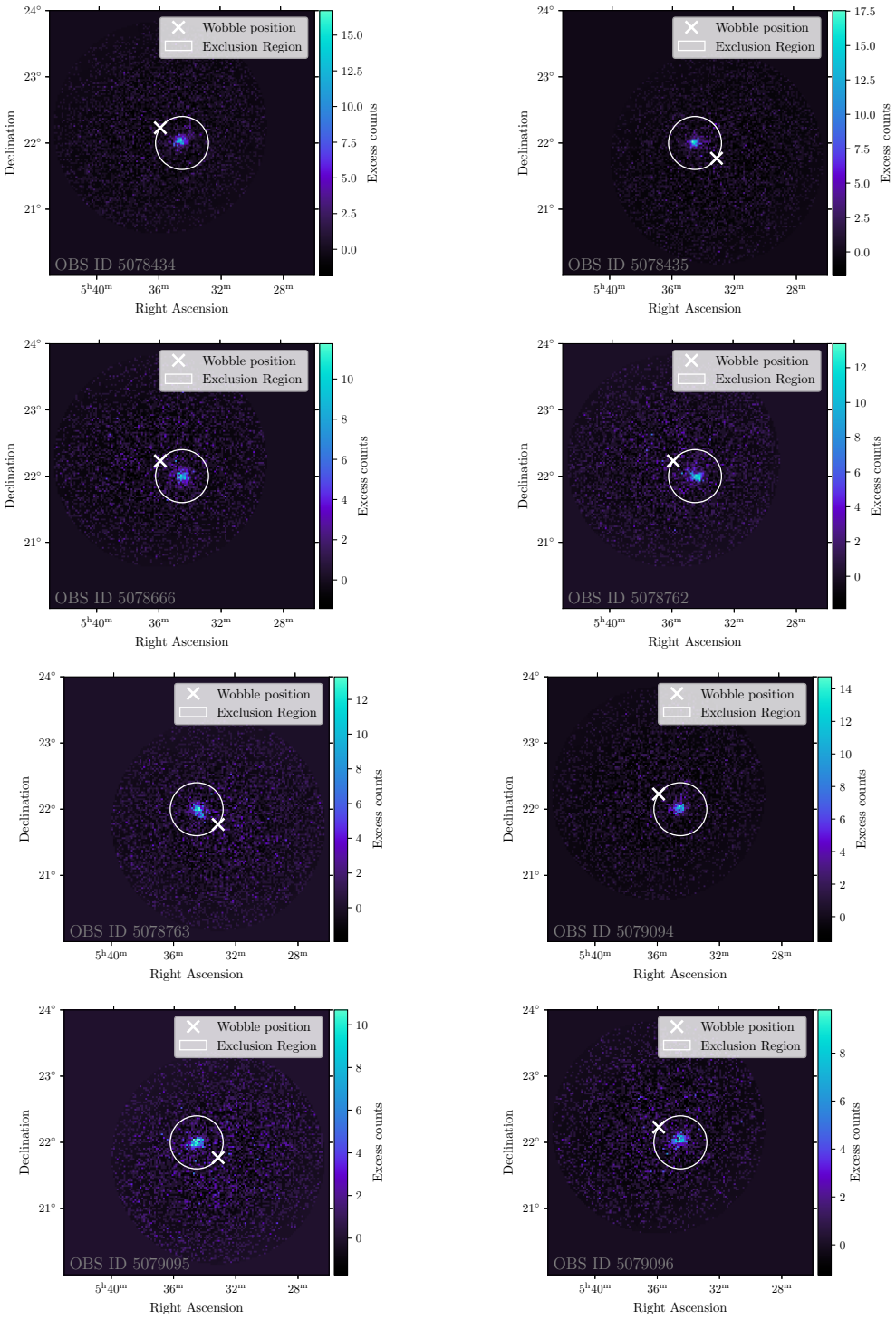

Figure D.7: (continued)

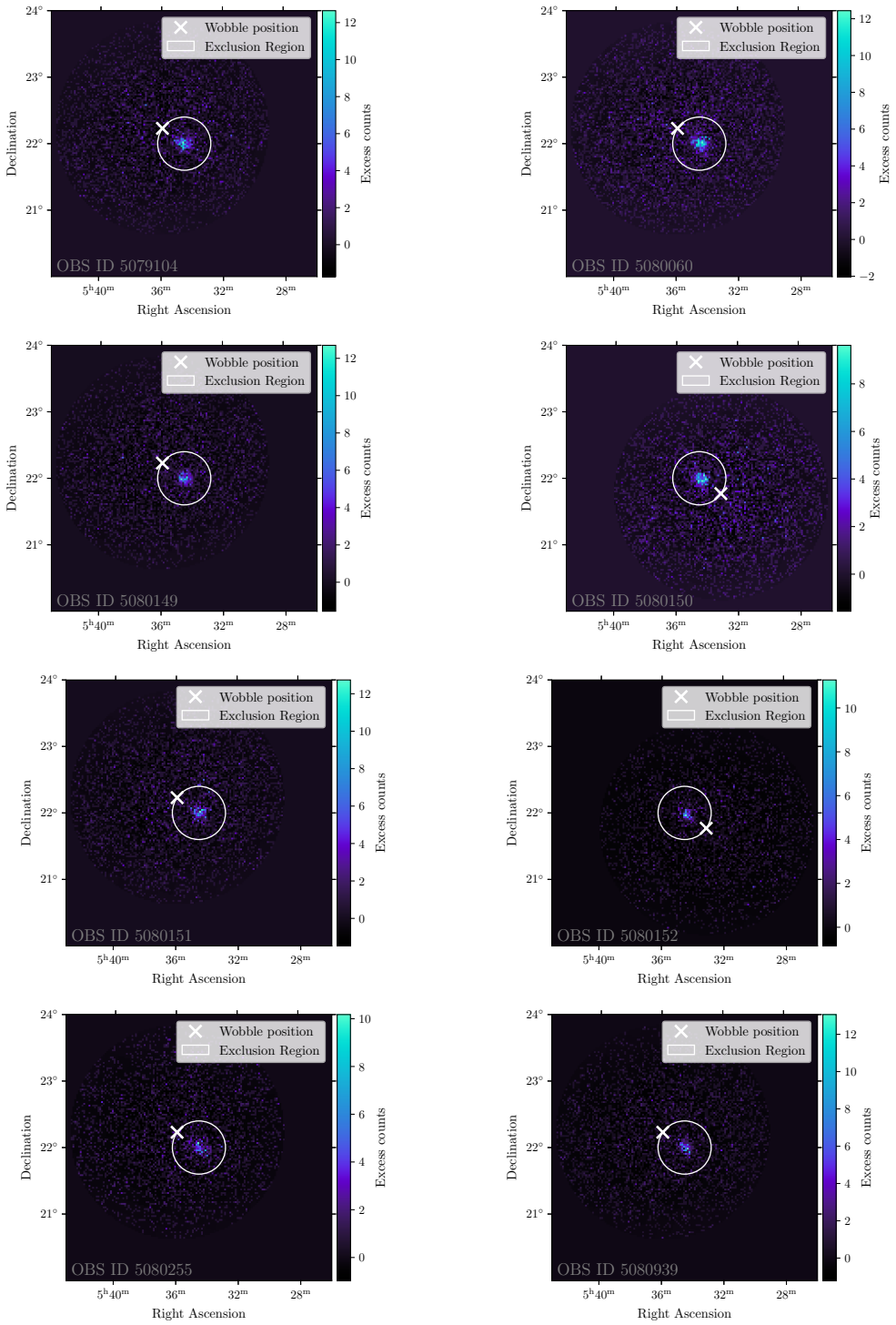

Figure D.7: (continued)

D.2 TS Maps

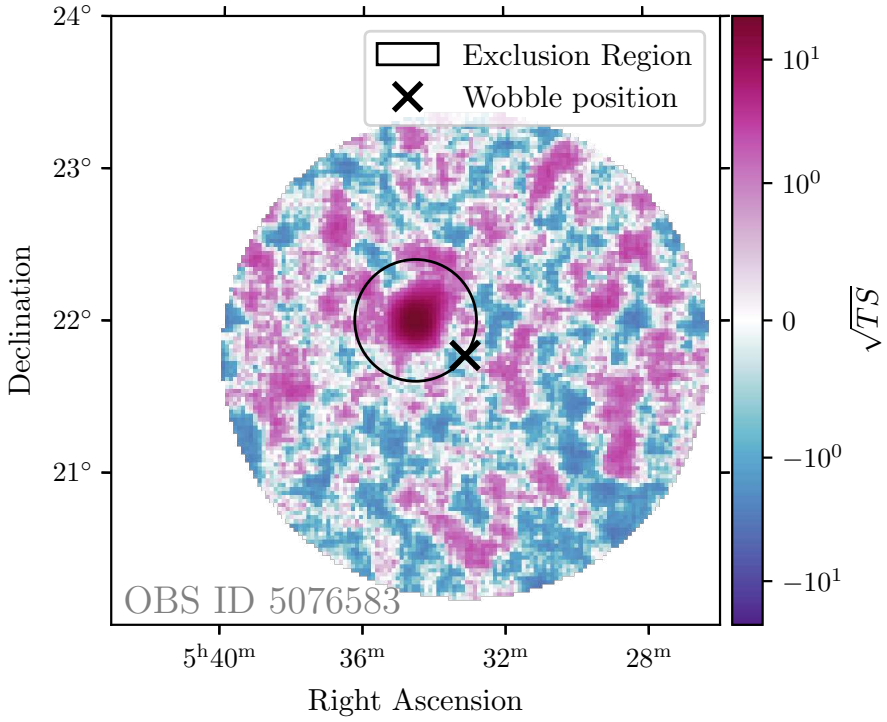

Figure D.8: Significance map of all Crab Nebula observation, integrated over the energy axis. The map is centered on the coordinates of the nebula. The black circle illustrates the exclusion region used for the background modelling, whereas the black cross denotes the Wobble position of the observation. Continued on following pages.

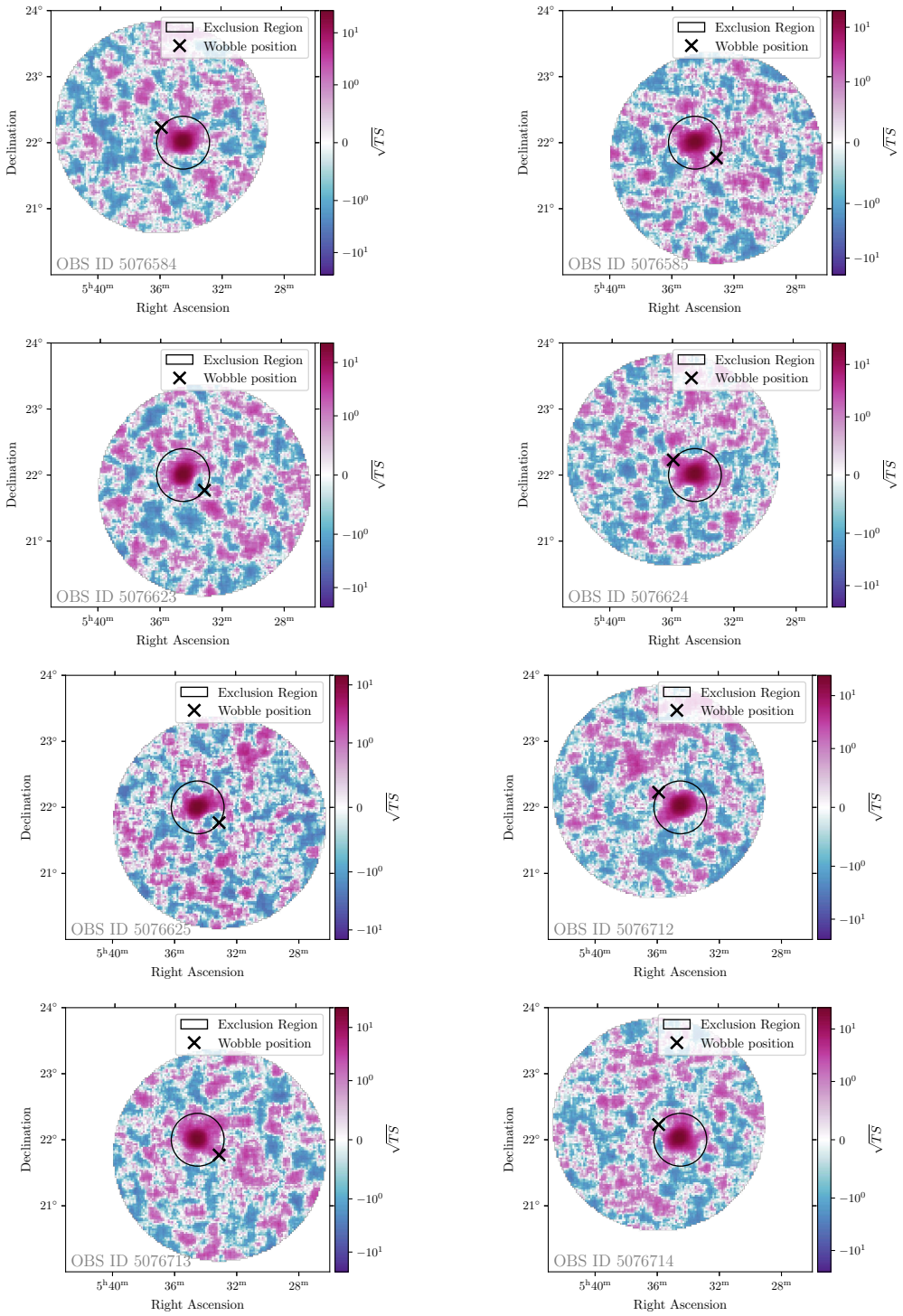

Figure D.8: (continued)

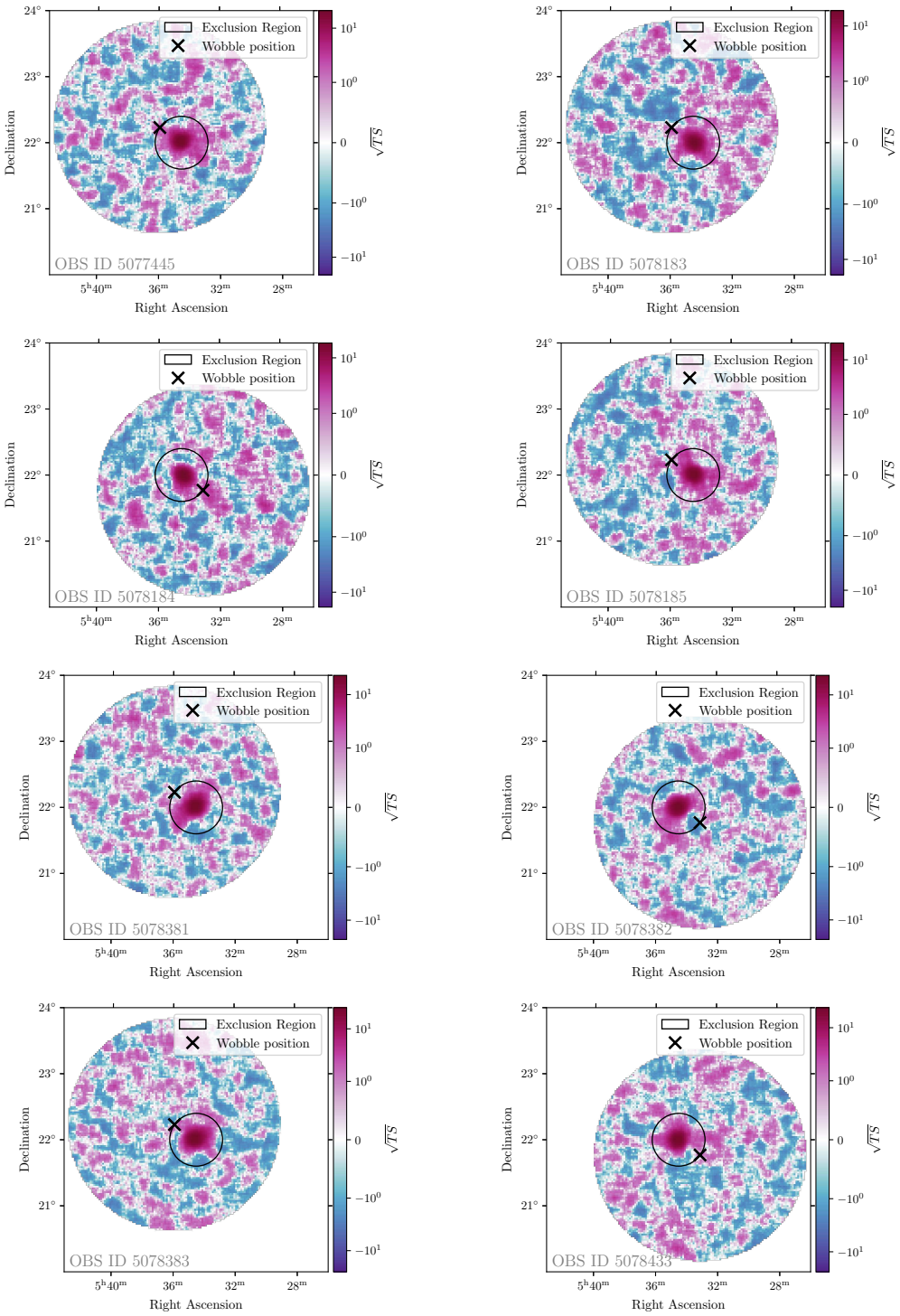

Figure D.8: (continued)

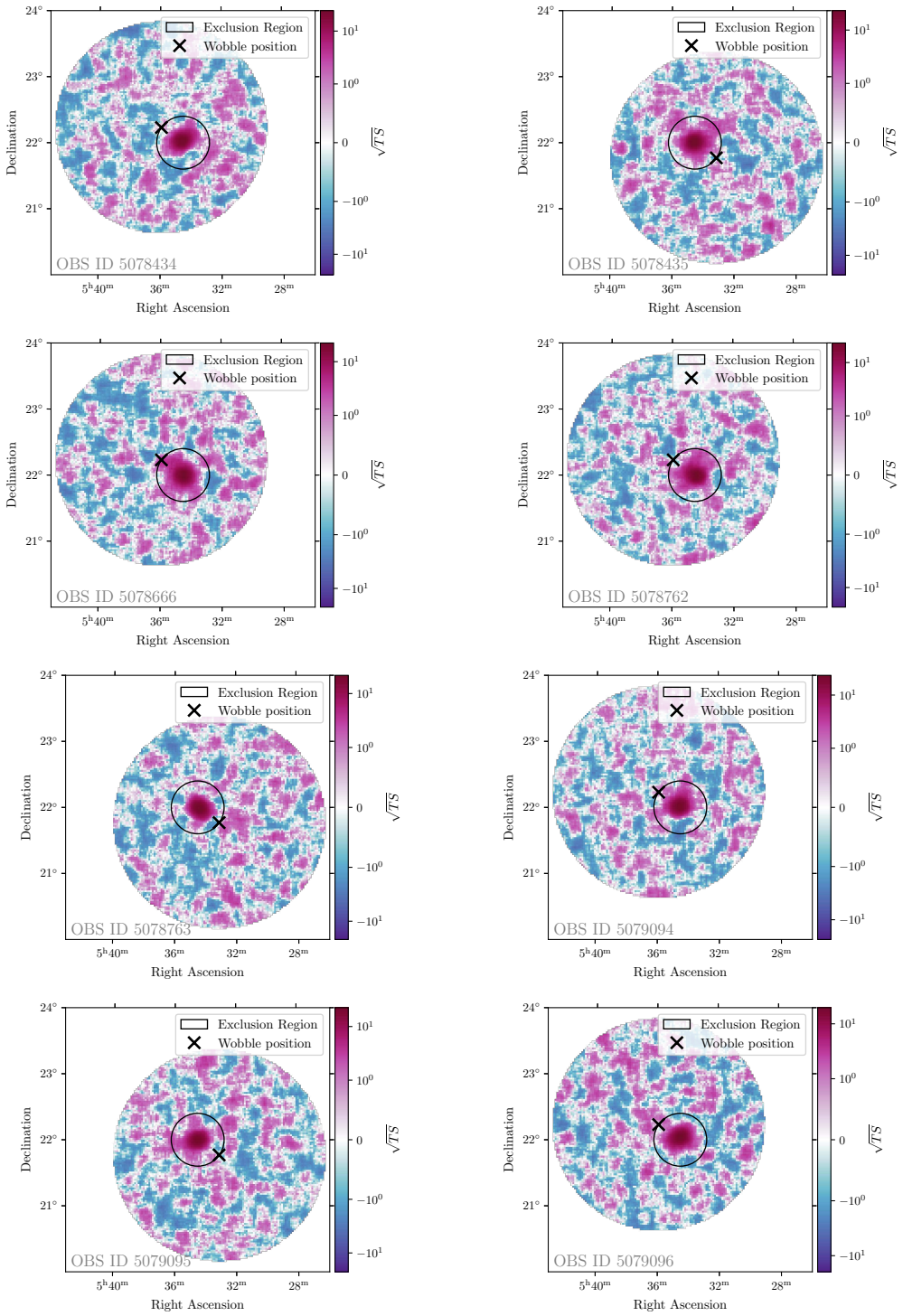

Figure D.8: (continued)

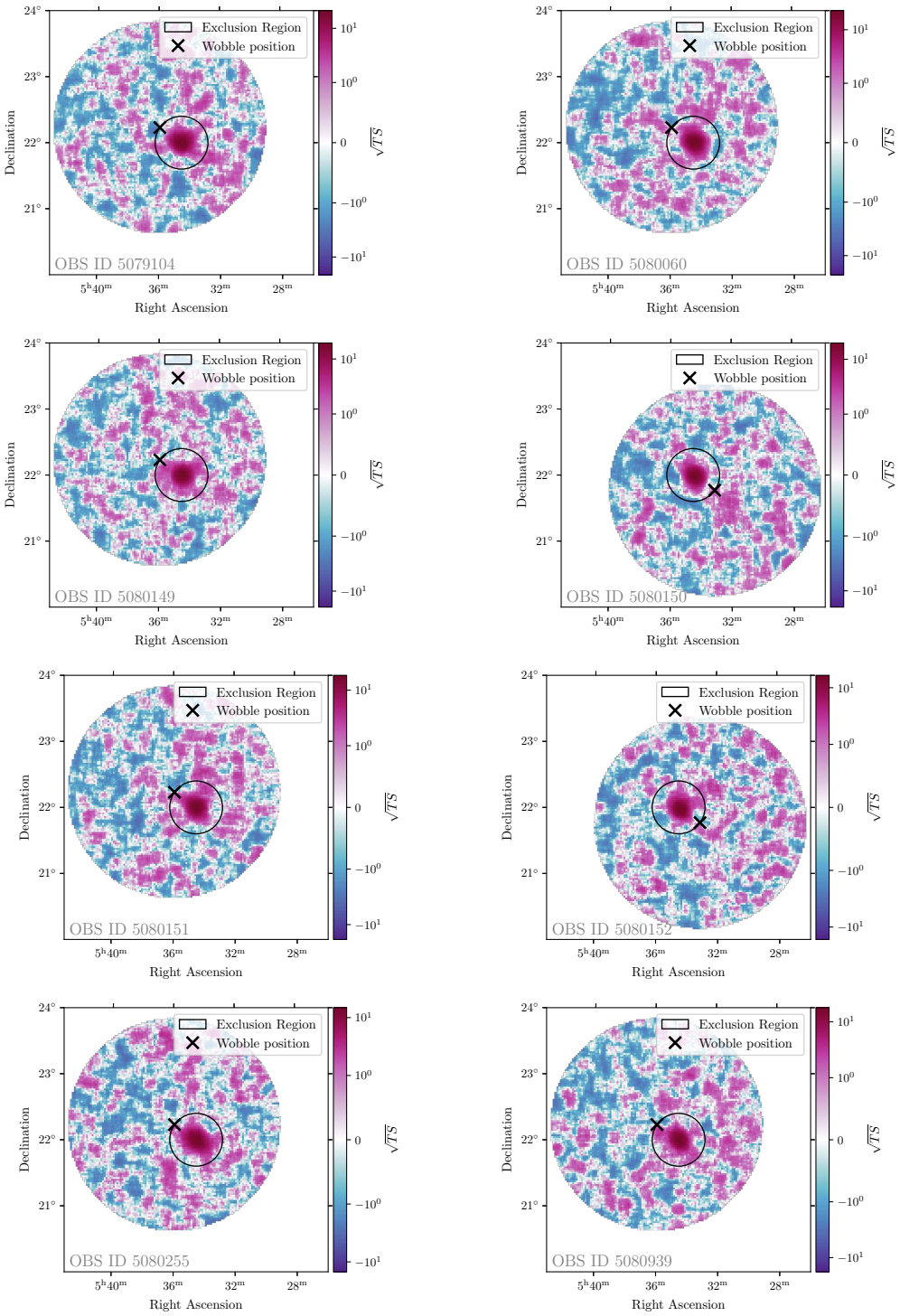

Figure D.8: (continued)

D.3 TS Histograms

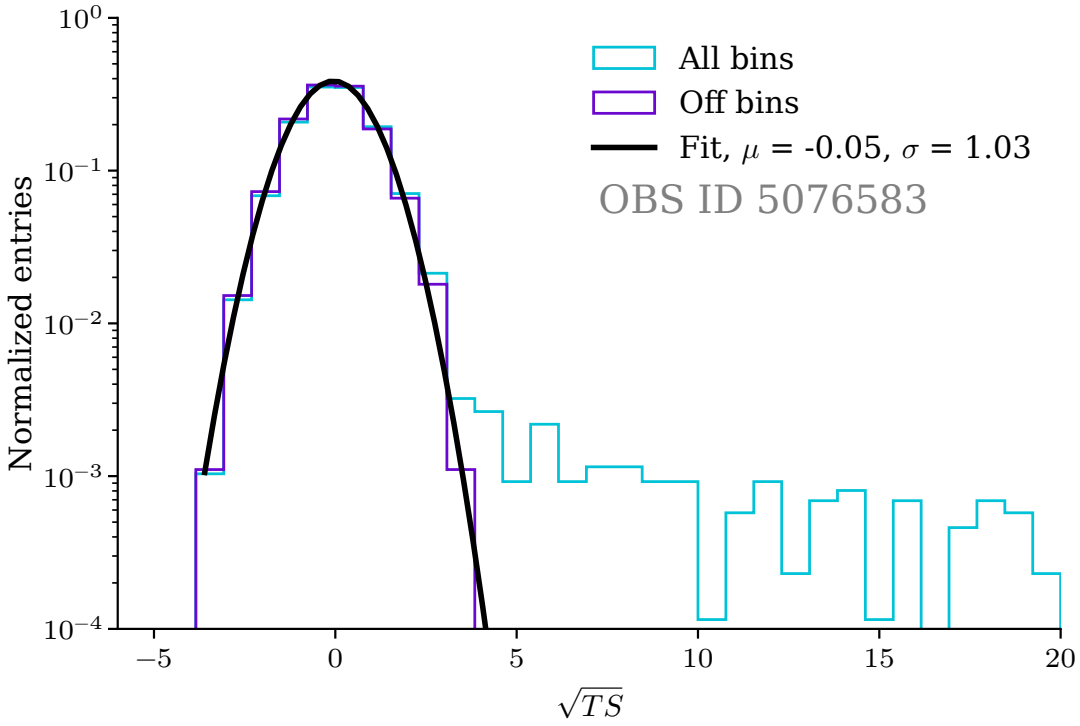

Figure D.9: Histograms for the significance values of for all Crab Nebula observations, outside the exclusion regions, *Off* bins, and within the complete map, *All* bins. A normal distribution is fitted to the *Off* bins. Continued on following pages.

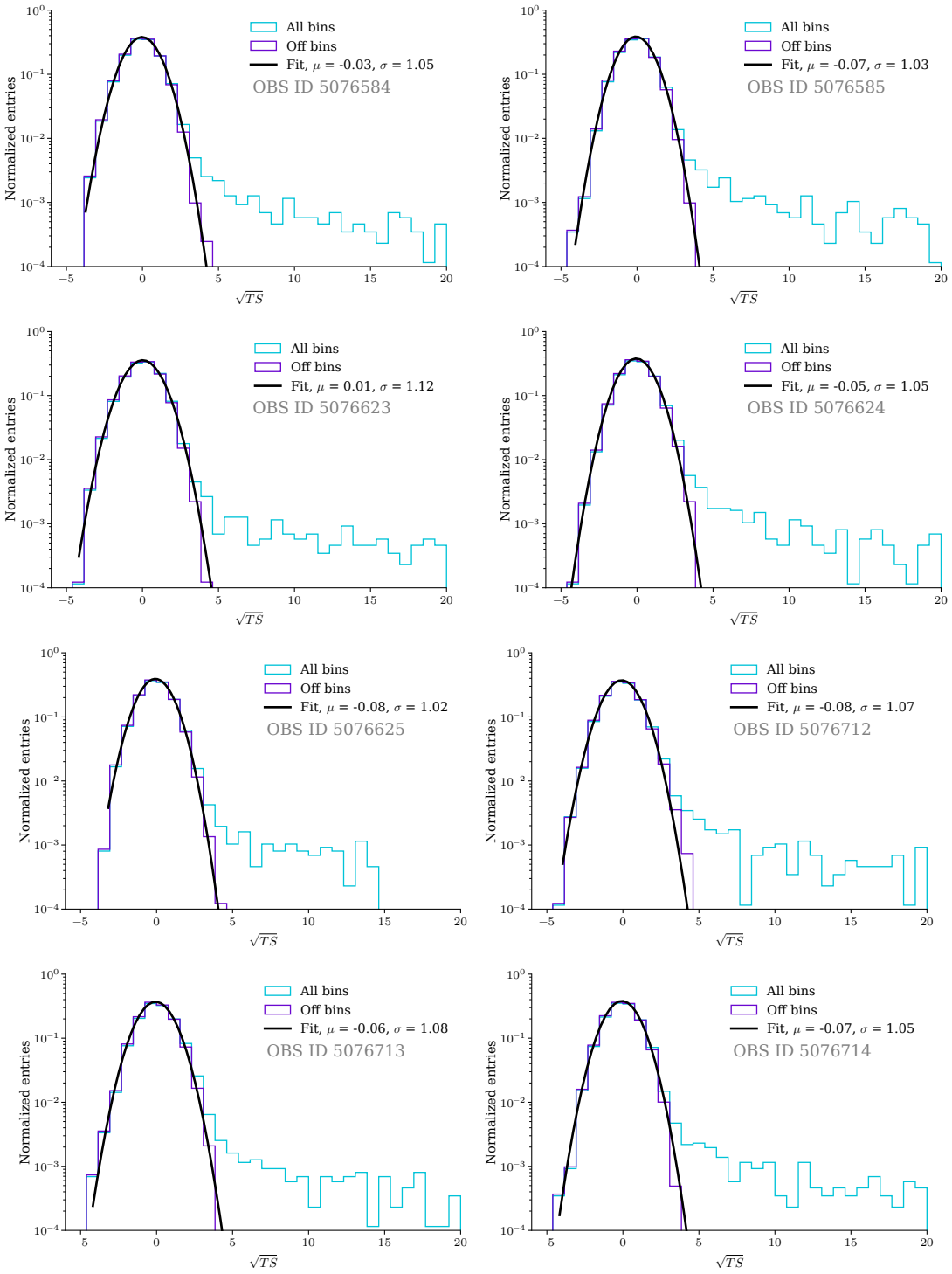

Figure D.9: (continued)

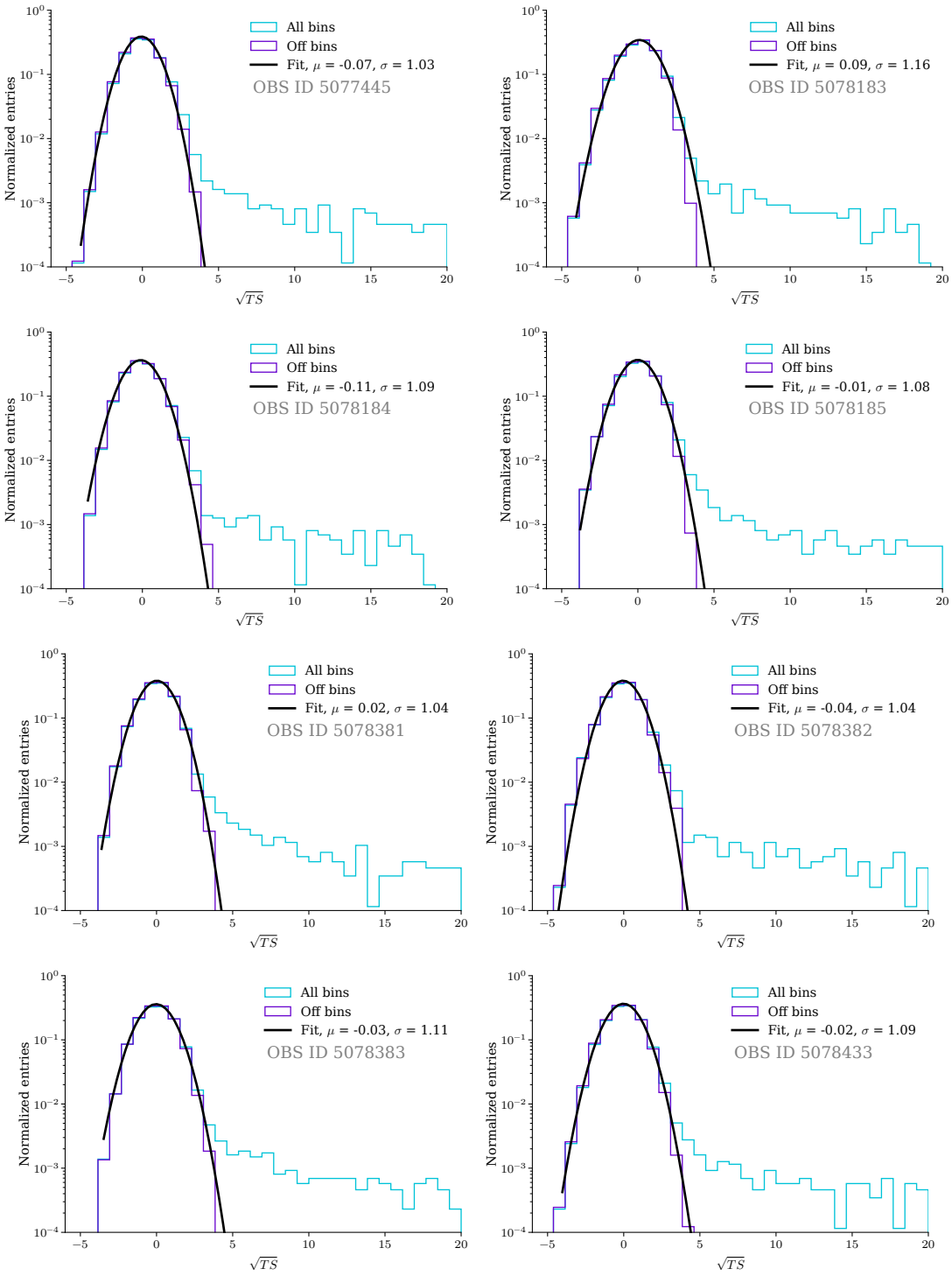

Figure D.9: (continued)

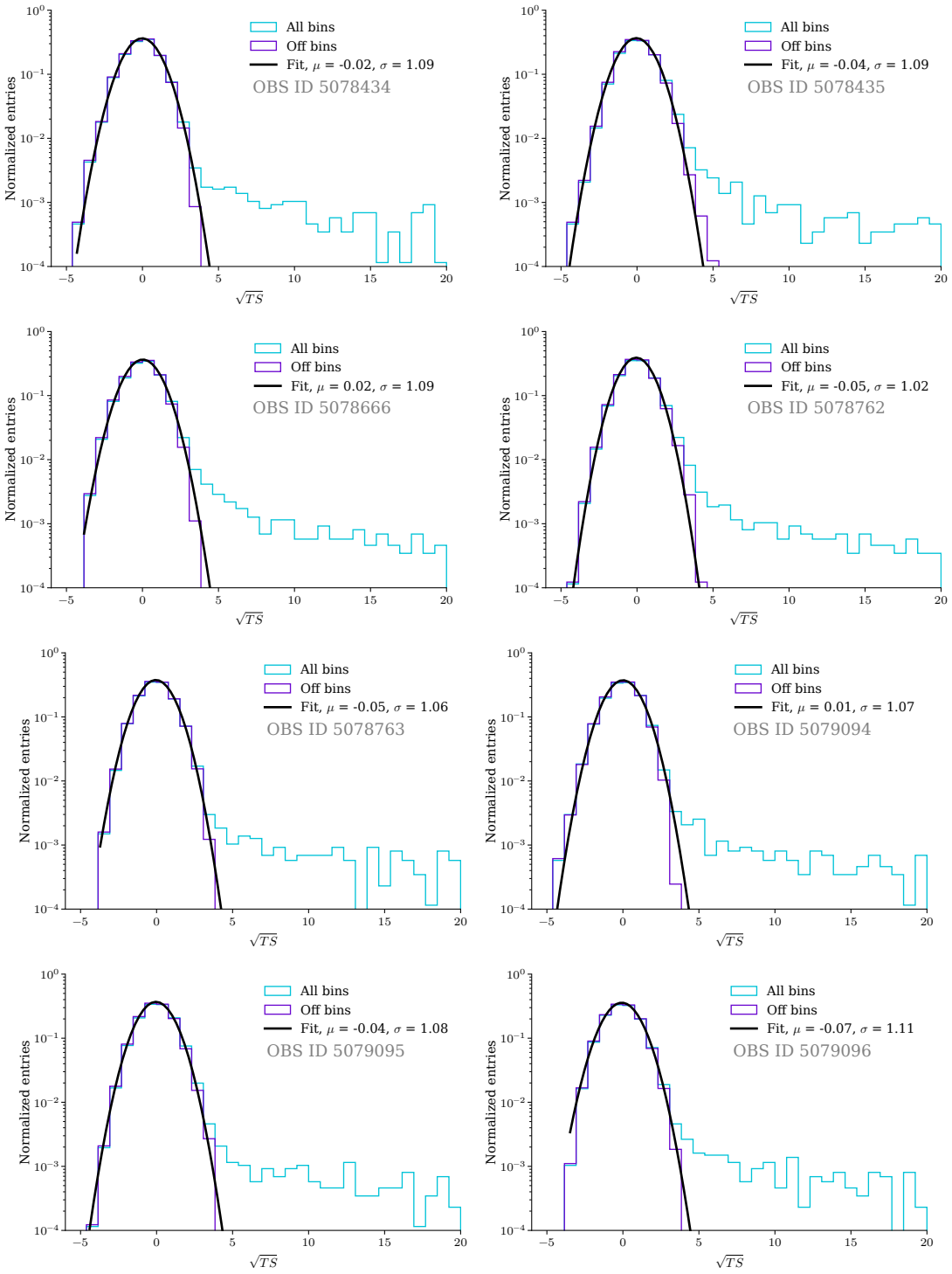

Figure D.9: (continued)

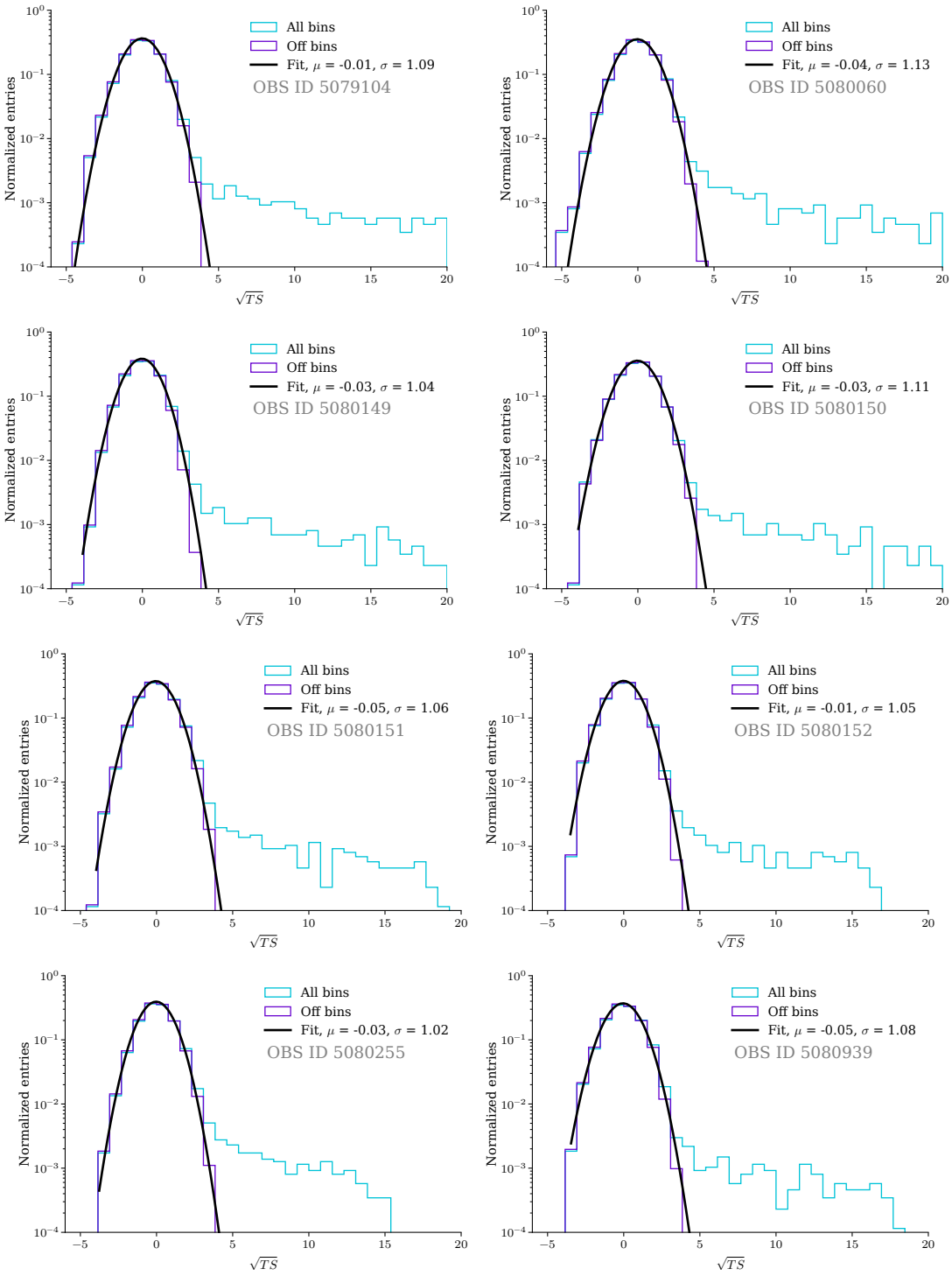

Figure D.9: (continued)

E Upper Limits

This chapter displays the validation curves for annihilation channels $b\bar{b}$, W^+W^-, $\mu^+\mu^-$, and $\tau^+\tau^-$ and masses 0.17 TeV, 1.53 TeV, 13.82 TeV, and 100 TeV for both the 1D and 3D analysis in Figure E.10 and Figure E.11, respectively. Furthermore, Figure E.12 displays the ULs on the 1D CBe dSph data computed with Asimov datasets and the CL_s method.

E.1 Asympotic Validation 1D

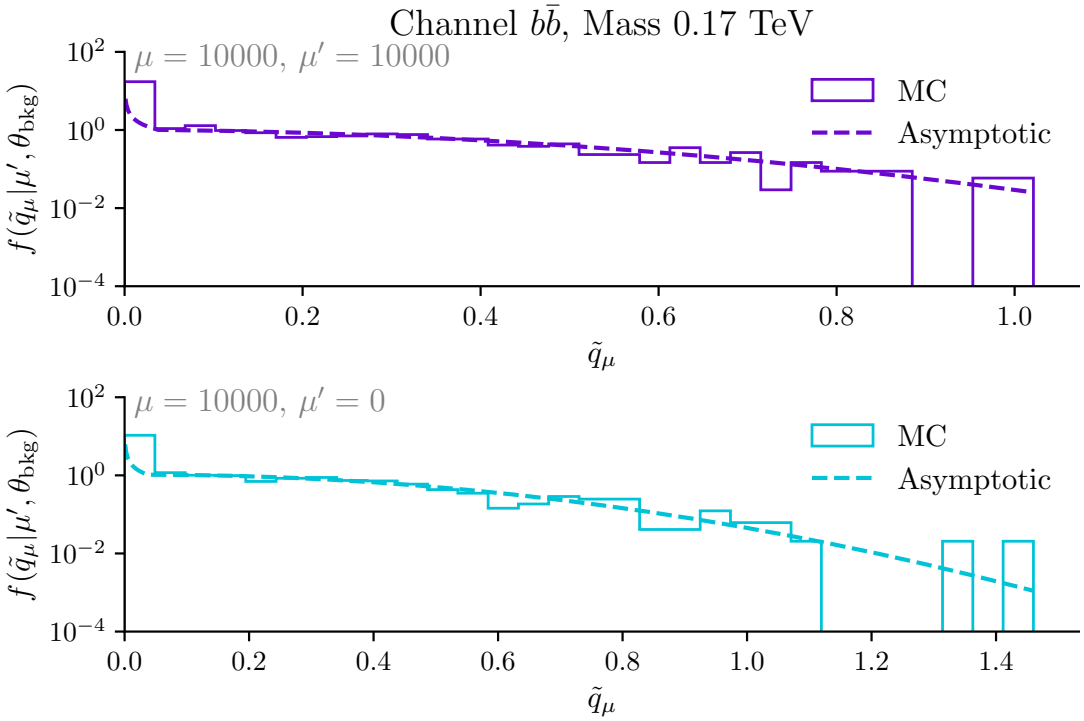

Figure E.10: Distribution of the TS, derived from computation of $\tilde{q}_\mu$ on 1000 1D MCs using `TITRATE`. The asymptotic limits, based on Cowen et al., are shown to display the approximation.

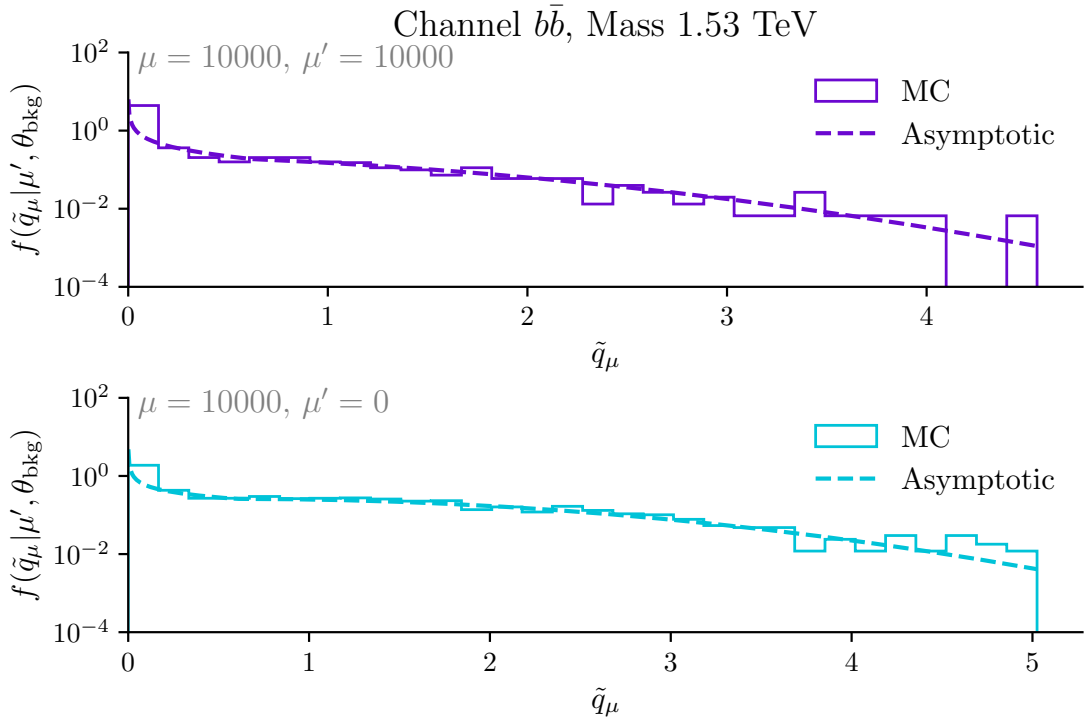

Figure E.10: (continued)

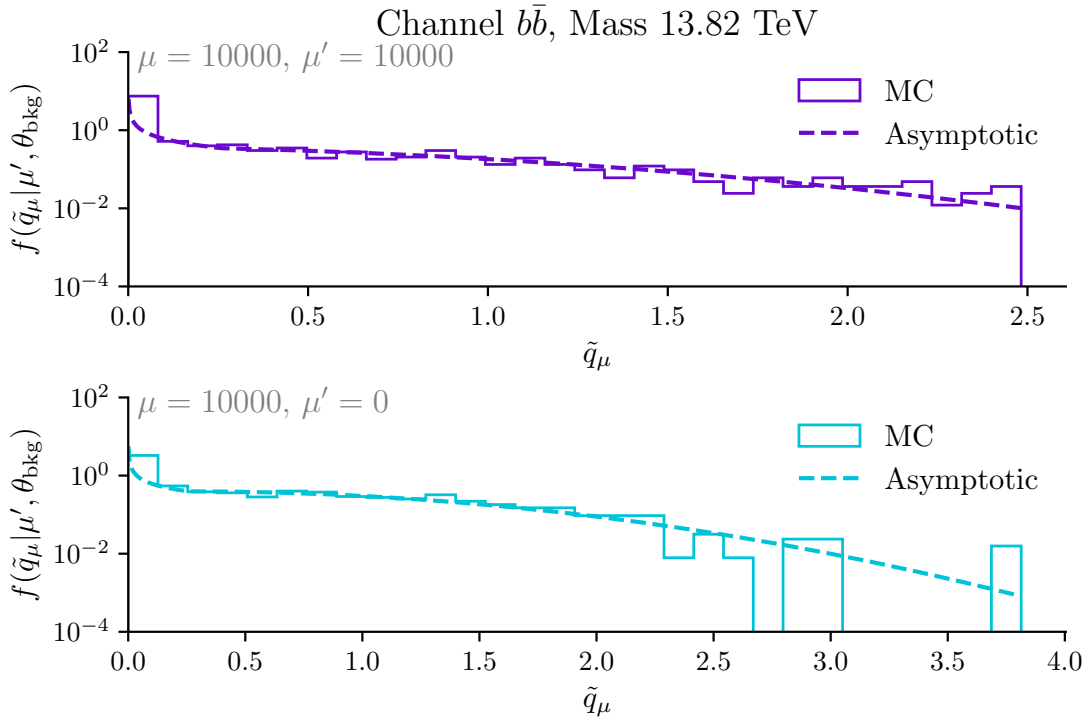

Figure E.10: (continued)

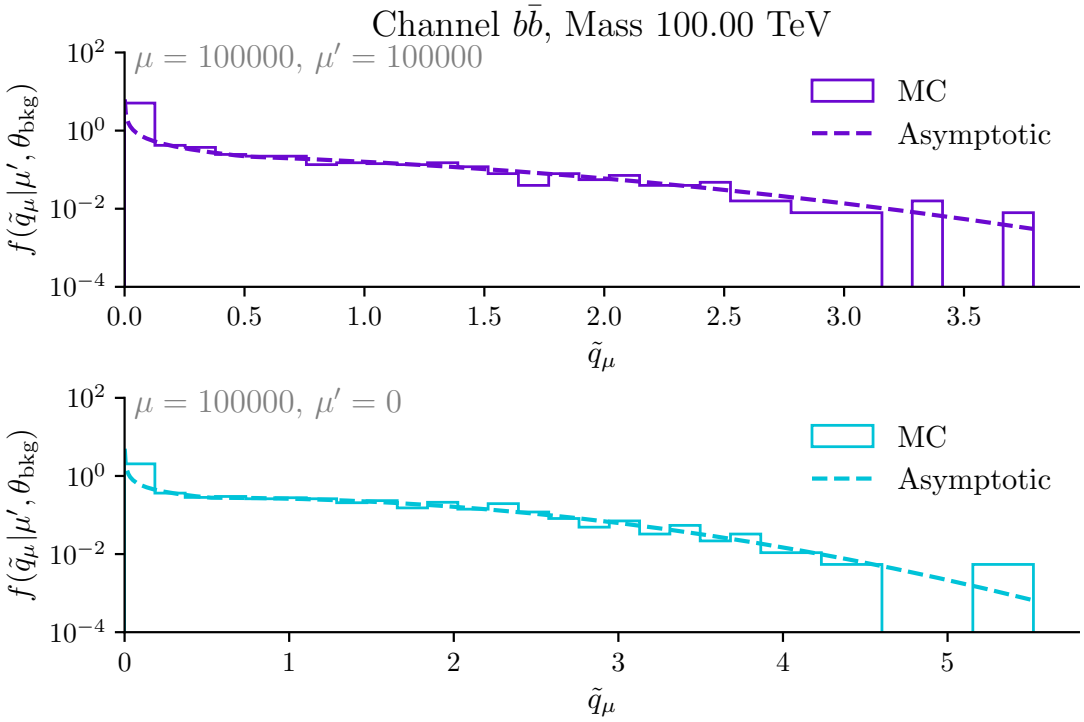

Figure E.10: (continued)

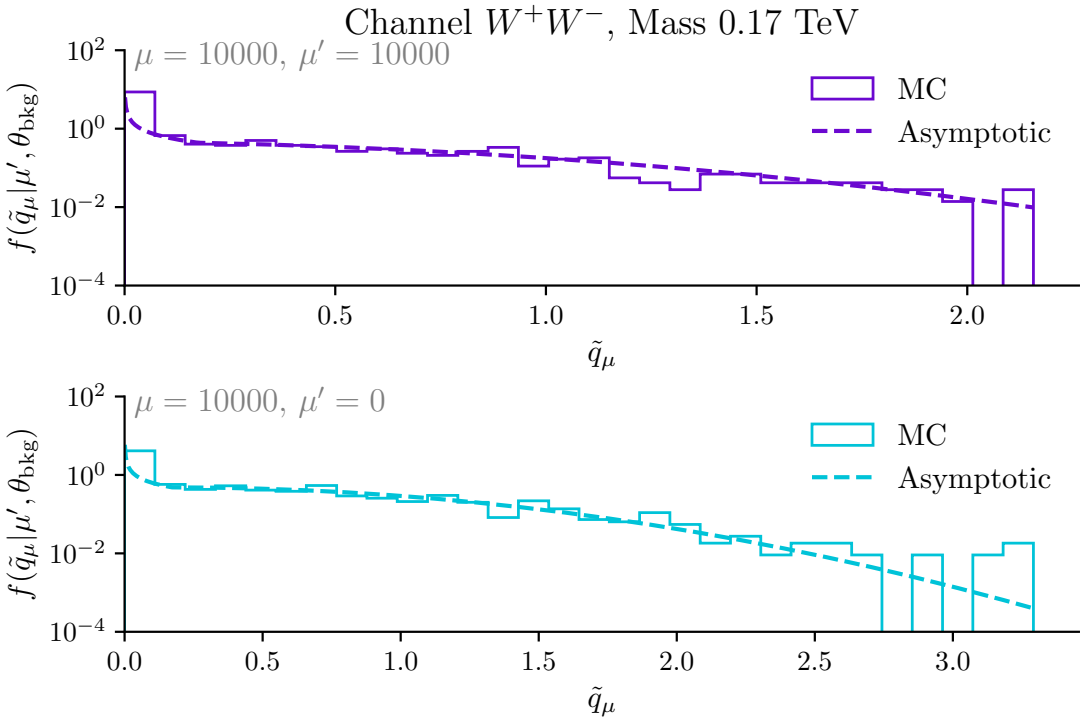

Figure E.10: (continued)

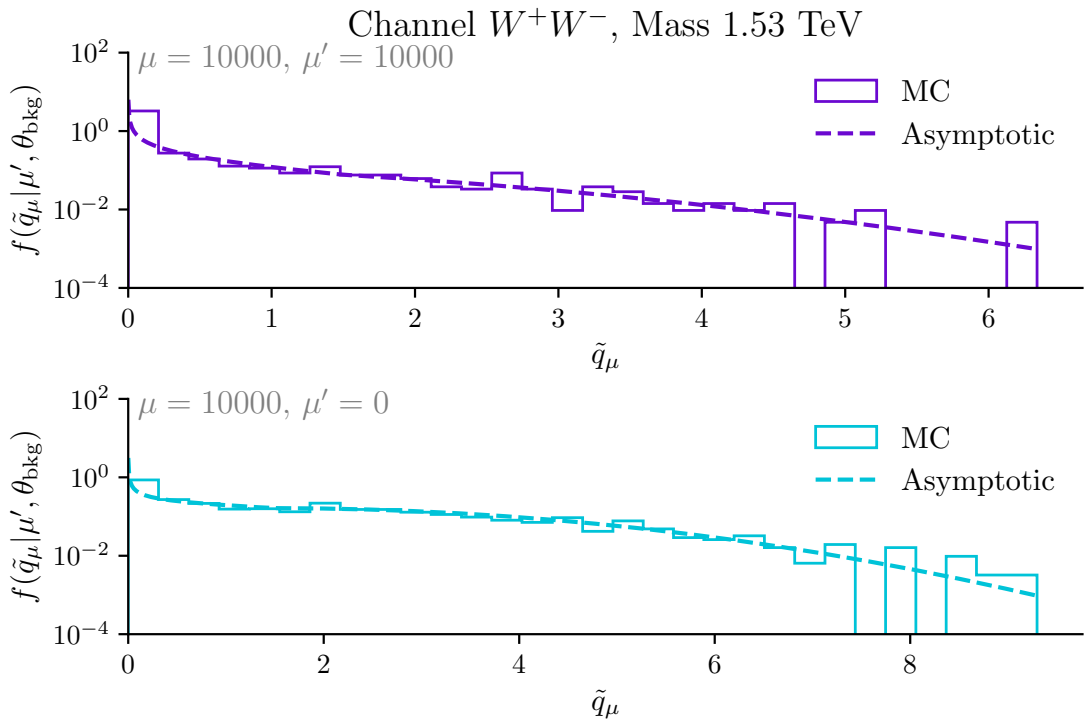

Figure E.10: (continued)

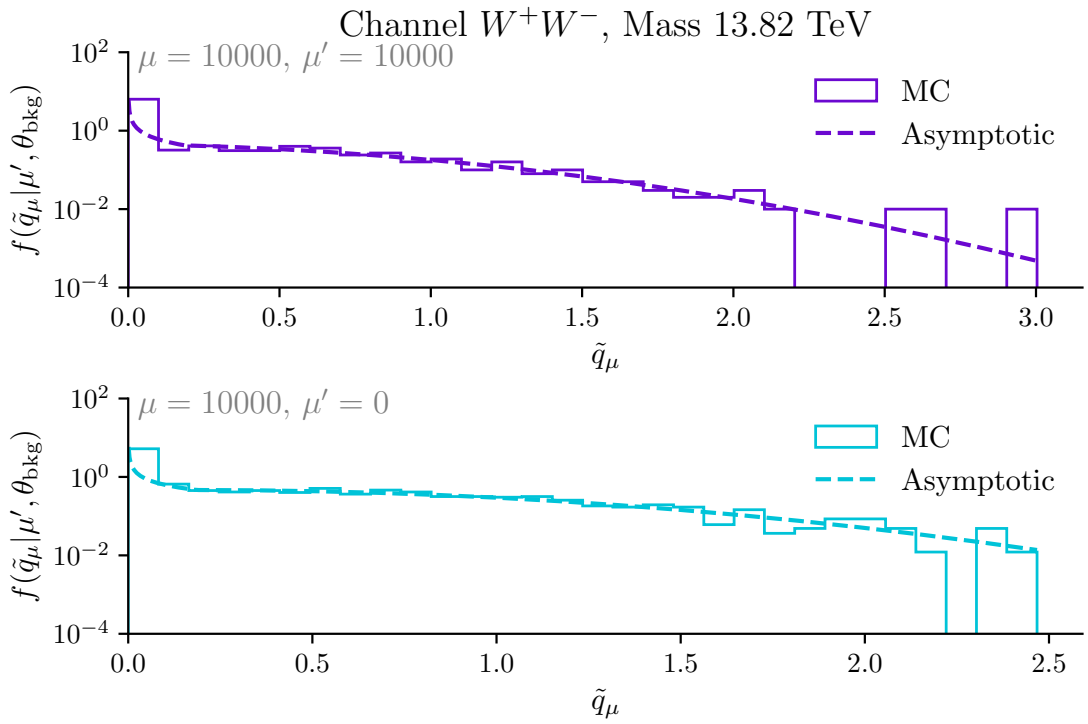

Figure E.10: (continued)

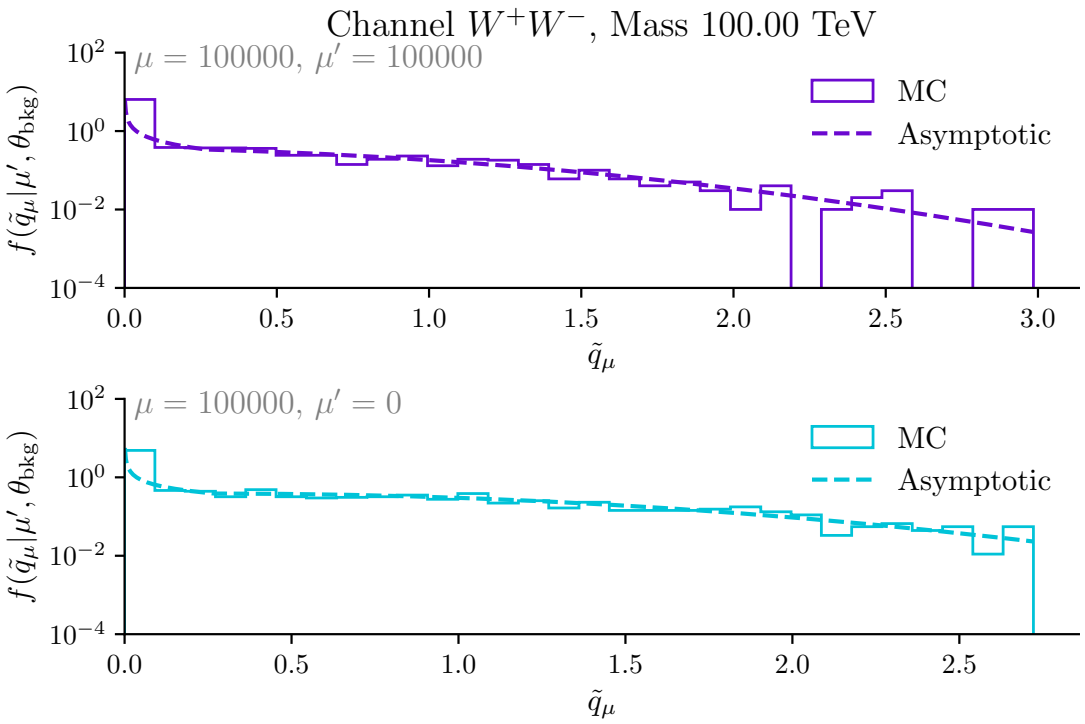

Figure E.10: (continued)

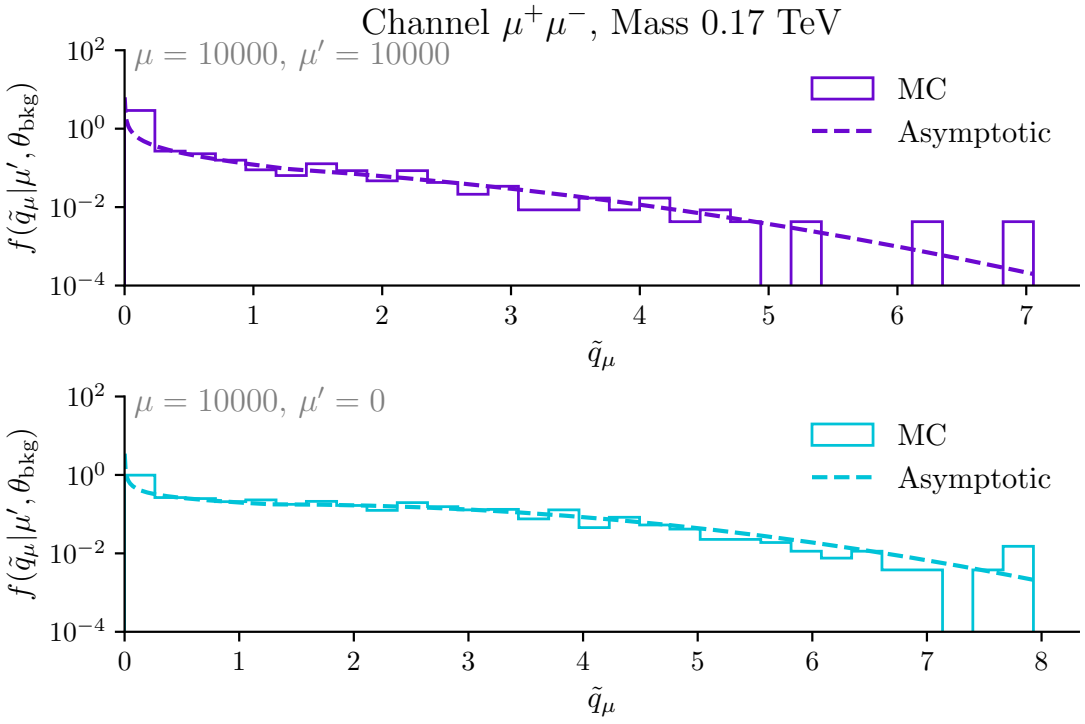

Figure E.10: (continued)

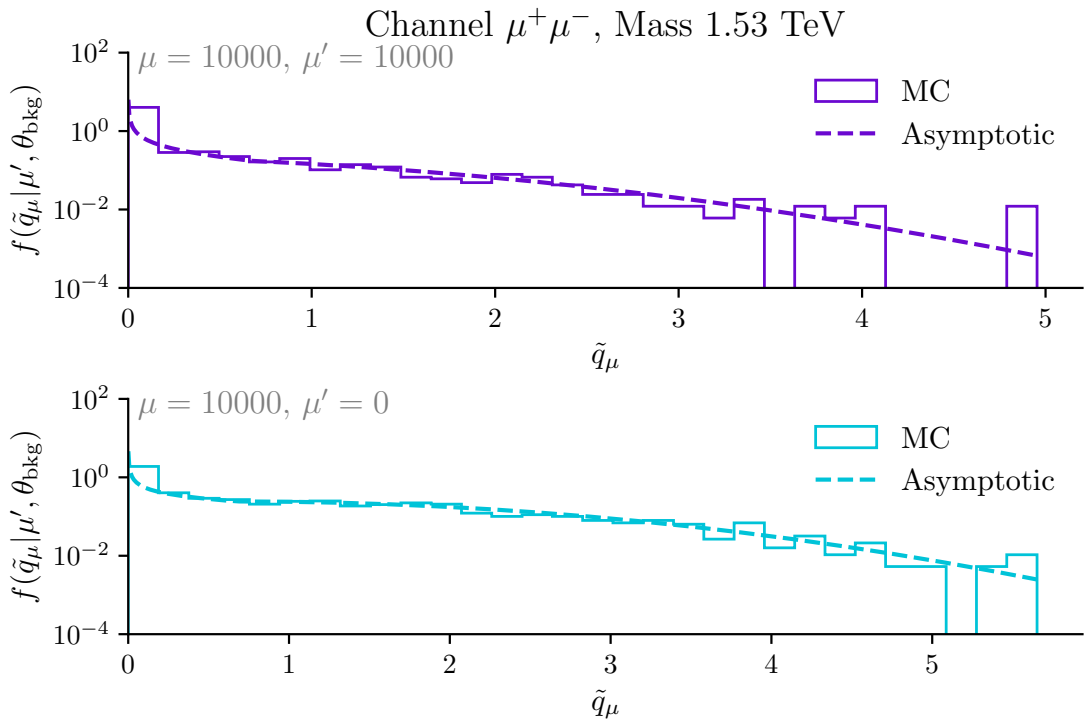

Figure E.10: (continued)

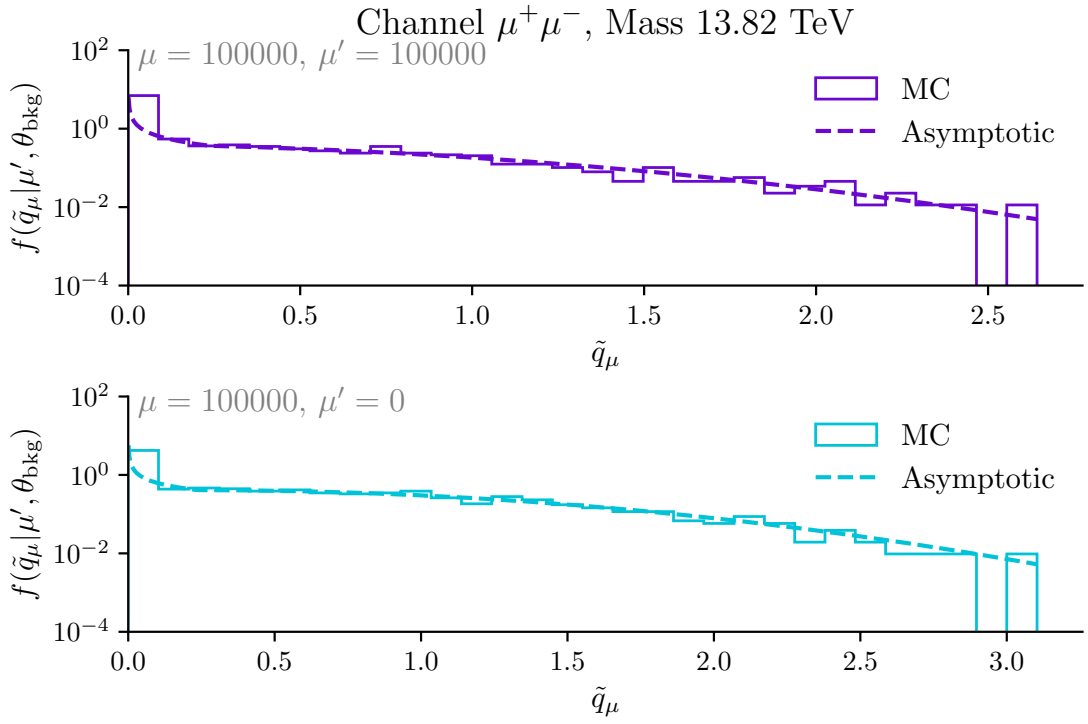

Figure E.10: (continued)

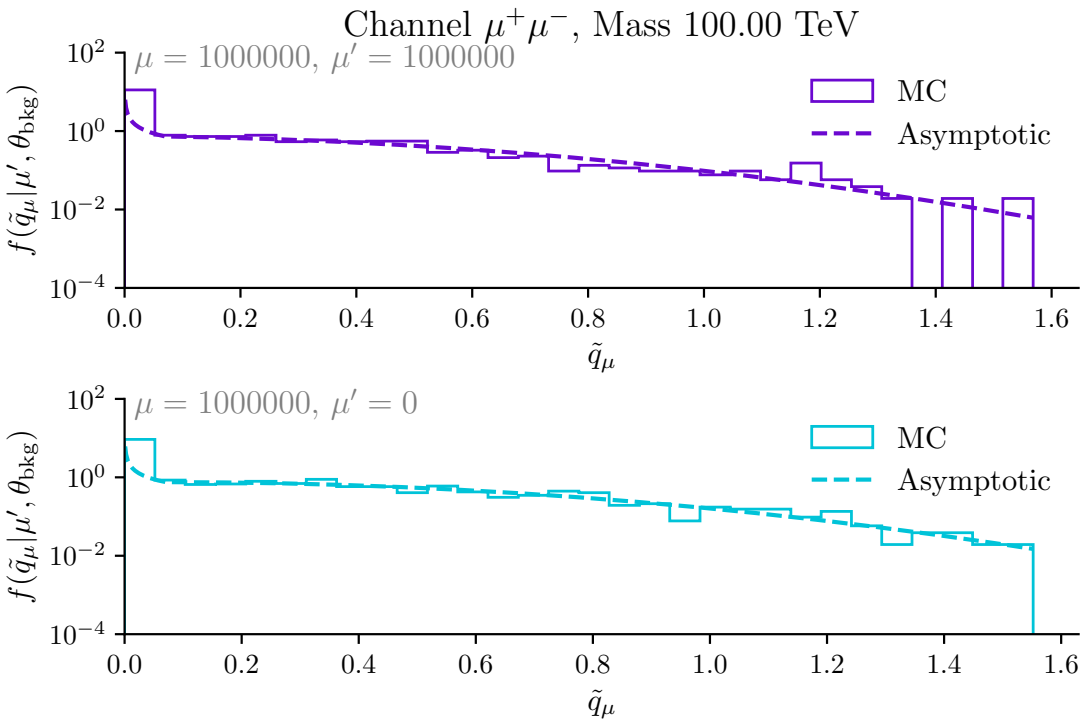

Figure E.10: (continued)

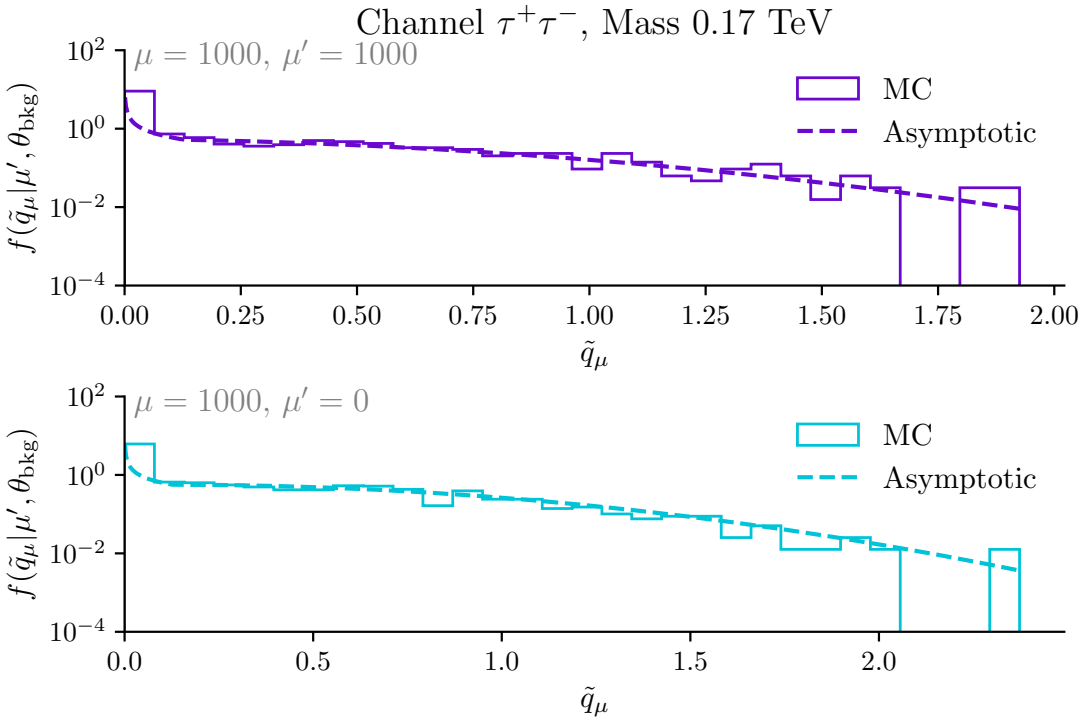

Figure E.10: (continued)

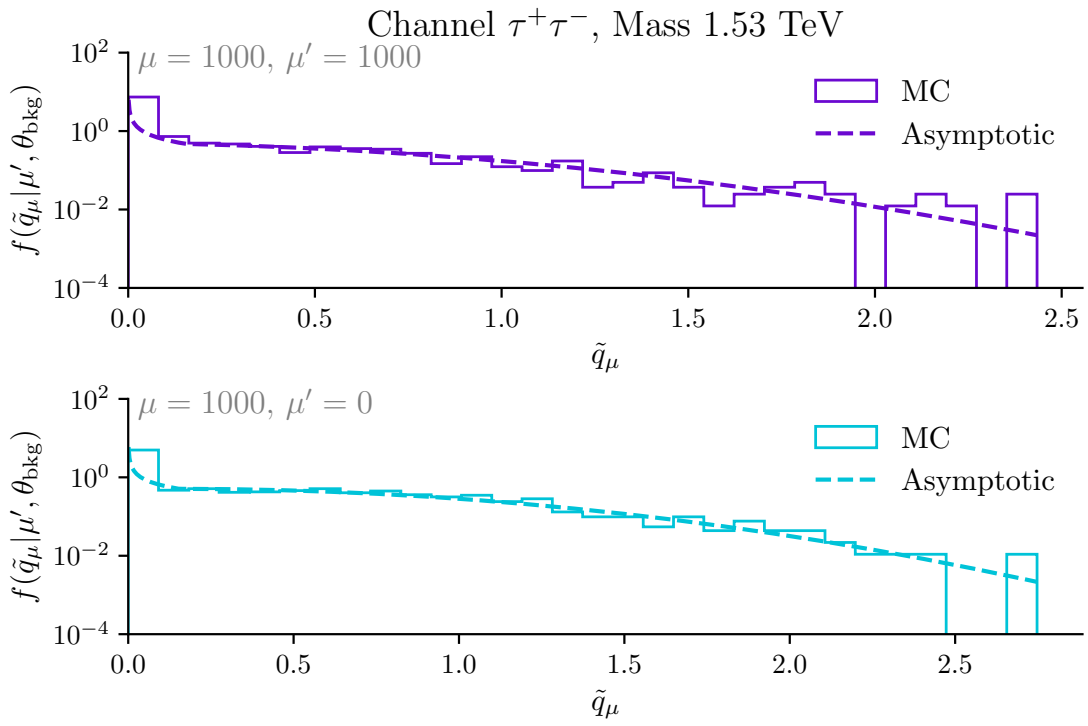

Figure E.10: (continued)

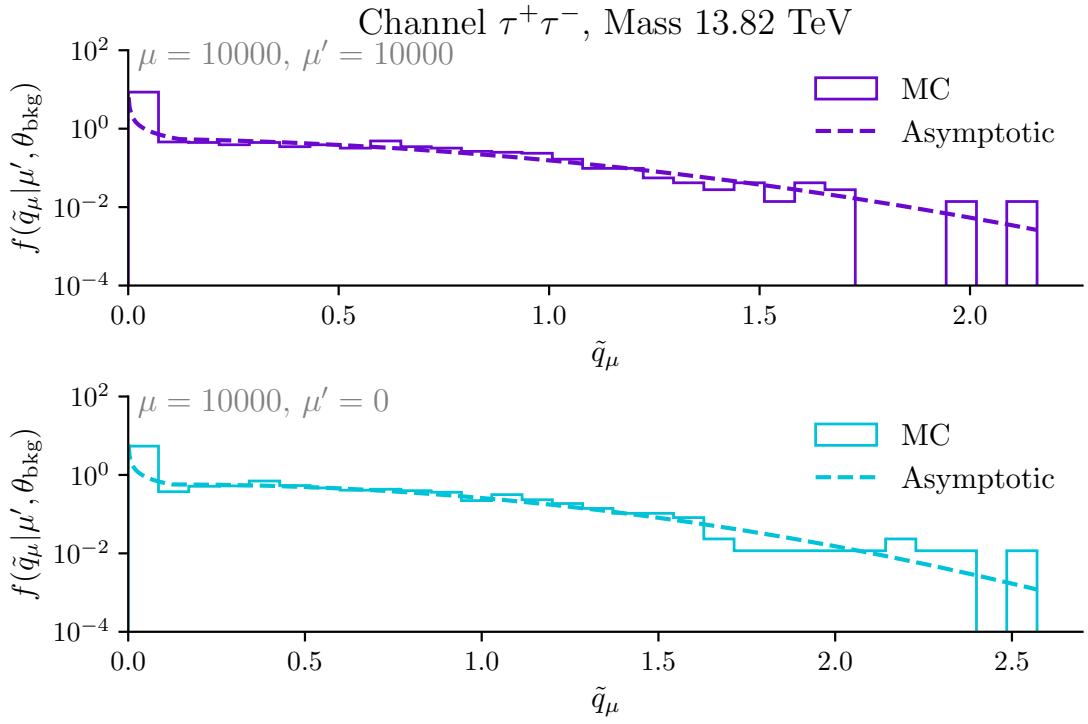

Figure E.10: (continued)

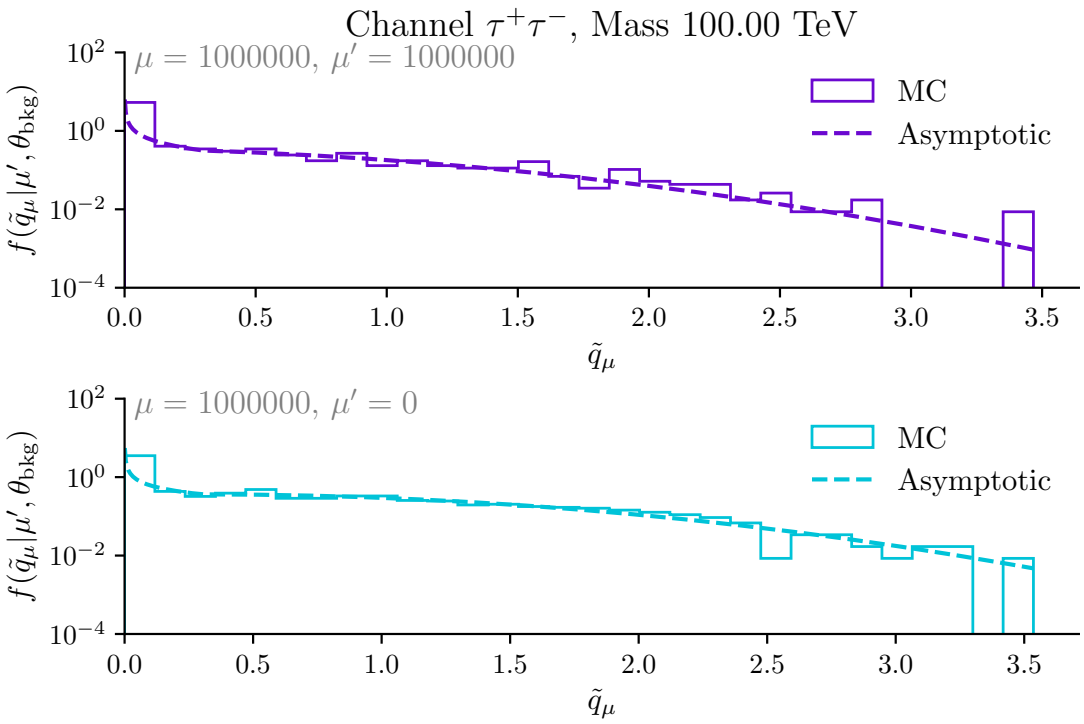

Figure E.10: (continued)

E.2 Asympotic Validation 3D

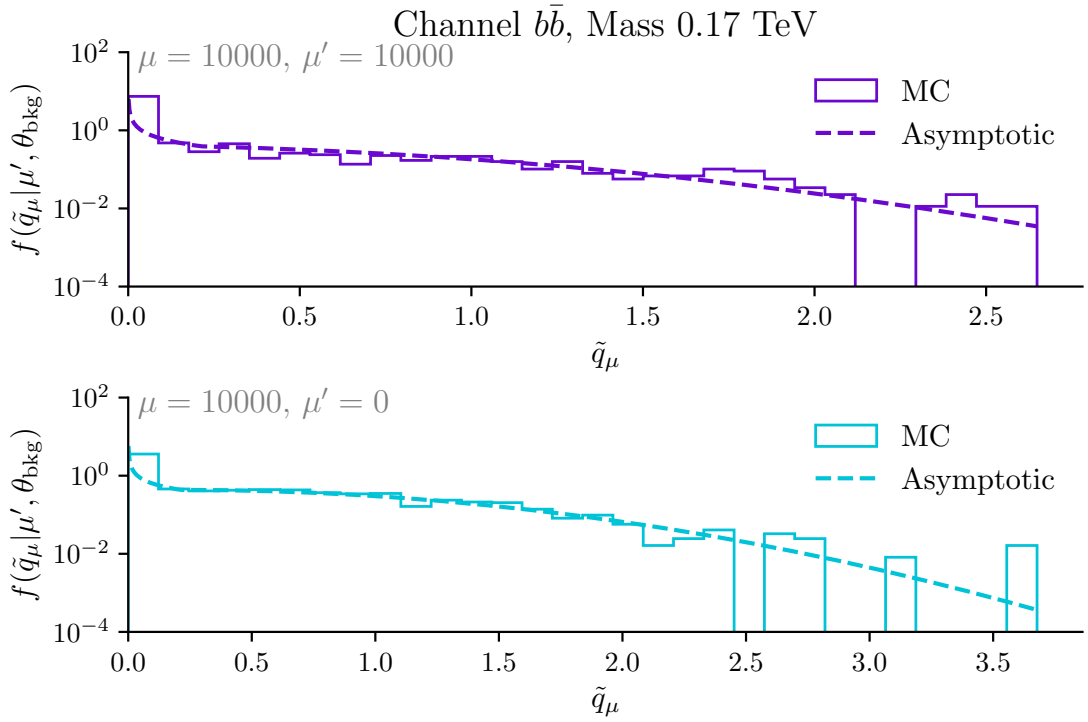

Figure E.11: Distribution of the TS, derived from computation of $\tilde{q}_\mu$ on 1000 3D MCs using `TITRATE`. The asymptotic limits, based on Cowen et al., are shown to display the approximation.

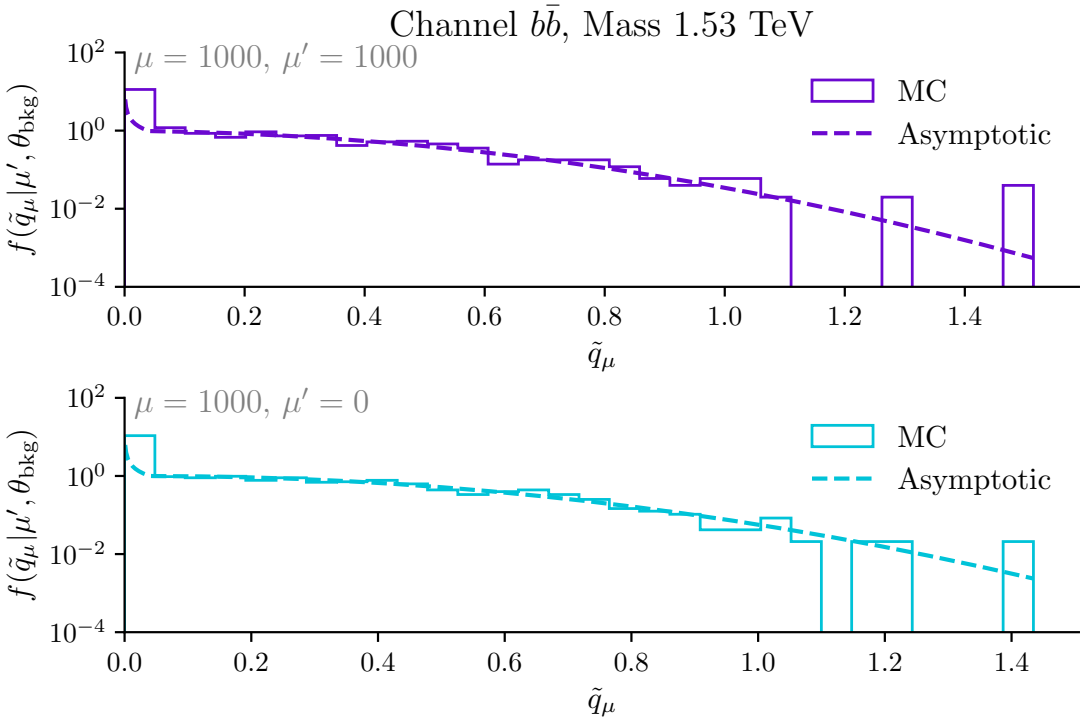

Figure E.11: (continued)

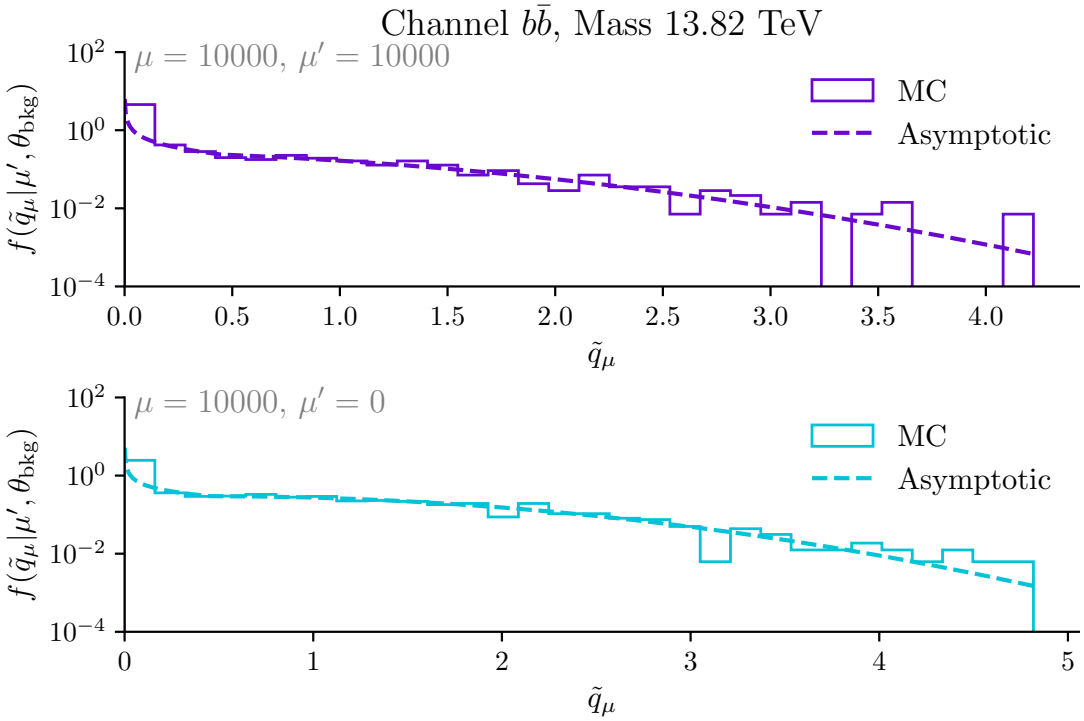

Figure E.11: (continued)

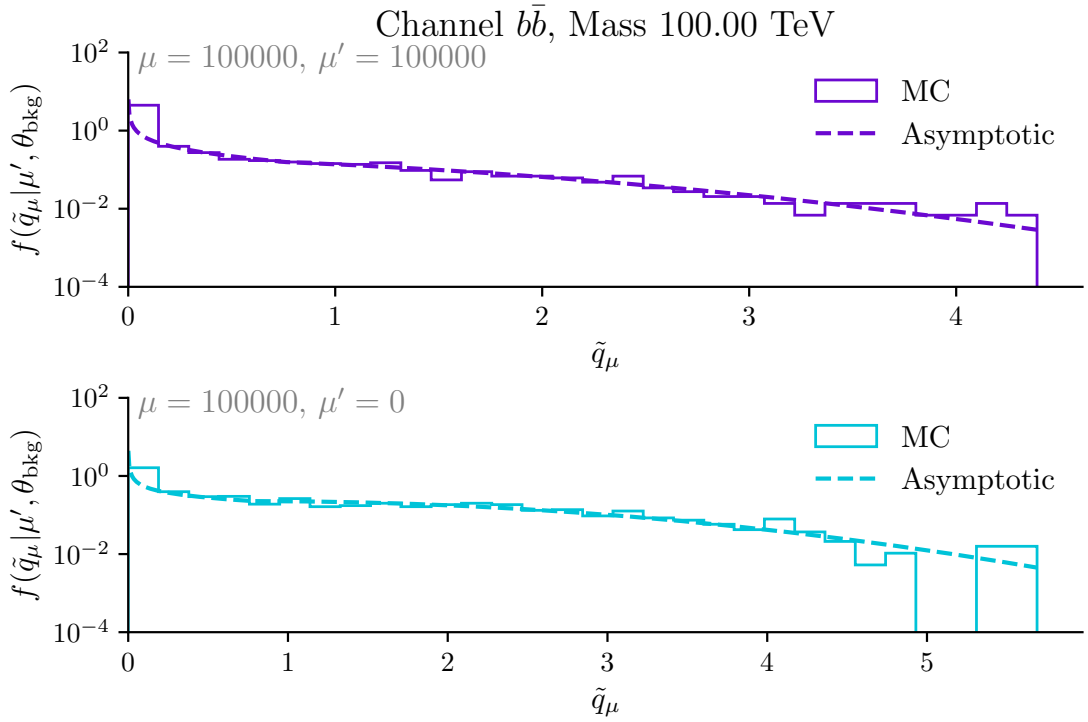

Figure E.11: (continued)

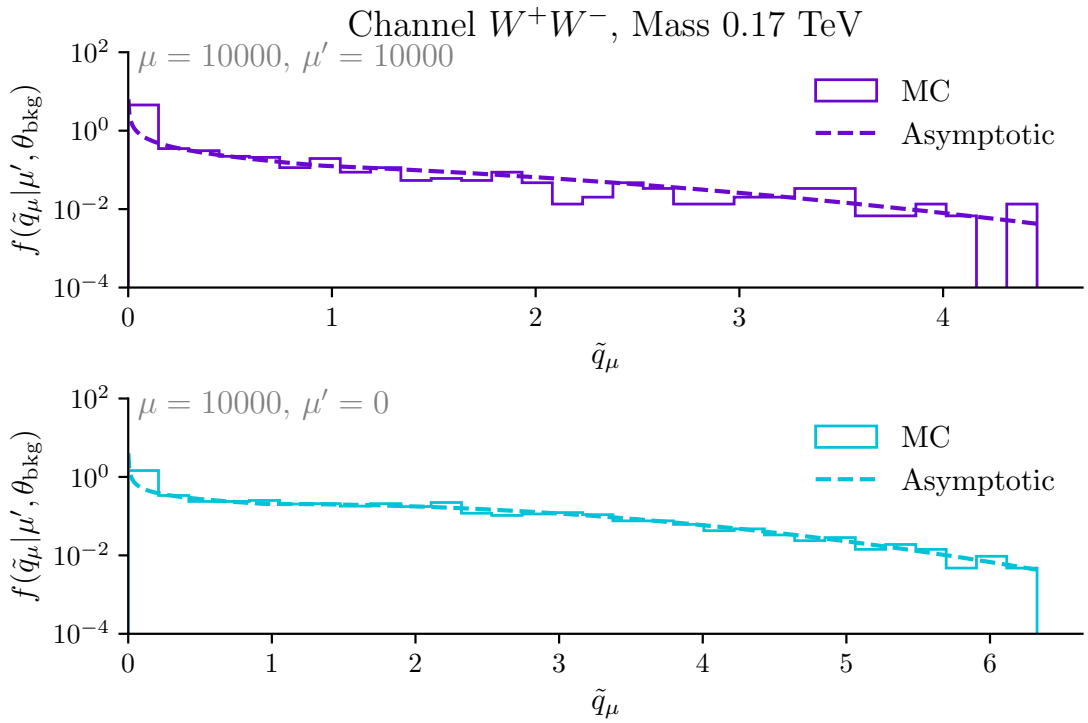

Figure E.11: (continued)

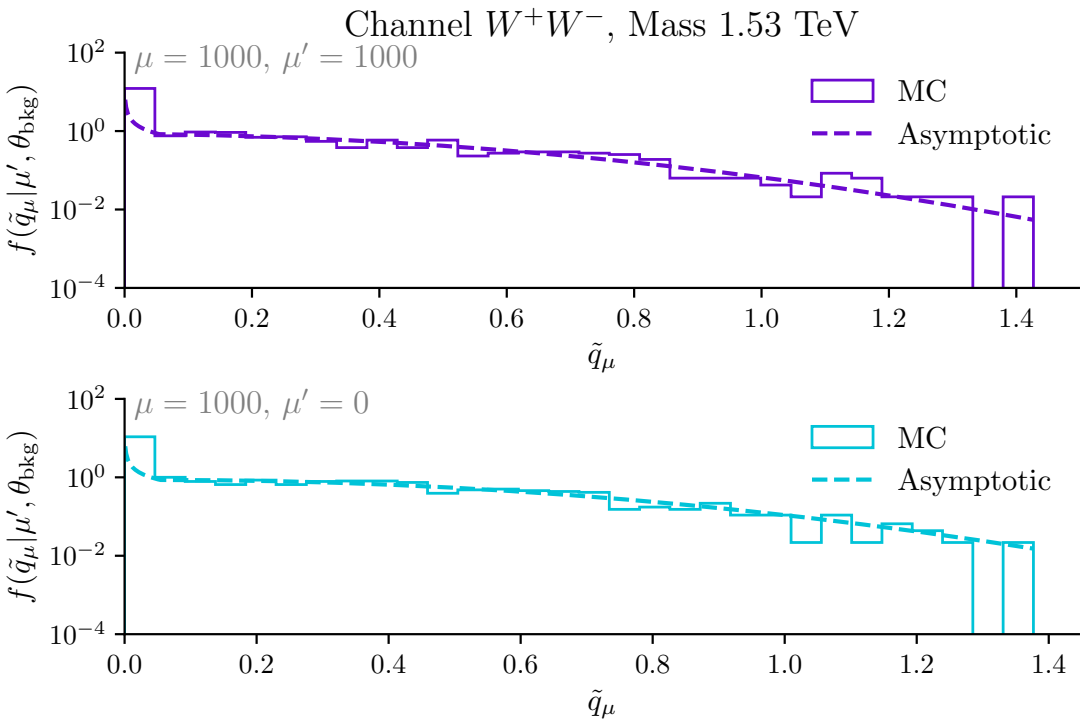

Figure E.11: (continued)

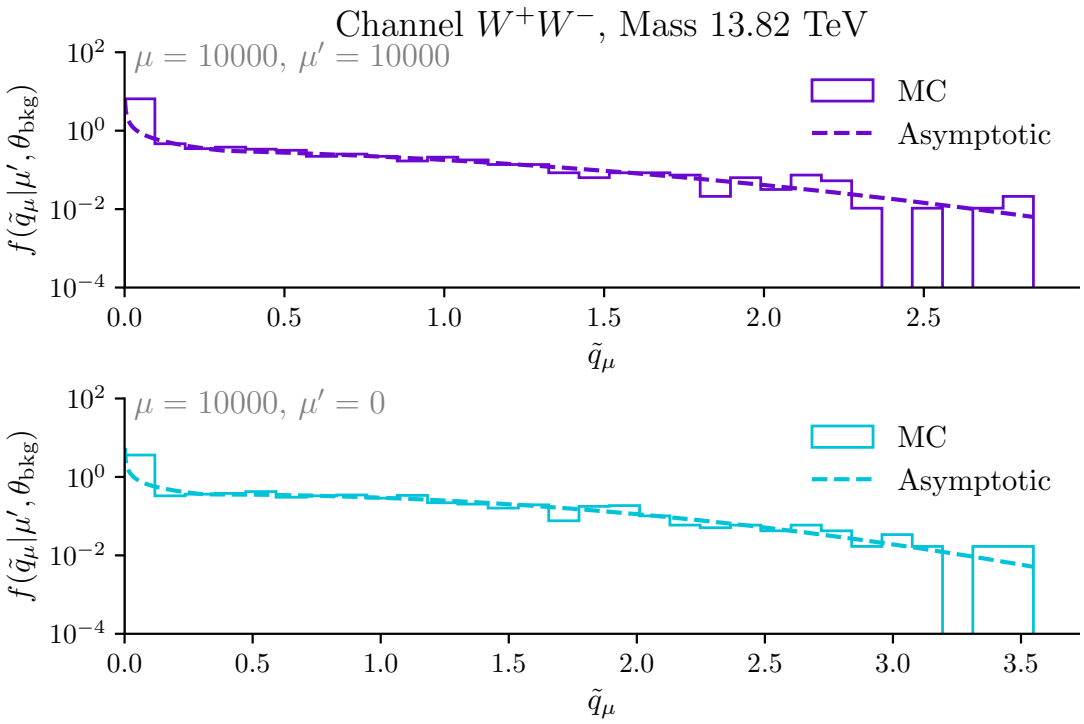

Figure E.11: (continued)

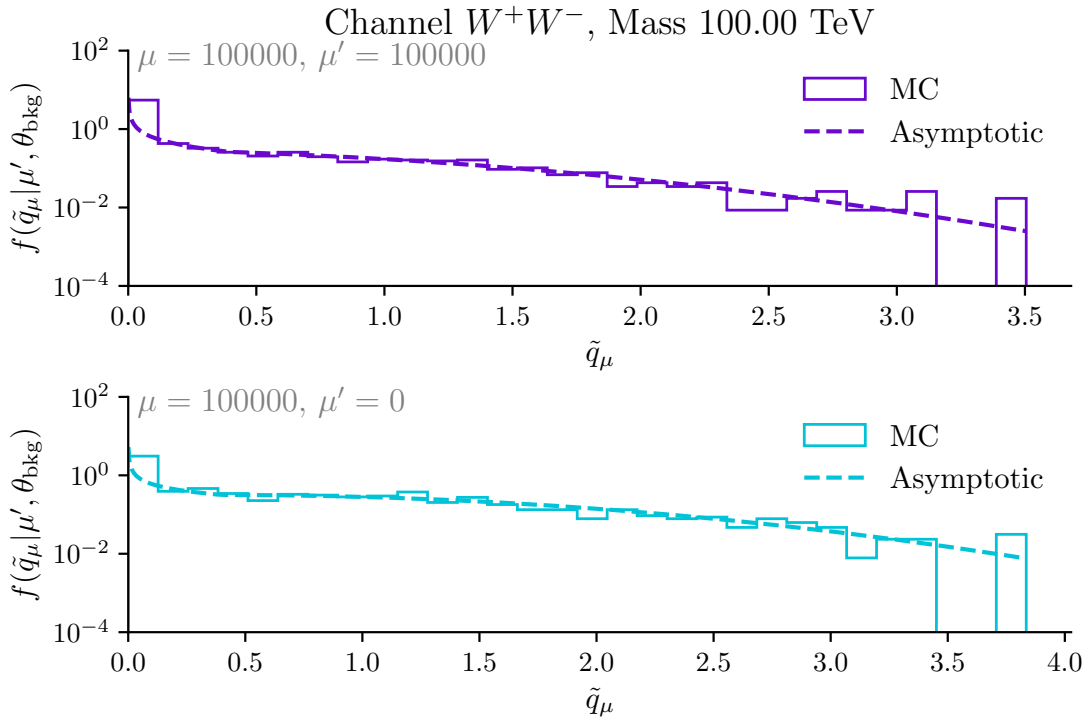

Figure E.11: (continued)

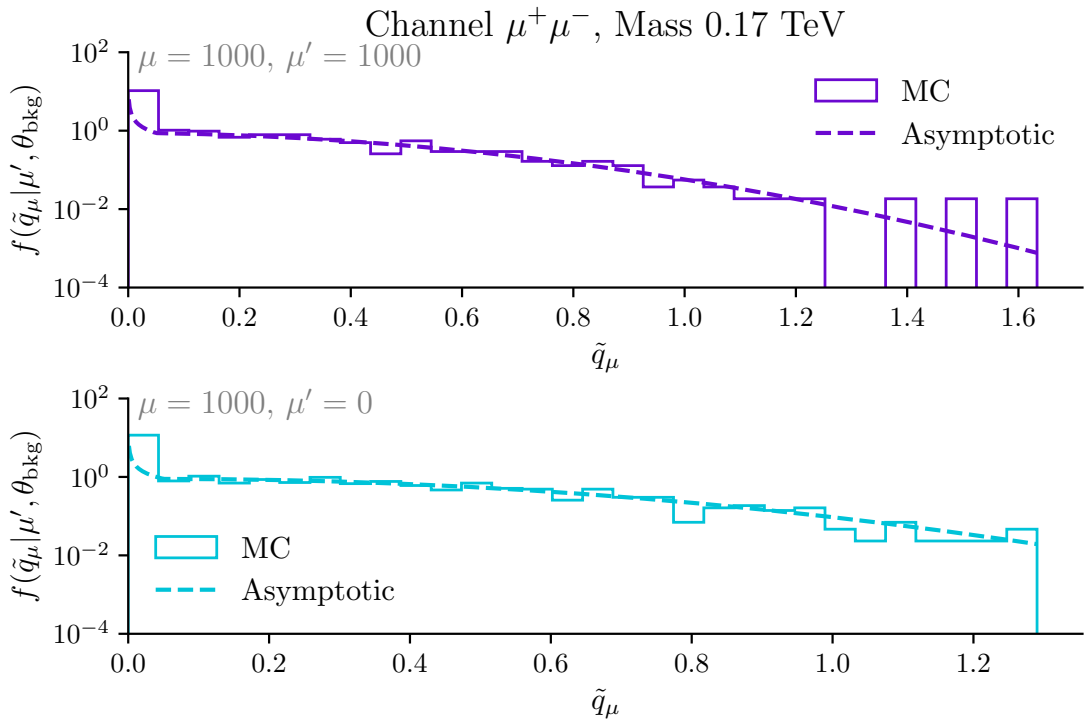

Figure E.11: (continued)

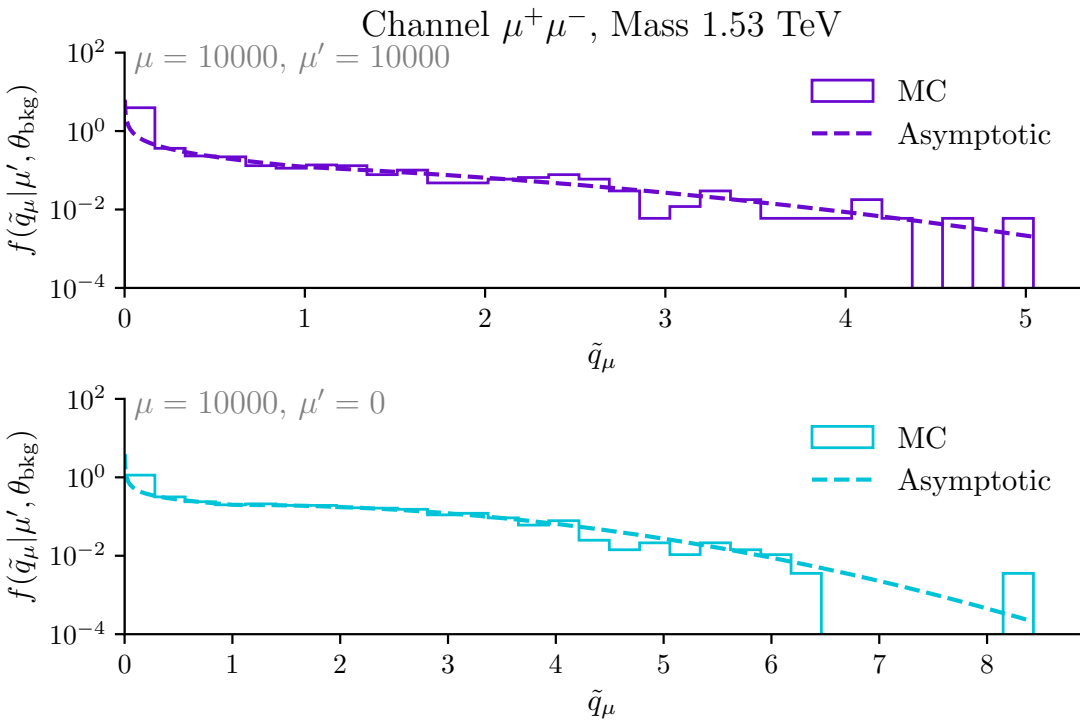

Figure E.11: (continued)

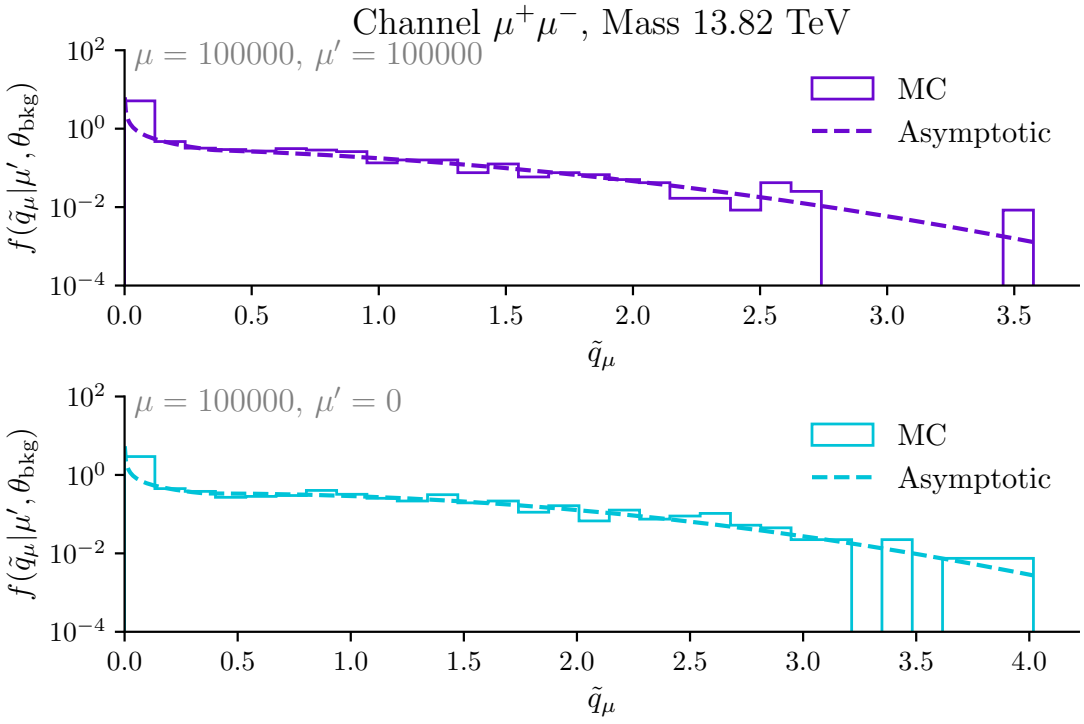

Figure E.11: (continued)

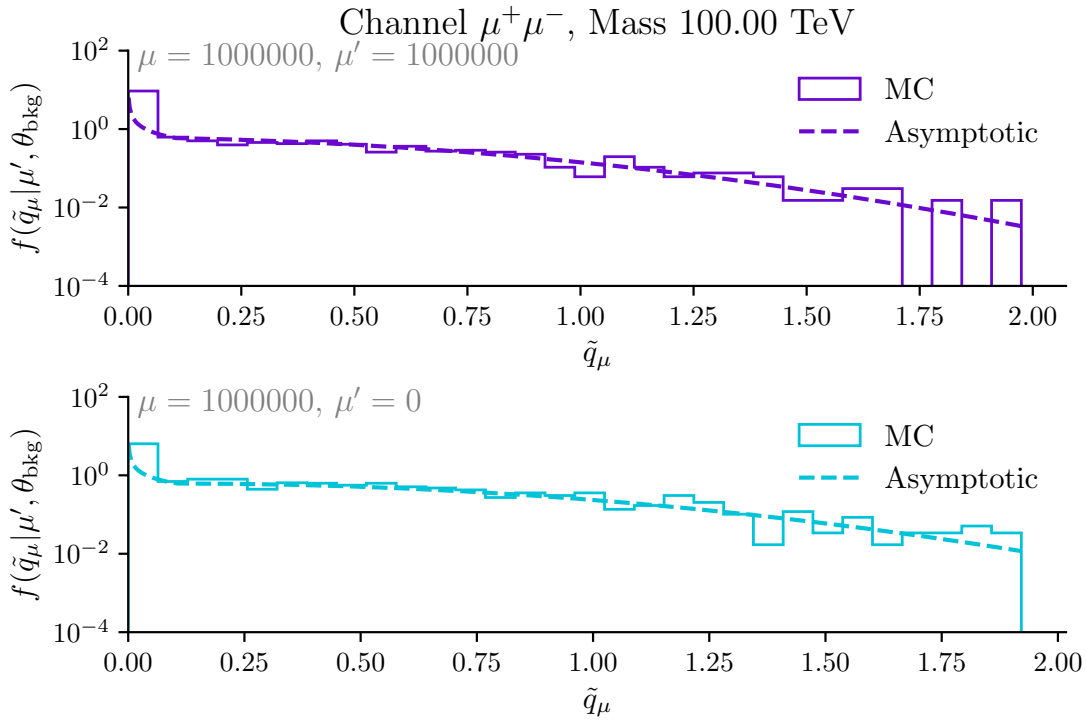

Figure E.11: (continued)

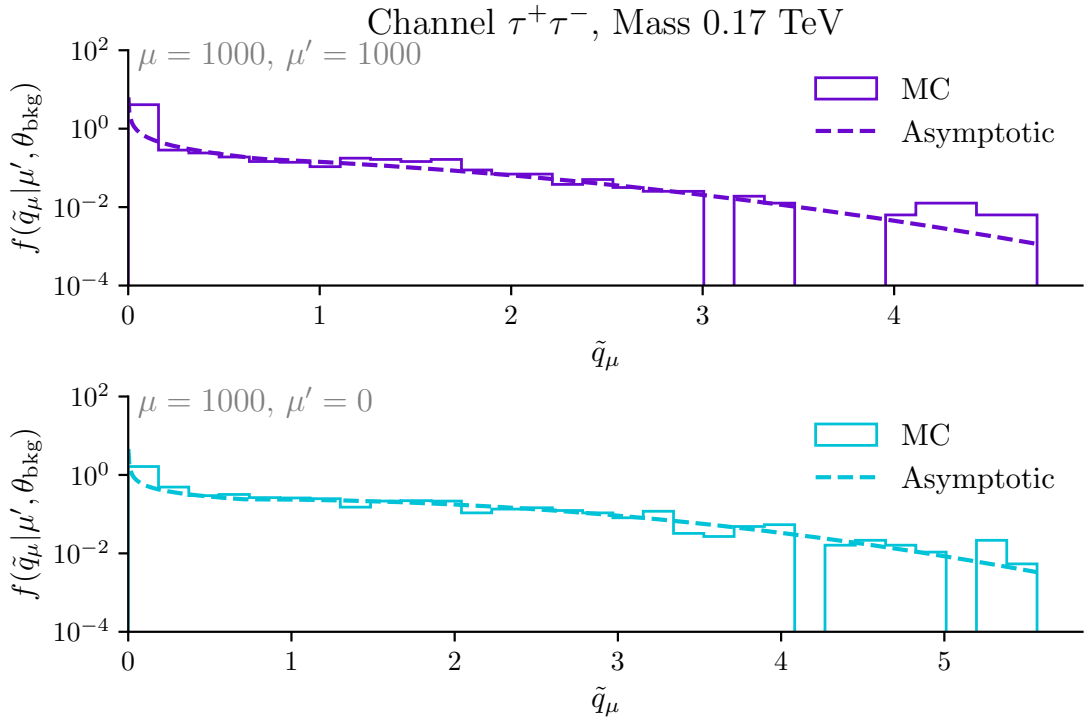

Figure E.11: (continued)

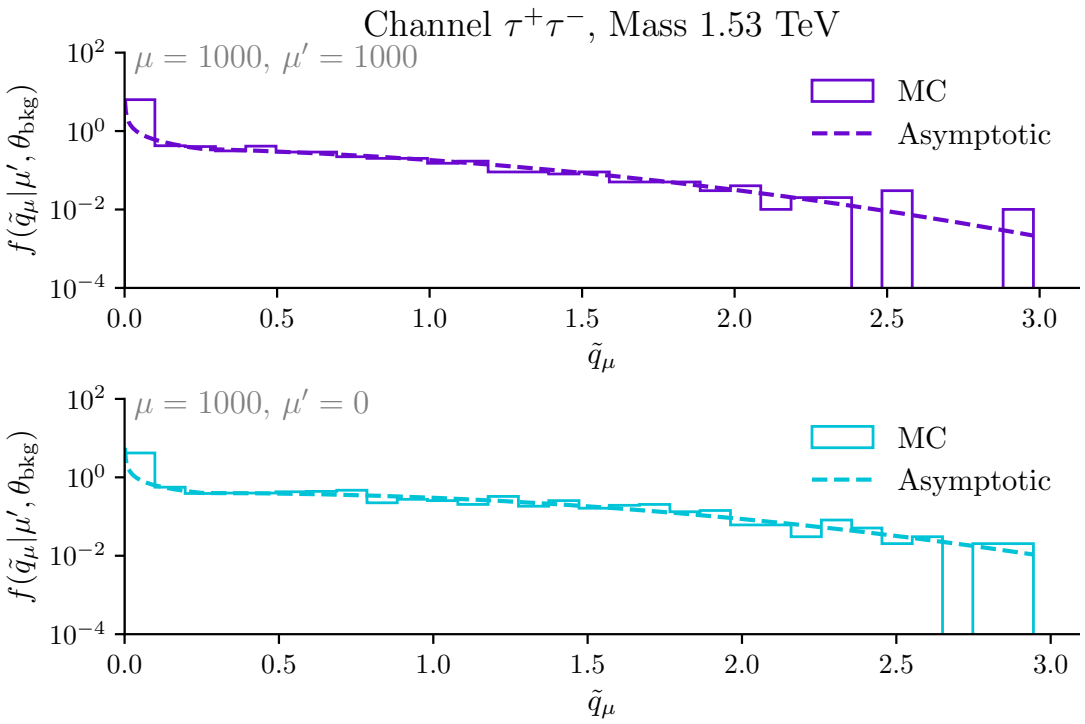

Figure E.11: (continued)

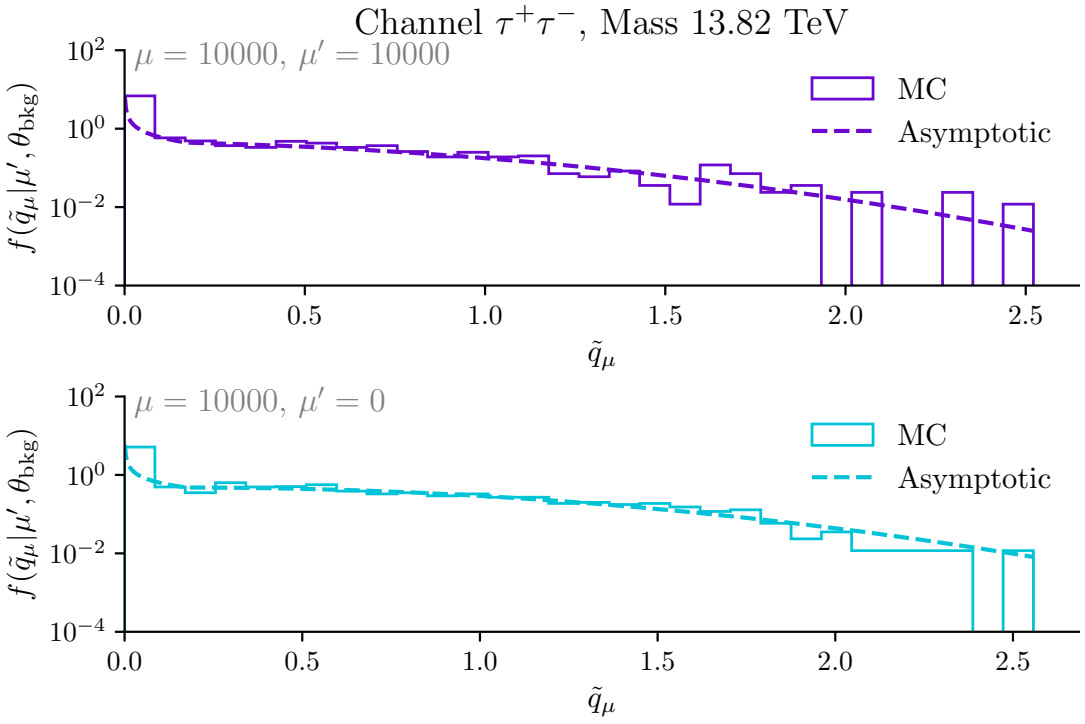

Figure E.11: (continued)

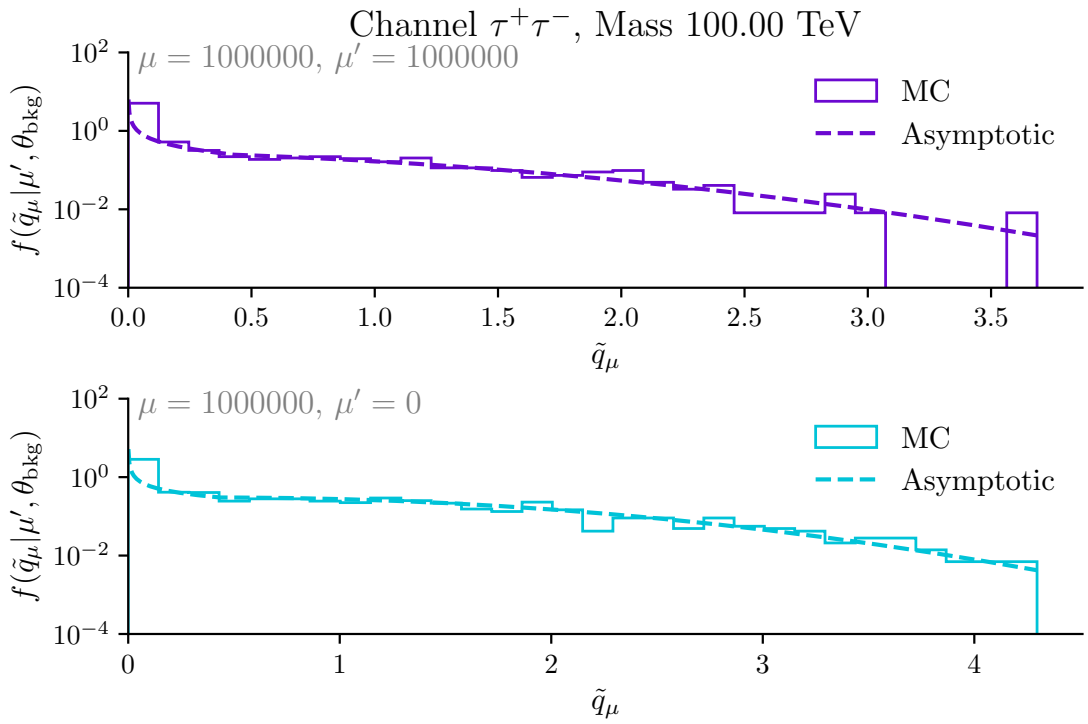

Figure E.11: (continued)

E.3 Asimov Upper Limits 1D - CL_s method

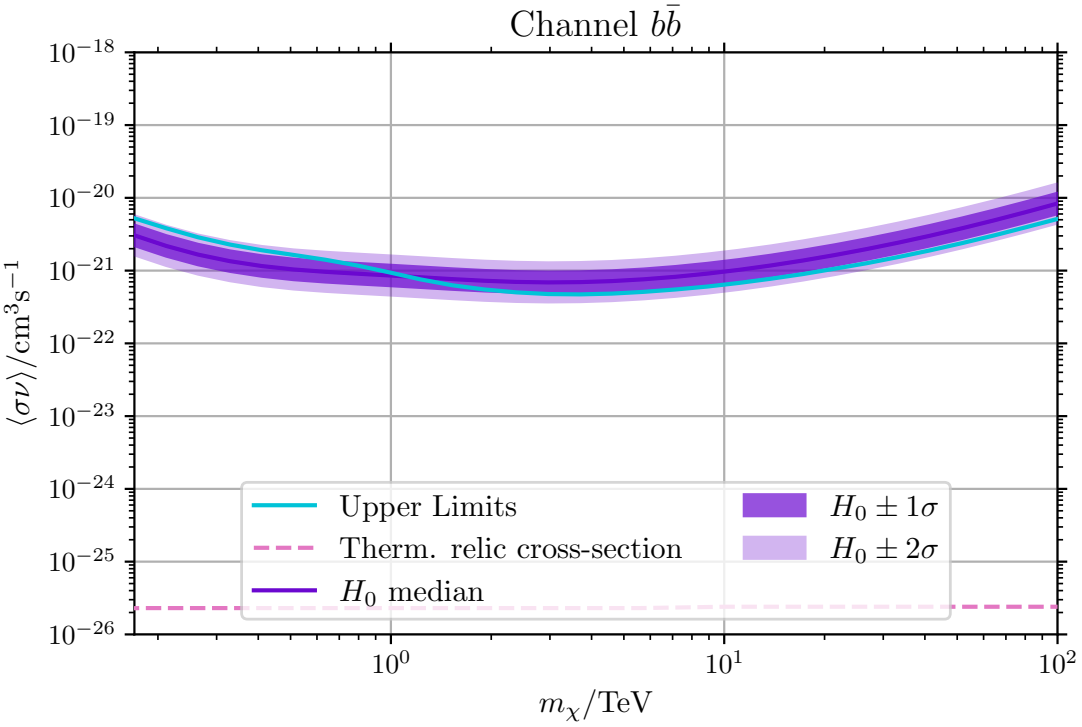

Figure E.12: CL_s ULs on the thermally averaged cross-section for annihilating DM into $b\bar{b}$, W^+W^-, $\mu^+\mu^-$, and $\tau^+\tau^-$ from $m_\chi = 0.17\,\mathrm{TeV}$ to $m_\chi = 100\,\mathrm{TeV}$. The limits are calculated using Asimov datasets on the 1D reduced CBe dSph observations. The ULs for the null hypothesis H_0 are calculated with one Asimov dataset per model.

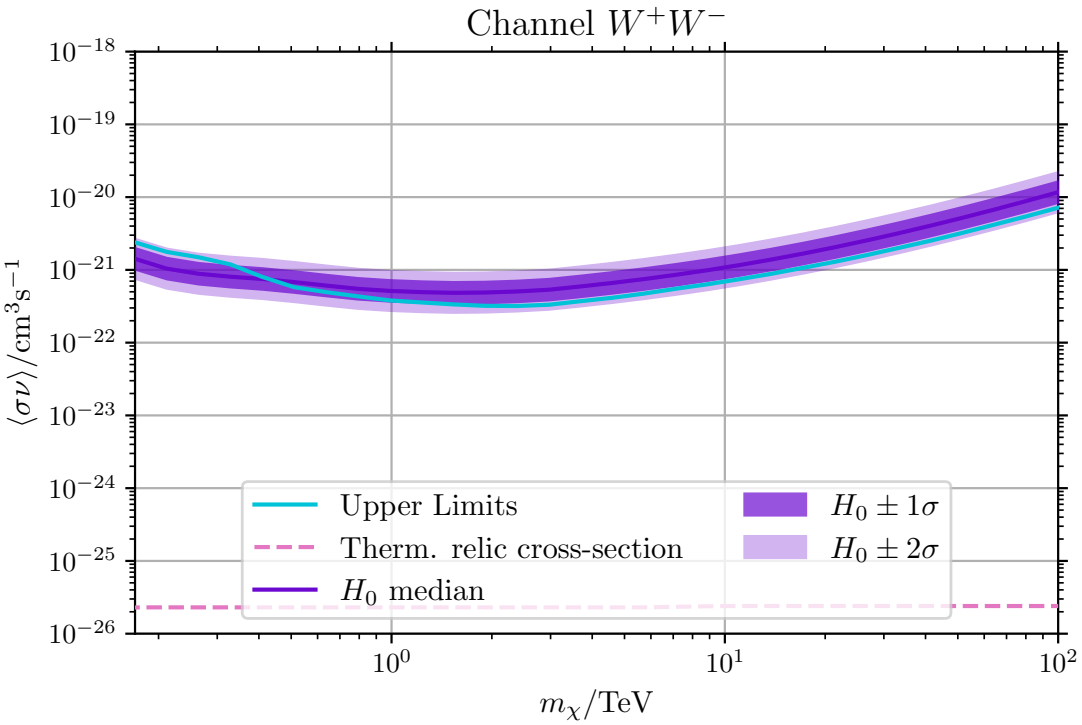

Figure E.12: (continued)

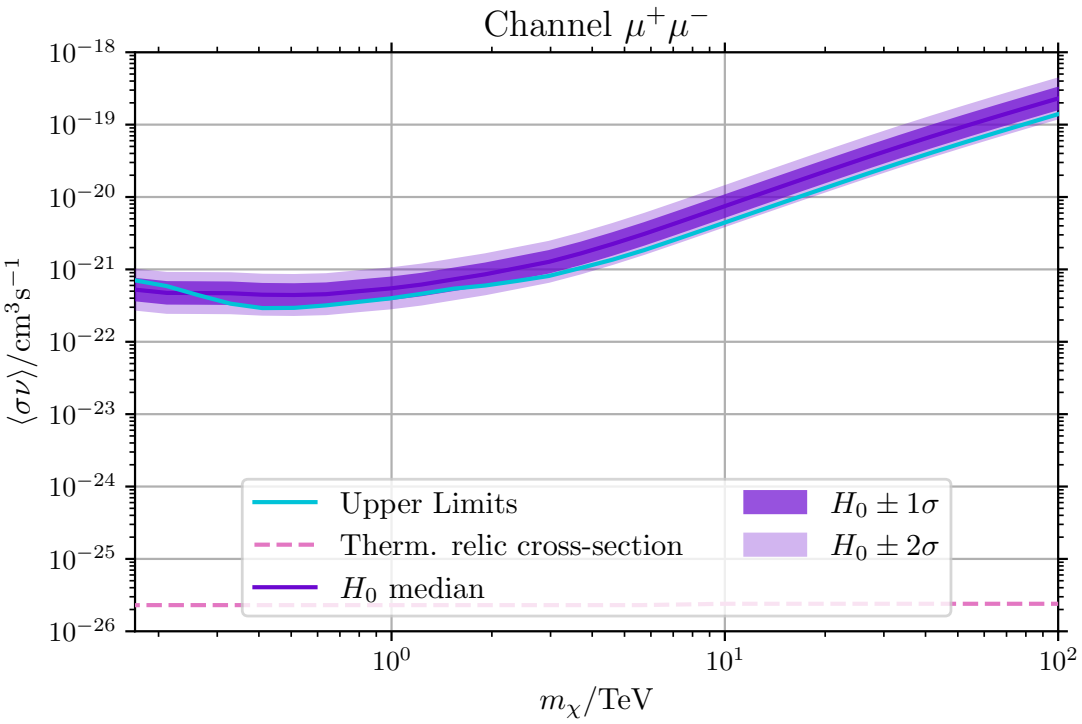

Figure E.12: (continued)

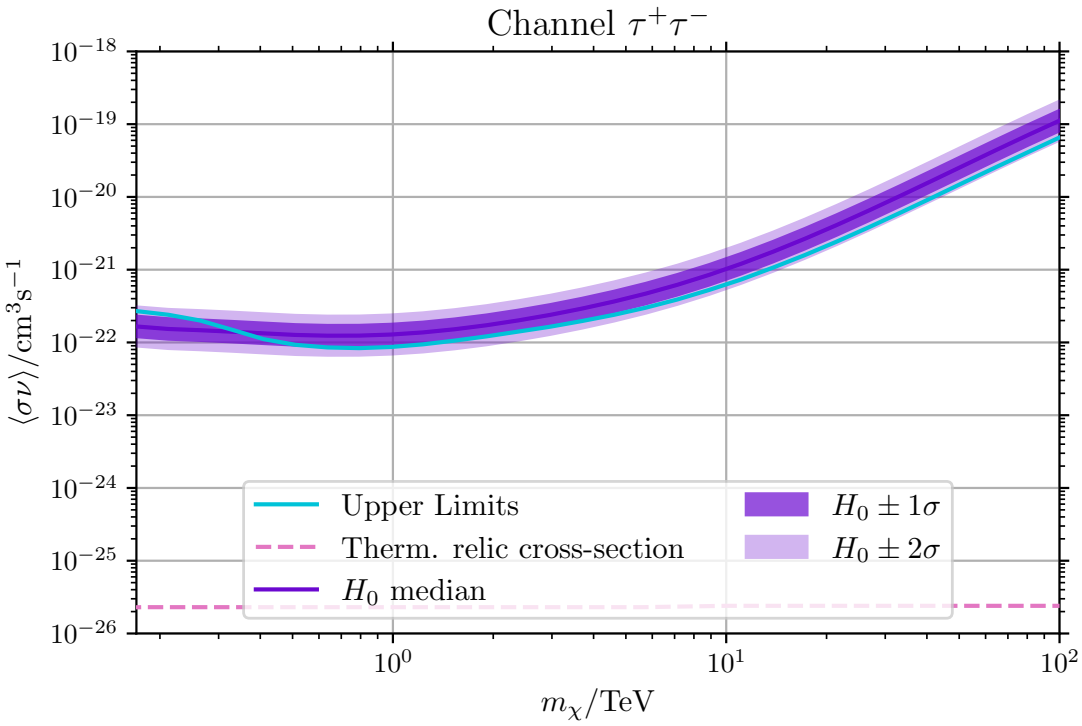

Figure E.12: (continued)

Acknowledgments

An dieser Stelle möchte ich mich gerne bei allen bedanken, die mich über die Jahre begleitet haben und ohne die ich wohl an der Abgabe dieser Dissertation gescheitert wäre.
Als erstes gilt mein Dank Dominik Elsässer! Du hast es immer wieder geschafft mich für die Astrophysik zu begeistern, was letzendlich zu der Möglichkeit geführt hat diese Dissertation bei dir zu schreiben. Danke für deine fachlichen und auch private Unterstützung bei all den Hürden, die es zu überwinden gab, und für deine Gelassenheit, wenn es darum ging Probleme zu lösen.
Auch gilt mein Dank Wolfgang Rhode für die Betreuung bei den statistischen Fragen und für die Möglichkeiten der Weiterentwicklung.
Vielen Dank an Chris Delitzsch für die Erstellung des zweiten Gutachtens dieser Arbeit und die flexible zeitliche Lösung rund um diese Dissertation.

Danke Andrea Teichmann, ohne dich würde der Laden einfach nicht laufen und auch mich hast du vor vielen Kopfschmerzen immer bewahrt. Und vor Allem danke, weil du es warst, die mich angerufen hat 2021, damit ich bei Dominik nach einer Promotionsstelle nachfrage!

An mein Büro und Alle mit denen ich es teilen durfte: Danke fürs da sein, fürs Reden, fürs Lachen! Ihr Alle habt die letzten Jahre zu tollen Erinnerungen gemacht, die mich mein Leben begleiten werden!

Simone, danke für die Hilfe am Anfang meiner Promotion, denn du hast dir für jede Frage Zeit genommen. Danke für die spannenden Gespräche und die persönlich Weiterentwicklung. (Und die ein oder andere Wette)

Jan Lukas, danke für deine Art in jeder Situation nüchtern über alles nachzudenken. Mit dir zu reden und spazieren zu gehen, wenn es mal wieder stressig wurde waren absolute Retter in jeder Situation. Um auf deine eigene Danksagung zu antworten, ich freue mich auf den nächsten Strandbesuch!

Tristan, danke für die fünf-minuten Pausen, irgendwann schaffen wir das Buch

einmal kommplett! Und danke für deine hurmorvolle Art, du hast gerade gegen Ende der Promotion es geschafft, dass ich nicht ganz die Hoffnung in die Physik verliere.

Alicia, dir möchte ich dir danken für die weltoffenen Gespräche. Du schaffst es immer wieder eine neue Perspektive aufzuzeichnen.

Pascal, Achtung Schlange! Danke, dass ich dich in Berkeley besuchen durfte. Die Zeit gehört zu einem unvergesslichen Urlaub.

Max und Lukas, vielen Danke für das Teilen eures Wissens, ohne euch hätte ich diese Analyse nicht schreiben können. Lukas, danke für die ganzen Diskussionen über Background Modelle und Upper Limits. `(message "Danke!")`

Anno, danke für die Hilfe bei allen möglichen TikZ und plotting fragen und für die Zeit im Studium, es war mir eine Freude!

Danke, an alle aus der Astroteilchen-Gruppe in Dortmund!

Danke an Anatoli Fedynitch und dem SFB1491 für die Möglichkeit für längere Zeit nach Taiwan zu kommen.

An den Hub:
Vielen Dank Martin Erdmann dafür, dass Sie mich in das ErUM-Data-Hub Team geholt haben! Ihre fachliche und menschliche Kompetenz hat mich immer beeindruckt.
Danke an das gesamte Hub Team, ihr habt mich so herzlich aufgenommen und jedes Meeting und jede School haben mir wahnsinning viel Spaß bereitet! Danke Angela und Peter für die persönlichen Gespräche und fürs Kölsch, gerne wieder! Und danke Peter für all die Diskussionen über Statistik!

Paul und Henning, danke für die jahrelange Freundschaft, ich kann mir mein Leben ohne euch nicht vorstellen und will ich auch garnicht! Ich freue mich endlich wieder etwas mehr Zeit zu finden und sie direkt in Factorio zu stecken.

Lars, „thank you for the music“, danke für deine Freundschaft und für die gemeinsamen Musicals! Ich hier freue mich bald wieder meine Zeit in Google Sheets zu stecken. Wahrscheinlich der beste Chat-Service den es gibt!

Janina, danke für die ganzen Jahre und deine Freundschaft! Es ist viel passiert in 2024 und will dir sagen: Finde deinen Weg! Du kannst das :)

An meine Familie: Danke für Alles was ihr einfach je getan habt. Danke an meine Eltern für die Unterstützung in all den Jahren und für die Möglichkeiten, die ihr mir gegeben habt. Diese Arbeit hätte es ohne euch nicht gegeben! Danke Marco

und Jasmin! Du bist der beste Bruder, den man sich nur Wünschen kann! Danke Opa, für den jahrelangen Taxi-Service und für deine Witze!

Mein letzter Dank gilt dir, Karo! Danke, dass ich dich so gut kennenlernen durfte, für dein Unterstützung das letzte Jahr und für deine Abenteuerlust. Ich freue mich mit dir die Welt zu erkunden und neue Erinnerungen mit dir zu schaffen!